

Springer Series in Materials Science 262

Xingcun Colin Tong

Functional Metamaterials and Metadevices

 Springer

Springer Series in Materials Science

Volume 262

Series editors

Robert Hull, Charlottesville, USA

Chennupati Jagadish, Canberra, Australia

Yoshiyuki Kawazoe, Sendai, Japan

Richard M. Osgood, New York, USA

Jürgen Parisi, Oldenburg, Germany

Tae-Yeon Seong, Seoul, Korea

Shin-ichi Uchida, Tokyo, Japan

Zhiming M. Wang, Chengdu, China

The Springer Series in Materials Science covers the complete spectrum of materials physics, including fundamental principles, physical properties, materials theory and design. Recognizing the increasing importance of materials science in future device technologies, the book titles in this series reflect the state-of-the-art in understanding and controlling the structure and properties of all important classes of materials.

More information about this series at <http://www.springer.com/series/856>

Xingcun Colin Tong

Functional Metamaterials and Metadevices

 Springer

Xingcun Colin Tong
Bolingbrook, IL, USA

ISSN 0933-033X ISSN 2196-2812 (electronic)
Springer Series in Materials Science
ISBN 978-3-319-66043-1 ISBN 978-3-319-66044-8 (eBook)
DOI 10.1007/978-3-319-66044-8

Library of Congress Control Number: 2017951443

© Springer International Publishing AG 2018

This work is subject to copyright. All rights are reserved by the Publisher, whether the whole or part of the material is concerned, specifically the rights of translation, reprinting, reuse of illustrations, recitation, broadcasting, reproduction on microfilms or in any other physical way, and transmission or information storage and retrieval, electronic adaptation, computer software, or by similar or dissimilar methodology now known or hereafter developed.

The use of general descriptive names, registered names, trademarks, service marks, etc. in this publication does not imply, even in the absence of a specific statement, that such names are exempt from the relevant protective laws and regulations and therefore free for general use.

The publisher, the authors and the editors are safe to assume that the advice and information in this book are believed to be true and accurate at the date of publication. Neither the publisher nor the authors or the editors give a warranty, express or implied, with respect to the material contained herein or for any errors or omissions that may have been made. The publisher remains neutral with regard to jurisdictional claims in published maps and institutional affiliations.

Printed on acid-free paper

This Springer imprint is published by Springer Nature
The registered company is Springer International Publishing AG
The registered company address is: Gewerbestrasse 11, 6330 Cham, Switzerland

*To my mother Wang BaoChun, who passed
away in 1979 from breast cancer, but
continues to live in our hearts forever.*

Preface

Metamaterials are artificially engineered composites with designed properties beyond those attainable in nature and with applications in all aspects of materials science. From spatially tailored dielectrics to tunable, dynamic material properties and unique nonlinear behavior, metamaterial systems have demonstrated tremendous flexibility and functionality in electromagnetic, optical, acoustic, thermal, and mechanical engineering. Furthermore, the field of metamaterials has been extended from the mere pursuit of various exotic properties towards the realization of practical devices, leading to the concepts of dynamically reconfigurable metadevices or functional metasurfaces. To meet the demands of students, scientists, and engineers for a systematic reference source, this book introduces, comprehensively and in a single voice, research and development progress in emerging metamaterials and derived functional metadevices. Coverage includes electromagnetic, optical, acoustic, thermal, and mechanical metamaterials and related metadevices. It explores the fundamental physics, design, and the engineering aspects, as well as the full array of state-of-the-art applications for electronics, telecommunications, antennas, and energy harvesting. Future challenges and potential in regard to design, modeling, and fabrication are also addressed.

It is my great pleasure to acknowledge all help and support I have received from my colleagues and friends who have contributed to my understanding of functional metamaterials and metadevices. I would like to express my sincere gratitude to Dr. David Packer and all other editing staff who have done a fantastic job on the publication of this book.

Bolingbrook, IL, USA

Xingcun Colin Tong

Contents

| | | |
|----------|---|-----------|
| 1 | Concepts From Metamaterials to Functional Metadevices. | 1 |
| 1.1 | Rationale for Metamaterials Exploration. | 1 |
| 1.2 | Classification of Metamaterials | 2 |
| 1.3 | Evolution of Metamaterials | 4 |
| 1.4 | Emerging Functional Metadevices. | 8 |
| 1.4.1 | Reconfigurable and Tunable Metadevices | 8 |
| 1.4.2 | Electro-Optical Metadevices | 10 |
| 1.4.3 | Liquid-Crystal Metadevices. | 12 |
| 1.4.4 | Phase-Change Metadevices | 13 |
| 1.4.5 | Superconducting Metadevices | 15 |
| 1.4.6 | Ultrafast Photonic Metadevices | 16 |
| 1.4.7 | Nonlinear Metadevices with Varactors | 18 |
| 1.4.8 | Metadevices Driven by Electromagnetic Forces | 19 |
| 1.4.9 | Acoustic Metadevice | 20 |
| | References. | 21 |
| 2 | Design and Fabrication of Metamaterials and Metadevices. | 23 |
| 2.1 | Common Design Approaches for Metamaterials. | 23 |
| 2.1.1 | Resonant Approach | 23 |
| 2.1.2 | Transmission Line Approach. | 24 |
| 2.1.3 | Hybrid Approach | 25 |
| 2.2 | General Tuning Methods for Metadevices. | 26 |
| 2.3 | Fabrication Technology | 27 |
| 2.3.1 | Photolithography | 27 |
| 2.3.2 | Shadow Mask Lithography | 27 |
| 2.3.3 | Soft Lithography | 28 |
| 2.3.4 | Electron Beam Lithography. | 30 |
| 2.3.5 | 3D Metamaterial Fabrication Techniques | 32 |
| 2.4 | Tuning Techniques. | 34 |
| 2.4.1 | Mechanical Tuning. | 34 |
| 2.4.2 | Electromechanical Displacement. | 35 |

| | | |
|----------|---|-----------|
| 2.4.3 | Lattice Displacement | 35 |
| 2.4.4 | Thermal Stimulation | 35 |
| 2.4.5 | Material Tuning | 36 |
| | References. | 36 |
| 3 | Electromagnetic Metamaterials and Metadevices | 39 |
| 3.1 | Fundamental Theory of Electromagnetic Metamaterials. | 39 |
| 3.2 | Single-Negative Metamaterials | 41 |
| 3.2.1 | Metamaterials with Negative Effective Permittivity in the Microwave Regime | 41 |
| 3.2.2 | Metamaterials with Negative Effective Permeability in the Microwave Regime | 43 |
| 3.3 | Double-Negative Metamaterials | 44 |
| 3.4 | Zero-Index Metamaterials | 45 |
| 3.5 | Electromagnetic Bandgap Metamaterials | 48 |
| 3.5.1 | Types of EBG Structures | 48 |
| 3.5.2 | Numerical Modeling of EBG. | 48 |
| 3.5.3 | EBG Applications | 50 |
| 3.6 | Bi-isotropic and Bi-anisotropic Metamaterials | 52 |
| 3.7 | Microwave Metamaterial-Inspired Metadevices | 53 |
| | References. | 55 |
| 4 | Terahertz Metamaterials and Metadevices | 57 |
| 4.1 | Introduction | 57 |
| 4.2 | Passive-Type Terahertz Metamaterials. | 58 |
| 4.2.1 | Terahertz Metamaterials with Electric Responses | 58 |
| 4.2.2 | Terahertz Metamaterials with Magnetic Responses | 59 |
| 4.2.3 | Terahertz Metamaterials with Negative Refractive Indices | 60 |
| 4.2.4 | Broadband Terahertz Metamaterials | 61 |
| 4.3 | Active-Type Terahertz Metamaterials | 62 |
| 4.3.1 | Electrically Tunable THz Metamaterials | 63 |
| 4.3.2 | Optically Tunable THz Metamaterials. | 65 |
| 4.3.3 | Mechanically Tunable THz Metamaterials | 67 |
| 4.4 | Flexible THz Metamaterials. | 68 |
| | References. | 70 |
| 5 | Photonic Metamaterials and Metadevices | 71 |
| 5.1 | Introduction | 71 |
| 5.2 | Photonic Crystals | 73 |
| 5.2.1 | A Historical Account | 74 |
| 5.2.2 | Construction of Photonic Crystals | 75 |
| 5.2.3 | Applications of Photonic Crystals | 77 |
| 5.3 | Metamaterials Designed Through Transformation Optics. | 77 |
| 5.3.1 | Metamaterials Mimicking Celestial Mechanics. | 78 |
| 5.3.2 | Metamaterial Gradient Index Lensing | 79 |
| 5.3.3 | Battlefield Applications | 79 |

- 5.4 Hyperbolic Metamaterials 80
 - 5.4.1 Hyperbolic Media in Retrospect 80
 - 5.4.2 Design and Building Materials 83
 - 5.4.3 Photonic Hypercrystals 85
 - 5.4.4 Applications of Hyperbolic Metamaterials 87
- 5.5 Superconducting and Quantum Metamaterials 90
 - 5.5.1 Low-Loss Metamaterials 92
 - 5.5.2 Compact Meta-Atom Structure 93
 - 5.5.3 Superconducting Metamaterials with Nonlinearity
and Tenability. 94
 - 5.5.4 Superconducting Metamaterials with Magnetic Flux
Quantization and Josephson Effect 95
 - 5.5.5 Diamagnetic Metamaterials 95
 - 5.5.6 Quantum Metamaterials. 96
- 5.6 Nanomechanical Photonic Metamaterials 99
 - 5.6.1 Electrostatic Actuation. 101
 - 5.6.2 Thermal Actuation 102
 - 5.6.3 Magnetic Actuation 103
 - 5.6.4 Optical Actuation 104
- References. 105
- 6 Chiral Metamaterials and Metadevices 107**
 - 6.1 Historical Perspective 107
 - 6.2 Chirality Parameter and Ellipticity 108
 - 6.3 Typical Chiral Metamaterials. 109
 - 6.3.1 Chiral Metamaterials with Negative Refractive Index. 109
 - 6.3.2 3D Chiral Metamaterials 112
 - 6.3.3 Self-assembled Chiral Metamaterials 114
 - 6.3.4 Gyroid Metamaterials 117
 - 6.3.5 Nonlinear Chiral Metamaterials. 118
 - 6.4 Chiroptical Effects 118
 - 6.4.1 Extrinsic Chirality 118
 - 6.4.2 Superchiral Fields 120
 - 6.5 Typical Applications of Chiral Metamaterials 121
 - 6.5.1 Chiral Metamaterial Sensors 121
 - 6.5.2 Nonlinear Optics in Chiral Metamaterials 121
 - 6.5.3 Chiral Light–Matter Interactions 122
 - 6.5.4 Active Chiral Metamaterials 125
 - References. 127
- 7 Plasmonic Metamaterials and Metasurfaces 129**
 - 7.1 Plasmonic Meta-atoms and Their Interactions 129
 - 7.2 Plasmonic Metamaterials Implementing Negative Refraction
and Negative Refractive Index 131
 - 7.3 Plasmonic Metasurfaces. 134
 - 7.4 Graphene-based Plasmonic Metamaterials 139

| | | |
|----------|---|------------|
| 7.5 | Self-assembled Plasmonic Metamaterials | 143 |
| 7.6 | Application Perspective | 146 |
| 7.6.1 | Optical Nanocircuits and Nanoantennas | 146 |
| 7.6.2 | Functional Metasurfaces | 150 |
| 7.6.3 | Plasmonic Metamaterials for Sensing | 152 |
| | References. | 152 |
| 8 | Metamaterials Inspired Frequency Selective Surfaces | 155 |
| 8.1 | Evolution of Frequency Selective Surfaces | 155 |
| 8.2 | Design of Metamaterial-Based Miniaturized-Element Frequency Selective Surfaces | 158 |
| 8.3 | Printed Flexible and Reconfigurable Frequency Selective Surfaces | 160 |
| 8.4 | Metamaterials Inspired FSS Antennas and Circuits. | 164 |
| 8.4.1 | Ultra-Wideband Antennas and Microstrip Filters | 165 |
| 8.4.2 | Microstrip Antennas with HIS Ground Plane | 165 |
| 8.4.3 | Fabry–Pérot Antenna | 166 |
| 8.5 | Metamaterials Inspired Microfluidic Sensors | 167 |
| 8.6 | Metamaterials Inspired Rotation and Displacement Sensors. | 170 |
| | References. | 170 |
| 9 | Nonlinear Metamaterials and Metadevices | 173 |
| 9.1 | Introduction | 173 |
| 9.2 | Implementation Approaches to Manufacture Nonlinear Metamaterials. | 174 |
| 9.2.1 | Insertion of Nonlinear Elements | 174 |
| 9.2.2 | Nonlinear Host Medium | 175 |
| 9.2.3 | Local Field Enhancement | 177 |
| 9.2.4 | Nonlinear Transmission Lines | 178 |
| 9.2.5 | Intrinsic Structural Nonlinearity | 179 |
| 9.2.6 | Nonlinear Metamaterials with Quantum and Superconducting Elements | 180 |
| 9.3 | Nonlinear Responses and Effects. | 180 |
| 9.3.1 | Nonlinear Self-Action | 180 |
| 9.3.2 | Frequency Conversion and Parametric Amplification | 182 |
| 9.3.3 | Surface Effects | 185 |
| 9.3.4 | Nonlinear Guided Waves and Solitons. | 187 |
| 9.3.5 | Discreteness Effects. | 187 |
| 9.4 | Applications of Nonlinear Metamaterials Toward Functional Metadevices | 188 |
| 9.4.1 | Controlling Light with Nonlinear Metamaterials | 188 |
| 9.4.2 | Nonlinear Terahertz Metadevices | 191 |
| 9.4.3 | Control of Quantum Dot Emission | 194 |
| 9.4.4 | Metamaterial RF Limiter | 195 |
| 9.4.5 | Metamaterials-Based Energy Harvesting. | 196 |
| 9.4.6 | Nonlinear Metamaterials for Holography | 198 |
| | References. | 199 |

10 Acoustic Metamaterials and Metadevices 201

10.1 Historical Perspective and Basic Principles 201

10.2 Dynamic Negative Density and Compressibility 202

10.3 Membrane-Type Acoustic Materials 204

10.4 Transformation Acoustics and Metadevices with Spatially Varying Index 209

10.5 Space-Coiling and Acoustic Metasurfaces 210

10.6 Acoustic Absorption 212

10.7 Active Acoustic Metamaterials 214

10.8 Emerging Directions and Future Trends 214

10.8.1 Nonlinear Acoustic Metamaterials 214

10.8.2 Nonreciprocal Acoustic Devices 215

10.8.3 Elastic and Mechanical Metamaterials 215

10.8.4 Graphene-Inspired Acoustic Metamaterials 215

10.8.5 Acoustic Metamaterials with Characteristics Describable by non-Hermitian Hamiltonians 216

10.8.6 Future Trends 216

References 217

11 Mechanical Metamaterials and Metadevices 219

11.1 Introduction 219

11.2 Auxetic Mechanical Metamaterials 221

11.2.1 Reentrant Structures 222

11.2.2 Auxetic Chiral Structures 226

11.2.3 Rotating Rigid and Semirigid Auxetic Structures 228

11.2.4 Dilational Metamaterials 228

11.2.5 Potential Applications of Auxetic Metamaterials 230

11.3 Penta-Mode Metamaterials 230

11.4 Ultra-Property Metamaterials 232

11.5 Negative-Parameter Metamaterials 233

11.6 Mechanical Metamaterials with Tunable Negative Thermal Expansion 234

11.7 Active, Adaptive, and Programmable Metamaterials 236

11.8 Origami-Based Metamaterials 237

11.9 Mechanical Metamaterials as Seismic Shields 239

11.10 Future Trends 239

References 241

12 Perspective and Future Trends 243

12.1 Emerging Metamaterials Capabilities and new Concepts 243

12.1.1 Virtual Photon Interactions Mediated by Metamaterials 243

12.1.2 Routes to Aperiodic and Correlation Metamaterials 244

12.1.3 Mathematical Operations and Processing with Structured Metamaterials 246

12.1.4 Topological Effects in Metamaterials 248

- 12.2 Manipulation of Metasurface Properties 250
 - 12.2.1 Functionally Doped Metal Oxides for Future Ultrafast Active Metamaterials 250
 - 12.2.2 Optical Dielectric Metamaterials and Metasurfaces 252
 - 12.2.3 Beam Shaping with Metasurfaces 254
 - 12.2.4 Control of Emission and Absorption with Metamaterials. 256
 - 12.2.5 Control of Far-Field Thermal Emission Properties through the use of Photonic Structures 257
- 12.3 Research Trends of Nonlinear, Active and Tunable Properties 257
 - 12.3.1 Engineering Mid-Infrared and Optical Nonlinearities with Metamaterials. 257
 - 12.3.2 Directional Control of Nonlinear Scattering from Metasurfaces 259
 - 12.3.3 Coherent Control in Planar Photonic Metamaterials 260
 - 12.3.4 Nanomechanical Photonic Metamaterials 261
- 12.4 Emerging Metadevices and Applications. 262
 - 12.4.1 RF Beam Steering Module with Metamaterials Electronically Scanned Array 262
 - 12.4.2 Smart Metamaterial Antennas 263
 - 12.4.3 Energy Harvesting Enhanced with Metamaterials. 263
 - 12.4.4 Focus Magnetic Stimulation 264
 - 12.4.5 Thermophotovoltaics 264
 - 12.4.6 Transparent Thermal Barrier 265
 - 12.4.7 Passive Radiative Cooling 265
- 12.5 Prospective Manufacturing and Assembly Technologies of Metamaterials and Metadevices 265
 - 12.5.1 Nanoparticles for Complex Multimaterial Nanostructures 265
 - 12.5.2 Eutectics as Metamaterials. 266
 - 12.5.3 Large Area Roll-to-Roll Processing. 268
- References. 268

Index 271

Abbreviations

| | |
|-------|--|
| 2DEG | Two-dimensional electron gas |
| AANR | All-angle negative refraction |
| ADM | All-dielectric metamaterial |
| AFM | Atomic force microscope |
| ALCP | Absorbance of left circularly polarized (light) |
| AM | Additive manufacturing |
| AMC | Artificial magnetic conductor |
| AMM | Acoustic metamaterials |
| AOS | Amorphous oxide semiconductors |
| API | Active pharmaceutical ingredient |
| ARCP | Absorbance of right circularly polarized (light) |
| AZO | Aluminum-doped zinc oxide |
| BSCCO | Bismuth strontium calcium copper oxide |
| BST | Barium strontium titanate ($\text{Ba}_{0.5}\text{Sr}_{0.5}\text{TiO}_3$) |
| CAM | Cavity array metamaterial |
| CCW | Coupled cavity waveguide |
| CD | Circular dichroism |
| CDZM | Conjugated double Z metasurface |
| CELC | Complementary electric field-coupled |
| CFSS | Curved frequency selective surface |
| CIPT | Continuous-index photon trap |
| CL | Cathodoluminescence |
| CMC | Constant mean curvature |
| CMOS | Complementary metal–oxide–semiconductor |
| CMR | Coupled magnetic resonance |
| COC | Cyclic olefin copolymer |
| CPS | Coplanar stripline |
| CPW | Coplanar waveguide |
| CRLH | Composite right/left-handed |
| CSRR | Complementary or composite split ring resonator |
| CTE | Coefficient of thermal expansion |

| | |
|------|--|
| CW | Cut wire; continuous-wave |
| DC | Direct current |
| DIW | Direct ink writing |
| DLW | Direct laser writing |
| DMR | Decorated membrane resonator |
| DNA | Deoxyribonucleic acid |
| DNGM | Double negative material or left-handed metamaterial |
| DVD | Digital versatile disc |
| ENGM | Epsilon negative material or electrical metamaterial |
| EBG | Electromagnetic band gap |
| EBL | Electron beam lithography |
| EBM | Electron Beam Melting |
| ECS | Environmental control system |
| EELS | Electron energy-loss spectroscopy |
| EH | Energy harvesting |
| ELC | Electric-field-coupled; electronic liquid crystal |
| EIT | Electromagnetically induced transparency |
| EM | Electromagnetic wave |
| EMI | Electromagnetic interference |
| EMT | Effective medium theory |
| ENP | ϵ -near-pole |
| ENZ | ϵ -near-zero |
| EPD | Electrophoretic deposition |
| ESRR | Electric split ring resonator |
| EWE | Evanescence wave enhancement |
| FACT | Freedom, actuation, and constraint topologies |
| FDTD | Finite difference time domain |
| FF | Fundamental frequency |
| FH | Fundamental harmonic |
| FIB | Focused ion beam |
| FMS | Focus magnetic stimulation |
| FOM | Figure of merit |
| FPGA | Field programmable gate array |
| FPR | Fabry-Perot resonator |
| FSS | Frequency selective surface |
| FZP | Fresnel zone plate |
| GND | Gold ground plane |
| GoSM | Graphene on a silicon membrane |
| GPS | Global positioning system |
| GRIN | Gradient index |
| GST | Germanium-antimony-tellurium (GeSbTe) |
| GZO | Gallium-doped zinc oxide |
| HBV | Heterostructure barrier varactor |
| HIS | High-impedance surface |
| HMM | Hyperbolic metamaterial |

| | |
|-------|--|
| HTS | High-temperature superconductor |
| IDC | Interdigitated capacitor |
| IGZO | In-Ga-Zn-O |
| IMI | Impact ionization |
| IR | Infrared |
| ITO | Tin-doped indium oxide |
| IZO | Indium-doped zinc oxide |
| KKR | Korringa–Kohn–Rostoker (method) |
| LC | Liquid crystal, inductive-capacitive |
| LCP | Left circularly polarized |
| LED | Light-emitting diode |
| LHM | Left handed media or left-handed material/metamaterial |
| LHTL | Left-handed transmission line |
| LSP | Localized surface plasmon |
| LWA | Leaky wave antennae |
| MBE | Molecular beam epitaxy |
| MDM | Metal-dielectric-metal |
| MEMS | Microelectromechanical systems(s) |
| MESA | Metamaterial electronically scanned array |
| ML | Modular layer; multilayer |
| MNGM | Mu-negative material or magnetic metamaterial |
| MoSM | Metamaterial on a silicon membrane |
| MPA | Microstrip patch antenna |
| MoM | Method of moments |
| MPL | Membrane projection lithography |
| MQW | Multi-quantum-well |
| MTM | Metamaterial |
| MWPT | Microwave wireless power transmission |
| NEMS | Nanoelectromechanical systems |
| NIM | Negative index metamaterial |
| NIR | Near infrared |
| NLPC | Nonlinear photonic crystal |
| NLMPC | Nonlinear metamaterial-based photonic crystal |
| NSOM | Near-field scanning optical microscopy |
| NP | Nanoparticle |
| NW | Nanowire |
| OAM | Orbital angular momentum |
| OTT | Optical topological transition |
| PBC | Periodic boundary condition |
| PCB | Printed circuit board |
| PDMS | Polydimethylsiloxane |
| PDOS | Photonic density of states |
| PDS | Photonic density of states |
| PEN | Polyethylene naphthalene |
| PET | Polyethylene terephthalate |

| | |
|--------|---|
| PhC | Photonic crystal |
| PI | Polyimide |
| PML | Perfectly matched layer |
| PMMA | Polymethyl methacrylate |
| PmSL | Projection microstereolithography |
| PSMM | Plasmonic semiconductor metamaterial |
| PV | Photovoltaics |
| PVP | Polyvinylpyrrolidone |
| QD | Quantum dot |
| QSHE | Quantum spin Hall effect |
| RCP | Right circularly polarized |
| RF | Radio frequency |
| RHM | Right handed media or right handed material |
| RIU | Refractive index unit |
| SAM | Spin angular momentum |
| SEM | Scanning electron microscope |
| SG | Single gyroid |
| SH | Second harmonic |
| SHG | Second-harmonic generation |
| SHE | Spin Hall effect |
| SLR | Surface lattice resonance |
| SML | Shadow mask lithography |
| SNGM | Single negative metamaterial |
| SPP | Surface plasmon polariton |
| SQUID | Superconducting quantum interference device |
| SRDS | Split ring resonators with double splits |
| SRR | Split-ring resonator |
| TCO | Transparent conductive oxide |
| TE | Transverse electric |
| TFT | Thin-film transistor |
| TL | Transmission line |
| TM | Transverse magnetic |
| TMN | Transition metal nitride |
| TO | Topology optimization |
| VAEH | Vibroacoustic energy harvesting |
| UHMWPE | Ultra-high molecular weight polyethylene |
| UV | Ultraviolet |
| WPT | Wireless power transmission |
| ZEP | 1:1 copolymer of α -chloromethacrylate and α -methylstyrene, a highly sensitive, stable, and durable positive-tone resist |
| ZIM | Zero-index medium (metamaterial) |

Chapter 1

Concepts From Metamaterials to Functional Metadevices

1.1 Rationale for Metamaterials Exploration

A metamaterial is a heterogeneous hybrid material that can be designed and manipulated to obtain extraordinary properties arising from the combination of its structure and composition beyond those that a classical composite of the same constituent materials exhibits. “Meta” comes from Greek and means “beyond” or “more than.” The metamaterial generally has several key distinguishable properties (Vehmas 2015): (a) metamaterials are artificial composite materials consisting of inclusions called meta-atoms or metamolecules, which can be either periodically or randomly organized (amorphous) and are layered with or embedded into some dielectric materials; (b) as the meta-atoms are structured on a size scale smaller than the wavelength of external stimuli, metamaterials can be treated as effectively homogeneous materials at the frequency of operation and can, therefore, be characterized by some effective material parameters (i.e., artificial composites can be considered as metamaterials only when operating below a certain frequency); (c) metamaterials exhibit properties found neither in their constituent materials nor in conventional natural materials (excluding some very specific, rare, and usually unstable substances such as plasma); and (d) metamaterials are innately dispersive unless active elements are included.

Metamaterials have become an emerging technology with applications in a range of diverse areas (KTN 2015). Since the early work of Veselago in the 1960s in conceptualizing materials with negative electromagnetic parameters, and the later work by Pendry in developing practical manifestations of metamaterials, the field has mushroomed—encompassing areas but not limited to electromagnetic metamaterials, such as RF and microwave, terahertz and infrared, optics, acoustics, thermal, and mechanical metamaterials with negative compressibility and auxetics, for instance.

Electromagnetic metamaterials have been the most explored, exhibiting properties not available in natural systems such as negative permeability and permittivity and displaying anomalous behavior, such as negative refraction, superlensing,

backward wave propagation, and reverse Doppler shifting. As a result, there are many applications including energy harvesting, object cloaking, high data rate communications, sensors and detectors, imaging, anti-vibration, noise reduction, seismic protection and antennae, and more, which can be implemented using metamaterials technologies (KTN 2015). Though metamaterials have their roots in electromagnetics and the term metamaterial is often considered synonymous with the more exact term electromagnetic metamaterial, the metamaterial concept has also been extended to many other fields of physics such as thermodynamics, acoustics, and mechanics (Vehmas 2015). Metamaterials can either be used to improve the performance of existing applications or in some cases to allow the design of radically new devices and structures. Hence the exploration in the area of metamaterials is expanding, and the maturation of the technologies is leading to a wide range of applications from healthcare, information technology, automotive, communications, aerospace to defense.

1.2 Classification of Metamaterials

The initial prediction of a possibility of negative refractive index and the early work of flat lenses based on negative-index materials (NIMs) stimulated the development of the entire field of metamaterials. Various types of metamaterials have been explored, such as electromagnetic metamaterials through manipulation of transverse waves from radio waves, microwaves, tetra waves, infrared waves to visible light waves; acoustic metamaterials manipulated with longitudinal waves associated with vibrations seismic metamaterials (transverse and longitudinal waves), and more and more emerging metamaterials like thermal metamaterials and mechanical metamaterials. Here electromagnetic metamaterials would be taken as a representative to demonstrate the classification methodology of the metamaterials.

Any electromagnetic wave can be expressed by Maxwell equation:

$$\nabla^2 \Psi + n^2 \frac{\omega^2}{c^2} \Psi = 0 \quad (1.1)$$

Where

$$n^2 = \epsilon\mu \quad (1.2)$$

The response of any material to applied electromagnetic wave can be characterized by two electromagnetic parameters, magnetic permeability μ and electric permittivity ϵ . These two physical characteristics are combined in a product to define the square of a refractive index $n = \pm\sqrt{\epsilon\mu}$, which measures how fast the material transmits light and how light is bent on entering the material—the higher the refractive index, the slower the propagation and the stronger the deflection. With different

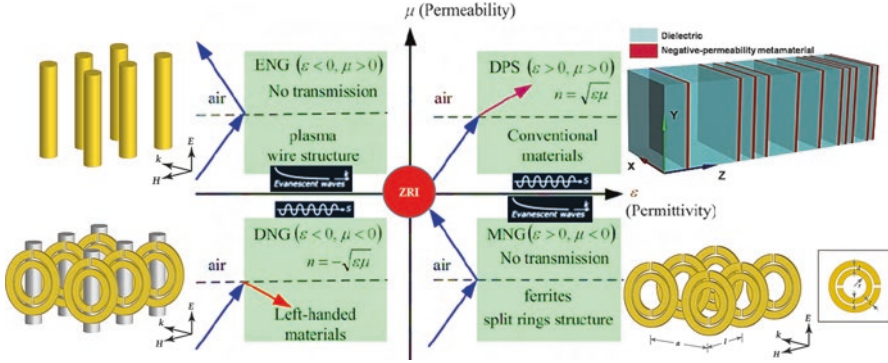


Fig. 1.1 Classification of electromagnetic metamaterials on the basis of permeability (μ) and permittivity (ϵ) (Chen et al. 2014)

permittivity ϵ and permeability μ , the classification of metamaterials can be graphically illustrated as shown in Fig. 1.1.

Materials with simultaneously positive permittivity and permeability ($\epsilon > 0$, $\mu > 0$) are called as double positive (DPS) materials or right-handed metamaterials (RHM). Abundant naturally occurring materials like most dielectrics fall under this designation.

Materials with permittivity less than zero and permeability greater than zero ($\epsilon < 0$, $\mu > 0$) are called as epsilon-negative (ENG) materials or electrical metamaterials. In certain frequency regimes, limited natural materials like many electrical plasmas exhibit these characteristics, such as noble metals at optical wavelengths, ferroelectric materials, and doped semiconductors at certain frequencies below the plasma frequency.

Materials with permittivity greater than zero and permeability less than zero ($\epsilon > 0$, $\mu < 0$) are called as Mu-negative (MNG) materials or magnetic metamaterials—not naturally occurring at optical frequencies. In certain frequency regimes, some gyrotropic or ferrite materials exhibit this characteristic. The magnetic responses of which, however, quickly fade away above microwave frequencies.

Materials with both permittivity and permeability less than zero ($\epsilon < 0$, $\mu < 0$) are called as double-negative (DNG) materials or left-handed metamaterials (LHM). This class of materials has only been demonstrated with artificial constructs. In nature there is no such material. However, the Maxwell’s wave Eqs. (1.1) or (1.2) is equally valid for signal propagation both in case of RHM and LHM.

When $\epsilon \rightarrow 0$ or $\mu \rightarrow 0$, and/or both is close or equal to zero, metamaterials with near-zero refractive index or zero refractive index can be obtained. Light inside such materials experiences no spatial phase change and extremely large phase velocity, as well as properties that can be applied for realizing directional emission, tunneling waveguides, large area single-mode devices, and electromagnetic cloaks (Moitra et al. 2013). In other words, when a material’s refractive index is reduced to zero, there is no phase advance, meaning light no longer behaves as a moving wave,

traveling through space in a series of crests and troughs. Instead, the zero-index material creates a constant phase—all crests or all troughs—stretching out in infinitely long wavelengths. The crests and troughs oscillate only as a variable of time, not space. This uniform phase allows the light to be stretched or squashed and twisted or turned, without losing energy. A zero-index material that fits on a chip could have exciting applications, especially in the world of quantum computing (Li et al. 2015).

Another criterion of metamaterial classification is the dimensionality of the array of constituents which form the bulk (3D) structures are structures with a large number of constitutive elements in any direction. Surface (2D) materials correspond to the case when the structure is a thin film with only 1–3 constitutive elements across its thickness. Metamaterials of the surface type are usually called metasurfaces or metafilms. Linear (1D) structures with nano-sized inclusions are optical waveguides with nanoinclusions and plasmonic and polaritonic nanochains. They are also called metawaveguides.

Based on the domain of functional applications, metamaterials have been investigated from negative-index metamaterials, chiral metamaterials, designer dispersion metamaterials, artificial magnetism, and transformation optics metamaterials to emerging research areas such as metamaterial light sources, as well as sensor, memory, and phase change, MEMS and NEMS, nonlinear and switchable, and superconducting and quantum metamaterials. The next stage of this technological revolution will be the development of active, controllable, and nonlinear metamaterials surpassing natural media as platforms for optical data processing and quantum information applications. Metamaterials are expected to have an impact across the entire range of technologies where electromagnetic radiation is used and will provide a flexible platform for modeling and mimicking fundamental physical effects as diverse as superconductivity and cosmology and for templating electromagnetic landscapes to facilitate observations of phenomena that would otherwise be difficult to detect (Zheludev 2010).

Again, the term metamaterial is also used in connection with artificial materials designed to exhibit advantageous and unusual properties for waves of other nature, for example, photonic metamaterials have been designed to control sound waves. Sometimes waves of other nature provoke electromagnetic waves (sound waves in piezoelectric or spin waves in nanostructured magnetic materials), and there is no solid boundary between electromagnetic and non-electromagnetic materials. An analogous classification can be suggested for non-electromagnetic metamaterials, such as acoustic metamaterials, mechanical metamaterials, and other emerging metamaterials.

1.3 Evolution of Metamaterials

The origin of metamaterials can be dated back centuries ago, examples like Pyramid brick wall, Parthenon columns, and medieval ruby glass, as shown in Fig. 1.2. Furthermore, the work on rotation of the plane of polarization by artificial twisted

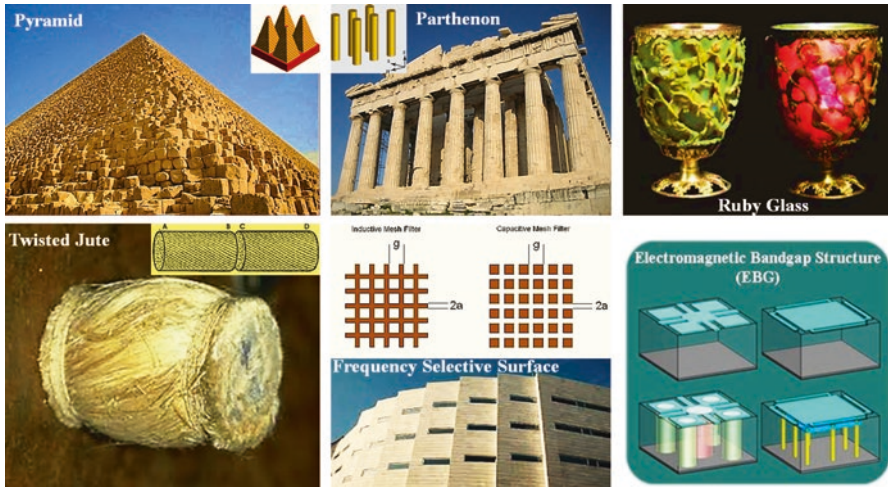


Fig. 1.2 Examples of original metamaterials (Leonhardt 2007; Wu 2016)

structures in 1898 and artificial dielectrics for microwave antenna lenses in 1945, as well as later artificial structured electromagnetic materials such as frequency selective surfaces (FSS) and electromagnetic band gap (EBG) structures, are other examples of metamaterials. However, the modern metamaterial (formally named) caused attention when Prof. Pendry and his team predicted that conducting wire arrays can work as a relatively lower frequency plasma (<200 THz) with a negative value of effective permittivity, while arrays of split-ring resonators (SRRs) can support strong magnetic resonances leading to a negative value of effective permeability. By combining these two structures and overlapping the frequency bands of negative permittivity and permeability, the first modern metamaterial with negative refractive index was demonstrated in 2000; in a negative-index medium, the directions of wave vector and energy flux are opposite, which is also known as backward waves. These proved predictions of exotic behavior for negative-index materials by Prof. Veselago in 1968, such as negative refraction, reversed Doppler effect, and reversed Cherenkov radiation (Liu 2015).

The approach for pushing the concept of negative refractive index toward higher frequencies was initially to scale down unit cell sizes from the microwave regime (such as SRRs), as the magnetic resonance frequency of the SRR is inversely proportional to its size. For example, changing the double SRR to a single one and reducing the size of the structure, the metamaterials were realized from microwave, to THz range and near-infrared optical range (up to 200THz). However, this scaling the single SRRs breaks down for higher frequencies because, for wavelengths shorter than the 200 THz range, the metal starts to strongly deviate from an ideal conductor. For a small SRR, non-ideal metal behavior leads to a modified scaling law where the frequency approaches a constant and becomes independent of the SRR size. This scaling limit combined with the fabrication difficulties of making nanometer-scale SRRs along with metal wires led to the development of alternative

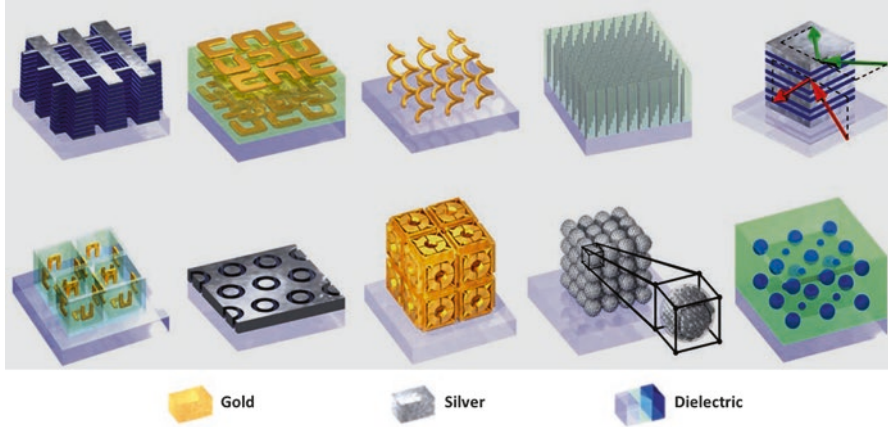


Fig. 1.3 Examples of metamaterial structures fabricated through repetition of meta-atoms or metamolecules (Soukoulis and Wegener 2011)

designs that are more suitable for the THz and optical regimes. One suitable design for optical NIMs is based on pairs of metal rods (also called “cut wires”) or metal strips, separated by a dielectric spacer. Such structures can provide a magnetic resonance $\mu < 0$ originating from antiparallel currents in the strips. An electric resonance with $\epsilon < 0$ can result from the excitation of parallel currents in the same strips. However, normally it is difficult to get the $\epsilon < 0$ and $\mu < 0$ regions to overlap so a different design was proposed, the so-called “fishnet” structure. (Tong 2014). So far NIMs at optical wavelengths have been successfully demonstrated by using coupled cut wires, fishnet structures, and coaxial waveguide arrays (Liu 2015). In addition, many theoretical concepts have been suggested based around nanofabricated composites. One example is metal nanowires and nanowire plasmonic materials, where nanowires arranged into parallel pairs can act as a left-handed material with the effective magnetic permeability and dielectric permittivity that are both negative in the visible and near-infrared spectral ranges. Various composites as shown in Fig. 1.3, based on metallic and dielectric nanostructures that have macroscopic negative refraction and act as left-handed materials, have been developed (Kivshar 2015).

On the other hand, the application of metamaterials such as the superlens that can overcome the diffraction limit attracted great attention and further stimulated the development of the metamaterials. The initial quest for negative refraction in anisotropic media brought in the concept of indefinite media and hyperbolic dispersion, generally referred to hyperbolic metamaterials. Such type of metamaterials can possess a giant photonic density of states, which would find application in a multitude of topics from super-resolution imaging, quantum photonics to nonlinear optics, biosensing, and optical circuit components (Liu 2015; Kivshar 2015).

With the rapid development of the field, it was soon realized that metamaterials possess much broader potential. In contrast to the Bragg resonances in photonic crystals, localized resonances of the composite units (meta-atoms) play a dominant

role in the properties of metamaterials. This provides a possibility for manipulation of the local electric and magnetic response of the structure, simply through modifying the geometry of each meta-atom. Based on such great flexibility, the new and fruitful research areas of transformation optics have skyrocketed since 2006, which provides a powerful methodology for designing structures with unconventional electromagnetic behavior, such as invisibility cloaks, exotic lenses, and light-harvesting structures. A further direction is to achieve the dynamic control over the exotic properties of metamaterials by including nonlinear or tunable elements into passive metamaterials, such as liquid crystals; alternatively, one can design metamolecules with deformable structures. For example, mechanical tuning is now widely used in THz metamaterials. A post-processing approach for mechanical tuning of the electromagnetic properties of metamaterials has been proposed, which may be used in applications which require precise engineering of metamaterial resonances (Kivshar 2015). Although early theoretical and experimental studies on metamaterials and transformation optics were conducted with electromagnetic waves, the concepts were soon extended to other fields, including the manipulation of various acoustic and mechanical waves, heat flows, and even matter waves (Liu 2015).

Due mainly to the complexity of fabricating three-dimensional metamaterials, many studies revisited the thin planar version of metamaterials, now generally dubbed metasurfaces. For homogenizable metasurfaces (most studied thin metamaterials with periodic meta-atoms fall into this category), it is more meaningful to characterize the constitutive relation with surface susceptibility rather than effective permittivity and permeability for bulk materials. The strong resonances of meta-atoms can exert abrupt phase changes in their scattered waves; on account of Huygens' principle, metasurfaces with spatial phase gradient are able to mold the scattered wave fronts arbitrarily. Although, in terms of functionality, the design philosophy of gradient metasurfaces is closely related to the well-established fields of phase array antennas, holography, and diffractive optics, its underlying mechanism for generating abrupt phase change is totally different, and thus it provides much greater design flexibility in manipulating the phase, amplitude, and polarization by interacting with electric or magnetic component (or both) with optically thin devices from the subwavelength scale (Liu 2015). One of the important directions in the physics of metasurfaces is the use of graphene as a component of metadevices. For photon energies below a certain level, defined by a chemical potential, graphene exhibits a metal-like conductivity. In this regime, similar to metals, graphene can support transverse magnetic (TM) electromagnetic surface plasmon polaritons, and they represent coupled state of the electromagnetic field and electrons. For the range of frequencies above the chemical potential, graphene has dielectric characteristics, and it supports transverse electric (TE) surface waves. Graphene plasmonics is a rapidly growing new field of physics which utilizes concepts of conventional metal plasmonics combined with the unique electronic and optical properties of graphene. It can be expected that a future platform for highly integrated electromagnetic signal processing and distribution will emerge which will combine nonlinear, memory,

and switchable functionalities with transformation optics' ability to guide light via the engineered electromagnetic space, using metamaterials with spatially variable parameters (Kivshar 2015).

1.4 Emerging Functional Metadevices

The exploration of metamaterials is shifting toward integrated metadevices to achieve tunable, switchable, nonlinear, and sensing functionalities, which are realized by structuring of functional matter on the subwavelength scale. A wide range of researches have been carried out on and beyond photonic, terahertz, and microwave electromagnetic metamaterials and metadevices with functionalities attained through the exploitation of phase-change media, semiconductors, graphene, carbon nanotubes, and liquid crystals. More and more metadevices are emerging, such as microelectromechanical, acoustic, mechanical metadevices, and metadevices engaging the nonlinear and quantum response of superconductors, electrostatic and optomechanical forces, as well as nonlinear metadevices incorporating lumped nonlinear components.

1.4.1 Reconfigurable and Tunable Metadevices

Active tunability and switching of electromagnetic characteristics of metamaterials can be achieved by altering the shape, size, and composition of individual meta-atom or metamolecule resonators or by manipulating the near-field interactions between them. The latter can be attained by changing the relative position of rows of the metamolecular structure or by displacing arrays of metamolecules forming a three-dimensional metamaterial lattice, as shown in Fig. 1.4a (Zheludev and Kivshar 2012).

The microelectromechanical systems (MEMS) were initially used for electromagnetic metamaterials through the tuning of transmission lines. Then MEMS actuators were applied to reconfigure metamolecules to make tunable negative refractive index metamaterial arrays by controlling the resonant properties of the individual elements. Reconfigurable metamaterials at terahertz frequencies were originally produced by fabricating planar arrays of split-ring resonators on bimaterial cantilevers designed to bend out of plane in reaction to a thermal stimulus (Fig. 1.4b). Similar thermally activated structures may be used in infrared and terahertz detectors. One of the most elaborate designs with MEMS actuators is that the terahertz metamaterial can be dynamically tuned by manufacturing the metamaterial array on a MEMS-driven silicon-on-insulator (Fig. 1.4c). By adjusting the distance between the two rings using the MEMS actuators, the strength of dipole–dipole coupling can be tuned continuously, allowing efficient tailoring of the electromagnetic response. The reconfiguration of metamolecules also allows switching of polarization eigenstates of this anisotropic metamaterial (Zheludev and Kivshar 2012).

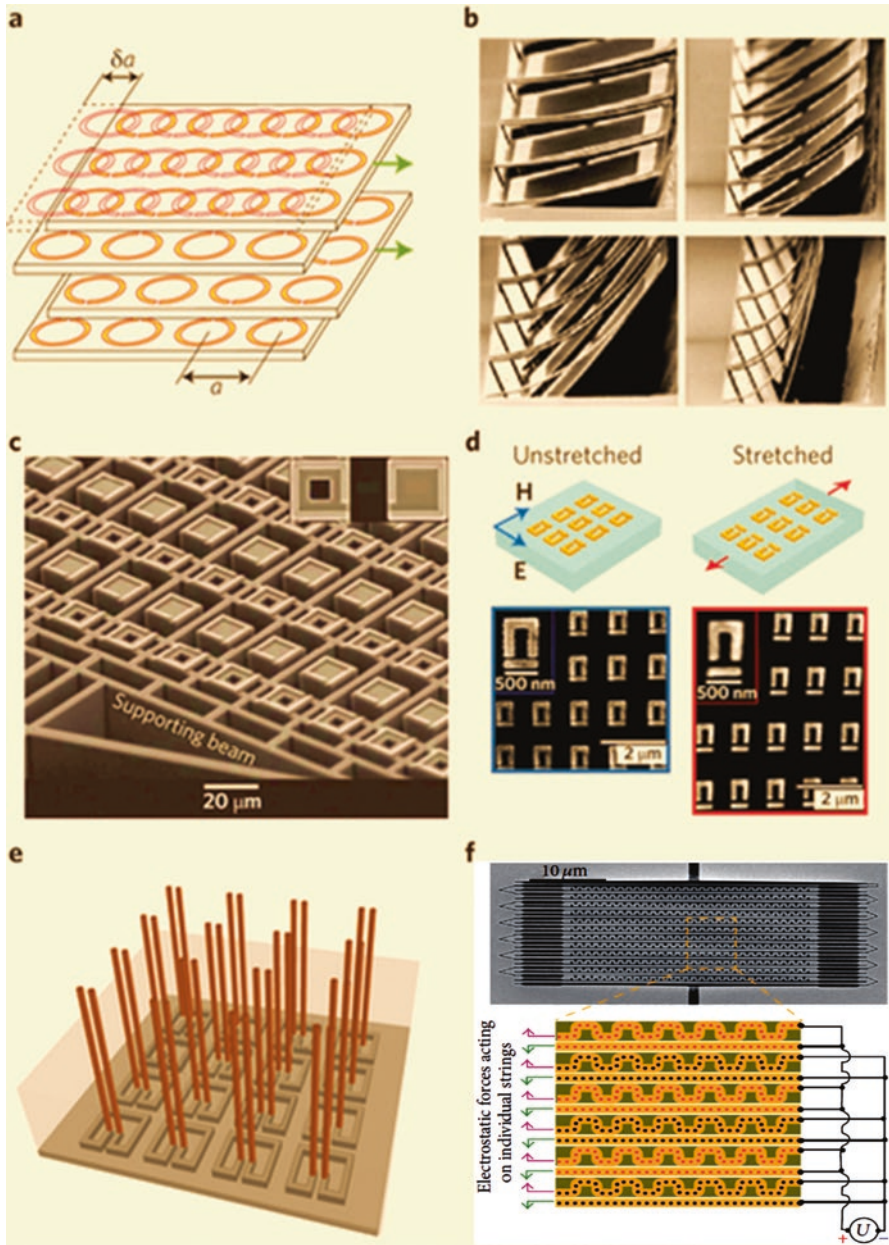


Fig. 1.4 Reconfigurable metamaterials (Zheludev and Kivshar 2012; Turpin et al. 2014): (a) Tuning by shifting the metamolecular planes of the lattice. (b) Arrays of metamolecules of a terahertz metamaterial are switched from one configuration to the other by thermal activation. (c) Terahertz metamaterial can be dynamically tuned by manufacturing the metamaterial array on a MEMS-driven silicon platform. (d) Photonic metamaterials manufactured on polymer films can be tuned by manipulation of resonator components by stretching the substrate. (e) Microwave metamaterial that can be switched by injecting liquid metallic mercury into the capillary array in the shape of split-ring resonators, (f) Plasmonic metamaterials manufactured on dielectric strings cut from a silicon nitride membrane can be driven electrostatically to megahertz frequencies

Manufacturing arrays of plasmonic resonators on flexible, stretchable polymer substrates offers a practical way to dynamically tune the response of photonic metamaterials and also allows them to be fabricated on curvilinear shapes (Fig. 1.4d). Microfluidics can also be used to reconfigure microwave metadevices when a conductive liquid (such as mercury) is injected into the network of metamolecules, changing their electromagnetic spectra (Fig. 1.4e). Moreover, a photonic metamaterial driven by electrostatic forces has been developed, consisting of a gold plasmonic nanowire pattern fabricated on a dielectric membrane (Fig. 1.4f). Operating in the optical telecommunication range of wavelengths, it can be used as a megahertz-bandwidth modulator consuming only a few microwatts of power and can also perform nonvolatile switching, providing high-contrast transmission change (Zheludev and Kivshar 2012).

Therefore, MEMS, NEMS, and micro-/nanofluidics technologies will have considerable impact on metadevices in the future. The mechanical oscillation frequencies of nanoscale components could be in the gigahertz range, allowing properly engineered arrays of metamolecules based on subwavelength-sized cantilevers to be driven at high bandwidth. In some applications this approach can directly compete with electro-optical modulators, simultaneously offering low-voltage operation and lending itself to high-density integration (Zheludev and Kivshar 2012).

1.4.2 *Electro-Optical Metadevices*

An active metadevice capable of efficient real-time control of radiation with electric signals was initially developed for the terahertz part of the spectrum. It consisted of a gold metamaterial array fabricated on a semiconductor substrate. The array and substrate together effectively formed a Schottky diode, where dielectric properties of the substrate can be controlled by injection and depletion of carriers. An electric signal applied to the metamaterial affects the high-frequency conductivity of the substrate in critical areas near the metamolecules and thus affects their resonant response (Fig. 1.5a). This approach allows modulation of the terahertz transmission by 50%. These types of hybrid metamaterial devices offer frequency and modulation bandwidth potentially up to 10 MHz. Figure 15b shows a multi-pixel 4×4 voltage-controlled spatial modulator for terahertz beams, which has been developed using this type of active terahertz metamaterials. In the modulator each pixel is an array of subwavelength-sized split-ring resonator elements fabricated on a semiconductor substrate and is independently controlled by applying an external voltage. The spatial modulator has a uniform modulation depth of around 40% and negligible crosstalk at the resonant frequency. It can operate at room temperature under small voltages, with low power consumption. Furthermore, carrier photogeneration in the silicon substrate supporting a chiral terahertz metamaterial can lead to a switching of its optical activity in the form of reversed circular dichroism. Moreover, a very substantial change in the dielectric properties of a nanometer-thick layer may be achieved in conductive oxides through the injection of free carriers, which should

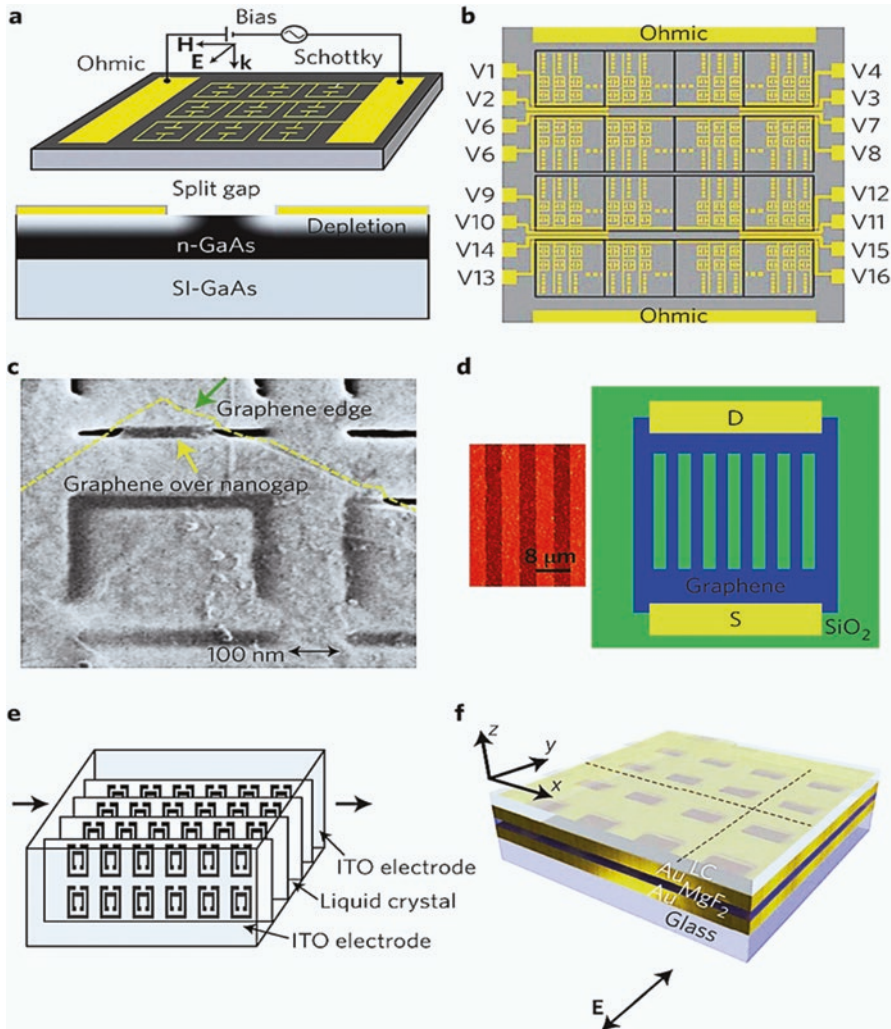


Fig. 1.5 Electro-optical and liquid-crystal metadevices (Zheludev and Kivshar 2012): (a) A terahertz metamaterial modulator fabricated on a semiconductor substrate can be controlled by injection and depletion of carriers in response to an electric bias. (b) Terahertz spatial light modulator based on metamaterial array elements that are individually addressable by electrical signals. (c) Graphene covering a metamaterial strongly modifies its plasmonic spectrum. (d) A terahertz electro-optical modulator consisting of graphene microribbons with electrical terminals on a dielectric substrate (*right*) and an atomic force microscope image of the graphene array (*left*). (e) A negative permeability microwave metamaterial consisting of an array of split rings infiltrated with nematic liquid crystals (artist’s impression) can be continuously and reversibly adjusted by an applied electric field (ITO—indium tin oxide). (f) Optical nonlinearity of photonic fishnet metamaterials infiltrated with nematic liquid crystal (LC). The material’s optical properties can be tuned by an electric field

be enough to control resonant transmission in a hybrid metamaterial. In addition, ferroelectrics can also be engaged in tuning a metamaterial response (Zheludev and Kivshar 2012).

Graphene is another favorite for constructing metamaterials with electro-optical capability, as shown in Fig. 1.5c, especially in the infrared and terahertz domains, by exploiting the modification of the electromagnetic response by an applied voltage. Such a terahertz electro-optical modulator consists of engineered graphene microribbon arrays (Fig. 1.5d). The graphene plasmon resonances have remarkably large oscillator strengths, resulting in prominent room temperature optical absorption peaks. Besides, the graphene's response can be tuned over a broad terahertz frequency range by electrostatic doping (Zheludev and Kivshar 2012).

The main advantage of the electro-optical metadevices is that they can achieve deep modulation in thin, often subwavelength. In many cases such metadevices can operate at low voltages, which is clearly a competitive advantage over conventional technology exploiting bulk and expensive electro-optical crystals (Zheludev and Kivshar 2012).

1.4.3 *Liquid-Crystal Metadevices*

Tunability and a strongly nonlinear response can be achieved in metamaterials by infiltrating them with liquid crystals (LCs). Electrical control of negative permeability in microwave metamaterials, made with a periodic array of split-ring resonators and infiltrated with nematic liquid crystals, showed a reversible change of the transmission resonance with a maximum shift of about 210 MHz (Fig. 1.5e). A similar approach was then applied to demonstrate the tunability of wire-pair and fishnet microwave metamaterials, where the external electric field changes the orientation of infiltrated molecules, leading to an effective index variation within the negative-index regime. In a similar way, the tunability can be achieved with magnetic field. In the near-infrared and optical regimes, thermal and ultraviolet-irradiation-induced tunability of optical metamaterials with liquid crystals has been demonstrated. Light-induced control of fishnet metamaterials infiltrated with liquid crystals was also achieved using a metal–dielectric (Au–MgF₂) sandwich nanostructure on a glass substrate infiltrated with a nematic liquid crystal (Fig. 1.5f). In such a device, the transmission can be modulated up to 30% by both the electric voltage and incident optical power at the telecommunications wavelength of 1550 nm. Therefore, liquid crystals can be a robust, proven, and affordable technology offering a highly practical solution for controlling metamaterial devices when ambient temperatures and speed of operation are not critical issues, given that in most liquid crystals the response relaxation time is in the millisecond ballpark (Zheludev and Kivshar 2012).

1.4.4 Phase-Change Metadevices

A radical change in the arrangement of atoms is called a structural phase transition or phase change. Phase-change functionality of semiconductor chalcogenide glass has been used for decades in optical compact disks and DVDs, where the rewritable memory function is underpinned by a transition from amorphous to crystalline phase. Phase-change functionality in polymorphic metals can also provide a way to achieve nanoscale optical and plasmonic switching devices that can be fast and require little energy to activate. Depending on the regime of stimulation and confinement of the active medium, phase changes can be either reversible or irreversible. The original phase-change nanocomposite material for nonlinear optics and nonlinear plasmonics was created by grain-boundary penetration of gallium into the network of domains of an aluminum film. Here, continuous and reversible changes occur through the intermediate coexistence of two different phases of gallium. The change may be induced in a few picoseconds, and it relaxes back on a timescale of microseconds or nanoseconds. This optically and temperature-driven composite metamaterial forms a mirror-like interface with silica and shows an exceptionally broadband phase transition-based switching response to optical excitation. It operates from the visible to near-infrared part of the spectrum and exhibits ~20% reflectivity change at optical fluence of about 1.5 mJ cm^{-2} with sub-100-ns response time (Zheludev and Kivshar 2012).

Another important example of a phase-change medium is vanadium dioxide (VO_2), which shows a phase transition of a percolative nature in which 5–10-nm metallic puddles emerge and grow in the insulating host (Fig. 1.6a). Hybridizing vanadium dioxide with a metamaterial shows 20% temperature activated tuning of the transmission in the terahertz range. Similar switching has also been demonstrated in the near-infrared using a dual-bar gold metamaterial array. A form of electrically activated memory function and persistent frequency tuning of a metamaterial, which allows lasting modification of its response by using a transient stimulus, has also been demonstrated in a hybrid VO_2 metadevice in the terahertz part of the spectrum (Zheludev and Kivshar 2012).

Combining the phase-change technology of chalcogenide glass semiconductors with metamaterials offers high-contrast, near-infrared, electronically and optically addressable gating and switching. Switching has been demonstrated by exploiting the frequency shift of a narrowband Fano resonance mode of a plasmonic planar metamaterial that was induced by a change in the dielectric properties of an adjacent 200-nm-thick film of chalcogenide glass. The material used was a gallium lanthanum sulfide chalcogenide glass, which was bistable and silicon-on-insulator compatible. An electrically stimulated transition between amorphous and crystalline forms of the glass brings about a 150-nm shift in the near-infrared resonance, providing transmission modulation with a contrast ratio of 4:1 in a layer of subwavelength thickness. One of the advantages of this technology is that devices may be structurally engineered to operate at any wavelength throughout the visible and infrared

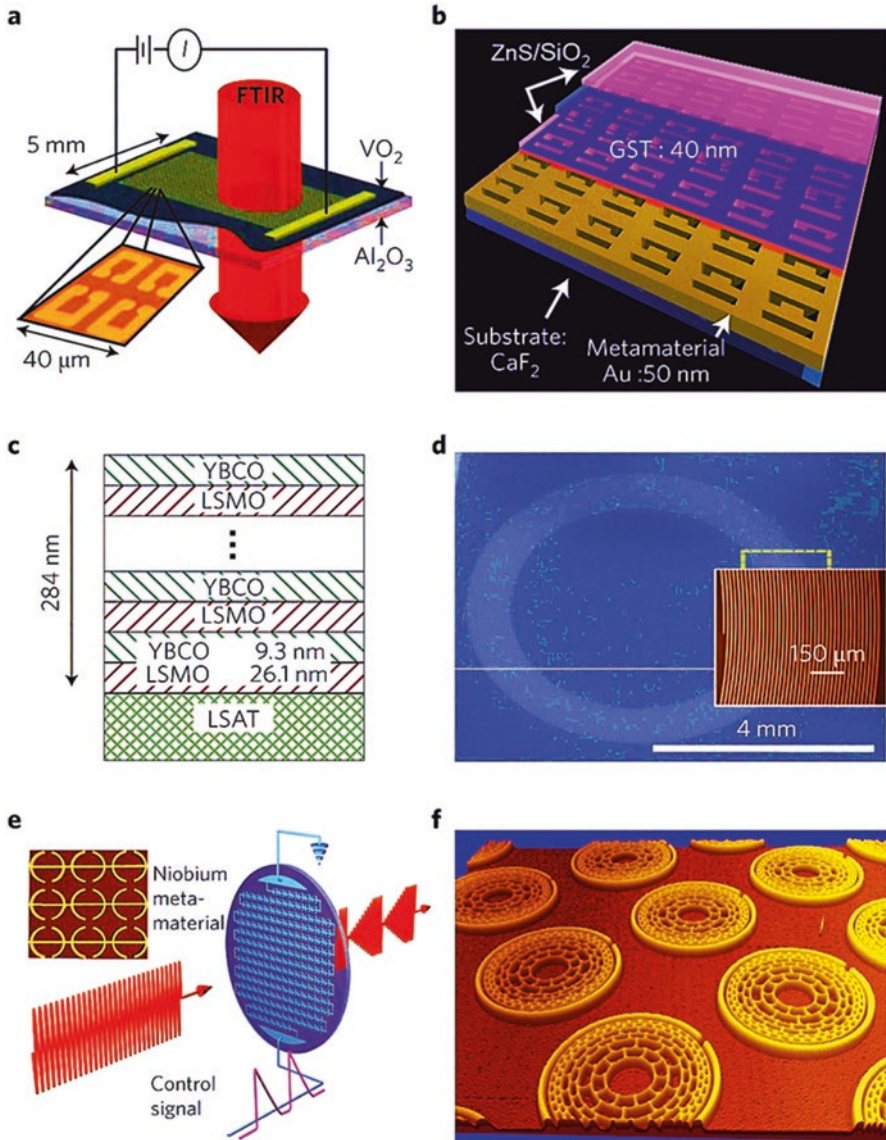


Fig. 1.6 Phase-change and superconducting metadevices (Zheludev and Kivshar 2012): (a) Metal-oxide memory hybrid metamaterial device exploiting the temperature-driven phase transition of a vanadium oxide film. (b) Structure of the metamaterial all-optical switch using phase-change chalcogenide glass GST: the hybrid device consists of a planar gold plasmonic metamaterial on a silicon nitride membrane, covered with chalcogenide glass. (c) Negative refraction, millimeter-wave metamaterial nanostructure based on ferromagnet-superconductor superlattice. (d) A spiral metamolecule made from superconducting niobium is about 700 times smaller than its resonance wavelength. (e) Controlling sub-terahertz transmission of niobium superconducting metamaterial with electric current running through the network of metamolecules (*inset* shows the network of metamolecules connected by the control wire). (f) Millimeter-wave quantum metamaterial exploiting the flux exclusion effect in superconductors manufactured from high-critical temperature superconductor YBCO

spectral range down to 11 μm . Moreover, fully reversible bidirectional optically activated switching has been developed in a gold plasmonic nanostructure combined with a conventional germanium–antimony–tellurium (GST) chalcogenide glass, making this technology compatible with real-world photonic applications (Fig. 1.6b). When nonvolatile switching is required, the combination of phase-change technology with metamaterials offers high-contrast switching response with response times as low as nanoseconds and beyond in devices of subwavelength thicknesses (Zheludev and Kivshar 2012).

1.4.5 Superconducting Metadevices

Negative dielectric constants and the dominant kinetic resistance make superconductors an intriguing plasmonic medium. As higher frequencies destroy the superconducting phase, however, applications of superconducting metamaterials are limited to the microwave domain for niobium-based metamaterials and to the terahertz spectral domain if high-temperature superconductors, such as perovskite-related cuprates and niobium nitride, are used. Microwave and terahertz metamaterials have been fabricated by replacing metals with superconductors in conventional metamaterial designs. As shown in Fig. 1.6c, negative refraction in a multilayer stack of ferromagnetic and superconducting thin films has also been demonstrated. Because a niobium thin film shows low losses at cryogenic temperatures, it allows the development of a metamaterial with extremely compact metamolecules that are as small as $1/658$ of the free-space wavelength and have resonances with quality factors in excess of 5000, as shown in Fig. 1.6d (Zheludev and Kivshar 2012).

Tuning of the superconducting metamaterial resonances by temperature and external magnetic field is easy to achieve. A superconducting metamaterial in the form of an interlinked network of subwavelength resonators can also be dynamically controlled by passing electrical current through it: using a niobium metamaterial, it was possible to achieve 45% intensity modulation at a carrier frequency of 100 GHz (Fig. 1.6e). The mechanism underpinning this functionality is a combination of the suppression of superconductivity by magnetic field and heat created by the control current. Superconducting metamaterials can be used in temperature-controllable slow light devices and other applications (Zheludev and Kivshar 2012).

Moreover, in superconducting metamaterials, it will be possible to switch from the plasmonic excitations of conventional metamaterial devices to quantum excitations underpinned by flux quantization and quantum interference effects. A much simpler quantum superconducting metamaterial could be constructed that would exploit the magnetic flux quantization for switching but would not require Josephson junctions (Fig. 1.6f). This metamaterial is an array of split-ring resonators enclosing a nest of superconducting rings. To achieve a quantum regime of switching, it exploits the quantum exclusion of the oscillating magnetic field penetrating the superconducting rings when a magnetic field is generated by the current in the outer split ring driven by the incident wave (Zheludev and Kivshar 2012).

A superconducting metamaterial can also be used to control static magnetic fields. For example, a purposely designed cylindrical superconductor–ferromagnetic bilayer can cloak uniform static magnetic fields. Consequently, superconducting metamaterials offer a radically new base for data processing and quantum information technologies. Superconductors not only provide far lower losses but also allow access to the extreme sensitivity of the superconducting state to external stimuli such as heat, electric and magnetic fields, light, current, and mechanical stress. The cryo-cooling requirement is no longer a serious technological limitation as compact cryo-devices are now widely deployed in telecommunications and sensing installations (Zheludev and Kivshar 2012).

1.4.6 Ultrafast Photonic Metadevices

Metamaterials, in which metal nanostructures are hybridized with nonlinear and switchable dielectric or semiconductor layers and controlled by ultrafast optical pulses, provide much faster switching than is attainable with MEMS/NEMS repositioning of parts, phase-change, or voltage-driven carrier injection, liquid crystals, or superconductivity modulation. A change in the refractive index or absorption in the layer adjacent to a plasmonic metamaterial array induced by the intense light modifies the plasmon spectrum of the nanostructure. This can lead to a strong change in the resonant transmission and reflection of the hybrid. Prime candidates for hybridization with metamaterials are semiconductors and semiconductor multiple-quantum-well structures used as substrates for a metallic framework, carbon nanotubes, and graphene implanted into the fabric of the metamaterials (Zheludev and Kivshar 2012).

The interaction of ultrafast optical pulses with metamaterial was initially studied for optical modulation of their terahertz responses: shunting the capacitive region of the metallic split-ring network by injecting optical carriers into the supporting ErAs/GaAs superlattice leads to a deep modulation of terahertz transmission characteristics of the planar metamaterial, with recovery time on the picosecond scale. In the optical part of the spectrum, the plasmonic resonance field enhancement created by the metamaterial network may be used to enhance the nonlinear response of the adjacent dielectric or semiconductor layer (Fig. 1.7a). A threefold improvement of pump–probe response was observed in the near-infrared part of the spectrum in a fishnet metamaterial manufactured on an α -silicon substrate exhibiting up to 60% light-induced modulation at an excitation fluence of about 0.5 mJ cm^{-2} . Here the relaxation of nonlinearity is controlled by the electron relaxation time and happens within 2 ps. Semiconductor carbon nanotubes are highly nonlinear media in their own right, where nonlinearity is associated with the optical saturation of excitonic transitions. Hybridization of single-walled carbon nanotubes with plasmonic metamaterials makes a photonic medium with an exceptionally strong ultrafast nonlinearity operating in the regime of plasmon–exciton coupling (Fig. 1.7b). More than tenfold enhancement of the nonlinearity of nanotubes was achieved in a plasmonic

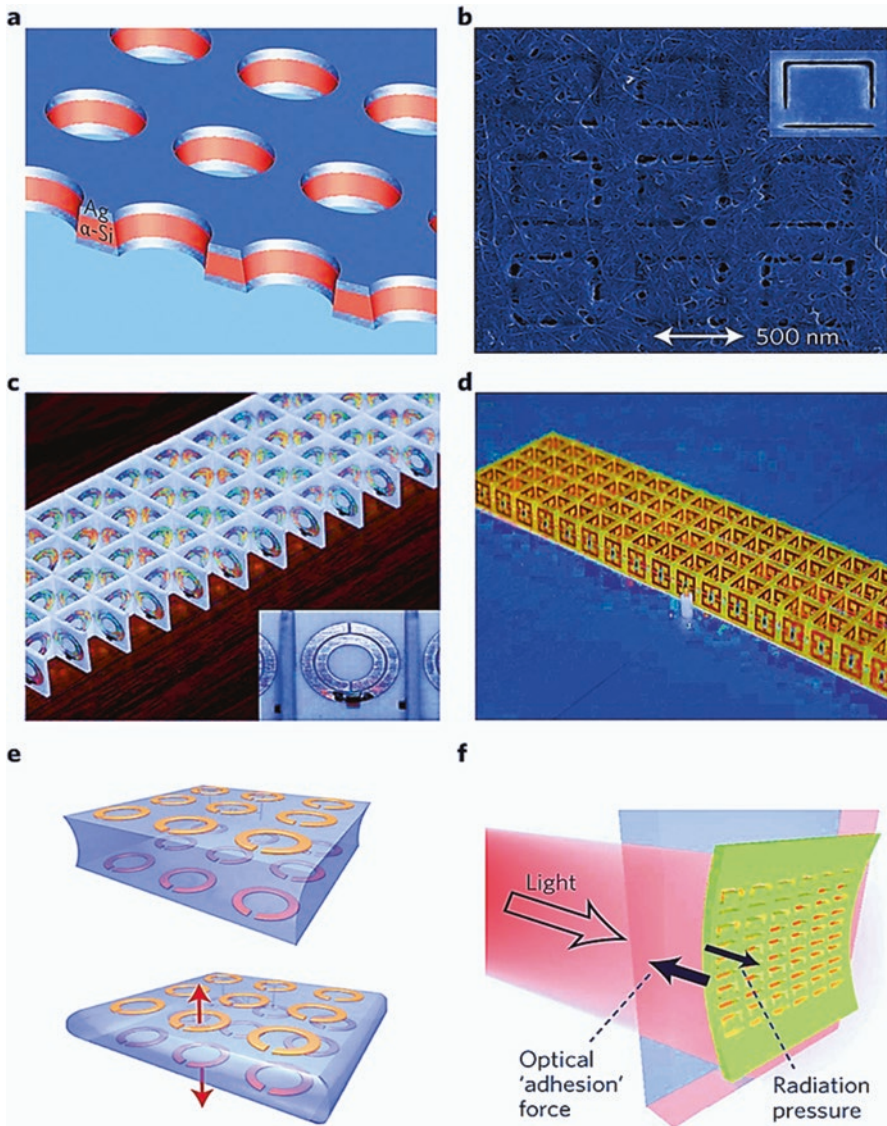


Fig. 1.7 Ultrafast metadevices, varactor metamaterials, and electromagnetic forces (Zheludev and Kivshar 2012): (a) A fishnet photonic metamaterial with sub-picosecond optical response exploits fast carrier dynamics in the α -Si substrate. (b) A plasmonic metamaterial functionalized with carbon nanotubes shows strong sub-picosecond exciton–plasmon nonlinearity in the near-infrared part of the spectrum. (c) A nonlinear magnetic metamaterial with lumped varactor diodes embedded in the metamolecules (*inset*: a unit cell of the metamaterial before deposition of carbon nanotubes). (d) Nonlinear electric metamaterials with varactor diodes. (e) A magnetoelastic metamaterial is driven by the Ampère’s force between excited metamolecules. (f) Optical gecko toe—a metamaterial film attracted by a beam of light to a dielectric surface

nanostructure supporting Fano-type resonances, so a fluence of only $40 \mu\text{J cm}^{-2}$ can create a 10% optical modulation with relaxation time less than 500 fs. Comparably, the broadband nonlinear optical response of graphene can be resonantly enhanced through hybridization with a plasmonic metamaterial. Transmission modulation close to 10% has been seen at a pump fluence of $30 \mu\text{J cm}^{-2}$. This approach allows the engineering of graphene's nonlinearity at a prescribed wavelength within a broad wavelength range, enabling applications in optical switching and pulse shaping (Zheludev and Kivshar 2012).

For data processing applications, one of the most important figures of merit is the product of the fluence necessary to create an acceptable modulation contrast and the recovery time of response. In the optical part of the spectrum, the metal metamaterial framework itself provides a source of nonlinearity that delivers one of the best performances. For instance, metamaterial nanostructuring of a thin gold film has increased the two-photon interband resonant absorption nonlinearity 300-fold, creating one of the fastest and brightest nonlinear optical medium. Moreover, depending on the spectral position with respect to the plasmonic resonance, nonlinearity may change sign, thus switching from nonlinear dissipation to enhanced transmission. Enhanced nonlinearity of a gold metamaterial has been used to demonstrate a giant effect of intensity-dependent polarization rotation that is millions of times stronger than previously observed in natural crystalline materials. As a result, enhancement of ultrafast nonlinearities with metamaterials may offer the brightest and fastest nonlinear media with potential ground-breaking applications for terahertz-rate all-optical data processing as well as ultrafast optical limiters and laser saturable absorbers (Zheludev and Kivshar 2012).

1.4.7 Nonlinear Metadevices with Varactors

Metamaterials can be tuned by taking advantage of the nonlinear response of lumped elements integrated into metamolecules of left-handed metamaterials. A similar approach has been explored for other types of metamaterial systems. For instance, resonance of the split-ring metamolecule can be controlled by adding the capacitance of a varactor diode in series with the distributed capacitance of the resonator when placed at a point of maxima in the electric currents. At low powers a split ring with embedded varactor exhibits nonlinearity of the second and third order, whereas at higher powers the nonlinear response becomes multivalued or bistable. An example of a nonlinear magnetic metamaterial operating at microwave frequencies is shown in Fig. 1.7c. Here the varactor diodes are placed in each element of the composite structure. By selecting the operating frequency to be near resonance, one can dynamically change the transmission properties of the metamaterial, for instance, from opaque to transparent, by varying the input power. If a point-like dipole source is placed near the metamaterial, the metamolecules closer to the source will experience stronger fields, making the metamaterial more transparent, which can be seen

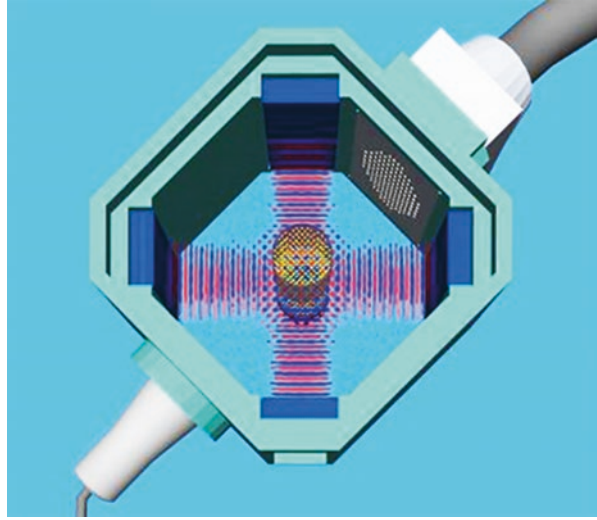
as beaming of radiation emerging from the metamaterial. A similar approach has been applied to the design of a tunable nonlinear electric response (Fig. 1.7d). Intensity-dependent (nonlinear) polarization rotation can also be achieved with a varactor-based chiral metadevice. This polarization effect is almost negligible in any natural crystals, whereas in the nonlinear metamaterial the response of the structure has strongly resonant features caused by the excitation of currents in the left-handed metamolecule by the left-handed circularly polarized wave. At the same time, the right-handed circularly polarized wave does not noticeably excite any resonances in the structure (Zheludev and Kivshar 2012).

Changing the power of the incident wave shifts the resonance of the gyrotropic response to a higher frequency and also leads to asymmetric transmission in the forward and backward directions. The quadratic nonlinear response of the varactor-loaded metamaterials can be used in various parametric processes, including phase conjugation, three- and four-wave mixing, and second harmonic generation in quasi-phase-matched and doubly resonant structures. An unusual effect of phase matching between the backward and forward waves can also be realized in metamaterials that display negative refraction, giving rise to a range of exotic transmission and reflection features. In applications that involve second-harmonic generation in metamaterials, momentum conservation can be satisfied in a process that creates backward harmonic radiation. All of all, integration of lumped electronic components with metamaterial offers a highly efficient playground for modeling nonlinear systems and also provides a straightforward way of developing highly nonlinear and switchable media for the microwave part of the spectrum (Zheludev and Kivshar 2012).

1.4.8 Metadevices Driven by Electromagnetic Forces

In metamaterials composed of an anisotropic lattice of resonant elements, such as split-ring resonators or capacitively loaded meta-atoms, the currents induced in the resonators not only affect each other through mutual inductance but also result in Ampère's force between the resonators (Fig. 1.7e), which is attractive, provided that the neighboring currents are in phase. If the resonators are allowed to move, this force will displace them from their original positions, thus changing their mutual impedance, which in turn affects the current amplitudes and interaction forces. The balance is maintained by a restoring Hooke force, which originates from the elastic properties of the host medium. It enables the electromagnetically induced forces to change the metamaterial structure, dynamically tuning its effective properties. Reconfigurable metamaterials exploiting this force have been branded magnetoelastic metamaterials. A strong light-driven force may be generated when a plasmonic metamaterial is illuminated in close proximity to a dielectric or metal surface (Fig. 1.7f). This near-field force can exceed radiation pressure and Casimir forces to provide an optically controlled adhesion mechanism mimicking the gecko toe: at illumination intensities of just a few tens of nanowatts per square micrometer, it is sufficient to overcome the Earth's gravitational pull, thus offering a new opportunity

Fig. 1.8 Schematic illustration of an acoustic metadevice capable of manipulating the acoustic space and controlling the propagation of waves (Caleap and Drinkwater 2014)



for designing metadevices driven by electromagnetic forces. The proliferation of nanostructured materials is magnifying the role of electromagnetic forces. In the future, these could become a practical source of optical nonlinearity and photonic switching (Zheludev and Kivshar 2012).

1.4.9 Acoustic Metadevice

The realization of a 3D colloidal metamaterial that is reconfigurable in real time represents a versatile means by which wave propagation phenomena can be controlled. As shown in Fig. 1.8, the reconfigurable material is assembled from microspheres in aqueous solution, trapped with acoustic radiation forces. The acoustic radiation force is governed by an energy landscape, determined by an applied high-amplitude acoustic standing wave field, in which particles move swiftly to energy minima. This creates a colloidal crystal of several milliliters in volume with spheres arranged in an orthorhombic lattice in which the acoustic wavelength is used to control the lattice spacing. The colloidal crystal behaves as a phononic metamaterial and exhibits clear band-pass and band-stop frequencies which are adjusted in real time (Caleap and Drinkwater 2014).

The use of acoustic assembly is attractive as it has advantages over other potential techniques, such as optical tweezers. Acoustic assembly is easily scalable with wavelength; it could be scaled from down to the order of micrometers before acoustic absorption and scattering become limiting. Conversely, there is no obvious upper limit on the wavelength. The ability to trap particles in an acoustic field requires contrast between at least one of the key fluid and particle acoustic properties: density, speed of sound, or compressibility. However, this is not a significant restriction

and allows most fluid–solid as well as many liquid–liquid combinations to be explored. Additionally, from a practical perspective, acoustic systems are relatively cheap and easy to integrate with other systems compared with their optical counterparts. The approaches used to assemble and reconfigure the 3D colloidal metamaterials described in Fig. 1.8 could be extended to gain real-time control of highly efficient filters, diodes, or superabsorbers with applications in both optics and acoustics. In the more immediate future these concepts will lead to, for example, the construction of a variety of reconfigurable quasicrystalline structures which would be difficult by self-assembly techniques. Indeed, the range of structures that can be constructed is limited only by the ability to produce the appropriate acoustic energy landscape. Multi-element array devices would further extend the versatility. Arrays with wide bandwidths could, in principle, be used to produce gradations in the lattice parameters which would lead to the ability to construct reconfigurable waveguides and acoustic cloaking devices. In addition, such arrays could actively control the detail of the lattice geometry to fabricate more perfectly symmetrical lattices than were possible. Tunability of the band structure could also be achieved with constitutive media with mixed properties such as acousto-optic or acousto-magnetic properties (Caleap and Drinkwater 2014).

References

- Caleap M, Drinkwater BW (2014) Acoustically trapped colloidal crystals that are reconfigurable in real time. *PNAS* 111(17):6226–6230
- Chen Z, Guo B, Yang Y, Cheng C (2014) Metamaterials-based enhanced energy harvesting: a review. *Phys B Condens Matter* 438:1–8
- Kivshar YS (2015) From metamaterials to metasurfaces and metadevices. *Nanosyst Phys Chem Math* 6(3):346–352
- KTN (2015) A state of the art review of smart materials – a review of metamaterials in the UK. <https://connect.innovateuk.org/documents/2854053/3676905/A%20Review%20of%20Metamaterials%20in%20the%20UK>
- Leonhardt U (2007) Invisibility cup. *Nat Photonics* 1:207–208
- Li Y, Kita S, Muñoz P, Reshef O, Vulis DI, Yin M, Lončar M, Mazur E (2015) On-chip zero-index metamaterials. *Nat Photonics* 9:738–742
- Liu M (2015) Nonlinear dynamics in chiral torsional metamaterials. PhD thesis. Australian National University, Canberra
- Moirra P, Yang Y, Anderson Z, Kravchenko II, Briggs DP, Valentine J (2013) Realization of an all-dielectric zero-index optical metamaterial. *Nat Photonics* 7:791–795
- Soukoulis C, Wegener M (2011) Past achievements and future challenges in the development of three dimensional photonic metamaterials. *Nat Photonics* 5:523–531
- Tong XC (2014) Advanced materials for integrated optical waveguides. Springer, New York
- Turpin JP, Bossard JA, Morgan KL, Werner DH, Werner PL (2014) Reconfigurable and tunable metamaterials: a review of the theory and applications. *Int J Antennas Propag* 2014:1–18
- Vehmas J (2015) Transmission-line metamaterials, bianisotropy, and transmission-line bianisotropy. Doctoral Dissertations, Aalto University, Unigrafia Oy, Helsinki
- Wu ZG (2016) Power integrity on PCB, package, and chip level. http://ntuemc.tw/index.php?node=power&content_id=1
- Zheludev NI (2010) The road ahead for metamaterials. *Science* 328:582–583
- Zheludev NI, Kivshar YS (2012) From metamaterials to metadevices. *Nat Mater* 11:917–924

Chapter 2

Design and Fabrication of Metamaterials and Metadevices

2.1 Common Design Approaches for Metamaterials

Take electromagnetic metamaterials as an example; the most common design approaches include resonant, transmission line, and hybrid approaches. These approaches can be accompanied with reconfiguring, tuning, or adding of active particles.

2.1.1 Resonant Approach

Resonant approach has no simple, rigorous analysis and design method. It is usually used to design highly dispersive resonant structures with lossy and narrow bandwidths. Since the left-hand behavior is obtained due to the resonant nature of the unit cell, the structures based on the applications of SRR are considered in resonant approach. In this approach, the left-hand behavior of metamaterials is developed, by combining two different particles into a unit cell in such a way that one particle possesses negative permittivity, being ENG metamaterial, and the others possess negative permeability, MNG metamaterial, as shown in Fig. 2.1. The functioning of this approach is based upon the principle that when SRR resonant material is exposed to the axial magnetic field, it exhibits the extreme values of effective magnetic permeability in the vicinity of resonance and showing highly positive in the narrow band below the quasi-static resonant frequency and highly negative in the narrow band above the quasi-static resonant frequency of the rings. This property can be used in filtering operation as an array of SRRs has filtering properties, when properly polarized, can inhibit signal propagation, thus offering an effective way to reject a frequency band in the vicinity of its quasi-static resonance (Radonić et al. 2007).

A microstrip line loaded with SRRs has been used to produce a single-negative medium, which exhibits a stop-band characteristic. To improve the coupling, the

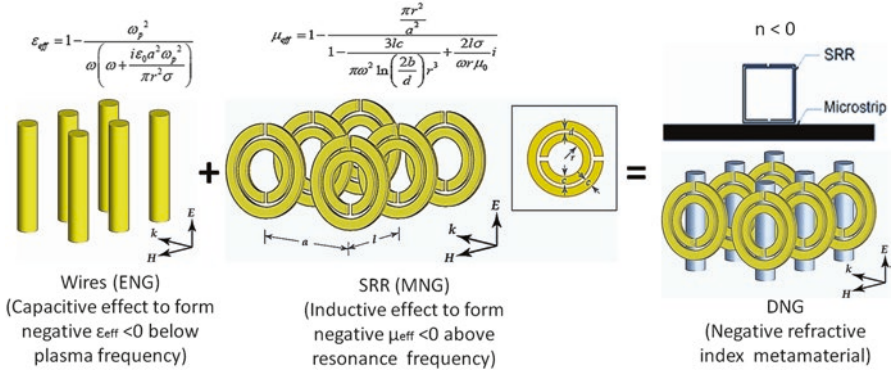


Fig. 2.1 Metamaterial designed through resonant approach

distance between the line and the rings should be as small as possible. In addition, SRR approach can also be used in waveguides as well to allow only those negative permeability signals propagating below the cutoff frequency. This approach no doubt can be successfully applied in the designing of filters and frequency selective surfaces, but it limits the designing for wide frequency ranges (Pandey and Rana 2016).

2.1.2 Transmission Line Approach

Transmission line approach uses transmission line analysis and circuit design methods to design nonresonant structures with low loss and broad bandwidths as well as moderate dispersions. Transmission line (TL) theory is an important tool for analysis and design of conventional (right-handed, RH) materials. The basic idea behind the TL approach to the design of metamaterials is that standard TL theory can be used to analyze and design LH metamaterials using a dual concept. A dual transmission line can be described by an equivalent circuit that is the dual of the circuit that models a conventional transmission line. In the dual case, the capacitors are connected in series, while the inductors are placed in a shunt configuration, as shown in Fig. 2.2. If the unit cells are sufficiently small (much smaller than the propagating signal wavelength), such structure can be regarded homogenous, i.e., effective permittivity and permeability can be calculated. It has been shown that dual transmission line exhibits negative effective permittivity and permeability in a certain frequency range and, therefore, behaves as LH transmission line. LH TL is obviously of high-pass nature, in contrast to the RH TL, which is of low-pass nature (Radonić et al. 2007).

Because of unavoidable RH parasitic series inductance and shunt capacitance, purely LH structure does not exist. Instead, a composite right/left-handed (CRLH) structure represents the most general model of a structure with LH attributes.

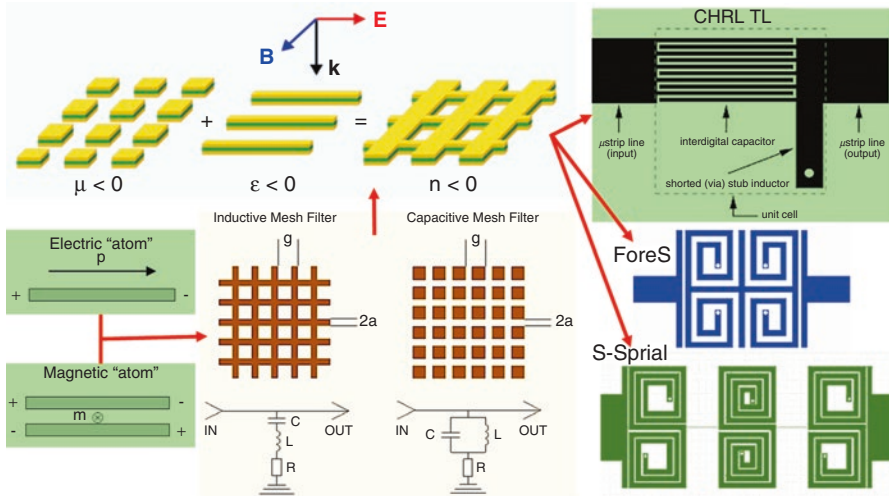


Fig. 2.2 Metamaterials designed through transmission line approach

The homogenous composite right/left-handed (CRLH) transmission lines do not exist in nature, but it can be constructed by cascading a number of CRLH unit cells, which can be realized through microstrip technology and semi-lumped components. Using this approach, a number of novel devices have been proposed like couplers, zeroth order resonator, planar lens, leaky wave antenna, etc. Comparing the response of these devices, this approach has achieved small dimensions due to the application of LH metamaterial but also giving the relatively high insertion losses. This drawback has been overcome by novel unit cells called ForeS and super-compact LH unit cells called S-spiral. Those structures show lower insertion loss at resonant frequency and higher quality factor (Radonić et al. 2007; Pandey and Rana 2016).

2.1.3 Hybrid Approach

The Hybrid approach combines the concept of both resonant and transmission line approach together. This approach basically uses the SRR (split-ring resonator) and CSRR (composite split-ring resonator) from one side, and gaps and shunted stubs from the other side. Generally, SRRs and gaps are providing negative permeability, while CSRRs and stubs are providing negative permittivity. Using various combinations of these particles, hybrid left-hand metamaterials can be designed. Unit cell that combines shunted stubs and CSRRs has been used for the design of compact ultra-wide band-pass filters. The performance of this approach is slightly differing because the passband obtained in this is not entirely LH in nature. Therefore, it is also possible to design LH lines with more than two inclusions. The third particle can be used to control the response (Radonić et al. 2007; Pandey and Rana 2016).

2.2 General Tuning Methods for Metadevices

A variety of tuning methods have been investigated to generate dynamic changes in a metamaterial's performance. These include direct changes to the unit cell's circuit model by varying capacitance or conductance, using electrically, chemically, thermally, or optically sensitive materials to change the constituent material properties of a structure and therefore change its electrical response and altering the geometry of the unit cell through stretching, shifting, or deforming all or part of the structure. Some of these techniques (such as varactor diodes) have been applied for operation at particular wavelengths, while others (such as phase-change materials) have been applied across the electromagnetic spectrum. In general, the tuning mechanisms that have been examined include (Turpin et al. 2014): (a) physical (shift, deformation, and microfluidics), (b) material (liquid crystal, ferromagnetic/ferroelectric, semiconductor, and phase change), and (c) circuit (open/short, semiconductor devices, MEMS, non-foster, and varactor).

The base unit cell on which a reconfigurable metamaterial device is designed determines the fundamental behavior of the structure. In most cases, the starting point for the reconfigurable device is a static design which is then augmented with the tunable component, material, or structure. The physical geometry of the unit cell determines the electromagnetic coupling into the metamaterial, provides (potentially desirable or undesirable) frequency selectivity, and can allow for cancellation of electric (in the case of the SRR) or magnetic (for the electric LC resonator) excitations as well as for strongly coupling the electric and magnetic responses. Especially at optical wavelengths, many unit cells do not explicitly couple to the electric or magnetic fields but are tuned to resonate simultaneously in the same geometry. Unit cells with well-defined resonant and EM-coupling properties are commonly used to implement metamaterials with desired material properties, while designs for scattering control or antenna enhancements may be less sensitive to cross-polarization or E-H field (magnetolectric) coupling. Most tunable metamaterials are based on common elemental building blocks or particles, such as the widely used SRR, the complementary split-ring resonator (CSRR), and their electric-field coupled cousin – the electric LC (ELC) resonator. Often, the structure is modified to a greater or lesser degree to accommodate the constraints of the tuning mechanism. Tunable impedance surfaces are generally constructed from grounded square patches (mushroom-type artificial magnetic conductor (AMC) structures). Although basing a design on an existing resonator can be useful, new structures can be developed subject to limitations or to specifically leverage the capabilities of a given tuning mechanism; this includes the use of reorientable or variable distributions of colloidal nanoparticles, interconnected grid structures, and metamaterials may not use such a recognizable geometric unit cell pattern as an SRR or spiral but achieve periodic behavior instead based on their equivalent circuit model (Turpin et al. 2014).

2.3 Fabrication Technology

The fabrication techniques for metamaterials have reached high levels of sophistication, which impart the capability to synthesize metamaterials across micrometer and nanometer scales even on unconventional substrates. The integration of hard materials, such as metals or dielectrics, onto flexible materials coupled with the development of advanced techniques to realize nanometer feature sizes has enabled flexible and stretchable devices across multidisciplinary domains such as photonics, electronics, and optoelectronics. Such developments across several disciplines have enabled rapid progress and refining of synthesis techniques, which has allowed the creation of flexible metamaterials that are capable of operating across a wide and tunable frequency spectrum. These techniques have enabled the development of novel metadevices, triggering new scientific and technological developments in the field of metamaterials (Walia et al. 2015).

2.3.1 Photolithography

Photolithography is a conventional microfabrication technique that can be employed to synthesize metamaterials that operate at terahertz frequencies. The ability to create high-resolution subwavelength structures operating at terahertz frequencies (corresponding to wavelengths of 30 μm –3 mm) with minimal complications makes this technique well suited for terahertz metamaterials and has been extensively used to fabricate single-layer and multilayer (3D) metamaterials (Walia et al. 2015).

Figure 2.3 shows an example of the reported metamaterial made on flexible substrates using the microfabrication technique (Choi et al. 2011). The resonators were patterned into the metal film (with an adhesion layer) deposited on spin-coated polyimide substrates post curing. Often, micron scale resolution patterns obtained by this technique are further encapsulated with a thin layer of polyimide to avoid delamination of metal layers. In general, photolithography microfabrication techniques are suitable only for substrates that can withstand organic and corrosive solvents.

2.3.2 Shadow Mask Lithography

Shadow mask lithography (SML) is an acid-free fabrication technique employed to create planar and multiple layer micro- and nanoscale features. This technique involves direct deposition onto a substrate through a stencil during the deposition of thin metal films, oxides, or other dielectric layers without the need of any photolithography and etching processes. It is analogous to the solder paste or conductive ink screen printing approaches.

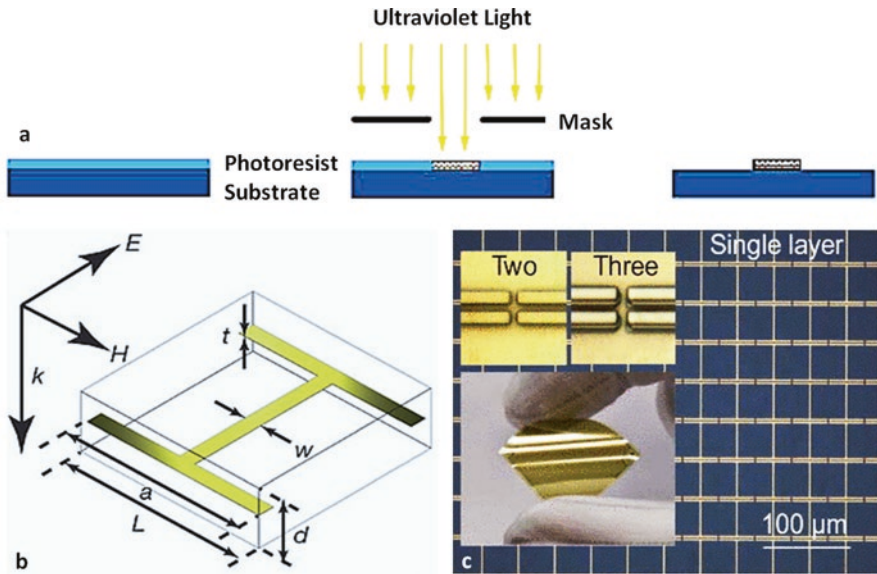


Fig. 2.3 Photolithography for metamaterial fabrication: (a) schematic process, (b) and (c) “I”-shaped resonators and dipole structures fabricated on spin-coated polyimide substrates (Choi et al. 2011)

Fabrication sequence in the SML technique is as shown in Fig. 2.4 (Walia et al. 2015). A stencil is prepared (Fig. 2.4a), usually made by through substrate etching of a silicon wafer or an aluminum foil. The stencil is placed either in direct contact or in close proximity to the substrate (Fig. 2.4b). Subsequently, metal or dielectric layers as required are deposited, predominantly by electron beam evaporation, to utilize its inherent line-of-sight deposition characteristics to create a 1:1 copy of the stencil on the substrate. Using the SML, features as small as 100 nm wide can be patterned on arbitrary substrates including polymers and plastics that are mechanically fragile and/or chemically sensitive (Figs. 2.4c, d). This approach enables large-area nano-patterning with high throughput. The stencils are reusable and demonstrate repeatable results with high-throughput replication of patterns. However, the resolution of the realized patterns often deteriorate over repeated cycles of deposition due to the contact and proximity placement of stencil with the substrate during the deposition (Aksu et al. 2011).

2.3.3 Soft Lithography

Soft lithography is a family of techniques for fabricating or replicating structures using elastomeric stamps, molds, and conformable photomasks. It is called “soft” because it uses elastomeric materials, most notably polydimethylsiloxane (PDMS).

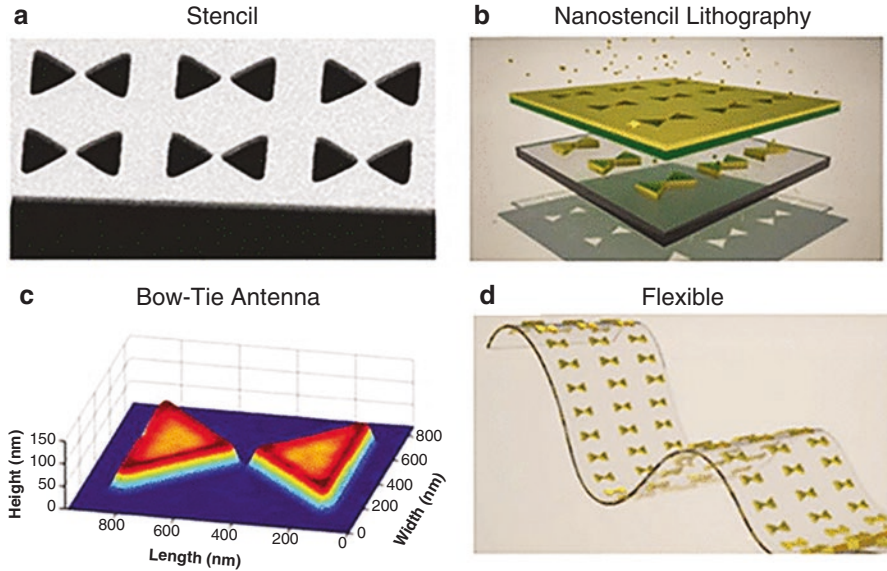


Fig. 2.4 Fabrication sequence in the shadow mask lithography (SML) technique (Walia et al. 2015): (a) A stencil defined with the pattern of interest, with bow tie antennas in this case with the side of the triangles of 500 nm. (b) Deposition through the stencil either with a small gap or in contact. (c) Atomic force microscopy profile of a nanostructure fabricated by SML. (d) Representation of a flexible devices realized using SML

Soft lithography allows multi-scale patterning of micro- and nanoscale patterns on polymers or other substrates.

Replica molding allows for high-resolution patterning of any polymer compatible with the PDMS stamp which even includes polymers that are not photolithographically definable. The prepolymer is simply applied onto a carrier and the stamp pressed firmly onto the surface. Post curing and removal of the stamp, an inverted copy of the stamp is fabricated, which can be removed from the carrier to form a free standing design (Walia et al. 2015).

Another prevalent fabrication method is transfer printing. Here, features of any desired materials, such as semiconductors, functional oxides, or metals, can be prepared on a silicon substrate. This allows for the use of established patterning techniques and high process temperatures. Subsequently, the patterns are “picked up” by the elastomeric stamp and placed onto the substrate of choice. The substrate can then be released from the carrier. The transfer printing method is very powerful but requires precise control over the adhesion of the features to the donor substrate, the stamp as well as the target substrate (Walia et al. 2015). Figure 2.5 shows 3D modular transfer printing for the assembly of heterogeneously integrated metamaterials/metadevices on universal substrates (Lee et al. 2016).

By using soft lithography techniques, limitations of plastic substrates such as high-temperature expansion, poor adhesion, low processing temperature, and chemical instabilities can be overcome. Additionally, these techniques are suitable for a wide range of structure sizes and enable patterning on nonplanar surfaces (Walia et al. 2015).

2.3.4 Electron Beam Lithography

Electron beam lithography (EBL) uses the extremely small wavelength of a beam of electrons at high accelerating voltages to obtain nanoscale patterns. Analogous to conventional photolithography, where a photoresist layer is exposed to ultraviolet (UV) light, the EBL technique requires the exposure of an electron beam resist, PMMA, or ZEP, by a high-energy electron beam. This causes a scission in the organic structure that is subsequently developed using a standard developing solution, whereby the exposed region dissolves completely in the developer. Subsequently, deposition of metal and/or dielectric layers is carried out following which the resist is dissolved to obtain the nanoscale patterns. This approach utilizes the “lift-off” process, and so, the initial pattern defined by EBL needs to be the inverse of the desired pattern. EBL provides the highly desirable ability to create nanoscale features below the diffraction limit of the standard photolithography processes and does not require a physical mask to transfer the patterns. For metamaterials, the EBL technique is employed to fabricate subwavelength resolution resonators operating at optical wavelengths. While EBL is a powerful technique to achieve nanometer and submicron features, three major limitations need to be overcome in creating large-area, high-performance metamaterials. These are long writing times due to the serial nature of the technique, stitching errors impacting periodicity, and the low stability and potential astigmatism of the electron beam. Additionally, the serial patterning process gives rise to issues such as instability of the beam due to drifting. Large-area patterning with multiple stage moves resulting in poor resolution and stitching defects. Second, stitching errors also hamper the ability to repeat the patterns over a large area without any misalignment. Finally, the stability and accuracy of the electron beam blanking as well as astigmatism are important factors that influence the effectiveness of this technique. The beam blanker is an external voltage source that is used to switch the electron beam “ON” and “OFF” while patterning the nanoscale features. During the large writing times that typically accompany this method, any fluctuations in the current can give rise to inconsistent exposure and result in variable developing times for PMMA as well as introduce geometrical errors (Walia et al. 2015).

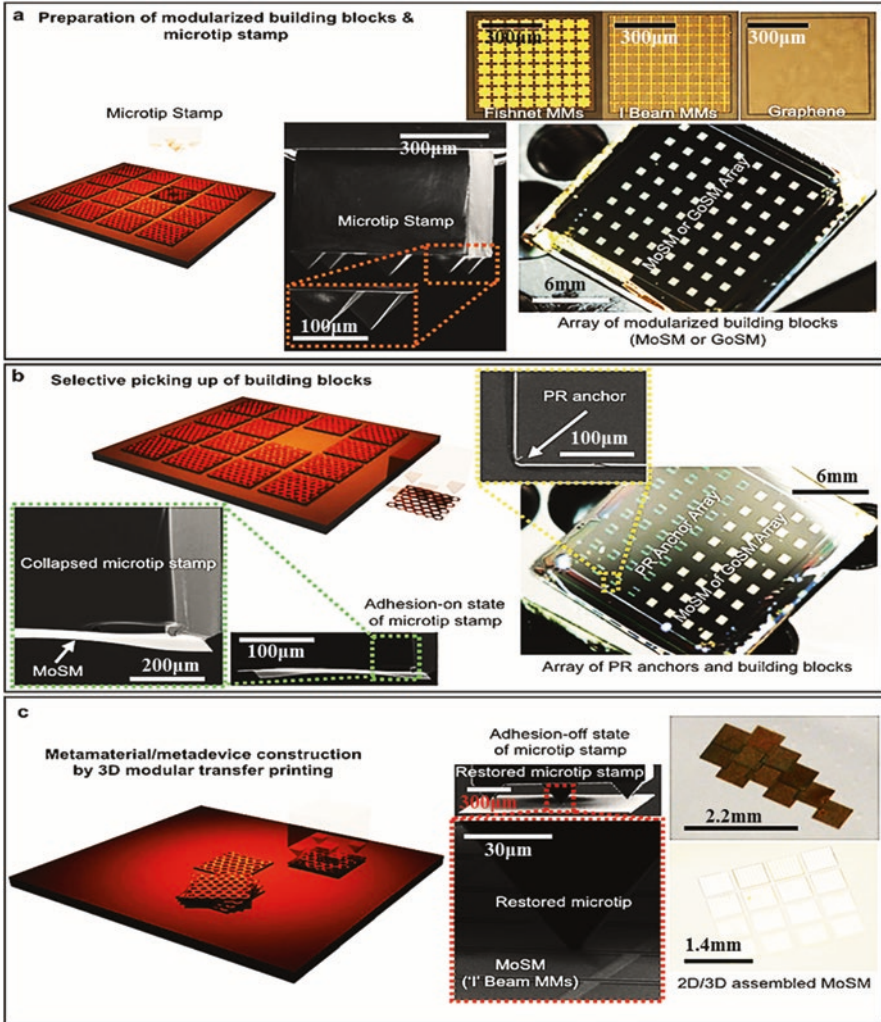


Fig. 2.5 3D modular transfer printing for the assembly of heterogeneously integrated metamaterials/metadevices on universal substrates (Lee et al. 2016): (a) preparation of the modularized basic building blocks (i.e., a metamaterial on a silicon (Si) membrane (MoSM) and graphene on a Si membrane (GoSM)) and an elastomeric 5-microtip stamp. (b) Picking up of MoSM and GoSM using the 5-microtip stamp. The elastomeric 5-microtip stamp with a lateral dimension that is comparable to the size of MoSM (*bright square*) and GoSM allows to selectively pick up each individual building block. (c) Construction of the metamaterial/metadvice via 3D modular transfer printing. Each individual building block (i.e., MoSM or GoSM) can be deterministically assembled into 2D and 3D metamaterials and metadvicees

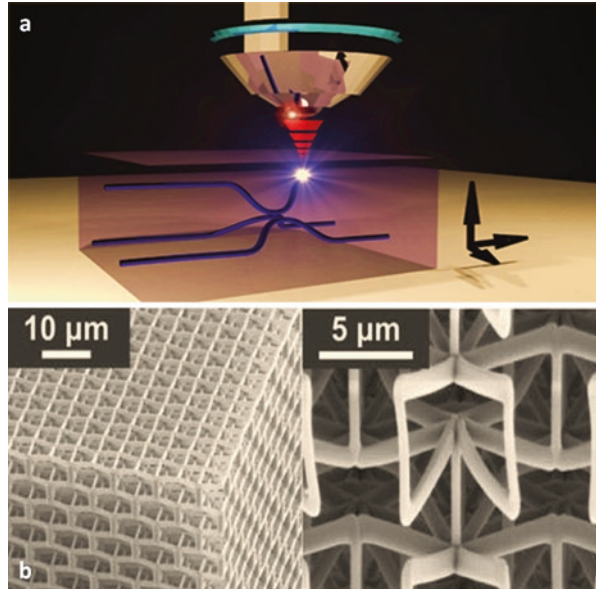
2.3.5 3D Metamaterial Fabrication Techniques

3D terahertz and optical metamaterials, for instance, can provide the ability of imaging below diffraction limit, cloaking, quantum levitation, and sensing. Planar fabrication techniques have been largely employed in the synthesis of multilayered 3D metamaterials owing to their simplicity. However, such multilayered metamaterials often suffer from anisotropic responses. Metamaterials with isotropic negative ϵ and μ cannot be achieved via planar fabrication processes. Further advances in fabrication techniques such as various additive manufacturing processes have been explored to achieve subwavelength dimension metamaterials with isotropic responses. These fabrication techniques include imprint lithography, vertical pillar superlattice, multiphoton polymerization, multilayer electroplating, direct ink writing, and interference lithography. However, such advanced 3D fabrication techniques are still limited by their fabrication complexity and ability for realization on or transfer onto flexible substrates (Walia et al. 2015).

There are many other fabrication techniques that have been developed, such as (Walia et al. 2015):

- (a) A combination of laser writing and chemical vapor deposition techniques has been explored to create a 3D split-ring resonator (SRR) metamaterial. The chemical vapor deposition technique allows uniform coating of metal films around the structure, which cannot be achieved through physical vapor deposition techniques.
- (b) Focused ion beam (FIB) milling is another 3D fabrication technique used to realize nanometer size features with high aspect ratios. For example, a 3D fishnet resonator was developed by multilayer deposition of metal and dielectric layers—21 alternating layers of silver (11 layers) and magnesium fluoride (10 layers). Subsequently, FIB milling was used to etch nanometer size features with high aspect ratios. In addition, the FIB milling can be replaced by plasma etching.
- (c) A combination of printing techniques with other large-area lithography techniques can be used to generate sophisticated negative index metamaterials.
- (d) 3D direct laser writing (DLW) fabrication technique can be used to develop complex geometry metamaterial structures, as shown in Fig. 2.6 (Bückmann et al. 2012; Meany 2014). The DLW technique involves a tightly focused laser beam incident onto a diffraction-limited spot within the volume of the photore-sist. This allows the creation of sub-micrometer-scale features in three dimensions, which can be patterned to arbitrary shapes and complex interconnected networks which cannot be fabricated using conventional lithography techniques. While direct write techniques can achieve high resolution, they suffer from low throughput and are compatible only with a select range of substrates. The resolution can be further improved using multiple wavelength stimulation/depletion techniques.
- (e) Membrane projection lithography (MPL) is another advanced fabrication technique capable of developing micrometer-scale 3D metamaterials. This technique

Fig. 2.6 Schematic of laser direct writing principle (a, Meany 2014) and 3D mechanical metamaterial defined using direct laser writing (b, Bückmann et al. 2012)



usually use a patterned membrane layer formed over a cavity to act as a mask layer to the underlying wall surfaces and bottom surface of the cavity. A beam to facilitate an operation comprising any of implantation, etching, or deposition can be directed through the pattern opening onto the underlying surface, with the opening acting as a mask to control the area of the underlying surfaces on which any of implantation occurs, material is removed, and/or material is deposited. The membrane can be removed, a new membrane placed over the cavity, and a new opening formed to facilitate another implantation, etching, or deposition operation. By changing the direction of the beam, different wall/bottom surfaces can be utilized to form a plurality of structures (Burckel et al. 2015). With a high degree of control over the pattern and deposition of thin films, MPL has the potential to revolutionize future 3D infrared and optical metamaterial structures with complex geometries.

Although these techniques are promising for the creation of 3D metamaterial structures, they are still not sufficiently versatile. Some are complex and require multiple fabrication steps which degrade the resolution of the structures, while others are limited by the materials used for patterning as well as choice of suitable substrates. In addition, transfer techniques rely on surface chemistry making them substrate dependent. Although complex fabrication techniques involving a fusion of soft lithography and photolithography have been used for direct transfer of patterns onto highly curved substrates, achieving high-resolution patterns ($<0.1 \mu\text{m}$) still remains a challenge (Walia et al. 2015).

2.4 Tuning Techniques

The limitations of metamaterials have been overcome by making devices on flexible and elastomeric substrates to achieve tunable broadband responses. Apart from mechanical tuning, a wide range of other techniques have also been explored, such as reconfigurable metamaterials via electromechanical displacements, lattice displacement, thermal annealing, and change in superfluid density. Incorporation of phase-change media, semiconductors, graphene, carbon nanotubes, nonlinear components, and liquid crystals with metamaterials is also a strategical tuning technique. The advancement of tuning mechanisms and continuous improvements in fabrication techniques are vital for the future of metamaterials and metadevices.

2.4.1 Mechanical Tuning

Mechanically deformable flexible substrates are commonly used to tune the resonance frequency of metamaterials. The application of a stretching force to the substrate alters the resonator geometry and also inter resonator electric and magnetic couplings, which consequently change the resonance frequency of the resonators. Such an approach has been used to demonstrate dynamic tuning of Fano resonances by applying uniaxial mechanical stress to a plasmonic nanostructure on a PDMS membrane. The mechanical tuning of plasmonic nanostructures offers a new pathway toward the development of tunable nanophotonic devices such as tunable filters and sensors. Mechanical tuning is particularly effective for plasmonic nanostructures exhibiting coupled plasmon resonances, due to its high sensitivity to changes in structural parameters. It also allows control over the symmetry of a nanostructure or nanostructured unit cell, on which optical properties are critically dependent (Walia et al. 2015).

The mechanical deformation tuning is a promising approach to make metamaterials tunable and to obtain adaptive response without adding any further complexity to the design and fabrication of the structures. This technique allows dynamic tuning of metamaterials without the need for bias voltages, nonlinear components, and MEMS switches. Also, mechanical tuning of metamaterials is not limited by the frequency of operation, and it can be extended from microwave, terahertz, to optical frequencies. The ability to mechanically tune metamaterials has provided new degree of flexibility in sensing at molecular levels by enhanced reflection signal of a dynamic surface infrared absorption. Metamaterials and plasmonic nanostructures on flexible substrates are highly sensitive to structural parameters, which opens up new possibilities for photonic circuits, biological systems, antennas, sensors (strain, temperature, dielectric, biomolecular, chemical, etc.), energy harvesters, tunable cloaking devices operating over wide frequencies that can overcome the current limitations of specific wavelength and angle operation, and superlenses to image at near atomic scales. Toward such applications, further research and development are

being carried out to develop devices with enhanced resolution of the resonator structures to operate at higher frequencies, large-area flexible structures, 3D metamaterials, isotropic response structures, and fast tuning capabilities of mechanically deformable metamaterials (Walia et al. 2015).

2.4.2 Electromechanical Displacement

Extending the concept of using mechanical deformation for tuning, the application of an electrical stimulus through microelectromechanical systems (MEMS), for example, to induce mechanical strain leads to a category of electromechanical tuning. In electromechanical tuning, an applied external bias voltage induces mechanical deformation of resonator structures.

2.4.3 Lattice Displacement

The lattice structure of reconfigurable metamaterials can be adjusted to the lattice structure for tuning the transmission or other characteristics of metamaterials. For instance, continuous tuning of resonance frequency has been done using this approach. This tuning technique can be applied to a wide range of electromagnetic frequencies and various resonator geometries. To realize such continuous tuning structures at higher frequencies, micro- and nanofabrication techniques that can generate large-area multilayer metamaterials are required, along with materials that enable good control over lattice displacements in all three directions (Walia et al. 2015).

2.4.4 Thermal Stimulation

Temperature control of permittivity has been demonstrated to tune the resonant frequency in the terahertz spectral regime. This relies on utilizing oxide materials with multifunctional properties, including susceptibility to temperature. Reconfigurable metamaterials that reorient in response to a thermal stimulus have also been used to tune metamaterials. A SRR metamaterial design supported by a cantilever beam that bends out of its plane in response to thermal annealing has been demonstrated to tune the electromagnetic response. However, the thermal annealing actuation process suffers from a passive tuning effect, where the SRR once reoriented never returns to its initial state. Hence, active tuning mechanisms such as resistive, piezoelectric, and electrostatic actuation must be explored to tune the metamaterial responses (Walia et al. 2015).

2.4.5 *Material Tuning*

While changing the shape of resonant elements provides a range of opportunities for tuning, the constituent materials that make up the unit cell ultimately control the properties of the metamaterial. There are a few candidate materials that have been used for permittivity tuning of metamaterials, including $\text{Ba}_{0.5}\text{Sr}_{0.5}\text{TiO}_3$ (BST) ferroelectric films, liquid crystal, and Ga-Sb-Te (GST) phase-change materials. Permeability tuning can also be achieved at RF using ferrite materials. While negative permeability constituent materials are not available at THz or higher frequencies, ferrite materials can be a useful tuning method at RF. The third general area for constituent material tuning is conductivity. Conductivity change is frequently accomplished using semiconductor materials with applied voltage or optical pumping. The semiconductor can be incorporated as a substrate under all elements or as an inductive load over part of the resonant elements to tune their resonant frequency. Graphene has also been used to inductively load resonant elements in a high-impedance surface HIS when under a voltage bias. A variety of techniques have also been employed to change the conductivity of the resonant elements themselves. Semiconductor SRRs have been used with a change in conductivity achieved thermally or by applying a magnetostatic field. Conducting polymers have also been used as resonant elements in metamaterial absorbers. The conducting polymers exhibit large changes in conductivity (i.e., from resistive to conductive) when stimulated by certain chemical analytes, which enables the metamaterial to reconfigure from reflecting to absorbing or to change resonant frequencies. VO_2 phase-change materials also exhibit large conductivity changes with a voltage bias and have been used to form the resonant elements in metamaterials (Turpin et al. 2014).

Bulk material-based tuning is ultimately limited by the range of electromagnetic responses available in the constituent substances, where each material system poses unique implementation challenges. For instance, BST and VO_2 offer useful permittivity and conductivity changes, respectively, but they are both sensitive to temperature and thus must be used in temperature controlled environments. GST phase-change material on the other hand does not suffer from temperature variation, but incorporating the heating and cooling mechanisms into the metamaterial to control the phase transitions between crystalline and amorphous states is challenging. Continued research and development are needed for tunable material systems that can be harnessed to meet application-specific reconfigurable metamaterial needs (Turpin et al. 2014).

References

- Aksu S et al (2011) Flexible plasmonics on unconventional and non-planar substrates. *Adv Mater* 23:4422–4430
- Bückmann T et al (2012) Tailored 3D mechanical metamaterials made by dip-in direct-laser-writing optical lithography. *Adv Mater* 24:2710–2714

- Burckel DB, Davids PS, Resnick PJ and BL Draper (2015) Membrane projection lithography. US Patent 8,981,337 B1
- Choi M et al (2011) A terahertz metamaterial with unnaturally high refractive index. *Nature* 470:369–373
- Lee S et al (2016) Heterogeneously assembled metamaterials and metadevices via 8D modular transfer printing. *Sci Rep* 6(27621):1–10
- Meany T (2014) Optical manufacturing: femtosecond-laser direct-written waveguides produce quantum circuits in glass. *Laser Focus World Magazine*. <http://www.laserfocusworld.com/articles/print/volume-50/issue-07/features/optical-manufacturing-femtosecond-laser-direct-written-waveguides-produce-quantum-circuits-in-glass.html>
- Pandey A, Rana SB (2016) Review of metamaterials, types and design approaches. *Int J Eng Sci* 17:359–363
- Radonić V, Jokanović B, Crnojević-Bengin V (2007) Different approaches to the design of metamaterials. *Microw Rev* 13(2):2–7
- Turpin JP et al (2014) Reconfigurable and tunable metamaterials: a review of the theory and applications. *Int J Antennas Propag* 2014:1–18
- Walia S et al (2015) Flexible metasurfaces and metamaterials: a review of materials and fabrication processes at micro- and nano-scales. *Appl Phys Rev* 2:011303

Chapter 3

Electromagnetic Metamaterials and Metadevices

3.1 Fundamental Theory of Electromagnetic Metamaterials

The response of a metamaterial to an incident electromagnetic wave can be characterized by ascribing to it an effective (averaged over the volume of a unit cell) permittivity $\epsilon_{\text{eff}} = \epsilon_0 \epsilon_r$ and effective permeability $\mu_{\text{eff}} = \mu_0 \mu_r$, when the size of the meta-atoms is much smaller than the wavelength λ , as shown in Fig. 3.1. As long as this criterion is fulfilled, it may normally assume that the metamaterial is homogeneous, i.e., that the values of ϵ_{eff} and μ_{eff} averaged over each meta-atom (unit cell) do not depend on the wave vector \mathbf{k} nor on the corresponding values of these parameters at neighboring unit cells. Hence, in such a medium, the effects of spatial dispersion may legitimately be ignored. This makes possible the manipulation of fields and waves at a subwavelength scale. Therefore, the basic properties of metamaterials can be described with Maxwell's equations (Wartak et al. 2011):

$$\nabla \mathbf{E} = -\mu_0 \mu_r \frac{\partial \mathbf{H}}{\partial t} \tag{3.1}$$

$$\nabla \mathbf{H} = -\epsilon_0 \epsilon_r \frac{\partial \mathbf{E}}{\partial t} \tag{3.2}$$

where the μ_r and ϵ_r are relative permeability and permittivity, respectively, and $\nabla = \left[\frac{\partial}{\partial x}, \frac{\partial}{\partial y}, \frac{\partial}{\partial z} \right]$. From Eqs. (3.1) and (3.2), the wave equation can be obtained:

$$\nabla^2 \mathbf{E} = -\epsilon_0 \mu_0 \epsilon_r \mu_r \frac{\partial^2 \mathbf{E}}{\partial t^2} \tag{3.3}$$

If losses are ignored and ϵ_r and μ_r are considered as real numbers, the wave equation is unchanged when the signs of ϵ_r and μ_r are simultaneously changed.

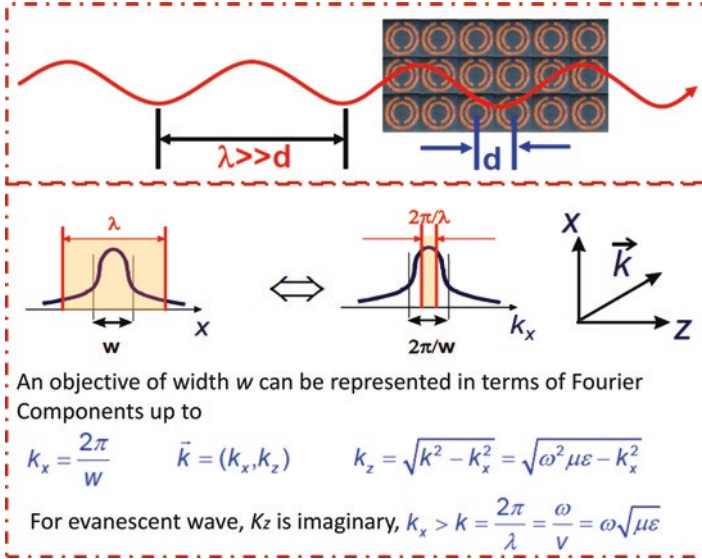


Fig. 3.1 Characterization parameters of electromagnetic metamaterials

Assuming a time-harmonic and plane-wave variation for fields in Maxwell's Eqs. (3.1) and (3.2), the equations can be transformed as (Wartak et al. 2011):

$$\mathbf{k} \times \mathbf{E} = -\omega \mu_0 \mu_r \mathbf{H} \quad (3.4)$$

$$\mathbf{k} \times \mathbf{H} = +\omega \epsilon_0 \epsilon_r \mathbf{E} \quad (3.5)$$

for $\epsilon_r > 0$ and $\mu_r > 0$ the vectors \mathbf{E} , \mathbf{H} , and \mathbf{k} form a right-handed triplet of vectors, and if $\epsilon_r < 0$ and $\mu_r < 0$, they form a left-handed system.

An important difference between regular dielectrics and left-handed metamaterials can be realized when a ray propagates through the boundary between left-handed and right-handed media, as shown in Fig. 3.2. Light crossing the interface at non-normal incidence undergoes refraction; there is a change in its direction of propagation. The angle of refraction depends on the absolute value of the refractive index of the medium, and it is described by Snell's law (Wartak et al. 2011). By matching the field components at the dielectric interfaces, it may readily verify that in the case where the – medium is double negative ($\epsilon_r < 0$, $\mu_r < 0$), the refraction of light occurs on the same side of the normal as the incident beam. The double-negative medium behaves as a medium exhibiting a negative (effective) refractive index ($n < 0$).

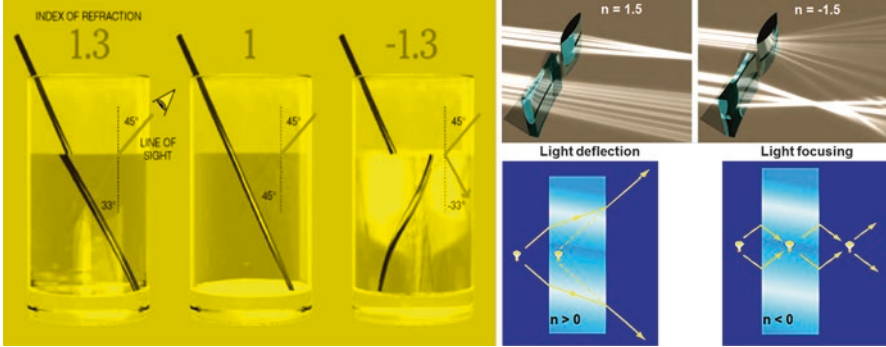


Fig. 3.2 Reflection and refraction at the interface of the media with $n > 0$, $n = 1$, and $n < 0$

3.2 Single-Negative Metamaterials

Single-negative (SNG) metamaterials have either negative relative permittivity (ϵ_r) or negative relative permeability (μ_r), but not both. They act as metamaterials when combined with a different, complementary SNG, jointly acting as a double-negative (DNG) metamaterial.

3.2.1 Metamaterials with Negative Effective Permittivity in the Microwave Regime

Epsilon negative media (ENG) display a negative ϵ_r , while μ_r is positive. Many plasmas exhibit this characteristic. For example, noble metals such as gold or silver are ENG in the infrared and visible spectrums.

Metals at optical frequencies are characterized by an electric permittivity that varies with frequency according to Drude relation (Wartak et al. 2011):

$$\epsilon(\omega) = \epsilon_0 \left[1 - \frac{\omega_p^2}{\omega(\omega + i\gamma)} \right] \tag{3.6}$$

where $\omega_p^2 = \frac{Ne^2}{m\epsilon_0}$ is the plasma frequency with which the collection of free electrons(plasma) oscillates in the presence of an external driving field. N , e , and m being, respectively, the electronic density, charge, and mass, and γ is the rate with which the amplitude of the plasma oscillation decreases. When $\gamma = 0$ and $\omega < \omega_p$, it is $\epsilon < 0$, i.e., the medium is characterized by a negative electric permittivity. Typical values for ω_p are in the ultraviolet regime, while for γ a typical value (e.g., for

copper) is $\gamma \approx 4 \times 10^{13}$ rad/s. Unfortunately, for all frequencies $\omega < \omega_p$ for which $\varepsilon < 0$, it is also $\omega < \gamma$, i.e., the dominant term in Eq. (3.6) is the imaginary part of the plasma electric permittivity, which is associated with losses (light absorption, Wartak et al. 2011).

With the wire structure as shown in Fig. 2.1, this limitation can be overcome, and a metamaterial with negative effective permittivity in the microwave regime is created. The thin metallic wires (infinite in the vertical direction, z) of radius r are periodically arranged on a horizontal plane (xy). The unit cell of the periodic structure is a square whose sides have length equal to a . If an electric field $\mathbf{E} = E_0 e^{-i(\omega t - kz)} \mathbf{z}$ is incident on the structure, then the (free) electrons inside the wires will be forced to move in the direction of the incident field. If the wavelength of the incident field is considerably larger compared to the side length of the unit cell, $\lambda \gg a$, then the whole structure will appear (to the incident electromagnetic field) as an effective medium whose electrons (confined in the wires) move in the $+z$ direction. Since the electrons are confined to move only inside the thin wires, the effective electron density of the whole structure (effective medium) is $N_{\text{eff}} = \frac{\pi r^2}{a^2} N$, with N being the electron density inside each wire. Thus, for sufficiently thin wires the effective electron density, N_{eff} , of the engineered medium can become much smaller compared to N , thereby substantially decreasing the effective plasma frequency, ω_p , of the engineered medium. For instance, for a wire radius $r = 1 \mu\text{m}$ and wire spacing $a = 5 \text{ mm}$, we find that $N_{\text{eff}} \approx 1.3 \times 10^{-7} N$, i.e., the effective electronic density of the new medium is reduced by seven orders of magnitude compared to that of the free electron gas inside an isolated wire (Wartak et al. 2011).

On other hands, the effective mass m_{eff} of a moving electron inside the wire effective medium is $m_{\text{eff}} = 0.5 \times \mu_0 N e^2 r^2 \ln(ar)$. Thus, for copper wires of radius $r = 1 \mu\text{m}$, being separated by $a = 5 \text{ mm}$, we obtain: $m_{\text{eff}} \approx 1.3 \times 10^4 m$, i.e., the effective mass of an electron in our engineered medium is increased by more than four orders of magnitude. This, combined with the fact that the effective electron density is reduced by approximately seven orders of magnitude, leads to an effective plasma frequency that is in the microwave regime (Wartak et al. 2011):

$$\omega_p^2 = \frac{N_{\text{eff}} e^2}{m_{\text{eff}} \varepsilon_0} = 5.1 \times 10^{10} [\text{rad/s}]^2 \rightarrow f_p = \frac{\omega_p}{2\pi} = 8.2 \text{ GHz} \quad (3.7)$$

Therefore, it can be calculated $\lambda_p = c/f_p \approx 7a$, considerably larger compared to the periodicity of the structure, justifying the description of the periodic structure as an effective medium. Thus, with this methodology, an engineered medium can be constructed that exhibits a negative electric permittivity in the microwave regime (with reasonably low losses and high field penetration inside the structure), thereby mimicking the interaction of light with real metals in the optical regime.

3.2.2 Metamaterials with Negative Effective Permeability in the Microwave Regime

Mu-negative media (MNG) display a positive ϵ_r and negative μ_r . Only some gyrotropic or gyromagnetic materials can exhibit this characteristic naturally. A gyrotropic material is one that has been altered by the presence of a quasi-static magnetic field, enabling a magneto-optic effect. In such a material, left- and right-rotating elliptical polarizations can propagate at different speeds. When light is transmitted through a layer of magneto-optic material, the polarization plane can be rotated, forming a Faraday rotator. This is so-called Faraday effect. Two gyrotropic materials with reversed rotation directions of the two principal polarizations are called optical isomers.

With split-ring resonator (SRR) as shown in Fig. 2.1, the metamaterials with negative effective permeability can be artificially created in the microwave regime. SRR is equivalent to a simple RLC circuit, R being the resistance of the metallic ring, L its inductance, and C (primarily) the capacitance between its unconnected ends. The rings residing on a given $x = x_i$ plane have the same axis (i.e., they are “concentric”) with the corresponding rings on the x -planes below and above them. The side of the square unit cell on an yz plane is equal to a . Assuming that a magnetic field $\mathbf{H} = H_0 e^{i(\omega t - kr)} \mathbf{x}$ is incident on the structure, the induced (electromotive) source is $U = i\omega\mu_0\pi r^2 H_0$, generating an electric current I that circulates in each ring. If the rings sitting on successive x -planes are close together (“solenoid” approximation), there will be negligible “loss” of magnetic flux between the rings in each column, and therefore the magnetic flux will be $\Phi = \mu_0\pi r^2 I/l$, l being the x -distance between corresponding SRRs lying on successive yz planes. Accordingly, the inductance L (in Henry) of each SRR will be: $L = \Phi/I = \mu_0\pi r^2/l$. It is assumed that the depolarizing magnetic flux lines generated by all rings are uniformly spread on a given yz plane, which results in a mutual inductance between two SRRs given simply by (Wartak et al. 2011):

$$M = \left(\pi r^2 / a^2 \right) L = FL \quad (3.8)$$

F being the fractional volume within a unit cell occupied by an SRR. Applying Ohm’s second law across a closed SRR “circuit” to obtain: $U = [R + i/(\omega C) - i\omega L + i\omega M]I$, where $R = 2\pi r\sigma$ is the (ohmic) resistance of each ring, σ being the resistance per unit length. Thus, the induced magnetic dipole moment per unit volume will be $M_d = I(\pi r^2)/(a^2 l)$. Therefore, the (relative) effective magnetic permeability associated with this medium (in the direction, x , that the incident magnetic field is polarized) will be obtained (Wartak et al. 2011):

$$\mu_r = 1 - \frac{F}{1 - \frac{1}{\omega^2 LC} + \frac{iR}{\omega L}} \quad (3.9)$$

μ assumes negative values in the range: $\frac{1}{\sqrt{LC}} < \omega_p < 1/\sqrt{LC(1-F)}$, where $\omega_0 = \frac{1}{\sqrt{LC}}$ is the resonance frequency of the Lorentzian variation of the medium's magnetic permeability, and $\omega_{mp} = 1/\sqrt{LC(1-F)}$ is the corresponding plasma frequency (where $\text{Re}\{\mu\} = 0$). Crucially, the resonant wavelength (λ_{m0}) of the structure depends entirely on the rings' effective inductance (L) and capacitance (C) and can therefore be made considerably larger than the periodicity a of the structure, thereby fully justifying its description as an effective medium. If placing the SRRs on the other two planes (xy and xz), similarly, obtained negative effective permeabilities in the other two directions, y and z can be obtained as well, and the variation with frequency of these permeabilities would have been given by an expression similar to Eq. (3.9). Thus, with the present methodology a three-dimensional, isotropic metamaterial exhibiting negative effective permeability can be constructed in a specified frequency region (Wartak et al. 2011).

Joining a slab of ENG material and slab of MNG material resulted in properties such as resonances, anomalous tunneling, transparency, and zero reflection. Like negative-index materials, SNGs are innately dispersive, so their ϵ_r , μ_r , and refraction index n are a function of frequency.

3.3 Double-Negative Metamaterials

Double-negative metamaterials exhibit a negative value of the refractive index for an electromagnetic wave over some frequency range. They are often referred to by any of other terminologies, such as left-handed media or left-handed material (LHM), backward wave media (BW media), media with negative refractive index, and other similar names.

The first actual double-negative metamaterial that worked in the microwave regime (about 4.3 GHz) was constructed of split-ring resonators and conducting straight wires (as unit cells), as shown in Fig. 2.1. The unit cells were sized from 7 to 10 mm. The unit cells were arranged in a two-dimensional (periodic) repeating pattern which produces a crystal-like geometry. Both, the unit cells and the lattice spacing were smaller than the radiated electromagnetic wave. This system relies on the resonant behavior of the unit cells with both the permittivity and permeability of the material were negative. With the frequency increases, alternative materials become more suitable for the terahertz and optical regimes, such as smaller horseshoe-shaped split-ring resonators, fishnet structures, coated rods made from a high dielectric core coated with a frequency-dependent dielectric plasmonic or Drude-type behavior at optical frequencies, small particles made from dielectric materials with large permittivity, paired metal nanorods or nanostrips, and special configurations of plasmonic nanoparticles (Chen and Lipton 2013).

In contrast to metamaterials that depended on resonant behavior, nonresonant phenomena could surpass narrow bandwidth constraints of the wire/split-ring resonator configuration. This design with a network of LC-loaded transmission lines translated into a type of medium with broader bandwidth abilities, negative refraction, backward waves, and focusing beyond the diffraction limit. The network was both scalable (from the megahertz to the tens of gigahertz range) and tunable. The negative refractive index transmission line has been employed as a subwavelength focusing free-space flat lens (Iyer and Eleftheriades 2007).

Double-negative materials offer great potential for applications in biomedical imaging, optical lithography, and data storage. Such media support electromagnetic waves for which the phase velocity is antiparallel to the direction of energy flow as well as other unusual electromagnetic effects such as the reversal of the Doppler effect and Cerenkov radiation (Chen and Lipton 2013).

The negative-index metadevices are being matched with conventional devices that broadcast, transmit, shape, or receive electromagnetic signals that travel over cables, wires, or air. The materials, devices, and systems that are involved with the metadevices could have their properties altered or heightened. For example, metamaterial antennas and related devices are commercially available. Other applications include wireless power devices, electromagnetic absorbers such as radar-microwave absorbers, electrically small resonators, waveguides that can go beyond the diffraction limit, phase compensators, advancements in focusing devices (e.g., microwave lens), and improved electrically small antennas. In the optical frequency regime, developing the superlens may allow for imaging below the diffraction limit. Double-negative metamaterials for optical nanolithography, nanotechnology circuitry, as well as a near-field superlens could be useful for biomedical imaging and subwavelength photolithography (Shalaev 2007).

3.4 Zero-Index Metamaterials

Zero or near-zero refractive index metamaterials exhibit unique properties, including a zero-phase delay. This delay implies a possibility of quasi-infinite phase velocity and infinite wavelength. The electromagnetic wave inside of the zero-index material is static in the spatial domain. Meanwhile, it is dynamic in the time domain, thereby allowing energy transport. As a result, every point within the metamaterial experiences a quasiuniform phase; the shape of the wave front at the output of such metamaterial depends only on the shape of the exit surfaces of the metamaterials. This property provides great flexibility in the design of the phase patterns of the light beams (Sun and Litchinitser 2016).

According to Snell's law, $n_1 \sin(\theta_1) = n_2 \sin(\theta_2)$, $n_1 = 0$ results in the critical angle of the total reflection equal to 0. As shown in Fig. 3.3, if the source is outside of the zero-index medium, then no light can be transmitted into the zero-index medium because of the total reflection. If the source is inside of the zero-index medium, no

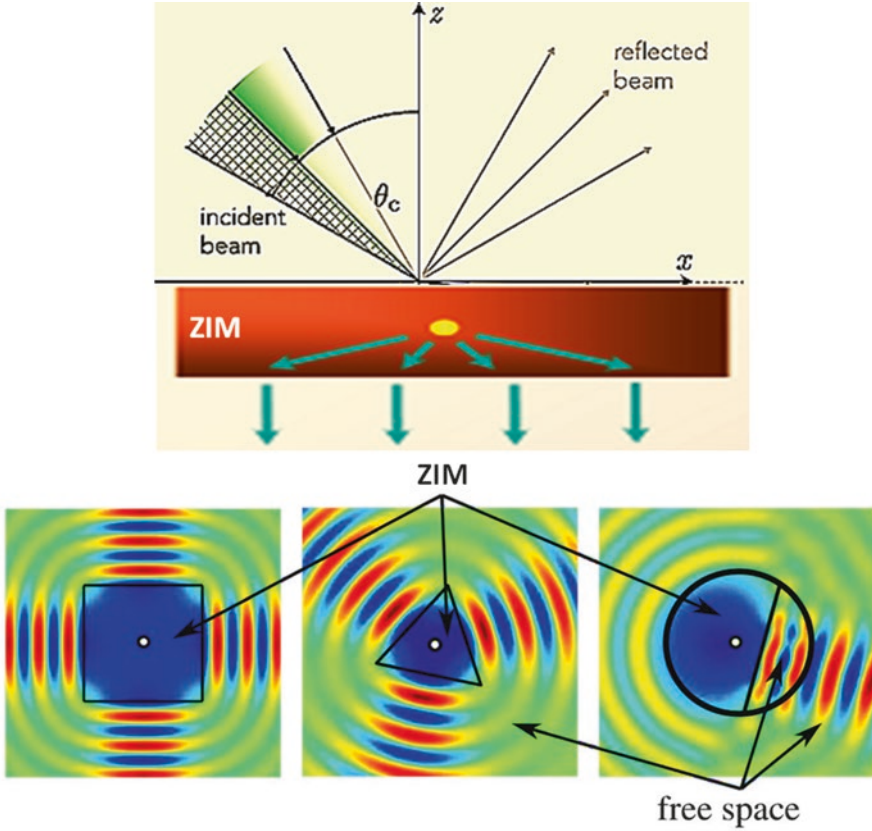


Fig. 3.3 Refraction of light in the near zero-index material when source is placed inside or outside of the material (Jiang et al. 2015)

matter what the kind of source, then the direction of the output beam will be perpendicular to the surface of the zero-index medium (Jiang et al. 2015).

From the equation $n = \sqrt{\epsilon\mu}$, that $n = 0$ can be achieved by three ways: $\epsilon = \mu = 0$; $\epsilon = 0, \mu \neq 0$; or $\epsilon \neq 0, \mu = 0$. When $\epsilon = 0$, it is called epsilon-zero material (ENZ); the magnetic field \mathbf{H} in an ENZ material is constant. Similarly, in $\epsilon \neq 0, \mu = 0$ material, the electric field \mathbf{E} is constant, whereas the \mathbf{H} field linearly changes along the propagation direction. For the $\epsilon = \mu = 0$ case, both the \mathbf{E} and \mathbf{H} fields are constant inside of the zero-index material (Sun and Litchinitser 2016).

The design strategy of the zero-index metamaterials is similar to that used for the realization of the NIMs. For instance, if a metal rod that has a Drude model dispersion is used to supply the negative permittivity in the microwave range, then one can take the near-zero permittivity around the plasma frequency of the Drude model and $\epsilon = 0$ at the plasma frequency (Sun and Litchinitser 2016). Figure 3.4a shows a zero-index metamaterial with a mesh structure in the microwave range. Similar to the utilization of the metal rod, the mesh structure was used to decrease the plasma

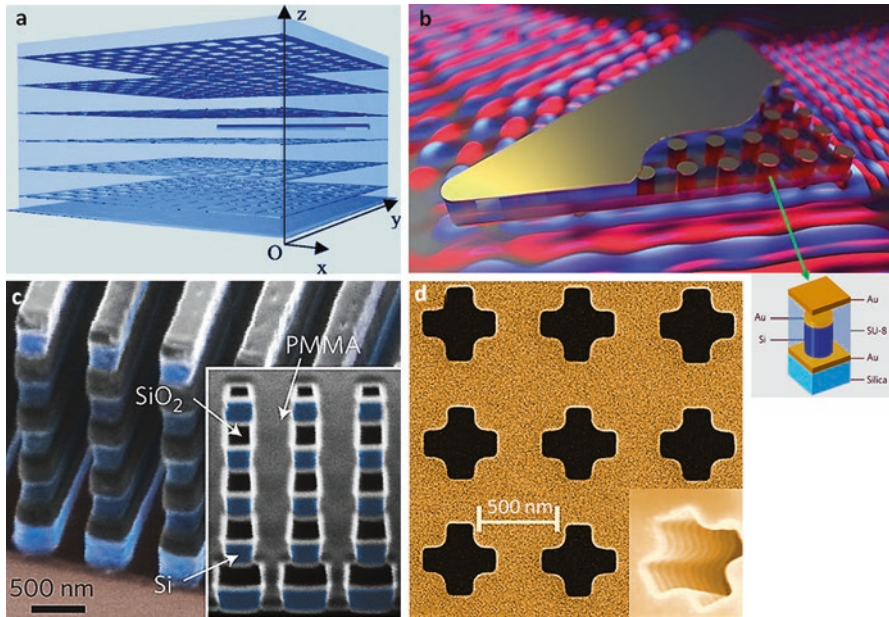


Fig. 3.4 Different kinds of near zero-index materials (Li et al. 2015; Sun and Litchinitser 2016): (a) ENZ material in the microwave range, (b) on-chip zero-index metamaterials, (c) ENZ made of a woodpile structure in the infrared range, and (d) zero permeability material in the microwave range

frequency of the metal so that the zero-index frequency could be moved to the microwave range. In the optical range, the plasma frequency of metals can be shifted by combining metals with dielectric materials, such as on-chip zero-index metamaterials as shown in Fig. 3.4b (Li et al. 2015). In addition, an all-dielectric woodpile structure can also enable zero-index material in the infrared range (Fig. 3.4c). In the fishnet structure, there is also a frequency that causes refractive index changes from positive to negative. Therefore, the fishnet structure can also be used to compose a zero-index material with $n = 0$, as shown in Fig. 3.4d (Sun and Litchinitser 2016).

As the wavelength inside of the zero-index material is infinitively large, it may enable many interesting properties, such as strong field enhancement, super coupling, phase front control, tunneling effect, and super cloaking. The most remarkable phenomenon occurring in graded-index structures is anomalous absorption near the zero-index transition. The graded-index structures are so-called transition metamaterials with dielectric permittivity and magnetic permeability gradually changing among positive, zero, and negative values. If the wave propagates in the graded-index material, strong, polarization-sensitive, anomalous field enhancement near the zero refractive index point under the oblique incidence of the plane wave on a realistic, lossy transition metamaterial layer would potentially enable various applications, including subwavelength transmission and low-intensity nonlinear optical devices (Sun and Litchinitser 2016).

3.5 Electromagnetic Bandgap Metamaterials

Electromagnetic bandgap (EBG) structures are defined as artificial periodic structures that avert or assist the propagation of electromagnetic waves in a specified band of frequencies for all incident angles and all polarization states. They are usually used as a component of microwave devices in order to improve the performance of devices especially to improve the radiation/gain patterns and to decrease the noise/losses in transmissions. EBG structures are also known as high-impedance surface due to their ability to suppress the surface wave at certain operational frequencies. They have been utilized in electromagnetic and antenna areas (Verma and Daya 2011).

3.5.1 Types of EBG Structures

EBG structures are periodic in nature, which may be realized by drilling, cuffing, milling, and etching on the metal or dielectric substrates. Other emerging fabrication processes such as additive manufacturing and 3D printing may also be used for realization of EBG structures. They may be formed in the ground plane or over the substrate. On the basis of dimensions, as shown in Fig. 3.5, EBG structures are categorized as one-dimensional (1D), two-dimensional (2D), and three-dimensional (3D) periodic structures that satisfy Bragg's conditions, i.e., inter-cell separation (period) is close to half-guided wavelength ($\lambda_g/2$). They are capable of forbidding electromagnetic propagation in either all or selected directions (Soukoulis 2002).

3.5.2 Numerical Modeling of EBG

The theoretical description of electromagnetic waves in EBG involves the exact solution of Maxwell's equations in a periodic medium. Several techniques have emerged for predicting the performance of EBG's (de Maagt et al. 2016):

1. Plane-Wave Expansion or Spherical Wave Expansion

This method starts with the Maxwell's equations in a generalized eigenvalue form. The plane-wave expansion allows this set of equations to be solved by converting them into a Hermitian eigenvalue problem, and many commercial packages exist to aid in their solution. Because the plane-wave method is easy to understand and is computationally very straightforward to implement, it became the first method to find widespread use. As many plane waves are usually required in order to obtain good convergence, this can limit the use of the method for treatment of more complicated crystals. Several means have been proposed to improve the convergence of the plane-wave expansion. Spherical waves may be used instead of

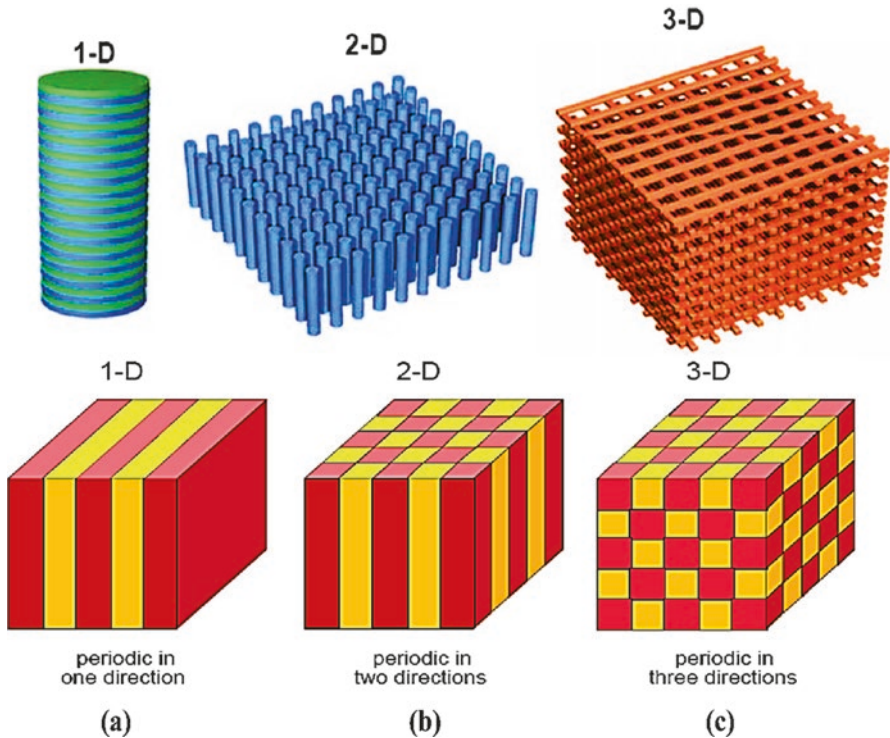


Fig. 3.5 Types of electromagnetic bandgaps based on geometrical shapes (Robinson and Nakkeeran 2013): (a) 1D, (b) 2D, and (c) 3D

plane waves as a basis set if the electromagnetic crystal is composed of spherical or cylindrical parts. This method is called the spherical wave expansion method of the vector KRR (Korringa–Kohn–Rostoker) method.

2. The Transfer Matrix Method

At a fixed frequency, the equations are solved in the plane perpendicular to the crystal surface normal for a given propagation depth through the crystal (boundary value problem). The field is then transferred throughout the crystal by successively applying Maxwell's Equations to obtain the scattering matrix for a single layer of crystal. By cascading the scattering matrix for each layer, the transmission and reflection coefficients can be propagated down through layers by successive matrix multiplication.

3. The Finite Difference Time Domain Method

The finite difference time domain (FDTD) method is capable of characterizing the broadband frequency response of arbitrary and inhomogeneous EBG elements in a single run and can be computational efficient. The application of the FDTD method in the modeling of EBG modeling can be straightforward; the structure is

meshed in a conventional Yee's Cartesian grid with absorbing boundaries such as the perfectly matched layer. To activate the structure, infinitesimal dipoles or plane waves with a Gaussian pulse waveform are usually used. EBG bandgap properties described in the scattering parameters can be extracted from the time domain electric and magnetic field responses. Different approaches have been developed to further improve the efficiency in the simulation. These include FDTD with periodic boundary conditions/perfectly matched layer (PBC/PML) and the split-field method for both normal and oblique wave incidence, FDTD/Prony technique for accurate bandgap parameter extraction over the short period of time, and nonorthogonal FDTD approaches for oblique wave incidence and potential conformal FDTD modeling on curved EBG elements without staircasing approximations. These modified approaches generally only consider a "unit cell" of the EBG structures, truncated with perfect boundary conditions, and are effective in modeling bandgap properties of complex 3D EBGs. However it is found that spatial harmonic effects are often neglected by these approaches. Although it has been demonstrated that the results are valid for the prediction of the bandgap, such an approach does not seem sufficient for evaluating the passband behavior.

4. Commercial Packages

There exists a number of commercially available software that can readily deal with analysis and simulation of EBG and associated structures as well as general periodic arrays, such as Ansoft-HFSS and Ansoft Designer, Fidelity, and IE3D by Zeeland software, EMPIRE by IMST, Microstripes by Flomerics, Sonnet and CST Microwave Studio and Microwave Office of Applied Wave Research. Whereas, planar array performance can be assessed using a 2.5D MoM, for generalized 3D structures one needs to use a 3D FEM, FDTD, or TLM package. There is a varying degree of accuracy depending on the mesh resolution that is normally traded off against the computational time. These methods are able to reproduce experimental results well and allow that the physics of some specific properties of electromagnetic crystals to be intuitively understood. The initial results from the plane-wave or spherical wave expansion method give the dispersion curves and allow modal visualization, while those of the transfer matrix method give the transmission and reflection coefficients of the EBG. As soon as 3D EBGs are analyzed, most methods become computationally demanding, but in some cases one can still play simple but effective computational tricks that allow to treat some special 3D structures.

3.5.3 *EBG Applications*

A multitude of basic EBG applications exist especially within the microwave and low millimeter-wave region, for example, in electronically scanned phased arrays, high-precision GPS, Bluetooth, mobile telephony, wearable antennas, and more EBG potentially inspired metadevices.

Phased array antennas are the key components to provide higher performance by manipulating and steering wireless signal beams toward the desired directions. Phased arrays involving phase shifters are conventionally used in several applications (Robinson and Nakkeeran 2013). For example, constellations of low Earth orbit satellites can be used for high data rate transmission for multimedia applications. These applications require scanned multi-beam antennas with relatively wide bandwidth. Each beam is usually working in dual circular polarization. Most of these constellations will work at frequencies up to 30 GHz. The use of active phased array made in microstrip technology is then an attractive solution. However, the need for bandwidth and scanning increases the undesirable effects caused by surface waves. A very promising way to eradicate the problems created by surface waves, e.g., scan blindness, while at the same time improving performance, is to substitute standard dielectric substrates by EBG (de Maagt et al. 2016).

Another microwave application is high-precision GPS. High-precision GPS surveying can make measurements with sub-centimeter accuracy levels. While software can greatly reduce multipath errors, extra precautions that can shield the antenna from unwanted multipath signals are needed to obtain these accuracies. Choke rings provide excellent electrical performance for GPS antennas, but they are usually very large, heavy, and costly. Making use of the fact that metallo-dielectric EBG antennas can behave as artificial magnetic conductors, one can design EBG solutions in printed circuit technology (de Maagt et al. 2016). There are two main advantages in using the metallo-dielectric EBG antennas, first they suppress surface currents, and second they introduce inphase image currents. For example, high-impedance surface using metamaterial for the directive emissions in the antennas has been designed (Robinson and Nakkeeran 2013).

More antenna configurations using EBG have already been studied, such as dipole antennas, slot antennas, patch antennas, bow tie antennas, spiral and curl antennas, superstrate antennas or resonant cavity antennas, parabolic reflector antennas, and combinations of the above. By using the EBG substrates for patch antennas, for instance, the surface wave effects are significantly reduced and are able to provide relatively broadband frequency performance. Uniplanar compact PBG substrate is also developed to reduce surface wave losses for an aperture coupled fed patch antenna on a thick high dielectric constant substrate. Some simple two-dimensional arrays of conducting elements have been used to improve the performance of patch antennas (Robinson and Nakkeeran 2013).

As the world goes wireless, data and voice transmission are bound to become even more common such as the use of Bluetooth. Moreover, for other applications like mobile phones, more attention is being paid to the electromagnetic shielding to eliminate the potential health hazard. EBG technology has proved useful in mobile antenna handset designs and reduces the radiation (specific absorption rate, SAR) into the operator's hand and head. Shielding is not only important to reduce health concern; it also plays a crucial role in multipoint communications. For example, devices placed on the side of a laptop interact with the screen and the case, resulting in a lower bit-rate between two computers. Therefore, electromagnetic bandgap

materials can meet more and more demanding needs in wireless, data, and voice transmission areas (de Maagt et al. 2016).

Future clothing may have a variety of consumer electronics built into the garments. Wearable antennas have received much interest due to the introduction of personal communication technology. Wearable antennas have been used in radio tagging and miniature remote cameras, for example, and eventually it may even help parents to pinpoint their child's position. Antennas play a paramount role in the optimal design of wearable or handheld units used in these services. Clearly in designing these antennas, the electromagnetic interaction among the antenna, wearable unit, and the human operator is an important factor to be considered. EBG technology has been proposed as a design solution (de Maagt et al. 2016).

Microwave filtering has also turned out to be an important area where electromagnetic bandgap materials play an important role. The broad stop band can be exploited to suppress spurious passbands always present in conventional microstrip filters. The sharp cutoff can also be used to improve the roll-off on a low-pass filter. Furthermore, combinations of conventional designs and electromagnetic bandgap materials could lead to very compact structures (de Maagt et al. 2016).

The area of conventional waveguides is another field where hybrid solutions could play an important role. Rectangular waveguides with uniform field distributions are of great concern for applications in quasi-optical power combining. A standard waveguide can be modified by placing of EBG on the two sidewalls of a waveguide, potentially creating a very efficient waveguiding structure. Moreover, the coupled cavity waveguides (CCW) have attracted considerable attention. This concept is believed to enable bends in the waveguide with very low bend reflection loss (de Maagt et al. 2016).

3.6 Bi-isotropic and Bi-anisotropic Metamaterials

Categorizing metamaterials into double or single negative, or double positive, is normally done based on the assumption that the metamaterial has independent electric and magnetic responses described by the parameters ϵ and μ . However in many cases of electromagnetic metamaterials, the electric field causes magnetic polarization, and the magnetic field induces an electrical polarization, i.e., magnetoelectric coupling. Such media are denoted as being bi-isotropic. Media which exhibit magnetoelectric coupling, and which are also anisotropic, are referred to as bi-anisotropic (Wikipedia 2017).

Intrinsic to magnetoelectric coupling of bi-isotropic media are four material parameters interacting with the electric (\mathbf{E}) and magnetic (\mathbf{H}) field strengths and electric (\mathbf{D}) and magnetic (\mathbf{B}) flux densities. These four material parameters are ϵ , μ , κ , and χ or permittivity, permeability, strength of chirality, and the Tellegen parameter, respectively. Furthermore, in this type of media, the material parameters do not vary with changes along a rotated coordinate system of measurements. In this way they are also defined as invariant or scalar. The intrinsic magnetoelectric

parameters, κ and χ , affect the phase of the wave. Furthermore, the effect of the chirality parameter is to split the refractive index. In isotropic media this results in wave propagation only if ε and μ have the same sign. In bi-isotropic media with χ assumed to be zero and κ a non-zero value, different results are shown. Both a backward wave and a forward wave can occur. Alternatively, two forward waves or two backward waves can occur, depending on the strength of the chirality parameter. In the general case, the constitutive relations for bi-anisotropic materials can be expressed as (Wikipedia 2017):

$$D = \varepsilon E + \xi H \quad (3.10)$$

$$B = \zeta E + \mu H \quad (3.11)$$

where ε and μ are the permittivity and the permeability tensors, respectively, whereas ξ and ζ are the two magnetoelectric tensors. If the medium is reciprocal, permittivity and permeability are symmetric tensors and $\xi = -\zeta^T = -ik^T$, where k is the chiral tensor describing chiral electromagnetic and reciprocal magnetoelectric response. The chiral tensor can be expressed as $k = \frac{1}{3}T_r(k)I + N + J$, where $T_r(k)$ is the trace of k , I is the identity matrix, N is a symmetric trace-free tensor, and J is an antisymmetric tensor. Accordingly, the reciprocal bi-anisotropic response can be classified with the following three main classes: (i) chiral media ($T_r(k) \neq 0$, $N \neq 0$, $J = 0$), (ii) pseudo-chiral media ($T_r(k) = 0$, $N \neq 0$, $J = 0$), and (iii) omega media ($T_r(k) = 0$, $N = 0$, $J \neq 0$). Generally the chiral and/or bi-anisotropic electromagnetic response is a consequence of 3D geometrical chirality: 3D chiral metamaterials are composed by embedding 3D chiral structures in a host medium, and they show chirality-related polarization effects such as optical activity and circular dichroism. The concept of 2D chirality also exists, and a planar object is said to be chiral if it cannot be superposed onto its mirror image unless it is lifted from the plane. On the other hand, bi-anisotropic response can arise from geometrical achiral structures possessing neither 2D nor 3D intrinsic chirality. For instance, the magnetoelectric coupling of extrinsic chiral metamaterials results from the geometric chirality of the whole structure, and the effect is driven by the radiation wave vector contributing to the overall chiral asymmetry (extrinsic electromagnetic chirality). The effective chiral tensor 1D chiral metamaterials is not vanishing if the system is geometrically one-dimensional chiral (the mirror image of the entire structure cannot be superposed onto it by using translations without rotations, Wikipedia 2017).

3.7 Microwave Metamaterial-Inspired Metadevices

The promising applications of microwave metamaterial structures and metadevices have involved both unusual physical aspects and device designs with enhanced characteristics and performance as compared to their conventional counterparts.

The first and possibly the most significant application of LHM and negative refraction is the so-called perfect lens, being able to focus the whole spectrum of the source (i.e., both the propagating and the evanescent spectrum). This is achieved by the evanescent part of the source spectrum being amplified within the NRI slab and, hence, recovered at its original magnitude at the two focal points. All these structures, which have been implemented employing either directly or indirectly the LC-loaded transmission line metamaterials, have been used to reconstruct point source images of subwavelength dimensions (Kokkinos 2010).

Another large class of the metamaterial applications is those involving artificial dielectrics and magneto-dielectrics exhibiting tailored values and forms of their effective dielectric constants. An extremely popular example of these applications is the controlling of electromagnetic waves using engineered dielectric/magneto-dielectric tensors (anisotropic artificial material profiles) and the synthesis of coatings (cloaks) that offer electromagnetic invisibility to coated scatterers. Another example of metamaterial applications involving artificial dielectrics with permittivities near to zero is those referring to the tunneling of electromagnetic energy through waveguides of arbitrary shapes filled with such artificial dielectrics. Finally, the most popular application of metamaterial magneto-dielectrics, composed of several nonmagnetic resonant modular elements, is their use to provide increased miniaturization factors, potentially without significantly reducing the operating bandwidth, in several antenna, mostly microstrip-based, applications. In such antenna applications, artificial magneto-dielectrics exhibiting high- μ values could provide similar miniaturization factors with those of conventional dielectrics while when used together with conventional dielectrics may be exploited to maintain the impedance level close to that of free space (Kokkinos 2010).

A third class of the metamaterial applications is those involving the use of AMC/HIS and other periodic metasurfaces or EBG structures for the size reduction and the radiating property enhancement of highly directive antennas and antenna arrays. Finally, the most extended class of metamaterial applications is those employing the LC-loaded transmission line structures for the design of microwave devices and antennas with enhanced performance as compared with their conventional counterparts. Given the compatibility of this type of metamaterial with standard microwave technologies (i.e., microstrip, CPW, CPS), its use for the development of such applications had been a straightforward procedure. A big portion of these applications are based on the phase-shifting lines of that exploit the backward and forward waves that can be supported simultaneously by 1D LC-loaded transmission lines to design phase shifters that can insert any required phase shift (positive or negative) independently of their physical dimensions (usually being of subwavelength dimensions). The possibility of controlling the phase of microwaves using devices of subwavelength dimensions can be employed for the miniaturization of the vast majority of microwave devices that involve phase-shifting lines (e.g., power dividers, baluns, couplers, etc.). Other applications of the LC-loaded transmission lines include spatial filtering applications, miniaturized filters, zeroth-order resonators, leaky-wave antennas able of scanning their beams with frequency from the backward to the forward direction, and other antenna designs that employ negative- and zeroth-order resonances of LC-loaded structures to achieve miniaturization (Kokkinos 2010).

Apart from microwave devices and antenna designs that involve directly metamaterial structures, there have been several other designs that even though they do not employ any of the well-known metamaterial structures, they can be considered to be metamaterial inspired. Examples of such designs include the small antenna design and the near-field plates of that can be employed to focus an impinging plane wave to a focal point of subwavelength dimensions (subdiffraction focusing). The near-field plate design has been directly inspired by Veselago–Pendry perfect lens given that the flat-plates operation is based on the reconstruction of the impedance profile along the second NRI/PRI interface of the Veselago–Pendry perfect lens (Kokkinos 2010).

References

- Chen Y, Lipton R (2013) Multiscale methods for engineering double negative metamaterials. *Photonics Nanostruct Fundam Appl* 11:442–452
- de Maagt P, Gonzalo R, Vardaxoglou JY (2016) Review of electromagnetic bandgap technology and applications. *Radio Sci Bull* 309:11–24. <http://antenas.unavarra.es/Publicaciones/Images/Pub79.pdf>
- Iyer AK, Eleftheriades GV (2007) A multilayer negative-refractive-index transmission-line (NRI-TL) metamaterial free-space lens at X-band. *IEEE Trans Antennas Propag* 55(10):2746–2753
- Jiang ZH, Turpin JP, Morgan K, Lu B, Werner DH (2015) Spatial transformation-enabled electromagnetic devices: from radio frequencies to optical wavelengths. *Philos Transact A Math Phys Eng Sci* 373:2049. pii: 20140363. doi:10.1098/rsta.2014.0363
- Kokkinos T (2010) Analysis and design of metamaterial-inspired microwave structures and antenna applications. A Doctoral Thesis, Loughborough University, Loughborough
- Li Y, Kita S, Muñoz P, Reshef O, Vulis DI, Yin M, Lončar M, Mazur E (2015) On-chip zero-index metamaterials. *Nat Photonics* 9:738–742
- Robinson S, Nakkeeran R (2013) Photonic crystal ring resonator based optical filters. In: Vittorio MN (ed) *Advances in photonic crystals*. Intech, Passaro. <http://www.intechopen.com/books/advances-in-photonic-crystals/photonic-crystal-ring-resonator-based-optical-filters>
- Shalaev VM (2007) Optical negative-index metamaterials. *Nat Photonics* 1(1):41–48
- Soukoulis CM (2002) The history and review of the modelling and fabrication of photonic crystals. *Nanotechnology* 13:420–423
- Sun J, Litchinitser NM (2016) Metamaterials. In: Haus JW (ed) *Fundamentals and applications of nanophotonics*. Elsevier, Amsterdam, pp 233–252
- Verma R, Daya KS (2011) Effect of forbidden bands of electromagnetic bandgap engineered ground plane on the response of half wave length linear microwave resonator. *J Appl Phys* 109:084505
- Wartak MS, Tsakmakidis KL, Hess O (2011) Introduction to metamaterials. *Phys Can* 67(1):30–34
- Wikipedia (2017) Metamaterials. <https://wiki2.org/en/Metamaterial>

Chapter 4

Terahertz Metamaterials and Metadevices

4.1 Introduction

The applications of terahertz (THz) waves are wide-ranging, from security screening, medical imaging, wireless communications, nondestructive evaluation, chemical identification, and so on. Due to their low photon energy, THz waves do not ionize biological cells and thus are much safer for human inspections, unlike using X-rays. In astrophysics and earth sciences, thermal emission for a wide variety of light weight molecules is specifically amenable to THz band. In fact, the universe is bathed in THz energy with most of it remain unnoticed and undetected. However, the region between 0.1 and 10 THz was ever called “THz gap” because natural materials at the THz regime cannot offer capability to make efficient components like source, detector, modulator, waveguides, and filters. For instance, conventional transmissive optical materials from which lenses or other traditional optical devices are made typically suffer high loss when operating at the THz range. Immediately following demonstration of metamaterials in microwave region, it has been moved on to adopt such structures in THz research. Many THz metamaterials and devices have been developed, such as absorbers, lenses, switches, modulators, sensors, as well as phase-shifting and beam-steering devices to control and manipulate THz waves. To extend the operation bandwidth of metamaterials or to have the devices actively responding to the need of the systems and adjust their operation frequency, active tunability of metamaterial response has been explored (Tanoto et al. 2013). In addition, flexible THz metamaterials and metadevices have also been developed for flexible electronics and wearable devices.

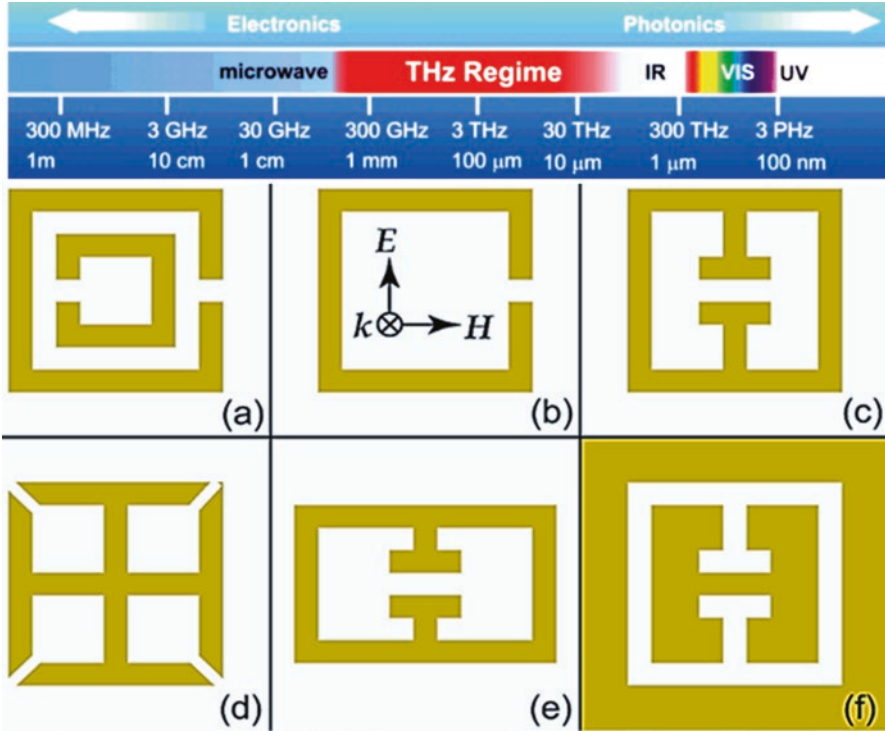


Fig. 4.1 Schematic illustrations of some SRR variants scaled to terahertz frequencies (Withayachumnankul and Abbott 2009): (a) double SRR, (b) single SRR, (c) eSRR, (d) fourfold rotational-symmetry eSRR, (e) rectangular eSRR, and (f) complementary eSRR. The common field orientation is indicated for all structures, excepting for the complementary eSRR that requires the in-plane 90° field rotation

4.2 Passive-Type Terahertz Metamaterials

Passive-type terahertz metamaterials have been developed through (a) engineered resonances including electric, magnetic, or electromagnetic responses; (b) anti-reflection; and (c) tuning of the bandwidth and resonance frequency.

4.2.1 Terahertz Metamaterials with Electric Responses

Electric responses at terahertz frequencies have mostly been demonstrated with planar SRRs, along with their variants, as illustrated in Fig. 4.1 (Withayachumnankul and Abbott 2009). Typically, their electrical coupling modes are excited by using wave propagation perpendicular to the SRR plane. In a study of double SRRs

(Fig. 4.1a) at terahertz frequencies, the effects of the shape (either square or circular), polarization, substrate, and lattice constant on the resonance properties are observed. For the polarization parallel to the gap-bearing side, LC and dipole resonances are present, but the LC resonance disappears in the other polarization. The lattice constant largely affects the dipole and not the LC resonances, while a higher dielectric constant of the substrate causes a redshift to every resonance. Moreover, the gap orientation among single SRRs (Fig. 4.1b) has a remarkable impact on the dipole resonance due to the inter-ring coupling nature. Regarding the effect of the thickness of SRRs, metallic SRRs with a sub-skin-depth thickness have a large resistance such that the characteristic resonances are damped and eventually become extinct.

A number of eSRRs are designed to resonate in the terahertz regime, as shown in Fig. 4.1c–f. The standard eSRRs (Fig. 4.1c) basically suppress a magnetic response in favor of a pure electric response, and the fourfold rotational-symmetry eSRRs (Fig. 4.1d) are not sensitive to polarization. The number and position of capacitive gaps present in eSRRs affect the position and the linewidth of the LC resonance. Rectangular eSRRs (Fig. 4.1e), as opposed to square eSRRs, allow tuning of the dipole resonance frequency. Provided that the area encircled by an SRR is fixed, the LC resonance frequency is kept constant, while the dipole resonance can be shifted to a higher frequency by shortening the SRR side that is parallel to an electric field. This tuning scheme can prevent the LC–dipole coupling that causes resonance reshaping. Terahertz eSRRs and their complements (Fig. 4.1f) demonstrate consistency with Babinet’s principle in that they display a transmission reversal, i.e., the transmission dips in eSRRs are manifested as the transmission peaks in complementary eSRRs. In the complementary eSRRs, a Drude response takes place as a result of a large metallic plane (Withayachumnankul and Abbott 2009).

4.2.2 Terahertz Metamaterials with Magnetic Responses

In addition to electric responses, artificial magnetic responses at terahertz wavelengths were also realized. Figure 4.2 shows the first example employing an array of planar double SRRs to produce a strong magnetism around 1 THz in response to obliquely incident waves. This artificial magnetic material exhibits resonant strength an order of magnitude larger than that of natural magnetic substances (Withayachumnankul and Abbott 2009).

Another structure containing multilayers of planar SRRs encapsulated in a polyimide film is magnetically active at a frequency range of about 0.4–0.8 THz, following an electric excitation on a gap-bearing side with the propagation direction normal to the SRR plane (Han et al. 2011). In this case, no magnetic response is actually observed at the far field, because the incident magnetic field is completely in the SRR plane and perpendicular to the induced magnetic dipole moment.

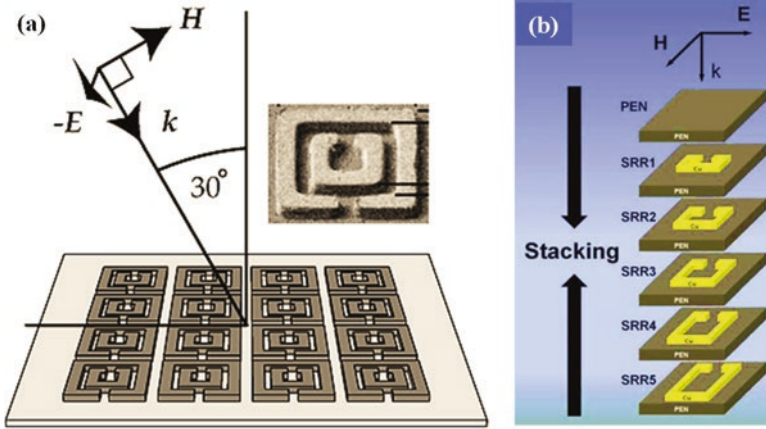


Fig. 4.2 Magnetically coupled SRRs: (a) the terahertz radiation incident on the SRRs at 30° from the normal. The configuration enables a magnetic field component to couple to SRRs, but prohibiting an electric LC coupling (Withayachumnankul and Abbott 2009). (b) Multilayers of planar SRRs encapsulated in a polyimide film (Han et al. 2011)

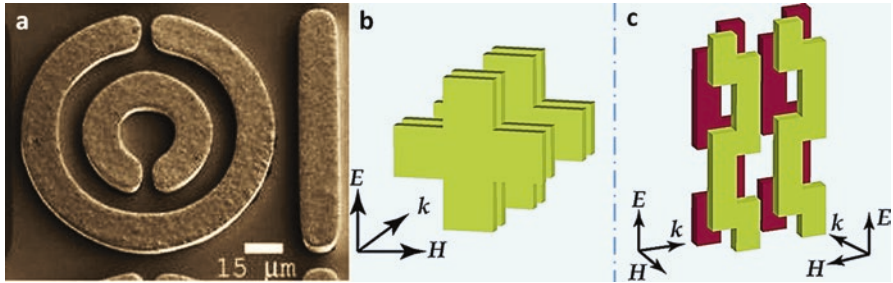


Fig. 4.3 Terahertz metamaterials with negative indices (Withayachumnankul and Abbott 2009): (a) NIM from a SRR–wire structure; (b) two unit cells of crossbars display a negative index in response to the wave incident normal to the surface; and (c) bilayer S-strings behave as a two-dimensional isotropic NIM, owing to the presence of current loops in either direction of propagation

4.2.3 Terahertz Metamaterials with Negative Refractive Indices

Beyond purely electric or magnetic media, terahertz metamaterials have been formed with ultrahigh refractive indices and NIMs that possess spectrally overlapping negative permittivity and permeability. In addition to the conventional wire–SRR combination, advanced NIM structures have also been developed with crossbars, S-strings, chiral media, etc. Figure 4.3a shows that terahertz NIMs, containing planar SRRs and wires fabricated on the same layer, allow properly aligned electric and magnetic field components to resonate and support a passband at around

4.92 THz. Another NIM structure involves double layers of metallic crossbars, as shown in Fig. 4.3b. Each metallic bar is responsible for an electric dipole and negative permittivity, while the two metallic layers, in substitution of an SRR, are responsible for a magnetic dipole and negative permeability. The crossbars at the terahertz scale show a NIM band around 1 THz with a figure of merit up to 11. In addition, the structure in Fig. 4.3b is polarization independent for the propagation direction normal to the cross plane, due to the orthogonal symmetry. By introducing a geometrical disparity into the perpendicular bars, the NIM bands for the two polarizations are no longer identical and the structure becomes birefringent. S-shape resonators, as illustrated in Fig. 4.3c, are scaled to function in the terahertz regime. The interplay between the strings permits antiparallel currents and magnetic resonances in two propagation directions. With freestanding S-strings, the NIM bands appear at 2.2 and 1.9 THz for the normal and 90° angle of incidence, respectively (Withayachumnankul and Abbott 2009).

Unlike other NIMs, chiral metamaterials emerge as a special class of NIMs that is not necessarily underpinned by simultaneous negative permittivity and permeability (will be discussed in Chap. 6). In a chiral material, the left-handed and right-handed circularly polarized waves travel with different phase velocities, and in the case of a strong chirality, the phase velocity of one circular polarization may become negative. The chiral effect is a result of the cross-coupling between electric and magnetic dipoles, which can be artificially reproduced by using nonplanar resonators. A terahertz chiral metamaterial produces a negative refractive index between 1.06 and 1.27 THz (Zhang et al. 2009; Withayachumnankul and Abbott 2009).

4.2.4 Broadband Terahertz Metamaterials

The operation of ordinary metamaterials is confined within a narrow spectral range, since dispersive resonances are exploited to control the permittivity and permeability. For broadband operation, multiresonance metamaterials and active resonance tunable metamaterials (will be discussed in Sect. 4.3) have been developed. At terahertz frequencies, the multiresonance approach has been realized with a few configurations. A straightforward configuration packs together two or more resonators with different geometries in a single unit cell. The number of resonance frequencies that the structure can display is determined by the number of different resonators. Terahertz metamaterials featuring either two or three planar eSRRs per unit cell are implemented using a checkerboard or beehive pattern, respectively, to maximize the fill factor (see Fig. 4.4a for the beehive metamaterial). Multiresonance structures of this type unavoidably compromise the resonance strength owing to the sparseness of identical resonators and the counteraction between different resonators. In the worst case, desired properties may be suppressed. The concept of a fractal that describes the self-similarity of a shape at different scales is an alternative. Metamaterials made of fractal H-shaped metallic lines or slits, as shown in Fig. 4.4b, are able to display electric resonances at multiple terahertz frequencies. Each fractal

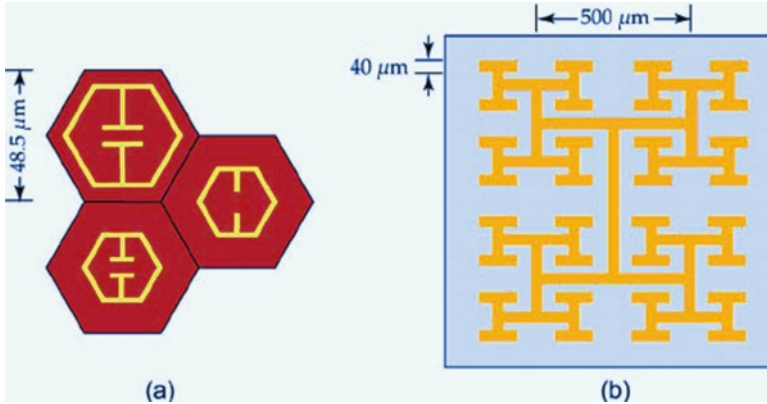


Fig. 4.4 Multiresonance metamaterials (Withayachumnankul and Abbott 2009): (a) a unit cell of metamaterial containing a triplet of distinct eSRRs exhibits three distinct resonances; and (b) an H-type fractal metamaterial displays several electric resonances corresponding to different wire lengths

level contains a set of wires with a unique length that is responsible for an electric dipole resonance. However, in practice, fractal metamaterials cannot accommodate self-similar patterns at ever-finer scales (Withayachumnankul and Abbott 2009).

4.3 Active-Type Terahertz Metamaterials

Although the realization of passive metamaterial-based THz components and metadevices, such as filters, polarizers, absorbers, etc., is of great importance for filling the THz gap and for the full manipulation and exploitation of THz waves, the achievement of active, dynamically controllable metamaterial elements is also essential, since it offers the possibility for the creation of a variety of active components, including tunable notch filters, switches, modulators, and more. With this target, many efforts have been devoted to the realization of frequency agile metamaterial components, mainly in the THz but also in the optical regime, in infrared, and in microwaves. Such metamaterials are realized by combining standard metamaterial elements with active materials, i.e., materials that can change optical properties by application of an external stimulus, such as voltage, light, temperature, mechanical stress, magnetic field, and so on (Kafesaki et al. 2012). Therefore, active-type THz metamaterials can generally be categorized as electrically tunable metamaterials, optically tunable metamaterials, and mechanically tunable metamaterials, according to the methods that are used to tune the electromagnetic properties (Lee et al. 2015). However, these approaches can also be combined with each other or simultaneously used for tuning various kinds of THz metamaterials. Based on the current tuning methods, more and more need approaches may be developed in the future.

The metamaterial component used for the creation of active metamaterials is typically based on various split-ring resonator (SRR) structures. Such resonators are usually characterized as effective capacitor–inductor circuits, and the role of the semiconducting material, for instance, if incorporated in the resonator system, is either to short the circuit or to alter its capacitance (C) or inductance (L), thus modifying its resonance frequency, $\omega = 1/\sqrt{LC}$. Using such various shaped ring resonators, known also as electric-field-coupled-LC (ELC) resonators, various electrically tunable (i.e., tunable using an external voltage) metamaterials have been obtained, showing either blue-shift or red-shift tunability or switching response. Moreover, a variety of optically controllable metamaterials have been realized, including blue- or red-shift tunable structures, single- and multiband switches, amplitude, and/or phase modulators (Kafesaki et al. 2012).

4.3.1 Electrically Tunable THz Metamaterials

Electrically tunable approach and optically tunable approach or combined electro-optical approach are generally based on the integration with the highly established semiconductor technology. To achieve tunability, the meta-atoms are deposited on the surface of semiconductors such as photosensitive semiconductors, using applied bias voltage (electrically tunable approach) or photoinduced conductivity phenomena (optically tunable approach to tune the metamaterials electromagnetic characteristics). Electrically tunable approach usually use the hybrid structure of meta-atoms/semiconductor in which a Schottky junction is formed at the interface. By applying a bias voltage between metallic meta-atoms and the substrate, charge carriers are depleted near the split gap, which cause a change in the resonance strength. Therefore, the amplitude and phase of the transmitted THz waves can be effectively controlled by the bias voltage (Lee et al. 2015).

Among the various ways of forming electrically tunable THz materials, one popular technique is by taking advantage of large doping density and high electron mobility in single-crystalline semiconductors such as Si, GaAs, and graphene. Upon carrier depletion, dynamically switchable THz metamaterial devices have been achieved in Schottky diodes fabricated on semi-insulating GaAs substrates. Constituent resonators can also be switched via external optical excitation of free charge carriers in Si islands or capacitor plates. For achieving ultrafast speed, high-mobility two-dimensional electron gas (2DEG) and graphene have been utilized by integration of transistors at the metamaterial unit cell level (meta-atoms or metamolecules). Using single-layer graphene as the active medium, as shown in Fig. 4.5, a graphene/metamaterial hybrid structure was fabricated within a flexible polyimide substrate and integrated with a THz transparent gate electrode. Unlike near-IR and visible light, THz waves are absorbed in the graphene layer via intraband transition. Here, the Fermi level of graphene and the degree of intraband transition were controlled by electrical gating. To increase the modulation depth, hexagonally shaped

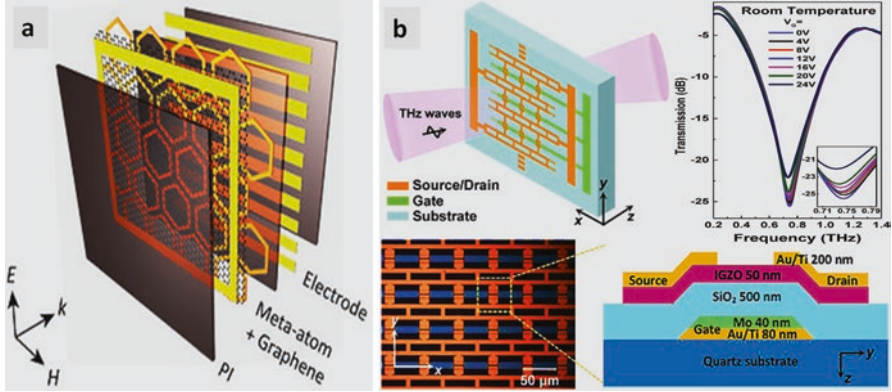


Fig. 4.5 Electrically tunable THz metamaterials (Lee et al. 2015; Xu et al. 2016): (a) graphene/metamaterial hybrid metadevices for switching THz waves and (b) electrically controlled THz metamaterial with a-IGZO TFTs

meta-atoms, which were strongly resonant at THz frequencies, were placed directly onto the graphene layer. With this approach, amplitude and phase of the transmitted THz waves could be controlled efficiently by electrical gating. Moreover, the metadvice showed hysteretic behavior in the THz transmission for a cyclic variation of gate voltage, and this hysteretic behavior could be utilized for electrically controlled, photonic memory operation (Lee et al. 2015).

However, despite their attractive properties, tunable metamaterials or modulators based on graphene and 2DEG materials are usually limited to relatively small area fabrication and actually pose more stringent requirement on complex growth process. Amorphous oxide semiconductors (AOS) typified by In-Ga-Zn-O (IGZO) exhibit a unique combination of high electron mobility ($10\text{--}50\text{ cm}^2/\text{Vs}$), high optical transparency, and low-temperature processing requirements. The mass production of AOS-based thin-film transistor (TFT) arrays with excellent uniformity can be realized at room temperature on large size substrates through a physical vapor deposition technique such as sputtering. These AOS transistors have been utilized as drive modules of backplanes for the production of high-speed switching devices used in high-motion-speed sensors/displays with ultrahigh definition, such as active-matrix liquid crystal displays and active-matrix organic-emitting diode displays. As compared to transistors based on 2DEG or graphene materials, the amorphous-IGZO (α -IGZO) TFTs exhibit extremely low off-state current ($<10^{-12}\text{ A}$), high on-to-off ratio ($>10^9$), small subthreshold swing ($<0.2\text{ V/dec}$), and high device yield (close to 100%) over a large area. Under excitation conditions, the IGZO channel conductivity can be widely tuned up to $\sim 5 \times 10^2\text{ S m}^{-1}$. All these characteristics indicate that IGZO TFT arrays may have great potential in the application of array-distributed active metamaterial devices with their advantages in energy saving, low cost, and high yields, as shown in Fig. 4.5b. In addition, α -IGZO TFTs exhibit excellent light insensitivity owing to the wide bandgap of over 3 eV. Thus great advantages can be obtained in applicability as compared to Si, GaAs, and graphene, since THz modulators based on

these narrow bandgap semiconductors may require light shielding to eliminate photoconduction-related effects. The high operation stability of α -IGZO TFT also ensures its tolerance to large temperature variations and severe environment. Therefore, the incorporation of AOS into metamaterials will offer a solution for the mass production of stable, uniform, and low-cost THz metadevices, which may expand the horizon of oxide electronics into the applications of THz modulation and imaging (Xu et al. 2016).

4.3.2 *Optically Tunable THz Metamaterials*

Optically tunable THz metamaterials have been realized mainly by employing active materials such as photoconducting semiconductors, which, by the application of an external pump light, can be switched between insulating and conducting states to alter the metamaterial response. To incorporate such semiconducting materials into the metamaterial, two main approaches have been applied (Kafesaki et al. 2012): (a) the semiconductor has been used as a metamaterial substrate or as a layer between the substrate and the metamaterial; and (b) the semiconductor is inserted locally into specific, critical parts of the metamaterial resonator. The first approach is easier in its fabrication, but by application of the pump light, the total frequency spectrum of the metamaterial response would be changed or modified (not just selected frequency regimes close to the SRR resonances). This feature can be advantageous, depending on the desired property or application foreseen for the metamaterial. For example, in the case of double resonant metamaterials, the frequency regime can be exploited between the two resonances, where interesting phase modulation properties can be achieved. The second approach, i.e., the inclusion of the semiconductor into specific parts of the metamaterial resonator, although more difficult in its implementation, has the advantage of affecting specific frequency regions of the metamaterial response, therefore, leaving unaffected the remainder of the metamaterial spectrum.

With these approaches, a variety of optically induced effects, including blue- and red-shift tunability of the metamaterial resonances, single- and multiband switching, and broadband phase modulation, have been demonstrated (Kafesaki et al. 2012). Besides, optically tunable metamaterials have great potential for the use in ultrafast modulation of THz waves when they are combined with semiconductor materials that possess short electron–hole recombination times. For example, ErAs/GaAs nanoisland superlattice or graphene could be a promising candidate of the semiconductor materials for this purpose because the recombination time of photo-excited carriers for these materials typically is of the order of a few picoseconds (Lee et al. 2015).

In addition, optically tunable metamaterials have been applied for manipulation of electromagnetically induced transparency (EIT) which enables a unique route to endow classical optical structures with aspects of quantum optical systems, as shown in Fig. 4.6. The unit cell of the EIT metamaterial consists of CWs (cut wires)

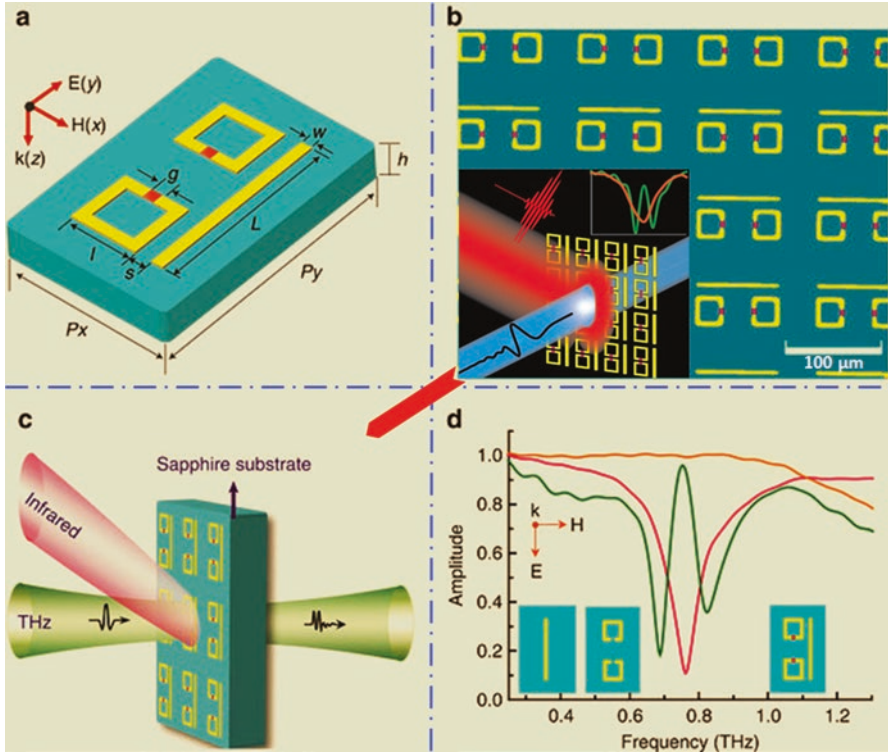


Fig. 4.6 Optically tunable THz metamaterials (Gu et al. 2012): (a) schematic of the unit cell with the geometrical parameters of $L = 85$, $l = 29$, $s = 7$, $w = 5$, $h = 495$, $g = 5$, $P_x = 80$, and $P_y = 120$ μm , respectively; (b) the fabricated metamaterial; (c) experimental schematic of the optical pump–terahertz probe measurements of the EIT metamaterial; and (d) measured amplitude transmission spectra of the sole-CW (pink), SRR-pair (orange), and the EIT metamaterial sample (olive). The insets in (d) are the structural geometries of the sole-CW, SRR-pair, and the EIT metamaterial samples from left to right, respectively

and two SRRs, with Si islands positioned in their gaps (Fig. 4.6a). As the resonances of CW and SRR are both determined primarily by their geometrical dimensions and the size of the subwavelength unit cell ensures that the terahertz waves do not diffract at normal incidence, thus the EIT metamaterial array behaves as an effective medium. The metamaterial structure was fabricated on a Si-on-sapphire wafer comprised of 500-nm-thick undoped Si film and 495- μm -thick sapphire substrate (Fig. 4.6b). The fabrication of the metamaterial sample began with patterning of Si islands by reactive ion etching, followed by deposition of 200-nm-thick aluminum that forms the CW and the SRR-pair patterns. An electro-optic time-resolved OPTP system (Fig. 4.6c) was used to carry out the measurements. The 2.5-mm diameter terahertz beam was collimated on the metamaterial array with electric field parallel to the CW. An optical pump beam (50 fs, 1.35 mJ per pulse at 800 nm with a 1-kHz repetition rate) with a spot diameter of 10 mm enables a uniform excitation aperture

for the terahertz transmission. To clarify the underlying mechanism of the EIT effect, three sets of samples were fabricated and measured. The first sample consists of a CW array, the second consists of an SRR-pair array, and the third (the EIT metamaterial sample) consists of both the CW and the SRR-pair. The measured amplitude transmissions of the first (CW only) and the second samples (SRR-pair only) are shown in Fig. 4.6d. The CW resonator array shows a typical localized surface plasmon (LSP) resonance at 0.74 THz whereas the SRR-pair that supports an inductive–capacitive (LC) resonance at the same frequency is inactive due to the perpendicular orientation of the incident electric field. Thus, the CW resonator and the SRR-pair serve as the bright and dark modes, respectively, for perpendicular electric field excitation. In the EIT sample, the CW is directly excited by the incident electric field along the CW. The near-field coupling between the CW and the SRR-pair excites the LC resonance in the SRRs. The destructive interference between the LSP and LC resonances leads to a sharp transparency peak in a broad absorption background at 0.74 THz. Therefore, the active optical control of metamaterial-induced transparency can be done through optically tuning the conductivity of the integrated Si islands (dark mode). Moreover, by integrating photoconductive silicon into the metamaterial unit cell, a giant switching of the transparency window occurs under excitation of ultrafast optical pulses, allowing for an optically tunable group delay of the terahertz light. The optically active tuning of EIT metamaterials may open up avenues for designing active slow light devices, ultrasensitive sensors, nonlinear devices, as well as chip-scale ultrafast devices that would find utility in optical buffering and terahertz active filtering (Gu et al. 2012).

4.3.3 Mechanically Tunable THz Metamaterials

The electromagnetic response of metamaterials was mainly determined by the structural shapes of the basic building unit cells (meta-atoms). Accordingly, THz modulation can be achieved by manipulating or modifying the structural shape directly or by arranging the meta-atoms. From this point of view, mechanically tunable metamaterials are also called reconfigurable metamaterials. They are usually tuned through microelectromechanical system (MEMS), thermomechanical, magnetomechanical, and altering the shape of the unit cells and/or substrate of flexible metamaterials (Lee et al. 2015).

Microelectromechanical system (MEMS) has been extensively used in tuning THz metamaterials. By using MEMS-based processes to fabricate platform structures to control the spacing and configuration of the resonant element, electromechanical mechanism has been used to control the shape and configuration of the resonant components of metamaterials in real time. One important advantage of using silicon-based MEMS is its CMOS compatible fabrication process for potential low-cost large-volume manufacturing. With the typical period of the micromachined metamaterial element in tens of micrometers, they are ideally suited for

working frequency in THz region. However, with response time in hundreds of microseconds, micromachined metamaterials are only suitable in applications where high-speed modulation is not essential (Tanoto et al. 2013).

Thermal tuning of metamaterials electromagnetic response by relying on the difference in the thermal expansion between metal elements and the surrounding matrix materials is also a promising approach. It enables reconfigurability with simple fabrication. In one design, the difference in thermal expansion coefficient of metal and semiconductor/dielectric is such that a change in temperature leads to a bending of a bi-material cantilever. Considering a few microns' actuation or less, thermal heating is efficient in terms of the power consumption, which makes it very useful to realize thermomechanical tunable metamaterials working in the THz region or beyond (Tanoto et al. 2013).

Magnetomechanical tunable THz metamaterials have also been developed. The micromachined cantilevers used to tune the metamaterial are actuated by the force generated by an external field on the magnetic material coating on the surface. The use of cantilevers enables continuous tuning of the resonance frequency over a large frequency range. The tunable metamaterial has field-induced nonlinearity, which is possible to be realized using current micromachining technologies. Magnetic actuation of single end fixed cantilevers in micromachined devices has been studied and demonstrated. In addition to translation, the magnetomechanical actuators can be used to rotate the micromachined structures. This may be useful in making micromachined tunable metamaterials with rotational metamaterial elements (Tanoto et al. 2013).

4.4 Flexible THz Metamaterials

Flexible substrates provide ideal platforms for exploring some of the unique characteristics that arise in THz metamaterials via mechanical deformation. These elastic substrates are of special interest owing to their natural ability to achieve large frequency tunability through mechanical deformation, thereby eliminating the need to integrate an external actuator or bias voltage to achieve desired tuning. The resonator structures fabricated on such elastic substrates exhibits high sensitivity to structural parameters, which allow small changes in dimensions to be sensed easily. Such mechanical tuning of metamaterials has been used to demonstrate wireless strain sensing, biological sensing, and absorbers. The most commonly used flexible substrates for metamaterials are PDMS and polyimide, due to their widespread use in flexible electronics. Other flexible substrates utilized for metamaterial devices include metaflex, polyethylene naphthalene (PEN), polyethylene terephthalate (PET), polymethyl methacrylate (PMMA), and polystyrene (Walia et al. 2015).

Fabricating metamaterials on flexible substrates with much thinner dimension than the metamolecules dimensions, tunable properties can be easily got through the structural change of the substrate, or three-dimensional metamaterials can also be built by stacking or rolling the film. Due to the flexibility, the flexible metamaterials

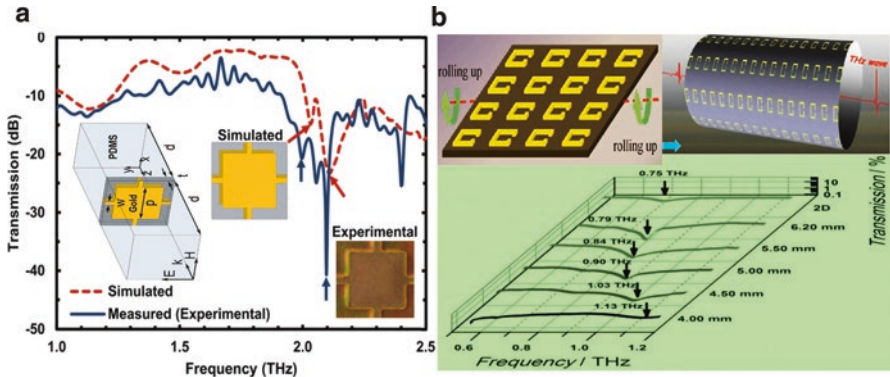


Fig. 4.7 Flexible THz metamaterials: (a) THz response of fishnet metamaterials on flexible PDMS substrate (Khodasevych et al. 2012); (b) 3D THz metamaterial tube and tunable response with hollow core (Zaichun et al. 2012)

can be coated on nonplanar surfaces for shielding, concentrator or absorber applications. Polyimide substrates, as thin as $5.5\ \mu\text{m}$, have been employed to demonstrate freestanding metamaterials. The devices were found to exhibit strong robustness with no degradation of properties even after rinsing in organic methanol and isopropanol, tearing and tweaking, and heating up to $350\ ^\circ\text{C}$. Quasi-three-dimensional THz electric metamaterials were then demonstrated on this substrate. From the transmission characteristics obtained through TDS, they show non-dependency between effective dielectric function and the number of layers. In addition, it was found that by decreasing the thickness of the polyimide substrates, the metamaterials show negative dielectric response (Tanoto et al. 2013).

Terahertz metamaterials have commonly been fabricated on polydimethylsiloxane (PDMS) substrate, by which the cost, inertness, and ease of fabrication are its main advantages. PDMS is also widely used in microfluidics, allowing potential metamaterials–microfluidics hybrid device development. For instance, flexible fishnet THz metamaterials were fabricated on $250\text{-}\mu\text{m}$ -thick PDMS substrate. Alternating layers of chromium (20 nm) and gold (200 nm) were used to minimize film stress and to improve adhesion. A thin layer of PDMS ($10\ \mu\text{m}$) is used to isolate two fishnet layers. Five layers of fishnet structure were obtained after repeated process. Figure 4.7a shows the simulated and measured THz response of the five-layer fishnet metamaterials, showing resonant dips at 2.0 THz and 2.1 THz and evidence of splitting in the high transmission area after the resonant frequency (Khodasevych et al. 2012; Tanoto et al. 2013).

Metamaterial tubes made of solid semiconductor materials were also found to exhibit unique THz properties. The semiconductor layers relax their strain upon release from the substrate by rolling up into microtubes similar to a rolled-up carpet. Strictly speaking, it is not a flexible metamaterials, but the fabrication process does involve the elastic characteristics of semiconductor layer. For optical metamaterial fabrication, the walls of rolled-up structures are treated as metamolecules, but for

THz frequency, the entire rolled-up structure is treated as a unit cell. Strong chiral properties were observed from an array of (In)GaAs/GaAs/Ti/Au microhelices of 11 μm in diameter and $52\text{--}53^\circ$ helix angle. Due to strong preferential rolling direction of self-rolling layers in the InGaAs materials, a well-defined angle can be realized. Circular dichroism and polarization rotation around 2 THz were found. The magnetic response is dependent on the number of rotation. A negative permeability is achievable when the rotation extends beyond one rotation and the resonance frequency can be approximated by a simple Lorentz oscillator model (Tanoto et al. 2013).

Tuning of the resonant peak was also found by rolling the THz metamaterials into a tube shape with hollow core. The three-dimensional metamaterial tubes are characterized as the THz wave propagates through the core of the tube. As shown in Fig. 4.7b, a tuning range of 50.6% within the frequency range of 0.75–1.13 THz was observed as the tube diameter decreases from 6.2 to 4.0 mm. The blue shift of the resonance frequency was attributed to the destructive magnetic interactions among the neighboring SRR unit cells on the increasingly curved surface. Therefore, the THz tube can be used to determine the unknown materials through the spectral signatures of the unknown materials. Refractive index changes as small as 0.0075 can be detected in conjunction with conventional THz-time-domain spectroscopy (Zaichun et al. 2012; Tanoto et al. 2013).

References

- Gu J et al (2012) Active control of electromagnetically induced transparency analogue in terahertz metamaterials. *Nat Commun* 3:1151(1–6). doi:10.1038/ncomms2153
- Han NR, Chen ZC, Lim CS, Ng B, Hong MH (2011) Broadband multi-layer terahertz metamaterials fabrication and characterization on flexible substrates. *Opt Express* 19(8):6990–6998
- Kafesaki M, Shen NH, Tzortzakis S, Soukoulis CM (2012) Optically switchable and tunable terahertz metamaterials through photoconductivity. *J Opt* 14:114008 (1–8)
- Khodasevych IE et al (2012) Elastomeric silicone substrates for terahertz fishnet metamaterials. *Appl Phys Lett* 100:061101 (1–3)
- Lee SH, Choi M, Min B (2015) Terahertz metamaterials. In: Song HJ, Nagatsuma T (eds) *Handbook of terahertz technologies: devices and applications*. Pan Stanford, Singapore, pp 277–297
- Tanoto H, Ding L, Teng JH (2013) Tunable terahertz metamaterials. *Terahertz Sci Technol* 6(1): 1–25
- Walia S et al (2015) Flexible metasurfaces and metamaterials: a review of materials and fabrication processes at micro- and nano-scales. *Appl Phys Rev* 2:011303 (1–14). doi:10.1063/1.4913751
- Withayachumnankul W, Abbott D (2009) Metamaterials in the terahertz regime. *IEEE Photon J* 1(2):99–118
- Xu W-Z et al (2016) Electrically tunable terahertz metamaterials with embedded large-area transparent thin-film transistor arrays. *Sci Rep* 6:23486. doi:10.1038/srep23486 (1–9)
- Zaichun C et al (2012) Realization of variable three-dimensional terahertz metamaterial tubes for passive resonance tunability. *Adv Mater* 24:143–147
- Zhang S, Park YS, Li J, Lu X, Zhang W, Zhang X (2009) Negative refractive index in chiral metamaterials. *Phys Rev Lett* 102(2):023901-1–023901-4

Chapter 5

Photonic Metamaterials and Metadevices

5.1 Introduction

Photonic metamaterials typically employ periodic, cellular structures or contain some kind of metallic nanoscale electromagnetic resonators, even though it is not always obvious from looking at the shapes of the structures that these act as resonators. An early approach, which has been taken over from previous work in the microwave domain, is based on split-ring resonators. These can be considered as simplified LC circuits, where the inductance has been replaced with a not fully closed metallic ring and the capacitor is formed by the opening in that ring. Such resonators can also have approximately rectangular forms or (if the opening is made larger) like horseshoes. The resonances of such a resonator can be in the mid-infrared domain (with wavelengths of a few microns) when its width is reduced to the order of a few hundred nanometers (multiple resonances with different frequencies may occur, but the lowest frequency resonance is often most relevant for the application). One layer of a photonic metamaterial can be made with metallic nano-resonators onto a nonconducting (dielectric) substrate. Three-dimensional structures (3D metamaterials) can also be made by stacking such arrays in the vertical direction with a period which is again well below the optical wavelength. When light impinges such nano-resonators, it can excite electromagnetic oscillations. These are particularly strong for frequencies near the resonance frequency, but the most interesting optical effects may occur somewhat above or below the resonance. When the period of the structure is well below half the optical wavelength, there are no photonic bandgap effects, and the effect on light propagation can be described with a (frequency-dependent) effective relative permittivity ϵ and relative permeability μ of the metamaterial and a bi-anisotropy parameter ξ for bi-anisotropy metamaterials, which describes the coupling of electric field strength \mathbf{E} and magnetic field density \mathbf{B} or magnetic field strength \mathbf{H} and electric displacement field \mathbf{D} . Such couplings can occur, e.g., because in a split-ring resonator electric field can induce a ring current, generating a magnetic field, and a magnetic field can induce a current

which leads to the buildup of an electric field. However, ξ can be zero for reasons of symmetry if structures are combined in a suitable way. Still more simplified forms of resonators may consist only of a periodic arrangement of short wires or of metallic pieces with other shapes. Such forms can be used at shorter wavelengths to reach the red end of the visible optical spectrum. There are also metamaterial structures where the whole metallic structure is electrically connected, or the metamaterials can be made with complete optical dielectrics. Furthermore, there are structures with genuinely three-dimensional building blocks, such as short helically wound wires (helical antennas), which are sensitive to the direction of circular polarization (Paschotta 2016).

As explained above, the optical properties of metamaterials can be described with the permittivity ϵ and the permeability μ and in some cases in addition the bi-anisotropy parameter ξ . Whereas for ordinary optical materials, μ is very close to 1, μ can have totally different values in metamaterials, even though these usually do not contain ferromagnetic materials. All three parameters are generally frequency-dependent and often also dependent on the propagation direction and polarization state of the light. Also, these parameters are not necessarily real (apart from ξ , which is zero at all frequencies for certain structures). The non-negligible optical losses of typical metamaterials (particularly when operating at high frequencies) lead to substantial imaginary parts of ϵ and μ . The magnitude of the refractive index is determined by the following equation (Paschotta 2016):

$$n^2 = \epsilon\mu - \xi^2 \quad (5.1)$$

For purely real ϵ and μ , and assuming $\xi = 0$, the refractive index n is real but can be positive, negative, or zero. The sign of the refractive index is chosen such that Snell's law correctly describes the direction of the refracted beam at an optical interface.

The impedance of a material is given by (Paschotta 2016):

$$z = \sqrt{\frac{\mu\mu_0}{\epsilon\epsilon_0}} \quad (5.2)$$

As the impedance depends on μ / ϵ , whereas the refractive index depends on $\mu \cdot \epsilon$, two media with the same refractive index do not need to have the same impedance, if μ can vary. (For ordinary optical media, the refractive index determines the impedance and vice versa, as μ is very close to 1.) Similarly, two media can have the same impedance while differing in the refractive index. This is relevant, e.g., for the magnitude of reflections from optical interfaces, which depends on the different impedances. For example, there would be no reflection at the interface between vacuum and a medium with $\mu = \epsilon = -1$, although the refractive index changes from +1 to -1: the impedance is the same on both sides of the interface.

If both ϵ and μ are negative (\rightarrow double-negative metamaterial) and ξ is zero, the phenomenon of negative refraction occurs at interfaces between vacuum and the

metamaterial. For a bi-anisotropic material with $\xi \neq 0$, negative refraction can also occur (Rill et al. 2009). A convex lens made of a negative-index material could be defocusing rather than focusing, and a concave lens could be focusing. Even a simple plate (with planar and parallel end faces) of a negative-index medium could act as a lens. If the refractive index is -1 , this could even lead to a superlens (perfect lens), creating images of objects with a resolution not limited by diffraction. There are superlenses based on effects other than negative refraction. In addition, very peculiar effects would occur if some object could be embedded in a negative-index metamaterial. Depending on its depth in the medium, it may appear strongly magnified and distorted for an observer outside the material. It should even be possible to make cloaking devices (invisibility cloaks), which can hide objects within them against viewing with light from outside, although probably only in a very limited frequency range (Merlin 2004; Paschotta 2016).

The chiral metamaterials containing metallic helical nanowires have a certain handedness, which can lead to substantially different optical effects for light with different directions of the circular polarization. It is possible to obtain metamaterials which are highly absorbing for one circular polarization direction and have a high transmission for the other polarization direction. The resulting device can be called a circular polarizer. A negative refractive index is not required for that phenomenon (Paschotta 2016).

However, fabrication of very fine structures of metamaterials for operation in the visible spectral region may still be challenging although some lithographic techniques, direct laser writing, or others can be employed. Besides, more fundamental limitations arise from the properties of the materials used. In particular, there are no perfect conductors for frequencies of hundreds of terahertz. Therefore, particularly devices for the highest frequencies exhibit relatively high optical losses (Paschotta 2016).

5.2 Photonic Crystals

The connection and distinction of photonic crystals and photonic metamaterials are shown in Fig. 5.1. Photonic crystals are composed of periodic dielectric, metallo-dielectric, or superconductor microstructures or nanostructures that affect the propagation of electromagnetic waves (EM) in the same way as the periodic potential in a semiconductor crystal affects the electron motion by defining allowed and forbidden electronic energy bands. Photonic crystals contain regularly repeating regions of high and low dielectric constant. Photons (behaving as waves) propagate through this structure—or not—depending on their wavelength. Wavelengths that are allowed to travel are known as modes; groups of allowed modes form bands. Disallowed bands of wavelengths are called photonic bandgaps. The periodicity of the photonic crystal structure must be around half the wavelength of the electromagnetic waves that are to be diffracted. This is ~ 200 nm (blue) to 350 nm (red) for photonic crystals operating in the visible part of the spectrum. The repeating regions

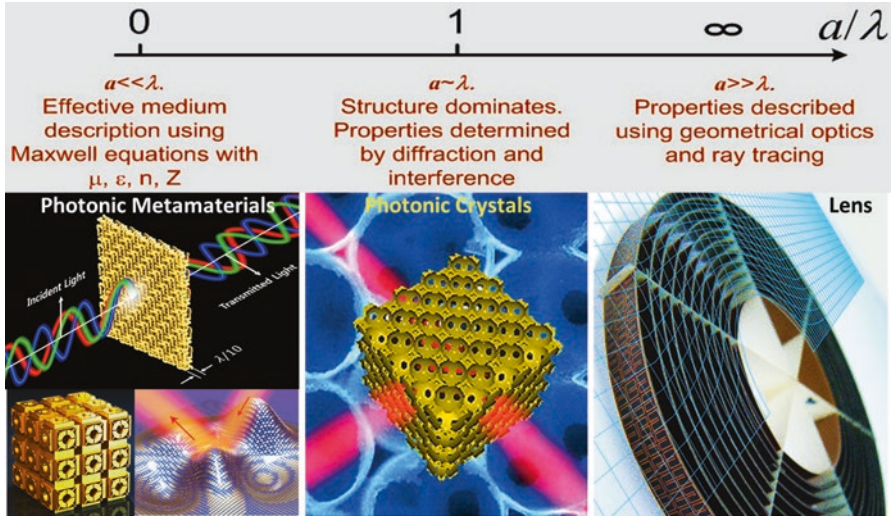


Fig. 5.1 Connections and difference of typical photonic crystals and metamaterials

of high and low dielectric constant must therefore be fabricated at this scale. As a result, photonic crystals can derive distinct optical phenomena such as inhibition of spontaneous emission, high-reflecting omni-directional mirrors, and low-loss wave-guiding, among others (Wikipedia 2016).

5.2.1 A Historical Account

Although photonic crystals have been studied in one form or another since 1887, the term “photonic crystal” was first used over 100 years later, after two papers of Sajeev John and Eli Yablonovitch published both in the same volume of *Phys. Rev. Lett.* in 1987. In such periodic materials with varying refractive index, spontaneous emission could be suppressed and light could be localized. There can be one-dimensional, two-dimensional, and three-dimensional photonic crystals with a one-dimensional photonic stopgap and two-dimensional and three-dimensional photonic bandgap, respectively. The one-dimensional photonic crystals are usually materials such as Bragg reflectors, interference filters which are manufactured by layer-by-layer deposition of materials with different refractive indexes. Two-dimensional ones can be in the shape of dielectric pillars embedded in another dielectric material (e.g., air) or air columnar holes embedded in dielectric material. Only the three-dimensional photonic crystals can have complete photonic bandgap (a direction and polarization independent) (Birner et al. 2001; Pawlak 2008).

The first three-dimensional bandgap was predicted theoretically in the structure of diamond and then obtained by Yablonovitch through drilling holes along three

crystallographic axes of diamond in a material with high refractive index (now called Yablonovite). The next structure which shows the complete photonic bandgap is a woodpile structure—originally invented by Sokoulis and then miniaturized by Noda with an advanced wafer fusion technique to such dimensions that the bandgap was observed at the telecommunication wavelength of 1.5 μm . Since then, many methods have been developed for manufacturing of photonic crystals, such as square spiral structure originally made by the glancing angle deposition method, different three-dimensional structures created by holographic lithography, self-organized eutectic micro- and nanostructures (Pawlak 2008), direct laser writing, and additive manufacturing. In order to make the photonic crystals useful, defects have been introduced into the lattice, which is comparable to doping in a semiconductor. A point defect in photonic crystal acts as a microcavity, which strongly traps and localizes photons, a line defect like a waveguide in which photons can propagate, and a planar defect like a perfect mirror. Photons are Bose particles, and one defect can trap and control many photons (unlike electrons which are fermions) (Pawlak 2008).

It has also been found that natural opal forms a photonic structure. Natural opals consist of a regular three-dimensional crystalline array of colloidal silica spheres, several hundred nanometers in size. In nature, synthetic opals have been formed by natural assembly of colloidal microspheres. The standard method for growing the initial opal is sedimentation of spheres from suspension. A synthetic opal can act as a template into which a semiconductor material can be infiltrated. Removing the template by annealing or etching leads to a three-dimensional photonic crystal with periodic air spheres embedded inside the material of high refractive index (Pawlak 2008).

Today, photonic crystal structures are used in a diverse range of applications from gas sensing, reflective coatings to enhancing the efficiency of LEDs to highly reflective mirrors in certain laser cavities. One major research goal of photonic crystals is to obtain ultra-small optical and optoelectronic integrated circuits incorporating: nano-ampere laser arrays with different oscillation frequencies, waveguides that incorporate very sharp bends, optical modulators, wavelength selectors, and so on (Pawlak 2008).

5.2.2 Construction of Photonic Crystals

The photonic bandgap (PBG) is essentially the gap between the airline and the dielectric line in the dispersion relation of the PBG system. To design photonic crystal systems, it is essential to engineer the location and size of the bandgap; this is done by computational modeling using different methods, such as plane wave expansion method, finite element method, finite difference time domain method, order- n spectral method, KKR method, Bloch wave-MoM method, and construction of the band diagram. The fabrication method depends on the number of dimensions that the photonic bandgap must exist in, including one-dimensional, two-dimensional, and three-dimensional photonic crystals.

In a one-dimensional photonic crystal, layers of different dielectric constant may be deposited or adhered together to form a bandgap in a single direction. A Bragg grating is an example of this type of photonic crystal. A graphene-based Bragg grating (one-dimensional photonic crystal) has been fabricated and demonstrated its capability for excitation of surface electromagnetic waves in the periodic structure by using 633-nm He–Ne laser as the light source. Besides, a novel type of one-dimensional graphene-dielectric photonic crystal can act as a far-IR filter and also is capable of supporting low-loss surface plasmons for waveguide and sensing applications. One-dimensional photonic crystals can be either isotropic or anisotropic, with the latter having potential use as an optical switch (Wikipedia 2016).

In two dimensions, holes may be drilled in a substrate that is transparent to the wavelength of radiation that the bandgap is designed to block. Triangular and square lattices of holes have been successfully employed. Moreover, the holey fiber or photonic crystal fiber can be made by taking cylindrical rods of glass in hexagonal lattice and then heating and stretching them; the triangle-like airgaps between the glass rods become the holes that confine the modes (Wikipedia 2016).

There are several structure types that have been constructed (Wikipedia 2016):

- (a) Spheres in a diamond lattice.
- (b) The woodpile structure—“rods”—is repeatedly etched using beam lithography, filled in, and new material is then deposited thereon, and the process is repeated on the next layer with etched channels that are perpendicular to the layer below, parallel to, and out of phase with the channels two layers below. The process is repeated until the structure is of the desired height. The fill-in material is then dissolved using an agent that can dissolve the fill in material but not the deposition material. It is generally hard to introduce defects into this structure.
- (c) Inverse opals or inverse colloidal crystals—spheres (such as polystyrene) can be allowed to deposit into a cubic close packed lattice suspended in a solvent. Then a hardener is introduced which makes a transparent solid out of the volume occupied by the solvent. The spheres are then dissolved using an acid such as hydrochloric acid.
- (d) A stack of two-dimensional crystals. This is a more general class of photonic crystals than Yablonovite, but the original implementation of Yablonovite was created using this method.

The major challenge for higher-dimensional photonic crystals is in fabrication of these structures, with sufficient precision to prevent scattering losses blurring the crystal properties and with processes that can be robustly mass-produced. For three-dimensional photonic crystals, various techniques have been used including photolithography and etching techniques similar to those used for integrated circuits. Some of these techniques are already commercially available. To circumvent nanotechnological methods with their complex machinery, alternate approaches have been followed to grow photonic crystals as self-assembled structures from colloidal crystals. Mass-scale 3D photonic crystal films and fibers can now be produced using a shear-assembly technique which stacks 200–300-nm colloidal

polymer spheres into perfect films of fcc lattice. Because the particles have a softer transparent rubber coating, the films can be stretched and molded, tuning the photonic bandgaps and producing striking structural color effects (Wikipedia 2016).

5.2.3 Applications of Photonic Crystals

Photonic crystals can be used for controlling and manipulating the flow of light. One-dimensional photonic crystals are already in widespread use in the form of thin-film optics with applications ranging from low to high reflection coatings on lenses and mirrors to color-changing paints and inks. Higher-dimensional photonic crystals are of great interest for both fundamental and applied research, and the two-dimensional ones are already available in the form of photonic-crystal fibers, which use a microscale structure to confine light with radically different characteristics compared to conventional optical fiber for applications in nonlinear devices and guiding exotic wavelengths (Tong 2014).

The three-dimensional counterparts may offer additional features such as optical nonlinearity required for the operation of optical transistors used in optical computers, when some technological aspects such as manufacturability and principal difficulties such as disorder are under control (Wikipedia 2016).

5.3 Metamaterials Designed Through Transformation Optics

Metamaterials made up of uniform arrays of subwavelength elements can be designed and manipulated to obtain unique properties. However, expanding designs to include nonuniform arrays of subwavelength elements greatly expands the options, opening the door to a field called transformation optics, which moves beyond ray optics to manipulate electromagnetic fields within the metamaterials. Maxwell's equations are exact at the classical level but lack transparency; Snell's law is elegantly visual, an aid to the imagination, but fails to account for many vital aspects of electromagnetism. Transformation optics retains an intuitive appeal, replacing the rays of Snell's law with the field lines of Maxwell whose equations are represented exactly (Pendry 2013). Therefore, transformation optics is a design method for creating novel and unique optical devices. It can go beyond cloaking (mimic celestial mechanics) because its control of the trajectory and path of light is highly effective. Transformation optics is a field covering optical and material areas embraced nanophotonics, plasmonics, and optical metamaterials. In fact, general coordinate transformations can be derived with compress or expand space, bend or twist space, or even change the topology (e.g., by mimicking a wormhole). Much current interest involves designing invisibility cloaks, event cloaks, field concentrators, or beam-bending waveguides.

5.3.1 *Metamaterials Mimicking Celestial Mechanics*

The interactions of light and matter with space time, as predicted by general relativity, can be studied using optical metamaterials that feature extraordinary abilities to bend light or electromagnetic radiation. If a metamaterial could be produced that did not have high intrinsic loss and a narrow frequency range of operation, then it could be employed as a type of media to simulate light motion in a curved space time vacuum. The specially designed optical metamaterials can mimic the periodic, quasi-periodic, and chaotic motions observed in celestial objects that have been subjected to gravitational fields. Hence, a new class of metamaterials with the nomenclature “continuous-index photon traps” (CIPTs) has been designed as optical cavities. As such, CIPTs can control, slow, and trap light in a manner similar to celestial phenomena such as black holes, strange attractors, and gravitational lenses. A composite of air and the dielectric gallium indium arsenide phosphide (GaInAsP), operated in the infrared spectral range and featured a high refractive index with low absorptions. This opens an avenue to investigate light phenomena that imitate orbital motion, strange attractors, and chaos in a controlled laboratory environment by merging the study of optical metamaterials with classical celestial mechanics. The optical cavities and photon traps can also be used for application in microscopic devices and lasers systems (Genov et al. 2009).

Twisting the optical metamaterial affects its “space” into new coordinates. The light that travels in real space will be curved in the twisted space, as applied in transformational optics. This effect is analogous to starlight when it moves through a closer gravitational field and experiences curved spacetime or a gravitational lensing effect. This analogue between classic electromagnetism and general relativity shows the potential of optical metamaterials to study relativity phenomena such as the gravitational lens. Observations of such celestial phenomena by astronomers can sometimes take a century of waiting. Chaos in dynamic systems is observed in areas as diverse as molecular motion, population dynamics, and optics. In particular, a planet around a star can undergo chaotic motion if a perturbation, such as another large planet, is present. However, owing to the large spatial distances between the celestial bodies and the long periods involved in the study of their dynamics, the direct observation of chaotic planetary motion has been a challenge. The use of the optical–mechanical analogy may enable such studies to be accomplished in a benchtop laboratory setting at any prescribed time (Genov et al. 2009).

Matter propagating in a curved spacetime is similar to the electromagnetic wave propagation in a curved space and in a homogeneous metamaterial. Hence, a black hole can possibly be simulated using electromagnetic fields and metamaterials. Figure 5.2 shows several designs of artificial black holes. In addition, engineering optical space with metamaterials could be useful to reproduce an accurate laboratory model of the physical multiverse. “This ‘metamaterial landscape’ may include regions in which one or two spatial dimensions are compactified.” Metamaterial models appear to be useful for nontrivial models such as 3D de Sitter space with one compactified dimension, 2D de Sitter space with two compactified dimensions, 4D de Sitter dS4, and anti-de Sitter AdS4 spaces (Smolyaninov 2011).



Fig. 5.2 Several different forms of artificial black holes

5.3.2 *Metamaterial Gradient Index Lensing*

Metamaterials designed through transformation optics are employed to increase capabilities of gradient index (GRIN) lenses. GRIN lenses are optical elements whose index of refraction varies within the lens. Control of the internal refraction allows the steering of light in curved trajectories through the lens. GRIN optics thus increase the design space to include the entire volume of the optical elements, providing the potential for dramatically reduced size, weight, element count, and assembly cost, as well as opening up new space to trade between performance parameters. Transformation optics and computational power provide a unique opportunity to design, assemble, and fabricate elements in order to advance the utility and availability of GRIN lenses across a wide range of optics-dependent systems, defined by needs. Figure 5.3 shows a design example of single X-band metamaterial GRIN lens disk (Pentry 2015)

5.3.3 *Battlefield Applications*

Metamaterials designed through transformation optics have potential applications for the battlefield. The versatile properties of metamaterials can be tailored to fit almost any practical need, and transformation optics shows that space for light can be bent in almost any arbitrary way. This is perceived as providing new capabilities to soldiers in the battlefield. For battlefield scenarios, benefits from metamaterials have both short-term and long-term impacts. For example, determining whether a cloud in the distance is harmless or an aerosol of enemy chemical or biological warfare is very difficult to assess quickly. However, with the metamaterials designed through transformation optics, the ability exists to see things smaller than the wavelength of light—something which has yet to be achieved in the far field.

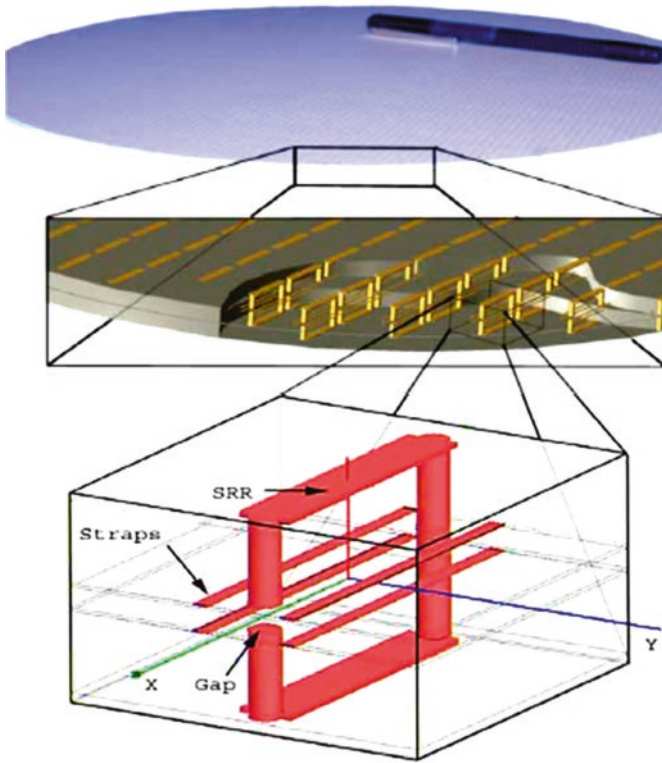


Fig. 5.3 Single X-band GRIN lens disk (Pentry 2015)

Utilizing metamaterials in the creation of a new lens may allow soldiers to be able to see pathogens and viruses that are impossible to detect with any visual device (Kyzer 2008).

Harnessing subwavelength capabilities then allow for other advancements which appear to be beyond the battlefield. All kinds of metamaterials manufactured with nano-manufacturing, which could go into electronic and optical devices from night vision goggles to distance sensors to other kinds of sensors. The cloaking metamaterials, as shown in Fig. 5.4, would provide “invisibility” by redirecting light (Kyzer 2008).

5.4 Hyperbolic Metamaterials

5.4.1 Hyperbolic Media in Retrospect

Hyperbolic metamaterials (HMMs), also called indefinite materials, are a kind of strongly anisotropic materials which combine the properties of transparent dielectrics and reflective metals. They behave as a metal when light passes through it in

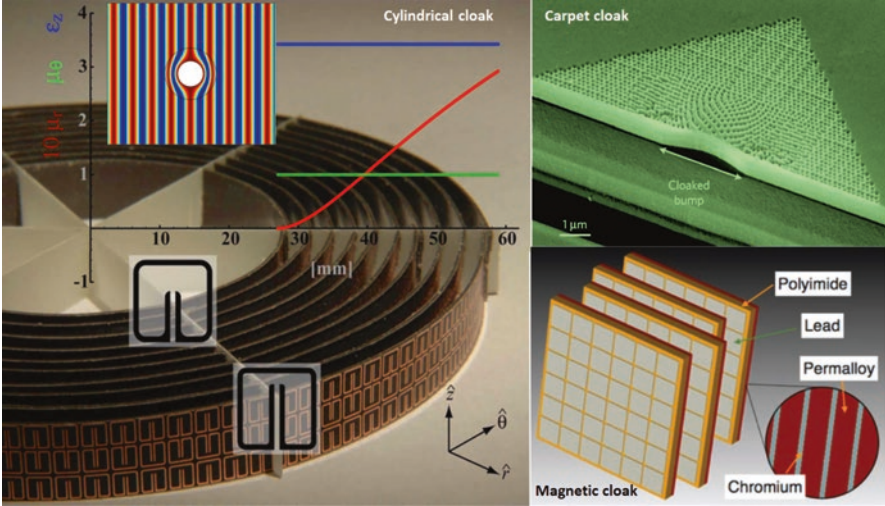


Fig. 5.4 Examples of metamaterial cloaks (Pentry 2015)

one direction and like a dielectric when light passes in the perpendicular direction. Their permittivity and permeability tensor elements (along principal axes) are of opposite signs, resulting in a strong anisotropy. The material’s dispersion relation forms a hyperboloid. The associated wavelength can in principle be infinitely small.

Hyperbolic metamaterials (HMMs) derive their name from the topology of the isofrequency surface. In vacuum, as shown in Fig 5.5a, the linear dispersion and isotropic behavior of propagating waves implies a spherical isofrequency surface given by the equation (Shekhar et al. 2014):

$$k_x^2 + k_y^2 + k_z^2 = \frac{\omega^2}{c^2} \tag{5.3}$$

where the wave vector of a propagating wave is given by $\vec{k} = [k_x, k_y, k_z]$, ω is the frequency of radiation, and c is the velocity of light in free space. Considering an extraordinary wave (TM polarized) in a uniaxial medium, this isofrequency relation changes to (Shekhar et al. 2014):

$$\frac{k_x^2 + k_y^2}{\epsilon_z} + \frac{k_z^2}{\epsilon_x} = \frac{\omega^2}{c^2} \tag{5.4}$$

The uniaxial medium has a dielectric response given by a tensor, $\vec{\epsilon} = [\epsilon_x, \epsilon_y, \epsilon_z]$, where the in-plane isotropic components are $\epsilon_x = \epsilon_y = \epsilon_{\parallel}$ and out-of-plane component is $\epsilon_z = \epsilon_{\perp}$. The spherical isofrequency surface of vacuum distorts to an ellipsoid for the anisotropic case. However, when an extreme anisotropy presents such that $\epsilon_{\parallel} \cdot \epsilon_{\perp} < 0$, the isofrequency surface opens into an open hyperboloid (Fig. 5.5b, c).

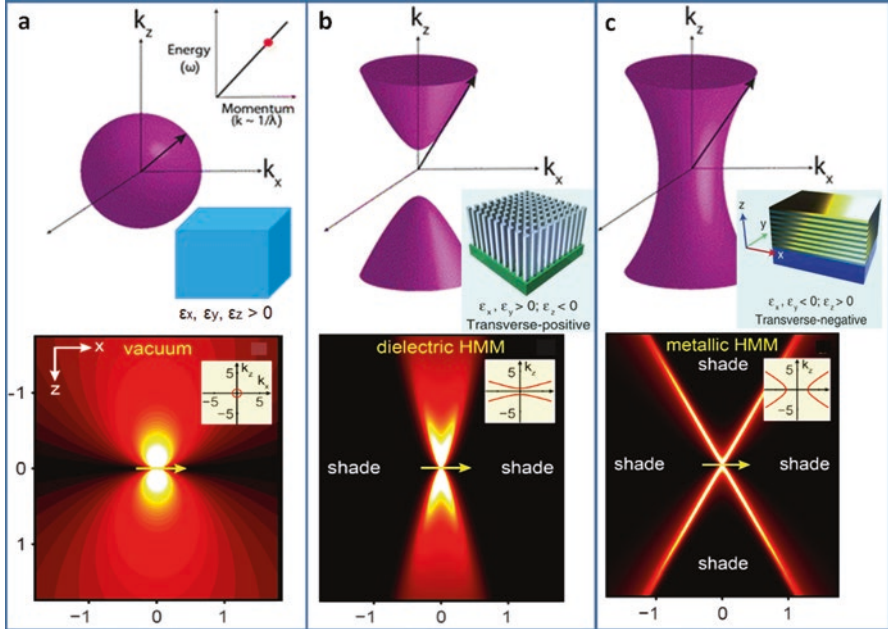


Fig. 5.5 k -space topology (Drachev et al. 2013; Shekhar et al. 2014): (a) spherical isofrequency surface for an isotropic dielectric, (b) hyperboloid isofrequency surface for a uniaxial medium with an extremely anisotropic dielectric response (Type I dielectric HMM: $\epsilon_z < 0; \epsilon_x, \epsilon_y > 0$), (c) hyperboloid isofrequency surface for an extremely anisotropic uniaxial medium with two negative components of the dielectric tensor (Type II metallic HMM: $\epsilon_x, \epsilon_y < 0; \epsilon_z > 0$). The Type I and Type II metamaterials can support waves with infinitely large wave vectors in the effective medium limit. Such waves are evanescent and decay away exponentially in vacuum

Such a phenomenon requires the material to behave like a metal in one direction and a dielectric (insulator) in the other. This does not readily occur in nature at optical frequencies but can be achieved using artificial nanostructured metamaterials (Drachev et al. 2013; Shekhar et al. 2014).

The most important property of such media is related to the behavior of waves with large magnitude wave vectors. In vacuum, such large wave vector waves are evanescent and decay exponentially. However, in hyperbolic media the open form of the isofrequency surface allows for propagating waves with infinitely large wave vectors in the idealistic limit. Thus, there are no evanescent waves in such a medium. This unique property of propagating high- k waves gives rise to a multitude of device applications using hyperbolic media. As shown in Fig. 5.5, Type I dielectric HMMs have one component of the dielectric tensor negative ($\epsilon_z < 0; \epsilon_x, \epsilon_y > 0$), while Type II metallic HMMs have two components negative ($\epsilon_x, \epsilon_y < 0; \epsilon_z > 0$). If all components are negative, a metal medium will be obtained; and if all components are positive, a dielectric medium will be. One striking difference between the Type I and Type II hyperbolic metamaterial is that the hyperboloidal surfaces are two-sheeted and single-sheeted, respectively. The Type II metamaterial is highly reflective since it is more metallic than the Type I counterpart (Shekhar et al. 2014) (Fig. 5.6).

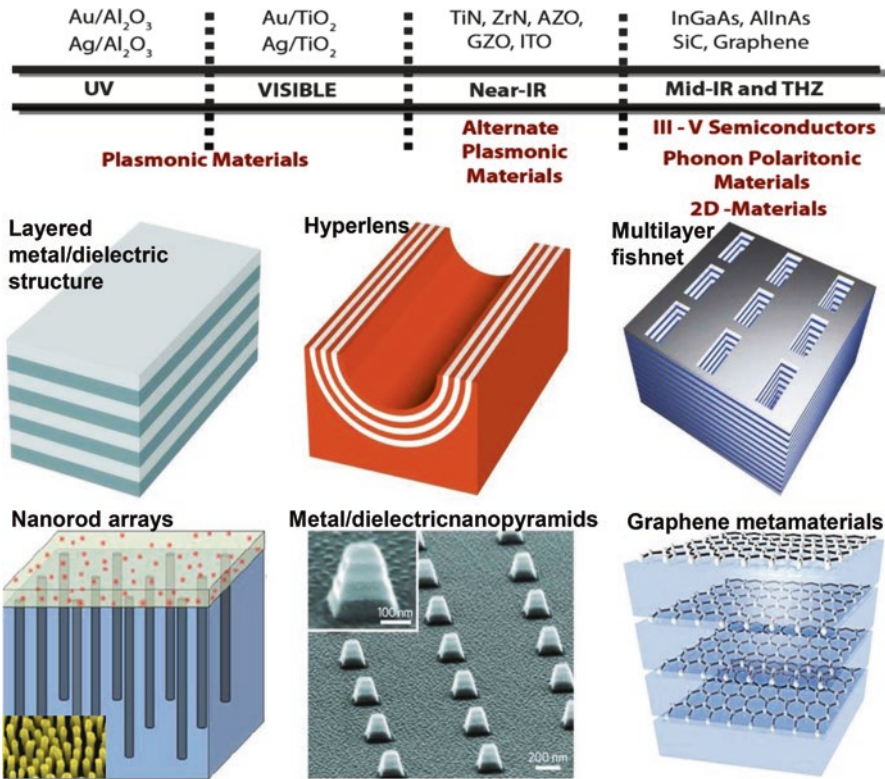


Fig. 5.6 Examples of materials and structures used to create hyperbolic metamaterials depending on region of operation in the electromagnetic spectrum (UV to mid-IR and THz frequencies) (Shekhar et al. 2014)

5.4.2 Design and Building Materials

Hyperbolicity requires metallic behavior in one direction, and insulating behavior in the other leads to the requirement that both metals and dielectrics must be used as building blocks. Microscopically, the origin of the high-*k* propagating waves relies on a metallic building block to create the hyperbolic dispersion of the material. The polaritonic properties of the metallic building blocks allow for the necessary light-matter coupling to create the high-*k* waves. Specifically, it is necessary to have a phonon-polaritonic (optically active phonons) or plasmon-polaritonic (free electron) metal to construct hyperbolic metamaterials. The high-*k* modes are a result of the near-field coupling of the surface plasmon polaritons (SPPs) at each of the metal dielectric interfaces in the structure. The high-*k* modes are the Bloch modes of the

metal-dielectric superlattice. Therefore, there are two basic practical approaches to achieve the hyperbolic dispersion (Shekhar et al. 2014):

- (a) A thin-film multilayer (superlattice) consisting of alternating layers of metal and dielectric gives rise to the desired extreme anisotropy. The layer thicknesses should be far below the size of the operating wavelength for the homogenization to be valid. A wide choice of plasmonic metals and high-index dielectrics can give rise to hyperbolic behavior in different wavelength regimes. At ultraviolet (UV) frequencies, gold and silver along with alumina forms the ideal choice for the metamaterial. Close to the plasma frequency of these metals, which is in the UV, their reflectivity decreases and an alternating metal dielectric superlattice achieves a Type I HMM with high transmission. To push this design to visible wavelengths, however, a high-index dielectric such as TiO_2 or SiN is needed. At near-infrared (IR) wavelengths, compensating for the reflective metallic behavior of naturally plasmonic metals like silver and gold is unfeasible and alternate plasmonic materials with tailored lower plasma frequencies are needed. These alternate plasmonic materials are based on transition metal nitrides or transparent conducting oxides and are ideally suited for hyperbolic media. In addition, their unique property of high melting point was also used to pave the way for high temperature thermal hyperbolic metamaterials. At mid-infrared wavelengths, one option for the metallic component in hyperbolic media consists of III–V degenerately doped semiconductors. The upper limit of doping concentration often limits their abilities to work as a metal at near-IR wavelengths; however, they are ideally suited to the mid-IR. Another option which is fundamentally different from plasmonic metals is silicon carbide, a low-loss phonon polaritonic metal. SiC has a narrow reststrahlen (residual rays) band at mid-IR wavelengths which allows it to function as a metallic building block for hyperbolic media. Multilayer graphene superlattices can also show a hyperbolic metamaterial response in the THz (far-IR) region of the spectrum.
- (b) Another approach to achieving hyperbolic behavior consists of metallic nanowires in a dielectric host. The choice of metals is usually silver and gold grown in a nanoporous alumina template. The major advantage of this design is the low losses, broad bandwidth, and high transmission.

Besides, some naturally occurring materials, such as graphite or graphite-like material (MgB_2) and crystal with perovskite-layer crystal structure (cuprate and ruthenate), as shown in Fig. 5.7, possess very similar structure to that of the layered hyperbolic metamaterials; therefore, they possess the indefinite property resulting from this multilayered structure. In fact, natural crystals with birefringence may show negative refraction in a limited condition because their anisotropy is not strong enough. In contrast to the birefringent crystals, these indefinite crystals always have two-dimensional conductivity mechanisms, which make them act as conductors or superconductors in macroscale. In the single crystalline state, the dielectric property in the direction along the conductive layer is entirely different from those in the direction perpendicular to the layer, which results in an indefinite dielectric tensor in the crystal (Sun and Litchinitser 2016).

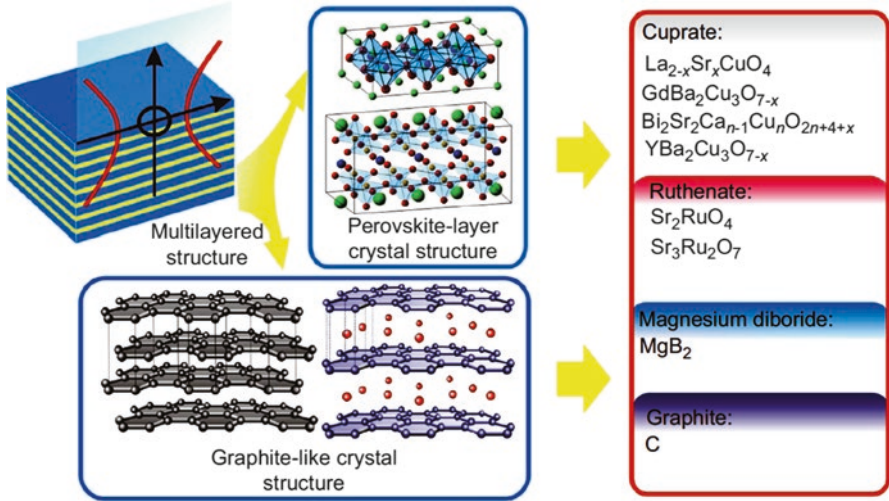


Fig. 5.7 Hyperbolic materials in nature (Sun and Litchinitser 2016)

5.4.3 Photonic Hypercrystals

Photonic hypercrystals combine the features of metamaterials and photonic crystals within the same medium, offering new ways to control electromagnetic radiation. The requirements on the unit cell being much smaller than the wavelength for metamaterials and on the order of the wavelength for photonic crystals make the two approaches incompatible within the same environment. The situation is dramatically different, however, in the world of hyperbolic metamaterials, where the opposite signs of the dielectric permittivity components in two orthogonal directions enable hyperbolic dispersion of transverse magnetic-polarized propagating waves, with the wave numbers unlimited by the frequency. As a result, a periodic variation in the dielectric permittivity—regardless of how small its period—causes Bragg scattering of these high wave number modes. This leads to the creation of photonic bandgaps and takes the physical phenomena from the field of photonic crystals to the metamaterial realm (Narimanov 2015).

Hypercrystals can be fabricated using a variety of materials and methods (Narimanov 2015): Figure 5.8a shows four examples of natural hyperbolic materials. Clockwise from the top are sapphire (hyperbolic in mid-IR), the high-temperature superconductor bismuth strontium calcium copper oxide (BSCCO) (hyperbolic in IR in its normal state), graphite (hyperbolic in IR and UV), and bismuth (hyperbolic in far-IR). Figure 5.8c shows a hyperbolic response by stacking thin conducting and insulating layers on top of each other. The inset shows the scanning transmission electron microscopy image of the hyperbolic metamaterial formed by layers of silver and silicon. Figure 5.8e shows a low-loss hyperbolic metamaterial using an array of parallel metallic nanowires in a dielectric matrix.

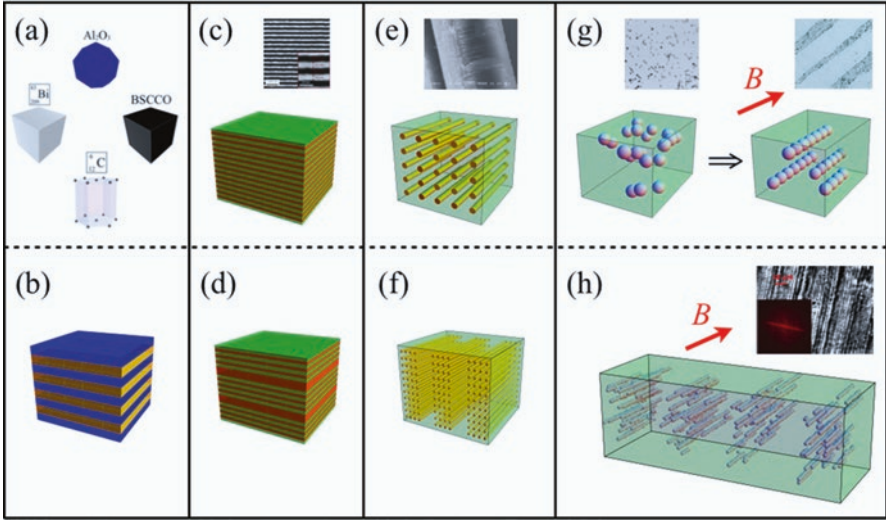


Fig. 5.8 Hyperbolic materials (*top row*) and their corresponding photonic hypercrystals (*bottom row*) (Narimanov 2015): (a) natural hyperbolic materials, (b) used in stacks of layers, (c) stacks of thin insulating and conducting layers, (d) with periodic thickness variations, (e) metallic nanowires in dielectric, (f) with periodically varying density. (g) A magnetic field (B) applied to a metallic ferrofluid causes self-assembly of nanocolumns and (h) also produces phase separation. Al_2O_3 sapphire, Bi bismuth, $BSCCO$ bismuth strontium calcium copper oxide, C graphite

The inset shows the scanning electron microscopy image of the etched side wall of such a metamaterial. Figure 5.8b and d shows a planar design hypercrystal, where the hyperbolic layers are formed by either natural media, such as sapphire or the hexagonal polytype of silicon carbide or by using existing planar hyperbolic metamaterials. In Fig. 5.8d, periodic variations in the thickness of the layers of one of the components turn the medium into a hypercrystal. Similarly, a periodic variation in the density of nanowires can transform the hyperbolic nanowire composite into a hypercrystal, as shown in Fig. 5.8f. Planar design hypercrystals can be fabricated using molecular-beam epitaxy or chemical vapor deposition. However, turning a nanowire-based hyperbolic metamaterial—shown in Fig. 5.8e—into the corresponding hypercrystal, as in Fig. 5.8f, is likely to be more challenging. The most interesting realization of an actual hypercrystal comes from the field of material self-assembly. When a strong external magnetic field is applied to a metallic ferrofluid (a liquid that contains magnetic nanoparticles), the magnetic nanoparticles in the liquid form nanocolumns aligned parallel to the magnetic field, as in Fig. 5.8g. Furthermore, in a striking example of a nonlinear pattern formation, ferrofluids generally exhibit phase separation into nanoparticle-rich and nanoparticle-poor phases, as in Fig. 5.8h. As this phase separation occurs on the scale 0.1–1 μm , the result is a self-assembled photonic hypercrystal.

Photonic hypercrystals have shown the potential for practical applications. In one example, a self-assembled hypercrystal successfully served as a sensor for organic components in a liquid solution. Moreover, the surface states formed at the interface of such photonic hypercrystals share the properties of the Tamm states in photonic crystals and the surface plasmon polaritons (very short wavelength surface waves) in metals. The contribution of Bragg scattering to the waves' formation means that they show both larger wave numbers and lower loss than their regular surface plasmon counterparts. Therefore, they offer a possible solution to the loss/confinement conundrum that has plagued modern plasmonics. Hypercrystals can be designed to exhibit a negative refractive index, without the negative magnetic permeability that is usually essential for such materials. In this way, it may be possible to use photonic hypercrystals for optical imaging, since a planar slab of such material can function as a Veselago lens. Photonic hypercrystals can also support Dirac dispersion cones, enabling the study of phenomena normally associated with the highly nontrivial physics of electrons in graphene. They may also be used for radiative heat transfer and control of thermal radiation (Narimanov 2015).

5.4.4 Applications of Hyperbolic Metamaterials

5.4.4.1 High-Resolution Imaging and Lithography

In contrast to conventional isotropic materials, emission of waves in hyperbolic systems is highly directional. The unique dispersion allows hyperbolic systems to preserve high-wave vector components of the wave packets that carry information about the subwavelength features of the source. Therefore, hyperbolic structures are capable of focusing radiation to subwavelength spots. As shown in Fig. 5.9a, a double-slit interference of resonant cones produced by slits in Cr film results in a sub-diffraction pattern, which is highly beneficial for nanolithography applications. Figure 5.9b, c show the flat Ag/SiO₂ hyperbolic structure forms a line of 90-nm width on the photoresist layer, which was simply brought in contact with the hyperbolic layer and detected then with an atomic force microscope (AFM). Further, the hyperbolic structures can be used to magnify the subwavelength objects and thus enable far-field super-resolution imaging. Super-imaging is a challenging problem that is typically addressed by near-field optical microscopy. A superlens made of metamaterial with both negative permittivity and permeability provides a way to translate the information about subwavelength objects. This approach was further developed to incorporate alternating layers with optical gain and to enlarge the objects in a cylindrical geometry. Curved hyperbolic metamaterials enable far-field magnification of 3D objects when subwavelength information, encoded in resonant cones is gradually translated into propagating information similar to the magnification by anisotropic structure. Magnifying lens based on hyperbolic metamaterials was realized for UV imaging in Ag/Al₂O₃ curved multilayer metamaterial (Fig. 5.9a) (Drachev et al. 2013).

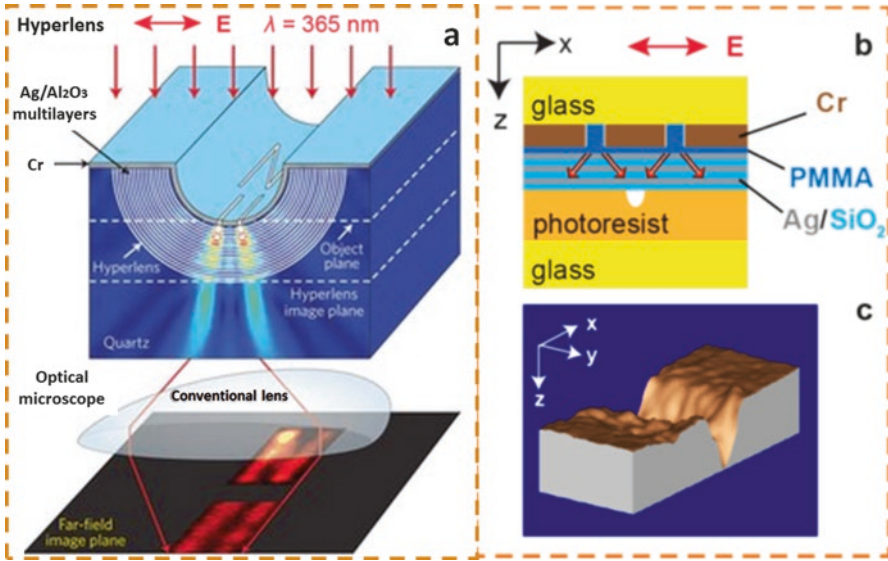


Fig. 5.9 Imaging (a) and nanolithography (b, c) with hyperbolic metamaterials (Drachev et al. 2013)

5.4.4.2 Spontaneous Emission Engineering

Fermi's golden rule with Purcell's effect links the radiative decay rate of spontaneous emission and photonic density of states, which can be modified due to environment in which fluorescent molecules are embedded. The most attractive property of the hyperbolic metamaterials is the broadband and strongly enhanced radiative decay rate for the fluorophore spontaneous emission near or inside a medium relative to free space (Purcell factor). The photonic density of states (PDS) in the metamaterial is related to the volume in k -space enclosed by the corresponding isofrequency surface and may have singularities. The isofrequencies have closed trajectories which eliminate singularities of the PDS. The value of the enhancement is theoretically limited only by losses or finite period-to-wavelength ratio. The finite size of the emitter distribution can limit the HMM density of states even at zero losses and the Purcell factor in hyperbolic metamaterials stays finite due to the discreteness of the actual structure and specific geometry (Drachev et al. 2013). Therefore, HMM has been used for spontaneous emission engineering.

5.4.4.3 Thermal Emission Engineering

The power emission of a black body at thermal equilibrium is ruled by Planck's law. Although this limit cannot be overcome in the far field, the same is not true in the near field, where the high PDOS of HMM leads to super-Planckian thermal emission. The potential applications of this phenomenon span from energy harvesting

and conversion to thermal coherent sources and thermal sinks. In order to engineer heat transfer, SiC, a phonon-polaritonic metal has been widely used. Its real part of permittivity becomes negative in the infrared region inside the reststrahlen band, delimited by the transverse and the longitudinal optical phonon resonance frequencies. HMM MLs formed by stacks of SiC and SiO₂ layers exhibit three advantages (Ferrari et al. 2015): (a) their high-k states can be thermally excited at moderate temperatures around 400–500 K, where the peak of the black body curve falls within the reststrahlen band; (b) phonon-polaritonic metals have lower losses compared to plasmonic metals, and therefore the contribution of high-k modes dominates that of lossy surface waves; and (c) as SiC/SiO₂ MLs operate in the wavelength interval 10–12 μm , the fabrication of subwavelength layers (period 50–100 nm) is relatively easy, and the effective medium theory is more accurate with respect to the optical range. For the same reason, the engineered near-field (distances $z \ll \lambda_0$) can be accessed experimentally with conventional detection systems.

Thanks to their capability of altering near-field thermal emission, HMMs can increase heat transfer from and to materials which support infrared surface polariton resonances. A lattice of Au NWs in vacuum can enhance non-resonantly the heat flux from a SiC emitter. Heat exchange through a tiny gap between two SiC/SiO₂ ML HMMs exceeds the performance of analogously arranged black bodies and is mainly influenced by the surface modes of the topmost layers. Thermophotovoltaic devices require heat transfer at high temperatures and near-infrared frequencies; to this end, the operating range of thermal hyperbolic MLs can be tuned to 1–3 μm by utilizing aluminum zinc oxide (AZO, plasmonic metal) and TiO₂ (Ferrari et al. 2015).

5.4.4.4 Active and Tunable Metadevices

Like in many other metamaterials designed for exhibiting extraordinary optical properties, the performance of hyperbolic media is limited by the ohmic damping associated with free charge carriers, which imposes a cutoff on the achievable wave number of the propagating modes. High wave numbers correspond to a stronger concentration of electric field inside metals: as a consequence, the associated modes experience larger ohmic losses which prevent long propagation, especially for the detection of subwavelength objects. Lossless HMMs can achieve much higher resolution than those with realistic ohmic damping. In addition, gain-compensated hypergrating structures were predicted to produce narrower focal points than their passive counterparts. It is therefore desirable to incorporate gain materials, such as dye molecules and semiconductors, in the HMM design. Due to the non-resonant nature of HMMs, loss compensation can be achieved with lower gain coefficients than those required by resonance-based artificial media (Ferrari et al. 2015).

A tunable behavior can be achieved in ML HMMs by means of graphene, a material that supports plasmonic resonances in the THz frequency range. Its attractive features include low loss, high confinement of electromagnetic energy, and fast response time. The conductivity of graphene can be tuned by shifting the Fermi

level with an external electric field. Therefore, a dramatic optical phase change from the elliptical to the hyperbolic regime through the ENZ point can be induced in graphene-based MLs by varying the electrical doping level. The ultrathin graphene sheets, with their strong in-plane polarizability would play the role of the metal, with the further advantage of lower absorption and a reduced overall ML thickness. A controllable elliptic–hyperbolic phase transition would imply sharp changes in reflection and transmission through the HMM, in the near-field absorption properties and in the Purcell effect (Ferrari et al. 2015).

In addition, by virtue of the high- k vectors supported, ML HMMs can be shaped into deep subwavelength three-dimensional cavities, with sizes down to $\lambda/12$. Besides the extreme confinement, HMM resonators also exhibit anomalous scaling properties: cavities of different sizes resonate at the same frequency, and higher-order modes oscillate at lower frequencies. Broadband light trapping can be realized by slowing down radiation in stop bands corresponding to different frequency-dependent positions along the tapered HMM waveguide. The large PDOS enhances the emission rate and therefore strengthens the phenomenon: the torque experienced by a dipole in a ML HMM is at least an order of magnitude higher than that in an anisotropic dielectric medium (Ferrari et al. 2015).

5.5 Superconducting and Quantum Metamaterials

Superconductivity is a macroscopic quantum state of matter that arises from a many-body correlated electron state associated with Cooper pairing of electrons. Under many circumstances, a superconductor can be described by a single coherent macroscopic quantum wave function with well-defined magnitude and phase. The magnitude of the superconducting order parameter is related to the density of superconducting electrons, while its phase variation is related to the supercurrents. Superconductivity sets in as the equilibrium thermodynamic state below a transition temperature T_c . A superconductor can carry a finite amount of dissipation-free direct current, called the critical current $I_c(T)$, before it reverts to the normal state at temperature $T < T_c$. It can also exist in the presence of a magnetic field up to a lower critical field $H_{c1}(T)$ (before the onset of vortex entry) and an upper critical field $H_{c2}(T)$ before superconductivity is completely destroyed in the bulk (for Type II superconductors). Superconductors bring the following unique properties to the metamaterial field (Jung et al. 2014): (a) low losses due to the primarily inductive electrodynamic response of a superconductor, (b) the compact meta-atom structures enabled by the strong inductive response, (c) the strong nonlinearity and tunability brought by superconductors at the extreme limits of their existence, (d) magnetic flux quantization and the Josephson effect, (e) quantum effects in which single photons interact with quantized states in meta-atom structures, and (f) the use of a strong diamagnetic response at low frequencies arising from the Meissner effect.

Figure 5.10 presents a set of realized and notional superconducting meta-atom and metamolecule styles (Jung et al. 2014). The meta-atoms are grouped in terms of

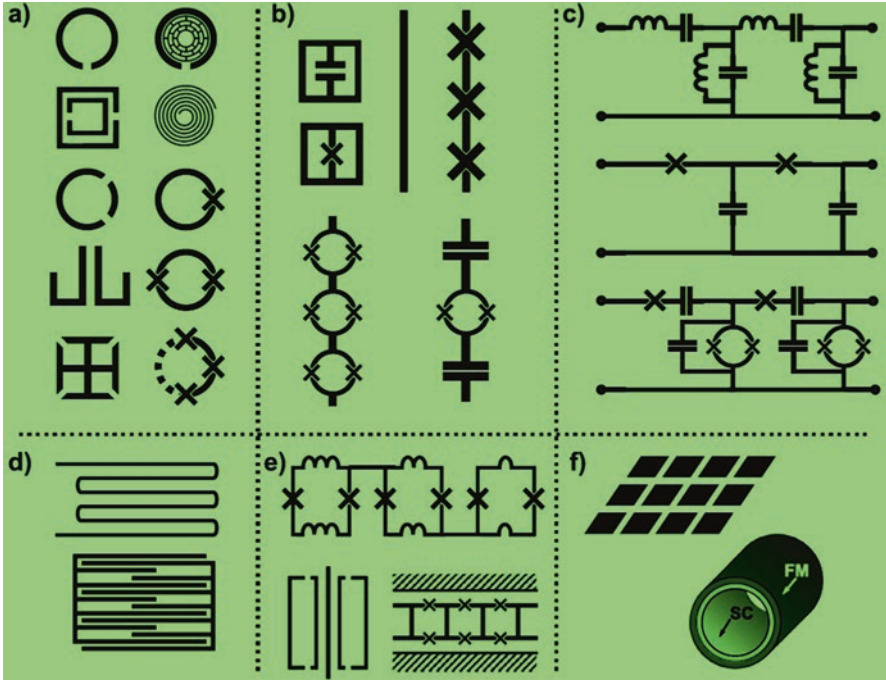


Fig. 5.10 Illustration of a subset of superconducting meta-atoms and metamolecules (Jung et al. 2014): (a) magnetically active meta-atoms, (b) electrically active meta-atoms, (c) transmission line metamaterials, (d) lumped-element meta-atoms, (e) various metamolecule realizations, and (f) dc magnetic cloak structures

their primary response. Figure 5.10a shows mainly magnetically active meta-atoms, although the split rings can also be excited electrically. The realizations include (from top to bottom) single- and double-split rings, two types of ASRs, the split-cross structure, the woodcut flux quantization split-ring resonator, the spiral, and rf -, dc -, and multi-junction SQUIDs and qubits. Figure 5.10b shows electrically active meta-atoms, ranging from the bare wire to Josephson-decorated wires, to wires augmented with field- or current-tunable dc -SQUIDs. Figure 5.10c shows implementations of the Josephson transmission line and the conventional composite right-/left-handed transmission line and its tunable version utilizing dc -SQUIDs. Figure 5.10d shows superconducting lumped-element inductors and capacitors acting as meta-atoms. Figure 5.10e shows several types of metamolecules, including one creating a classical analog of EIT, a superconducting quantum interference filter structure, and a dc -SQUID array transmission line. Figure 5.10f shows two realizations of dc magnetic cloak structures.

The superconducting metamaterials may play a crucial role in the future. With low-loss performance, plasmonic structures can guide tightly confined electromagnetic waves over significantly longer distances than normal metal structures. The addition of Josephson tunability combined with the low losses of superinductors

and bulk superconductors should allow the realization of strongly tunable devices that retain their low-loss properties, a key goal for quantum information processing and EIT with a high delay-bandwidth product. rf-SQUID arrays exhibit bistability and multi-stability. In the compact structure, smaller meta-atom designs as Josephson and SQUID inductances are included in various split-ring and spiral resonator designs, as well as transmission line realizations. Quantum metamaterials comprised of arrays of superconducting qubits are an emerging new field for fundamental studies in quantum optics, opening the possibility to explore collective quantum dynamics under very strong coupling between electromagnetic fields and artificial atoms (Jung et al. 2014).

5.5.1 Low-Loss Metamaterials

The low-loss properties of superconductors are particularly clear in the THz frequency scale. In this case one must utilize high-temperature superconductors (HTS) that have a maximum superconducting gap frequency beyond 1 THz. Split-ring resonators (SRRs) made up of HTS materials show a sharp onset of resonant interaction with THz radiation below the transition temperature. Even low transition temperature superconducting SRRs are found to produce high-quality factor resonances at frequencies of 0.14 THz, up to 1 THz (Jung et al. 2014).

5.5.1.1 Plasmonic Superconducting Metamaterials

The plasmonic behavior of superconducting meta-atoms has been examined (by Kurter et al. 2013): below the transition temperature and gap frequency, a superconductor acts as a nearly loss-less plasmonic material with a temperature-tunable plasma frequency. Therefore, the plasmonic properties of superconducting metamaterials can simply be tuned by varying temperature at essentially fixed frequency.

As for a nanoscale superconducting plasmonic waveguide for THz radiation, superconductors reject most of the electromagnetic fields from their interior due to Meissner effect; therefore, they are not good as a single-surface plasmonic waveguide for tightly confining fields, except perhaps at temperatures very near T_c . However, putting a second superconductor nearby allows for a very compact field confinement. Moreover, superconducting electrostatics explains most of the increase in extraordinary transmission of 75-GHz radiation through a subwavelength hole array in an HTS film. However, there is an enhancement of transmission about 10 K below T_c , and this may be due to plasmonic interaction between the holes or resonant excitation of a real (as opposed to virtual) surface plasmon polariton mode in the array. The array could be used for low-loss large dynamic-range amplitude modulation and temperature controlled terahertz devices (Jung et al. 2014).

5.5.1.2 Analogue Electromagnetically Induced Transparency Metamaterials

Meta-atoms can be combined into metamolecules in which the interactions between the atoms can give rise to qualitatively new phenomena. One of these phenomena is the creation of a classical analogue of the quantum effect of electromagnetically induced transparency (EIT) in atoms using coupled classical resonators, in which create coupling between two oscillators of dramatically different degrees of loss. The interference effect can create a strong transparency feature in the transmission spectrum and can lead to a significant slowing of light in that frequency band. One approach is to employ asymmetrically split rings (ASRs) that have a “dark” magnetic dipole mode (e.g., a low-loss superconducting Nb “dark” resonator) that is coupled to a nearby “bright” electric dipole mode (e.g., a lossy gold “bright” resonator), giving rise to Fano interference and a transparency window. Superconductor/normal metal hybrid metamolecules clearly offer the opportunity to create very strong classical EIT effects.

For instance, a hybrid HTS closed ring resonator and aluminum SRR system displayed a temperature tunable transparency window with a delay-bandwidth product on the order of 0.2 (Jung et al. 2014).

5.5.2 Compact Meta-Atom Structure

Superconducting structures can be miniaturized to a large extent because the magnetic screening scale is microscopic (10–100 s of nanometers) and because that losses do not scale adversely with reduced physical dimension. This advantage has been exploited in a number of fields that utilize meta-atom-like structures for various purposes. Examples include optical detectors that exploit changes in kinetic inductance or resistance when a single photon is absorbed by a resonant superconducting structure or superconducting qubits with transitions between quantized states in the microwave frequency regime (Jung et al. 2014).

Compact self-resonant superconducting spirals operating at radio frequencies maintain a high-quality factor, Q , and function in the deep subwavelength regime where their physical dimensions are 1000 times smaller than the free-space wavelength of the fundamental mode. HTS spiral resonators with unloaded Q values up to 10^3 for the fundamental mode and 30×10^3 for higher-order modes are comparable with natural atomic resonators such as the hydrogen atom, which has a similar size to wavelength ratio for visible light and possesses a Q around 15×10^3 for the Doppler broadened $H\alpha$ line in the Sun. Such high-quality factors and deep subwavelength operation can only be attained through compact superconducting resonators. More compact superconducting resonators at even deeper subwavelength scales may be obtained by nano-patterning the spiral resonator in order to further enhance the kinetic inductance of the device and lower its resonance frequency. Besides, meta-atoms were the platform for discovery of the anisotropic nonlinear Meissner effect in unconventional superconductors (Jung et al. 2014).

Superconducting meta-atom-like structures have been developed in other areas for a number of different purposes. First, superconducting microresonators have been employed for microwave kinetic inductance detectors, and as bolometers, and often employ either a compact meandering coplanar waveguide design, or lumped inductors and capacitors. The kinetic inductance optical detectors work by absorbing the photon which causes depairing in the superconductor, resulting in a change of the kinetic inductance and resonant frequency of the microresonator. The lumped-element designs allow for a larger collecting area, as compared to resonant transmission lines, because the current flow in the structure is more uniform, and therefore the change in kinetic inductance due to absorption of an optical photon has a greater impact. Compact lumped-element superconducting resonators have been developed for use as backward wave microwave filters. Superconducting multimode composite SRRs work as microwave filters, showing very low insertion loss and excellent out-of-band rejection. A compact fractal superconducting resonator has been developed utilizing only narrow superconducting lines, making it less susceptible to external magnetic fields. This 6-GHz resonator was so small that it could be integrated on to a quartz-tuning fork and used for near-field scanning microwave microscopy. Many compact self-resonant superconducting structures have been developed for use as quantum bits (qubits) (Jung et al. 2014).

5.5.3 Superconducting Metamaterials with Nonlinearity and Tenability

Superconducting metamaterials are particularly well suited for nonlinearity because they are typically made up of very compact (compared to the free-space wavelength) meta-atoms, resulting in strong currents and fields within the meta-atom. The superconducting material at high current locations can then display nonlinear response because of the nonlinear Meissner effect, localized heating, or magnetic vortex entry. For example, a connected array of asymmetrically split-Nb resonators shows current-tunable transmission in the sub-THz band due to localized heating and vortex entry. Alternatively, if nonlinear materials or devices are added at locations of extreme field or current, the meta-atoms can be very sensitively tuned by means of outside parameters. For example, the change in resonant frequency of Nb SRR with applied magnetic field was found to be quite complex and hysteretic, showing complex tuning with magnetic field at microwave frequencies using high-temperature superconducting SRRs and at sub-THz frequencies with Nb SRRs of similar design. Moreover, the temperature-tunable dielectric properties of superconductors play a central role in superconducting cloaking structure in the THz regime. The kinetic inductance of superconductors is strongly tunable, particularly in thin-film structures (with at least one dimension on the order of the superconducting penetration depth) as a function of temperature. Such tuning has been accomplished at THz frequencies by varying temperature in HTS and NbN thin-film SRRs. It was also

demonstrated that the temperature tunability was enhanced by decreasing the thickness of the HTS films making up square SRRs. The tuning of HTS SRRs with variable THz beam intensity could even be accomplished on *ps* timescales (Jung et al. 2014).

5.5.4 Superconducting Metamaterials with Magnetic Flux Quantization and Josephson Effect

Magnetic flux quantization and the Josephson effect come together when a superconducting loop is interrupted by one or more Josephson junctions. Here, the phase difference across the junction(s) depends on the externally applied magnetic flux. This is commonly known as a superconducting quantum-interference device (SQUID, or more specifically an rf-SQUID in the case of a single junction). Since the rf-SQUID meta-atom is a nonlinear and tunable analogue of the SRR, the electromagnetic properties of the SQUID near its self-resonant frequency can be examined. For small detuning of the photon frequency above the transition from the ground state to the first excited state, the medium presents a negative effective permeability. The frequency region of negative permeability is diminished by a non-zero dephasing rate, and negative permeability will disappear for dephasing rates larger than a critical value. For a two-dimensional array of rf-SQUIDs, the Josephson junction was treated as a parallel combination of resistance, capacitance, and Josephson inductance. Near resonance, a single rf-SQUID can have a large diamagnetic response. An rf-SQUID array displays a negative real part of effective permeability for a range of frequencies and magnetic fields. The permeability is oscillatory as a function of applied magnetic flux and is suppressed with applied fields that induce currents in excess of the critical current of the Josephson junction. In addition to the tunability by temperature and magnetic field that is common in all superconducting resonators, their resonance can be very sensitively tuned using small *dc* magnetic fields at rates on the order of 10 s of terahertz per gauss. Unlike implementation with bare superconducting Nb wires, the Josephson inductance will allow for electrical current- or field-tunable changes in the plasma frequency over a substantial range. For example, the “superinductors,” made up of high linear density Josephson arrays, are engineered to have a large tunable inductance with a minimum increase in loss. Therefore, Josephson devices remain one of the most intriguing and promising candidates for the future of superconducting metamaterials since they offer an unrivaled level of nonlinearity and tenability (Jung et al. 2014).

5.5.5 Diamagnetic Metamaterials

While traditional shielding techniques using materials of either very high or low permeability (i.e., μ -metal and superconductors) can shield an object from an external field, they also distort the field lines thus making the object detectable. This can

be avoided by using a shell made from a magnetically anisotropic material. For example, good cloaking can be achieved for this purpose using a cylindrical shell with a locally uniform, anisotropic μ . The condition required to achieve this effect is only that the radial and angular component of the relative, magnetic permeability, μ_r and μ_θ , have to fulfill the equation $\mu_r \cdot \mu_\theta = 1$ (Jung et al. 2014). This ensures that the field outside the shell remains essentially unaltered by the presence of the shield. The fields inside the shell, however, also depend on the ratio between μ_r and μ_θ : if $\mu_r \gg \mu_\theta$, the fields are concentrated on the interior of the shell. This can be implemented using superconducting and ferromagnetic wedges or prisms for magnetic field concentration. In the opposite case, $\mu_\theta \gg \mu_r$, the interior of the shell remains essentially field-free. Therefore, classic cloaking case can be realized by combining paramagnetic layers with superconducting plate arrays or using arrays of superconducting (like Pb plate) and ferromagnetic (permalloy, for instance) strips. An additional superconducting layer on the inside of the shield could be used to ensure that fields from sources inside the shell cannot leak out. This design can be applied for carpet cloak.

In addition, bilayer design should effectively cloak an object in a uniform static magnetic field even for the case of thin-film superconductor and paramagnetic layers or when the superconductor is in the critical state (filled with magnetic vortices). It can maintain some of its cloaking properties for very low frequencies. This *ac* effect, however, is significantly disturbed by the hysteretic behavior of the ferromagnet (Jung et al. 2014; Yampolskii and Genenko 2014).

5.5.6 Quantum Metamaterials

Quantum metamaterial is an artificial optical media that (a) comprise quantum coherent unit elements with desired (engineered) parameters; (b) quantum states of (at least some of) these elements can be directly controlled; and (c) maintain global coherence for the duration of time, exceeding the traversal time of the relevant electromagnetic signal. These properties control macroscopic quantum coherence that makes a quantum metamaterial a qualitatively different system, with a number of unusual properties and applications (Zagoskin et al. 2016).

5.5.6.1 Superconducting Quantum Metamaterials

Superconducting quantum metamaterials containing large numbers of artificial atoms offer a wide range of prospects, as shown in Fig. 5.11a, b, from detecting single microwave photons to quantum birefringence and superradiant phase transitions. In contrast to natural atoms or molecules, superconducting qubits allow for a very strong effective dipole coupling to the external electromagnetic field. This opens up unique opportunities of designing artificial quantum structures made of meta-atoms that have ultra-strong and coherent coupling to the electromagnetic

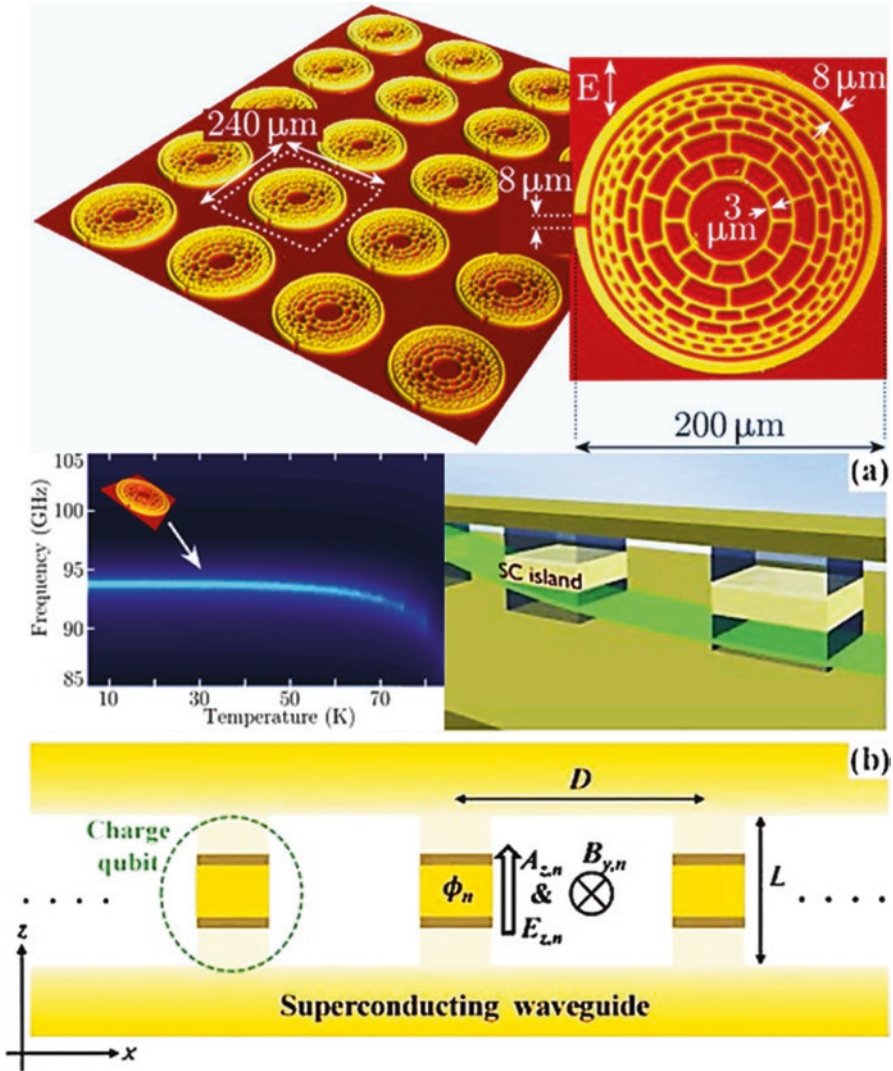


Fig. 5.11 Superconducting quantum metamaterials (Savinov et al. 2012; Zagoskin et al. 2016): (a) a 2D superconducting quantum metamaterial (300-nm-thick YBCO film deposited onto 1-mm thick sapphire substrate); (b) a realization of a 1D superconducting quantum metamaterial: charge qubits in a transmission line

fields in a transmission line or a cavity (Fig. 5.11b). The major technical challenge for artificially made quantum metamaterials will be making the qubits as identical as possible, as the energy level separation varies for physically different meta-atoms. This problem can be circumvented by utilizing very strong coupling of the meta-atoms to the electromagnetic field, similar to the way of overcoming the

effects of inhomogeneous broadening in lasers made of natural atoms. This should allow for novel ways of generating and controlling nonclassical electromagnetic waves, such as light squeezing, coherent down- and up-conversion, and so on (Jung et al. 2014).

5.5.6.2 Optical Quantum Metamaterials

Quantum metamaterials in the optical, or near IR, region of the spectrum denote a structure in which quantum degrees of freedom, such as quantum dots and quantum wells, are inserted. Quantum dots provide the gain to counteract the losses due to the presence of metallic inclusions, while quantum wells are inserted in a photonic structures allowing electromagnetically control through an effective permittivity tensor over the behavior of the structure (Zagoskin et al. 2016).

The full quantum processes that occurs between the quantized electromagnetic field and two level atoms have been studied with a 2D network of coupled atom-optical cavities, called a cavity array metamaterial (CAM). Figure 5.12 illustrates design for a reconfigurable quantum superlens based on the CAM, where the Jaynes–Cummings Hubbard (JCH) system is manipulated to produce a perfect image using single photons. Designed using a two-dimensional photonic crystal membrane, this system exhibits a quantum phase transitions with effects of cloaking and negative refraction and could be used as a quantum simulator. An effective

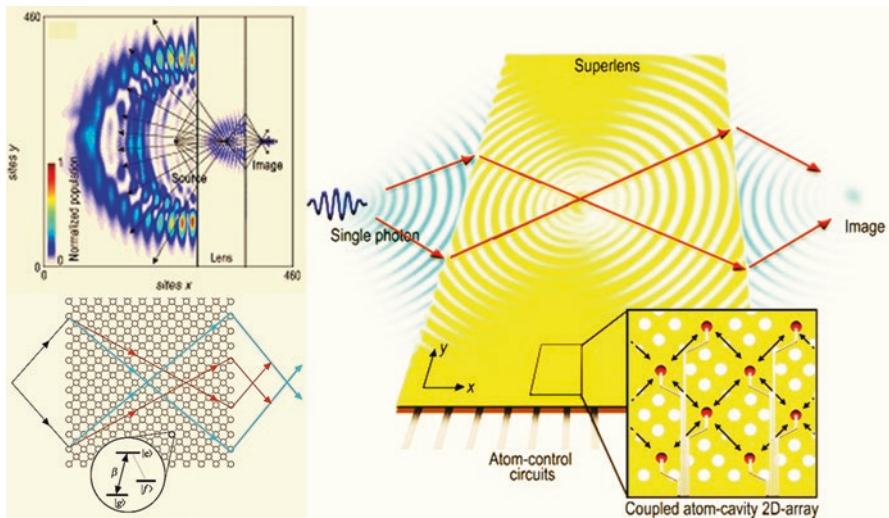


Fig. 5.12 A reconfigurable optical quantum superlens built from a cavity-array metamaterial. By allowing all-angle negative refraction and evanescent wave enhancement, the superlens surpasses the diffraction limitation of conventional lenses. Inset: electrostatic tuning of the intracavity atoms (solid circles) in the cavity lattice provides dynamic control over the light guiding and resonance properties of the lens (Quach et al. 2011)

permittivity that is nonlocal in time and space could be derived, in exactly the same way as for natural material. As with photonic crystal (PhC) implementations, CAMs have the advantage of being ideally lossless and do not require the operating wavelength to be larger than the constituent element spacing. Further, because the transition energy of each atom in the system can be individually controlled via a Stark shifting control voltage, CAMs have the distinct advantage of being highly tunable and reconfigurable: features not possible using conventional designs. To form a perfect image requires the lossless convergence of the propagating and evanescent light components. Conventional lenses only focus the propagating fields, and so the resolution of the image is fundamentally limited to features greater than the optical wavelength. Subwavelength features are carried by the high spatial frequency components encoded by the evanescent fields. The loss of the evanescent components leads to the diffraction limit. Near-field scanning optical microscopy overcomes this problem by scanning a probe in close proximity to the object, but this is often undesirable for applications such as optical lithography and sensing. Moreover, a lens built from NIMs can produce perfect far field imaging, exhibiting all-angle negative refraction (AANR) and evanescent wave enhancement (EWE). Because of their ability to overcome the diffraction limit and the lack of optical axis and curved surfaces that AANR affords, such a lens is termed superlens. Negative indexing however is not a prerequisite for superlensing. A different class of metamaterial from that of NIM, is formed by photonic crystals (PhCs) which uses Bragg scattering. PhCs have also been shown to exhibit AANR and EWE and have the advantage of low loss. The disadvantage of PhCs as a superlens is that not all the evanescent components can be uniformly amplified. In relation to the PhC as a metamaterial, it is of note that since the size and periodicity of the scattering elements in PhCs are on the order of the operating wavelength, the medium cannot be considered as homogeneous, which is a necessary condition to identify a meaningful permeability and permittivity (Quach et al. 2011).

However, a genuine quantum metamaterial requires the active coherent control of the quantum state of the “atoms” inserted in the photonic structure, so as to induce a control over the collective properties of the medium. Such a system could be implemented by considering a photonic crystal in which quantum oscillators are inserted, under the guise of quantum dots, for instance. Optical elements based on quantum metamaterials would provide new methods for image acquisition and processing. Nevertheless, a quantum metamaterial would be a natural test bed for the investigation of quantum–classical transition, which makes this class of structures interesting also from the fundamental point of view (Zagoskin et al. 2016).

5.6 Nanomechanical Photonic Metamaterials

Nanomechanical photonic metamaterials aim to provide the optical properties on demand through technology for growing high-quality freestanding nanomembranes, such as ultrathin films of silicon nitride, silicon, and diamond, that are supported by

bulk semiconductor frames is well established. Potential applications range from tunable filters, switchable gratings, and variable lenses to holographic 3D displays, programmable transformation optics devices, and generally adding tunability to the various unique functionalities that metamaterials can provide (Plum 2016, Zheludev and Plum 2016).

At the submicrometer dimensions of the metamolecules in photonic metamaterials, electromagnetic Coulomb, Lorentz, and Ampère forces compete with elastic forces and can thus be used to reconfigure the shape of individual metamolecules or to change their mutual arrangement. Even small movements can lead to a substantial change of the metamaterial's optical properties. The nanoscale metamaterial building blocks can be moved fast, potentially offering modulation at gigahertz frequencies. Such structures can also be driven thermoelastically or by light, through optical forces arising within illuminated metamolecules (Fig. 5.13). Elastic structured nanomembranes are the ideal platform for such nanomechanical reconfigurable metamaterials (Zheludev and Plum 2016).

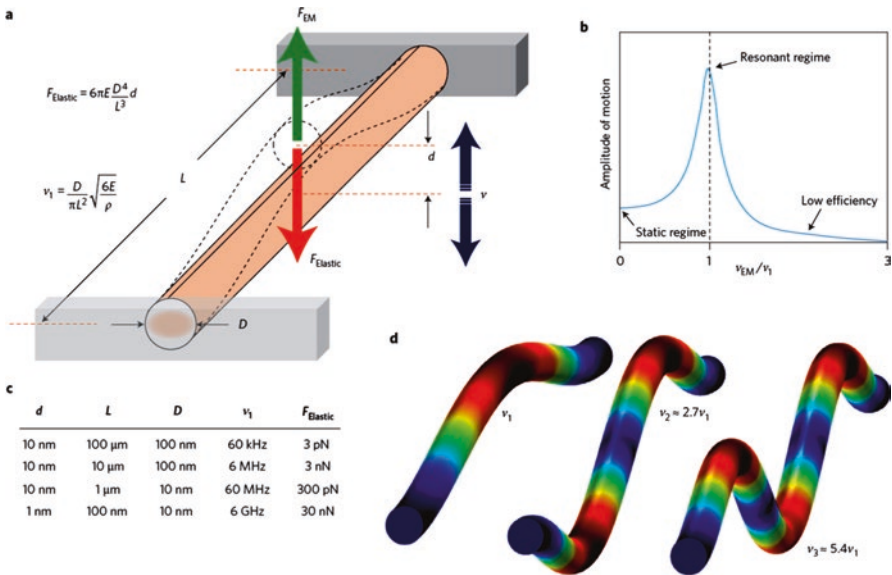


Fig. 5.13 Motion at the nanoscale for reconfiguring nanomechanical photonic metamaterials (Zheludev and Plum 2016): (a) a nanowire anchored at both ends of length L , diameter D , Young's modulus E , and density ρ will have a fundamental natural frequency v_1 that will rapidly increase with decreasing size of the wire; (b) generic resonance curve of a driven oscillator—driving with an external electromagnetic force F_{EM} at the mechanical resonance $v_{\text{EM}} \approx v_1$ will lead to enhanced motion; (c) a static displacement d of the Si nanowire's center against the elastic force F_{Elastic} depends on the size and aspect ratio of the nanowire; (d) odd and even higher-order modes can be excited, where in-plane and out-of-plane modes of oscillation are allowed

5.6.1 Electrostatic Actuation

Engagement of the Coulomb force allows for the development of membrane-based devices and metamaterials controlled by electrostatic actuation through electrical signals, which work in the visible and near-infrared spectral bands. They are orders of magnitude faster and far more compact than electrically reconfigurable terahertz MEMS comb-drive metamaterials and in contrast to metamaterials with opaque adjustable ground plane designs, membrane-based metamaterials can be used in transmission and reflection modes. For example, a large, irreversible 250% transmission jump around the wavelength of 1200 nm and 110% reflectivity changes around 1600 nm occurred due to the change of electromagnetic coupling between the plasmonic wire and meander structures (Fig. 5.14). Below the critical switching

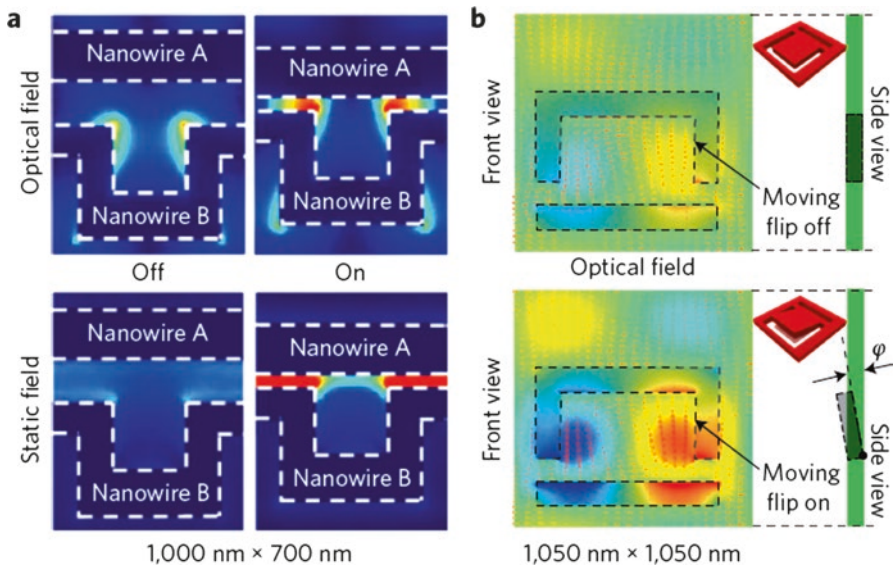


Fig. 5.14 Nanoscale motion and fields (Zheludev and Plum 2016): (a) In a plasmonic metamaterial with a 1000-nm \times 700-nm unit cell relative displacement of electrically charged nanowires A and B toward each other by about 125 nm driven by the Coulomb force leads to a large change of the resonant optical field trapped in the structure around 1800-nm wavelength (*top row*) and thus to a change in the optical reflectivity and transmission of the metamaterial array. The distribution of the static electric field that drives the reconfiguration also changes dramatically (*bottom row*). *Blue* and *red* indicate the smallest and largest electric field, respectively. (b) A dielectric metamaterial with a 1050-nm \times 1050-nm unit cell consisting of an asymmetric split-ring aperture in a silicon nanomembrane creating a moving flip. *Dashed lines* indicate areas where the membrane was removed. Both images show optical field maps (colors indicate the field strength along the unit cell's symmetry axis, where *blue* and *red* correspond to largest fields of opposite sign) and displacement currents (*arrows*) for illumination at a wavelength of 1280 nm. The field distribution changes significantly when the flip is turned by an angle $\varphi = 10^\circ$ out of the plane of the membrane. In-phase oscillations of the flips in the metamaterial array may be caused by optical forces and will lead to a change of the metamaterial's optical properties

voltage, the structure can be driven reversibly up to megahertz frequencies (the main natural frequency of the strings is about 1 MHz). Driving the array at mechanical resonance frequencies enhances the amplitude of motion and modulation of its optical properties. The metamaterial exhibits a complex dependence of its optical response on the frequency of electrical modulation with initial roll-off at about 0.5 MHz and resonant peaks at 1.3 and 1.6 MHz. The effective electro-optical coefficient of such an electrically driven nanomechanical metamaterial is on the order of 10^{-5} – 10^{-6} m V⁻¹ (at 1600-nm wavelength), which is about four to five orders of magnitude greater than in a natural electro-optic media, such as lithium niobate (3×10^{-11} m V⁻¹ at 633-nm wavelength). Thus, electro-optical nanomembrane metamaterials could become a compact alternative for modulator applications at frequencies well into the megahertz range, where they can complement and compete with conventional bulky modulators based on the electro-optical Pockels effect in crystals. The energy required to switch the metamaterial device from the off state to the on state can be estimated as the energy required to charge the capacitive nanostructure and is as little as ~ 100 fJ for the entire array. Such reconfigurable metamaterials can be operated with microwatt power consumption, making them suitable for applications in ultracompact tunable spectral filters, displays, switches, modulators, adaptable transformation optics devices, protective optical circuitry, and reconfigurable optical networks (Zheludev and Plum 2016).

5.6.2 Thermal Actuation

The tunable nanomembrane metamaterial for the optical part of the spectrum exploited thermally activated deformations of a multilayered plasmonic structure has been built by sophisticated dual-side ion beam milling on a silicon nitride membrane. As shown in Fig. 5.15a, it consisted of an array of plasmonic metamolecules supported by pairs of strings cut from the membrane and designed in a way that one string of the pair exhibited temperature-activated deformation while the other did not. The thermally activated string was a two-layer sandwich of materials with different thermal expansion coefficients: a 50-nm-thick gold layer and a 100-nm-thick silicon nitride layer. On increasing the ambient temperature, the bimorph string bent toward its gold side, as the thermal expansion coefficient of gold is five times larger than that of silicon nitride. The other, thermally insensitive string of the pair had a symmetric three-layered structure made of gold, silicon nitride, and gold films. The alternating thermally active and thermally passive strings supported rows of C-shaped aperture resonators (split rings) with a 500-nm \times 500-nm footprint. On change of the ambient temperature, relative displacement of neighboring strings caused a change in the electromagnetic coupling of adjacent split rings. Such reconfiguration of the metamaterial, which involved nanoscale displacements of rows, strongly affected the transmission spectrum of the entire array: a temperature increase from 76 to 270 K caused a transmission change of up to 50% at plasmonic resonances in the spectral range from 1200 to 1700 nm. For metamaterial arrays

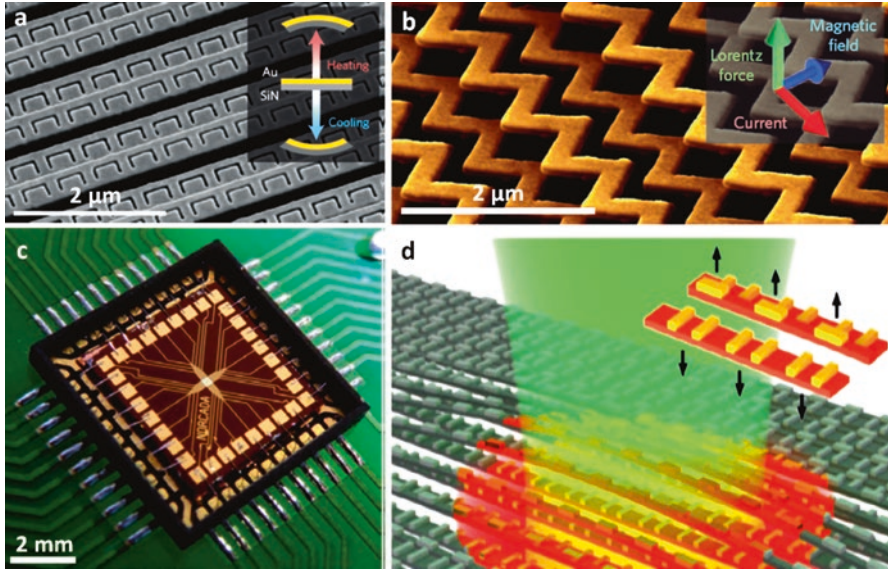


Fig. 5.15 Implementations of spatially reconfigurable nanomembrane metamaterials (Zheludev and Plum 2016): (a) a thermally reconfigurable metamaterial driven by differential thermal expansion between gold and silicon nitride layers; (b) a magneto-optical modulator–nanowire structure actuated by the Lorentz force that is controlled by currents and magnetic field; (c) packaging arrangement for the spatial light modulator—electrically addressable metadvice randomly reconfigurable in one dimension; (d) an all-optical modulator, plasmonic metamaterial actuated by a milliwatt of light power at telecom wavelengths, a pump beam (red) reconfigures the nanostructure (inset) resulting in modulation of a probe beam (green)

with an overall size of tens of micrometers, the response time is typically on the microsecond to millisecond scale, but the practically achievable reaction time is likely to be controlled by the rate at which the ambient temperature can be changed, unless the nanostructure’s temperature is controlled directly using local resistive heating by electrical currents or heating by pulses of light or an electron beam. Potential applications of this thermally activated metamaterial include temperature sensors, tunable spectral filters, switches, and modulators (Zheludev and Plum 2016).

5.6.3 Magnetic Actuation

Engaging the Lorentz force provides another mechanism for reconfiguring nanomembrane metamaterials. As shown in Fig. 5.15b, an artificial chevron gold nanowire structure is fabricated on an elastic dielectric nanomembrane; the Lorentz force drives reversible transmission changes on application of a fraction of a volt when the structure is placed in a magnetic field of a fraction of 1 T. Typically, the current is less than 1 mA in each of the actuated wires of the array. The chevron pattern was

chosen because it is easy to fabricate and has good longitudinal elasticity due to its springlike shape while providing plasmonic optical resonances and continuous electrical paths for control currents. The metamaterial was placed between the poles of permanent neodymium magnets in such a way that the field was directed along the surface of the array, but perpendicular to the nanowires. The electrical current used as the control signal is run through every second nanowire, forcing out-of-plane motion of alternating strips. The magneto-electro-optical response of this metamaterial can be separated from its thermal response caused by resistive heating by observing modulation at different frequencies. The change of the dielectric properties is reciprocal, as it does not depend on the wave propagation direction and the phenomenon is therefore radically different from the conventional magneto-optical Faraday effect. By engaging highly sensitive zero-balance phase detection techniques, this magnetically actuated metamaterial could be used to realize micrometer-size magnetic field sensors with sensitivity at the nanotesla level (Zheludev and Plum 2016).

5.6.4 Optical Actuation

Optical forces allow photonic metamaterials to be driven by light, and this leads to optical nonlinearity. Figure 5.15d shows a nano-optomechanical metamaterial to realize optical actuation and nonlinearity using plasmonic resonant structures rather than dielectric ones. The nonlinearity also results from the reversible light-induced reconfiguration of the structure. Cross-wavelength modulation of light with light using continuous-wave milliwatt power telecom diode lasers operating at wavelengths of 1310 nm and 1550 nm was demonstrated in a nanostructure of only 100-nm thickness. To allow mechanical reconfiguration of the 700-nm \times 700-nm plasmonic metamolecules, their constituent parts were supported by different flexible silicon nitride strips of 28 μm length spaced by alternating nanoscale gaps of different width. Plasmonic resonances play a key role here: a plasmonic resonance increases the driving force that reconfigures the metamaterial. Moreover, a steep plasmonic resonance near the wavelength of light probing the nanostructure enhances transmission and reflection changes caused by the reconfiguration. The optical response of the structure can be modulated to up to a few megahertz frequency, and it exhibits a complex pattern that corresponds to different modes of mechanical oscillation of the strips. At such frequencies, the viscosity of air significantly damps oscillations: placing the metamaterial in a vacuum cell increases the quality factor of its mechanical resonances and thus the magnitude of the nonlinearity (Zheludev and Plum 2016).

Consequently, nonlinear, switching, electro-optical, and magneto-optical functionalities in nanomechanical devices have been used to develop novel optical functional metamaterials and metadevices. Nanomechanical metamaterials will impact photonic technology significantly, as they can provide light modulation in micrometer-size devices. Indeed, high-index dielectric resonators promise lower

losses and larger optical forces than plasmonic structures. Silicon and silicon nitride membranes as scaffolding materials may be replaced by diamond membranes that offer higher mechanical resonances and superior thermal properties. Furthermore, photonic metamaterials providing random access in a single spatial dimension have already been realized using nanomembrane technology (Fig. 5.15c). Such devices can function as re-focusable lenses or dynamic dispersion elements and could be used for signal multiplexing in multimode or multi-core optical telecommunication technology (Zheludev and Plum 2016).

References

- Birner A, Wehrspohn RB, Gosele UM, Busch K (2001) Silicon-based photonic crystals. *Adv Mater* 13:377–388
- Drachev VP, Podolskiy VA, Kildishev AV (2013) Hyperbolic metamaterials: new physics behind a classical problem. *Opt Express* 21(12):15048–15064
- Ferrari L, Wu C, Lepage D, Zhang X, Liu Z (2015) Hyperbolic metamaterials and their applications. *Prog Quantum Electron* 40:1–40
- Genov DA, Zhang S, Zhang X (2009) Mimicking celestial mechanics in metamaterials. *Nat Phys* 5(9):687–692
- Jung P, Ustinov AV, Anlage SM (2014) Progress in superconducting metamaterials. *Supercond Sci Technol* 27:073001, 13pp
- Kurter C, Abrahams J, Shvets G, Anlage SM (2013) Plasmonic scaling of superconducting metamaterials. *Phys Rev B* 88:180510
- Kyzer L (2008) Army research on invisibility not science fiction. U.S. Army. <https://www.army.mil/article/11813/army-research-on-invisibility-not-science-fiction>. Accepted on 2 Nov 2016
- Merlin R (2004) Analytical solution of the almost-perfect-lens problem. *Appl Phys Lett* 84:1290–1292
- Narimanov E (2015) Photonic hypercrystals: the best of both worlds. SPIE. doi:10.1117/2.1201503.005744. <http://spie.org/newsroom/5744-photonic-hypercrystals-the-best-of-both-worlds>. Accepted on 7 Nov 2016
- Paschotta R (2016) Photonic metamaterials. https://www.rp-photonics.com/photonic_metamaterials.html. Accepted on 25 Oct 2016
- Pawlak DA (2008) Metamaterials and photonic crystals – potential applications for self-organized eutectic micro- and nanostructures. *Scientia Plena* 4(1):014801(1–11)
- Pendry J (2013) Transformation optics shapes metamaterials. Progress in electromagnetics research symposium abstracts, Stockholm, 12–15 Aug 2013
- Pentry J (2015) Metamaterials, transformation optics, & cloaks of invisibility. https://www.lorentz.leidenuniv.nl/lorentzchair/pendry/lectures/LeidenTalk_1.pdf. Accepted on 2 Nov 2016
- Plum E (2016) Nanomechanical photonic metamaterials. In: Roadmap on optical metamaterials. *J Opt* 18:093005 (35–36)
- Quach JQ, Su C-H, Martin AM, Greentree AD, Hollenberg LCL (2011) Reconfigurable quantum metamaterials. *Opt Express* 19(12):11018–11033
- Rill MS et al (2009) Negative-index bianisotropic photonic metamaterial fabricated by direct laser writing and silver shadow evaporation. *Opt Lett* 34(1):19–21
- Savinov V, Tsiatmas A, Buckingham AR, Fedotov VA, de Groot PAJ, Zheludev NI (2012) Flux exclusion superconducting quantum metamaterial: towards quantum-level switching. *Sci Rep* 2:450 (1–5)
- Shekhar P, Atkinson J, Jacob Z (2014) Hyperbolic metamaterials: fundamentals and applications. *Nano Convergence* 1:1–17

- Smolyaninov II (2011) Metamaterial 'multiverse'. *J Opt* 13(2):024004
- Sun, Litchinitser (2016) 9-Metamaterials. In: *Fundamentals and applications of nanophotonics*, edited by Joseph W Haus. Elsevier Ltd. pp 53–307
- Tong XC (2014) *Advanced materials for integrated optical waveguide*. Springer, New York
- Wikipedia (2016) Photonic crystal. https://en.wikipedia.org/wiki/Photonic_crystal. Accepted on 26 Oct 2016
- Yampolskii SV, Genenko YA (2014) Magnetic cloaking by a paramagnet/superconductor cylindrical tube in the critical state. *Appl Phys Lett* 104:143504
- Zagoskin AM, Felbacq D, Rousseau E (2016) Quantum metamaterials in the microwave and optical ranges. *EPJ Quantum Technol* 3(2):1–17
- Zheludev NI, Plum E (2016) Reconfigurable nanomechanical photonic metamaterials. *Nat Nanotechnol* 11:16–22

Chapter 6

Chiral Metamaterials and Metadevices

6.1 Historical Perspective

Chirality refers to the geometric property of a structure lacking any mirror symmetry plane. It exists in many forms in nature, ranging from molecules to proteins and to crystals. A chiral medium is composed of particles that cannot be superimposed on their mirror images, which has different responses for a left circularly polarized (LCP) wave and a right circularly polarized (RCP) wave due to the intrinsic chiral asymmetry of the medium. Also, there is cross-coupling between the electric field and magnetic field going through a chiral medium (Wang et al. 2009).

In the early nineteenth century, the optical rotation in quartz crystals as well as some liquids and gases had already been discovered by Biot, who also suggested that the phenomenon has a root in the molecules. The handedness nature of the molecules in optically active materials was confirmed by Pasteur in the 1840s. The discoveries turned out to be useful in areas such as analytical chemistry and pharmaceuticals. In 1873, Lord Kelvin first used the word “chirality” to describe the handedness. In the 1910s Lindeman managed to introduce the optical activity phenomenon in visible light to radio waves, with a collection of helical coils serving as artificial chiral “molecules” (Lindell et al. 1994). Since then, the chiral media in the microwave region had been applied in many areas such as antennas, polarizers, and waveguides. In 2003, Tretyakov et al. proposed the idea to fabricate a metamaterial composed of chiral particles, such as helical wires to get negative refraction for one of the circular polarizations with $\kappa \gg \sqrt{\epsilon\mu}$ (Tretyakov et al. 2003). In natural chiral materials such as quartz and sugar solutions, κ is generally much smaller than one, while $\sqrt{\epsilon\mu}$ is generally larger than one. So negative refraction is not possible in natural chiral materials. However, with chiral metamaterials, the macroscopic parameters can be designed. The idea of chiral nihility is that, when ϵ and μ of a chiral medium are small and very close to zero, the chirality can make the refractive index for one circular polarization to become negative, even when κ is small (Wang et al. 2009).

The metamaterial based on chiral nihility is a special case of chiral metamaterials. In 2004, Pendry discussed in general the possibility to achieve negative refraction in chiral metamaterials and proposed a practical model of a chiral metamaterial working in the microwave regime with twisted Swiss rolls as elemental structures. As long as the chiral parameter κ is large enough, negative refraction can be obtained in chiral metamaterials (Pendry 2004).

Chirality is of great importance in the study of chemistry and biology because molecules with different spatial configurations can lead to distinctly different physiological responses. However, the optical activity of a natural material is generally very weak, and therefore the chiral effect is detectable only when the optical path length is much larger than the wavelength of light. Chiral metamaterials exhibit a number of intriguing properties (Wang et al. 2016): (a) if the chirality is sufficiently strong, negative refractive indices can be realized in the microwave, terahertz, and optical regimes even though neither ε nor μ is negative; (b) extremely strong optical activity promises the ability to create compact broadband circular polarizers and asymmetric transmission; (c) superchiral electromagnetic fields in chiral plasmonic nanostructures are expected to substantially enhance the interaction between light and chiral molecules by several orders of magnitude, which may open a new avenue for chiroptical detection with unprecedented sensitivity.

6.2 Chirality Parameter and Ellipticity

Chiral media are a subset of bi-isotropic media where the electric and magnetic fields of light waves are coupled to each other. Thus, the electromagnetic or optical response of bi-isotropic media can be described by the following relations (Oh and Hess 2015):

$$\begin{pmatrix} D \\ B \end{pmatrix} = \begin{pmatrix} \varepsilon_0 \varepsilon & (\xi + ik) \sqrt{\mu_0 \varepsilon_0} \\ (\xi - ik) \sqrt{\mu_0 \varepsilon_0} & \mu_0 \mu \end{pmatrix} \begin{pmatrix} E \\ H \end{pmatrix} \quad (6.1)$$

where ε is the relative permittivity of the medium, ε_0 is the permittivity of vacuum, μ is the relative permeability of the medium, and μ_0 is the permeability of vacuum. The Tellegen parameter ξ is a dimensionless magnetoelectric parameter which describes the reciprocity of the material. When the material is nonreciprocal (reciprocal), $\xi \neq 0$ ($\xi = 0$). For chiral materials, the chirality parameter is $\kappa \neq 0$. Reciprocal ($\xi = 0$) and chiral ($\kappa \neq 0$) media is also known as Pasteur media. k is the chirality that measures the effect of cross-coupling between electric and magnetic fields. Due to the existence of k , the degeneracy of the two circularly polarized waves is broken; i.e., the refractive index is increased for one circular polarization and reduced for the

other. Assuming a time dependence of $e^{-i\omega t}$, the right circularly polarized (RCP, +) wave and left circularly polarized (LCP, -) wave are defined as $E_{\pm} = \frac{1}{2E_0} (\hat{x} \mp i\hat{y})$.

The refractive index for RCP and LCP waves is obtained as follows (Li et al. 2013):

$$n_{\pm} = \sqrt{\varepsilon\mu} \pm k = n_0 \pm k \quad (6.2)$$

At the same time, RCP and LCP waves have the same impedance of $Z = Z_0 \sqrt{\mu/\varepsilon}$, where Z_0 is the impedance of the vacuum. Given the fact that the chirality k is strong enough, negative refraction may occur for one circularly polarized wave even when both ε and μ are positive, while for the other circular polarization the refractive index remains positive.

6.3 Typical Chiral Metamaterials

6.3.1 Chiral Metamaterials with Negative Refractive Index

To achieve the negative refractive index, optical activity can be dramatically enhanced in chiral metamaterials or nanoplasmonic structures through rotating the electric field direction of linearly polarized in a very short distance while passing a chiral medium. As shown in Fig. 6.1a, a bilayer chiral structure (double twisted rosettes) has been used to enhance the chiral response with a giant polarization rotation. Figure 6.1b shows an arrangement consisting of a double-layer array of twisted crosses representing an effective form of bilayer chiral structure with a negative refractive index. Moreover, a conjugated gammadion array has been formed through breaking a mirror symmetry along the plane normal direction by placing two gammadion structures that are conjugated to each other on both sides of a dielectric slab (Fig. 6.1c). Since this conjugated gammadion array has inversion symmetry, the chiral response can be more easily understood and can be expressed using the Ω -particle model. A strong chiral metamaterial can have a negative refractive index for one circular polarization around resonance frequencies. Furthermore, a chiral resonator array made of gold demonstrates negative refractive index as shown in Fig. 6.1d. In addition, Fig. 6.1e shows a conjugated double Z metasurface (CDZM) with the local field enhancement caused by nanoscopic gaps between metals to enhance their optical activity. In order to enhance the strong intermolecular capacitive coupling, a conventional conjugated gammadion structure is morphologically transformed into the CDZM. The conjugated arrangement of the CDZM maintains the resonant chiral properties of the conjugated gammadion structure; the gaps between metallic elements of adjacent unit cells are made very small to enhance the intermolecular coupling, which can be characterized by an electric capacitance.

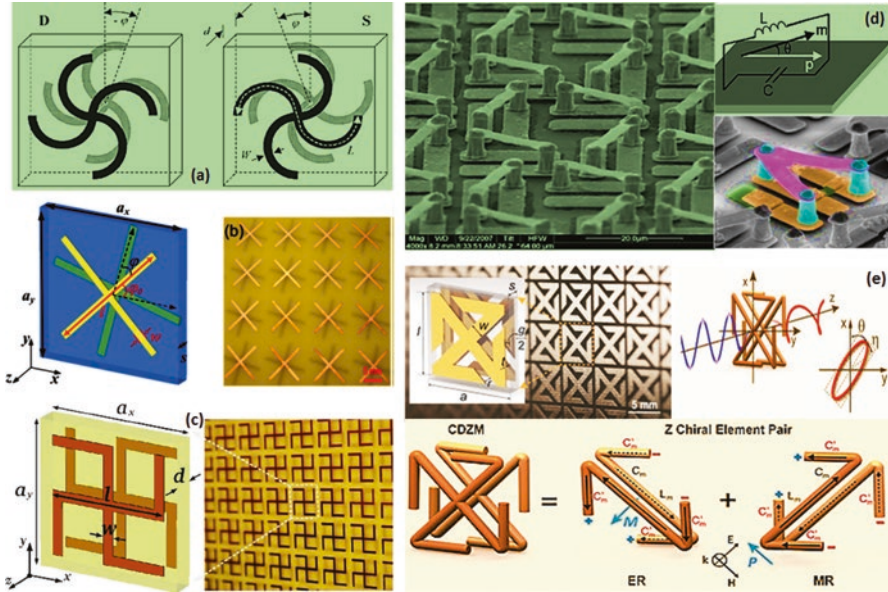


Fig. 6.1 Chiral metamaterials with negative refractive index due to strong optical activity (Oh and Hess 2015): (a) dextral (D, *right-handed*) and sinistral (S, *left-handed*) enantiomeric bilayer twisted Rosette structures; (b) an array of *left-handed* twisted gold crosses; (c) a conjugated bilayer gammadion structure; (d) chiral resonator array made of gold; and (e) a conjugated double-Z metamaterial (CDZM) composed of copper wire on Teflon substrate

Then the increased capacitance can draw more electrons, thereby increasing the electromagnetic coupling. The CDZM can not only enhance the optical activity but also reduce the ellipticity. Another way of enhancing the optical activity is to increase the number of electric dipoles, for example, by increasing the number of arms (Panpradit et al. 2011; Oh and Hess 2015).

For practical applications, the bandwidth and dispersion of chiral metamaterials need to be controlled. This comes with a challenge because chiral metamaterials normally rely on resonances for a strong optical activity or strong circular dichroism and thus only “work” within a limited frequency range. The dispersion is also strongly affected by the resonant features of chiral metamaterials. Therefore, by necessity, there is a compromise between enhanced optical activity (circular dichroism) and broad bandwidth. As shown in Fig. 6.2, nondispersive optical activity can be achieved using meshed helical metamaterials by exploiting a Drude-like response that is nonresonant. The meshed helical metamaterials show constant rotation angles and broadband zero ellipticity. The Drude-like response comes from the connectivity over the unit cells. Despite the nonresonant features, the meshed helical metamaterial shows strong magnetization induction (Fig. 6.2b) leading to relatively large chirality parameters (Park et al. 2014; Oh and Hess 2015).

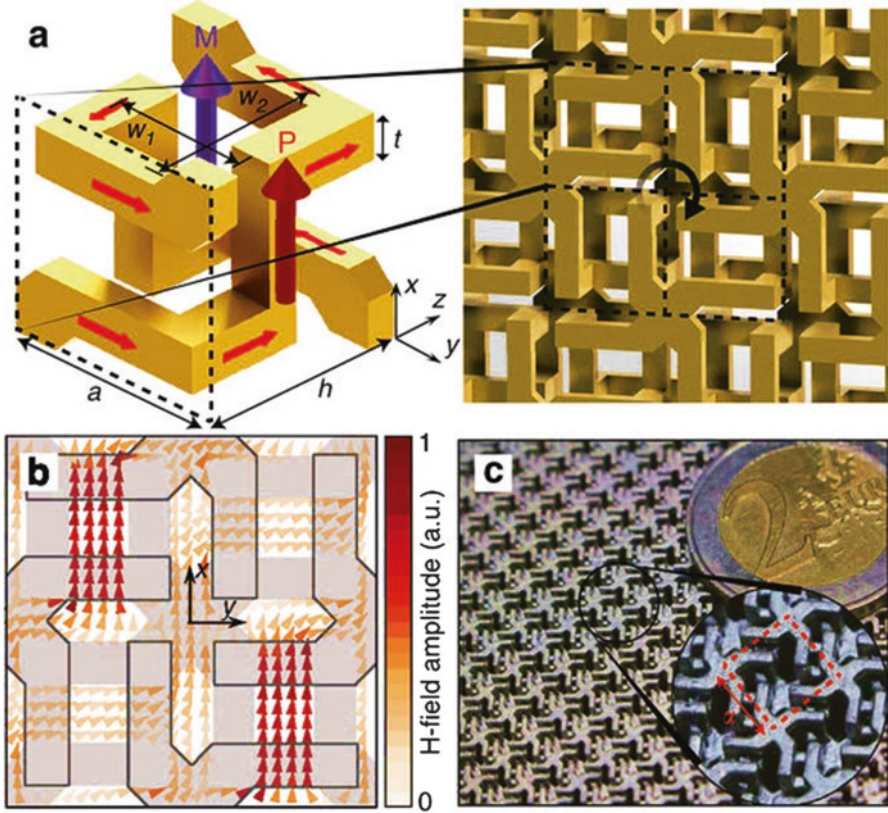


Fig. 6.2 Dispersionless ellipticity (Park et al. 2014): (a) a unit cell of a meshed helical metamaterial. At electrical resonance (ER), the incident electric field (E) induces the surface current and electric dipole moment P . The current excites the strong magnetic dipole moment M along the parallel direction of P . (b) The numerically calculated H field distribution at $z = -h/2$ plane of unit cell (at 7.2 GHz) is shown with impinging electric field polarized in the direction of the x -axis. (c) Photograph of the fabricated sample – the size of the fabricated sample was 170×170 mm. The lattice constant of the primitive unit cell (indicated as a red dashed square) is represented as $\alpha = 3.66$ mm. Samples with the following structural dimensions were tested: $a = 2.59$ mm, $w_1 = 1.15$ mm, $w_2 = 2.0$ mm, $t = 0.50$ mm, and $h = 2.5$ mm

In metal nanoparticle assemblies with a chiral arrangement, optical activity and circular dichroism can also be observed. Furthermore, chiral DNA structures have been used to fabricate ensembles of randomly oriented three-dimensional plasmonic chiral tetramers with circular dichroism, demonstrating switchable and enhanced circular dichroism by aligning the DNA-origami-scaffold nanoparticle helices (Oh and Hess 2015).

Dynamic control of optical activity and ellipticity is of great interest since it can allow the realization of new types of switching devices that control polarization states in real time. For instance, optical activity of a single-layer gammadion metamaterials can be controlled using infrared light. A larger rotation angle and

wider tuning range have been achieved using a conjugated double-layer gammadion structure. Moreover, reversal of circular dichroism can be realized using a metamolecule consisting of two different meta-atoms, one of which has tunable resonance frequencies (Zhang et al. 2012; Oh and Hess 2015).

6.3.2 3D Chiral Metamaterials

3D chiral metamaterials, especially for optical wavelength applications, consist of building blocks with feature sizes on the nanoscale level and more complex geometries than achiral metamaterials. They can generally be fabricated by the top-down and bottom-up approaches. The top-down approach uses various techniques, such as ion beam lithography, electron beam lithography, and direct laser writing, to cut, mill, and shape materials into the desired shape and order. The bottom-up approach, in contrast, usually seeks to arrange small components into more complex assemblies (Wang et al. 2016).

With these fabrication methods, many different structures have been built. As shown in Fig. 6.3a, a 3D array of chiral split SRRs is constructed to fabricate 3D isotropic chiral metamaterials (Oh and Hess 2015). Figure 6.3b shows a uniaxial

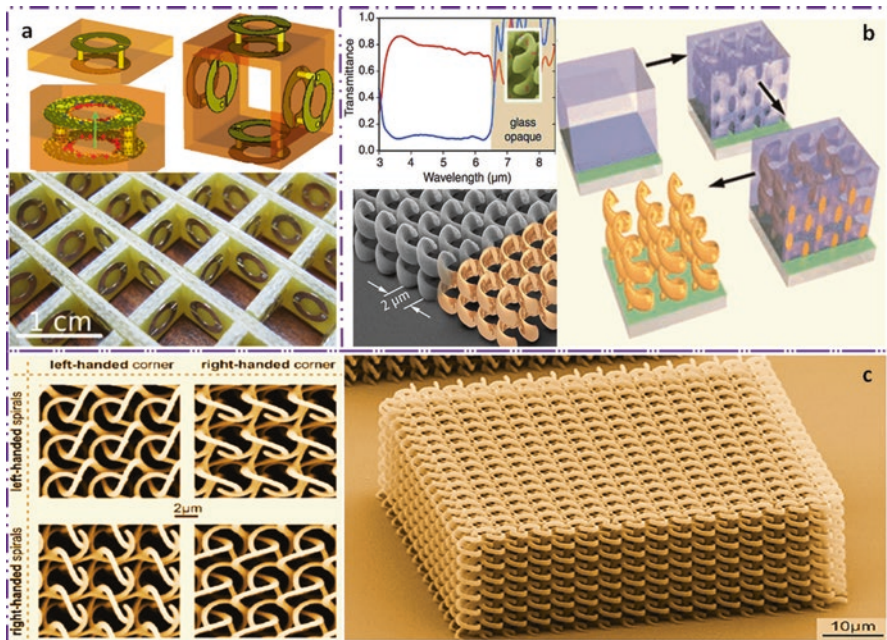


Fig. 6.3 3D chiral metamaterials (Oh and Hess 2015; Wang et al. 2016): (a) 3D isotropic chiral metamaterials composed of chiral SRR; (b) 3D helices fabricated by direct laser writing and electrochemical deposition of gold; (c) 3D bi-chiral photonic crystals composed of dielectric helices

photonic metamaterial composed of three-dimensional gold helices, which can be used as a broadband circular polarizer in the mid-infrared regime. Moreover, the circular transmission conversion, i.e., transmission from LCP to RCP or vice versa, is strongly affected by the pitch and radius of helices, wire radius, and the length of helices. These nanostructures are fabricated by direct laser writing of helical pores followed by electrochemical deposition of gold. To fabricate an array of helical pores, a positive-tone photoresist is selected and spun onto a glass substrate. Only those regions that are sufficiently exposed by light are removed. Deposition of gold is then controlled by the applied current density and the growth time. Plasma etching is finally used to remove the polymer and realize a square array of 3D gold helices on a glass substrate (Wang et al. 2016). Using 3D direct laser writing, as shown in Fig. 6.3c, bi-chiral dielectric photonic crystals have been fabricated, which are composed of three arrays of helices oriented along the three orthogonal directions. This structure shows two distinct types of chirality: one from an arrangement of helices and the other from the chirality of helices (Oh and Hess 2015).

Stacked planar structures are an alternative approach to accomplishing strong chiroptical responses. In general, such structures can be fabricated by electron beam lithography along with alignment in a layer-by-layer manner (Wang et al. 2016). Figure 6.4a shows a chiral structure of twisted split rings. The transmittance spectrum can be tuned by adjusting the twisted angle. For instance, when the angle is

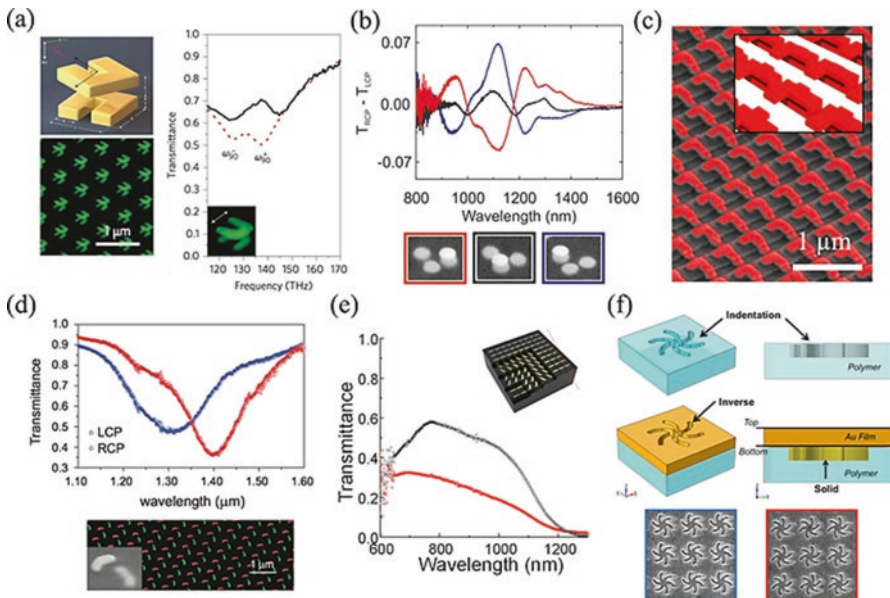


Fig. 6.4 Stacked planar chiral metamaterials (Wang et al. 2016): (a) a twisted gold split-ring dimer metamaterial; (b) three chiral oligomers; (c) L-shape chiral nanostructure; (d) twisted-arc chiral metamaterials and the corresponding transmission spectra; (e) multilayer twisted metamaterial as a broadband circular polarizer; (f) chiral metamaterials fabricated by depositing gold film on structured polycarbonate substrates

90° , the electric fields in the gaps of the two split rings are perpendicular to each other, and thereby no electric dipole–dipole interaction occurs. In addition, as the higher-order multipolar interaction is negligible in a first approximation, the electric coupling can be ignored. Therefore, the resonances are determined by magnetic dipole–dipole coupling. For the 90° twisted dimer, the magnetic dipoles in the two split rings at the two resonances (ω_{90}^- and ω_{90}^+) are aligned parallel and antiparallel, respectively, and thus produce chiroptical responses. Similarly, a cluster composed of several nanoparticles provides the possibility of configuring the hybridization of plasmonic resonances, thus enhancing the overall chiroptical responses in plasmonic oligomers (Fig. 6.4b). Diverse chiral nanostructures have been investigated based on this methodology, including bilayer L shapes (Fig. 6.4c), arcs (Fig. 6.4d), and so on. Broadband circular dichroism can also be achieved by cascading multilayer identical nanorod metasurfaces with a relative rotational twist. As shown in Fig. 6.4e, each layer of nanorod is intrinsically achiral. Nevertheless, the chiroptical response emerges when neighboring layers are stacked in a helical-like fashion. The transmission spectra of the four-layer twisted structure demonstrate a broadband circular dichroism in the visible regime. Moreover, a disposable plasmonic chirality has been built, where a metafilm is grown on a nanoindented polycarbonate substrate fabricated by high-throughput injection molding. The generated structure consists of a solid nanostructure and an identical shaped void directly above it (Fig. 6.4f). The switch of electric and magnetic fields between the solid and inverse structure gives rise to the chiroptical response. The optical properties can be tuned by changing the film thickness. This method offers a cost-effective and flexible way of manipulating the chirality in plasmonic structures (Wang et al. 2016).

6.3.3 Self-assembled Chiral Metamaterials

Compared with top-down fabrication methods, self-assembly technology provides an alternative bottom-up approach for realizing structures at the nanometer scale yet in a cost-efficient, highly tunable, and fast manner. With self-assembly technology, objects at the nanometer scale can be organized into equilibrium structures due to the delicate balance among various forces, which include van der Waals forces, capillary forces, static and/or transient electromagnetic forces, convective forces, friction forces, and so on. Based on such self-assembly methods, various metallic nanoparticles with different chemical compositions, geometries, and sizes can be precisely positioned and controlled. As a result, plasmonic metamaterial structures with tunable and controllable dimensions can be assembled in a programmable manner with nanometer precision (Wang et al. 2016).

The DNA base-pair interaction has been widely used for the synthesis of plasmonic chiral nanostructures. For instance, metallic nanoparticles can be assembled into pyramid geometries with DNA to enhance the chiral responses, in which DNA strands function as a scaffold for controlling the position of gold nanoparticles with different diameters (Fig. 6.5a). The building blocks in such multi-atom molecules

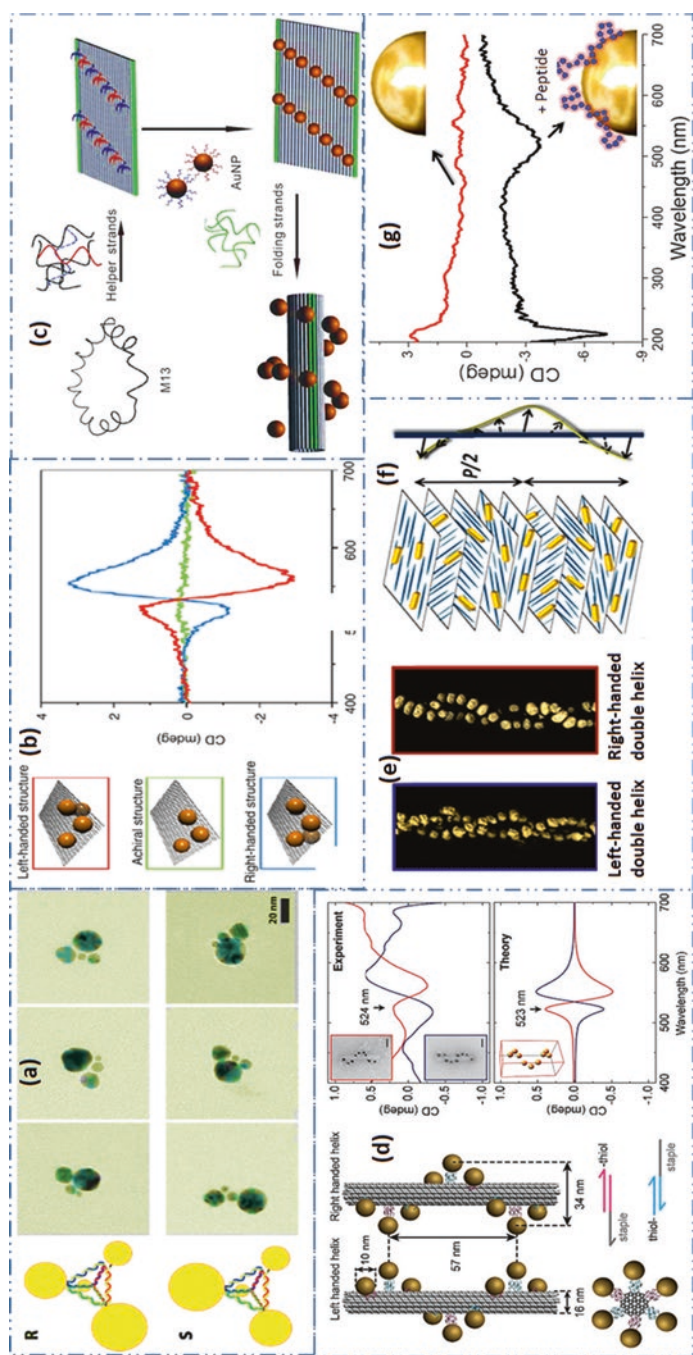


Fig. 6.5 Plasmonic chiral nanostructures based on a self-assembly method (Wang et al. 2016): (a) chiral pyramids of gold nanoparticles obtained with DNA scaffolds; (b) four gold nanoparticles assembled with bifacial DNA template in *left-handed*, *right-handed*, and achiral structures and the corresponding CD spectra of these structures; (c) synthesizing a 3D gold particle helix by rolling a planar DNA template into a 3D DNA origami tube; (d) DNA-guided self-assembly of plasmonic nanohelices with both left- and right-handedness and the corresponding CD signals; (e) double-helix nanoparticle superstructures by peptide-based assembly platforms, 3D surface renderings of the tomographic volumes show the left-handed or right-handed structure of double helices; (f) chiral plasmonic nanostructures assembled with gold nanorods and cellulose nanocrystals; (g) enhanced chiral dichroism after binding gold nanoparticles with peptide molecules that have chiral properties

are not limited to gold nanocrystals. It is possible to link other metallic and semiconductor particles via this method. The pyramidal structure consists of two pairs of nanoparticles with different sizes. The intensity, spectral characteristics, and handedness of the CD response can be tuned by changing the separation along the symmetry-breaking arm. Bifacial DNA origami templates can also be used to fabricate chiral nanostructures with metallic nanoparticles. For example, bifacial DNA origami templates can be used to assemble 3D chiral metamaterials with four gold nanoparticles; as shown in Fig. 6.5b, the rectangular DNA origami template is predesigned with three binding sites on the top surface and the fourth site on the bottom surface, right below one of the three top binding sites. Left-handed and right-handed structures can be obtained by setting the fourth binding sites in the left-handed or right-handed geometry. A characteristic bisignate CD spectrum is observed for left-handed and right-handed chiral nanostructures, compared with achiral nanostructures. Moreover, DNA strands have been folded to create artificial nanostructures of plasmonic chiral metamaterials (Fig. 6.5c). The gold nanoparticles coated with special DNA strands are able to bond with complementary DNA strands on the rectangular template at predesigned positions. Upon the use of folding strands, the rectangular DNA template will roll up and eventually become a 3D DNA origami tube. This DNA “origami” method enables the synthesis of both left-handed and right-handed metamaterials, which exhibit pronounced CD responses as shown in Fig. 6.5d. The signal of the left-handed chiral plasmonic metamaterials and the signal of the right-handed ones are complementary to each other. The CD spectrum can be controlled by depositing additional silver or silver–gold alloy shells on the gold nanoparticles. Since silver has a plasmonic resonance at a shorter wavelength, a blue shift of the CD resonance can be achieved when changing the metal composition. Metallic nanoparticles have also been assembled with other chiral templates, such as organogel, cysteine, peptide, cellulose nanocrystals, cholesteric liquid crystals, chiral mesoporous silica, supramolecular fibers, and block copolymer templates. As shown in Fig. 6.5e, mixing a gold nanoparticle precursor solution and a HEPES buffer with C_{12} -L-PEP_{au} or C_{12} -D-PEP_{au} will form left-handed or right-handed double-helix structures, respectively, which produce strong CD responses. The CD signal can be controlled by varying the thickness of the silver coating. In addition, plasmonic chiral metamaterials with cellulose nanocrystals have been assembled. Chiral plasmonic films were prepared by incorporating gold nanorods in self-assembled cellulose nanocrystals that have chiral arrangements, as shown in Fig. 6.5f. A blue shift in the CD spectrum was observed as the concentration of nanorods increases. The chiral optical activity can be tuned by changing nanorod dimensions and the helical pitch of the cellulose nanostructure. The helical pitch can be tuned by adding NaCl to the nanorod–cellulose nanocrystal suspensions (Wang et al. 2016).

Besides, plasmonic chiral nanostructures can be realized by binding chiral molecules with metallic nanoparticles. Chiral dichroism can be induced by binding peptide molecules on gold nanoparticles, as shown in Fig. 6.5g. Two types of hybrid structures have been investigated (Wang et al. 2016): One is E5-AuNPs, in which

E5 is a 38 amino acid helical peptide that links with the gold nanoparticles through a thiol linkage; the other is FlgA3-AuNPs, where the FlgA3 peptide is an unstructured random coil peptide that binds gold nanoparticles via noncovalent interactions.

6.3.4 Gyroid Metamaterials

A single gyroid (SG) metamaterial is a chiral structure that covers constant mean curvature (CMC) domain around a $1sr3s$ network. The shape of the CMC domain is derived from a gyroid surface, a triply periodic, bicontinuous minimal surface with zero mean curvature. The SG metamaterial can be found in nature in the wing scales of butterfly species and can be fabricated using the block copolymer self-assembly, selective etch, metal deposition, and polymer etch techniques, as shown in Fig. 6.6 (Oh and Hess 2015; Wiesner 2016). Figure 6.6a–c shows the SG cubic unit cell contains two left-handed screw helices with larger radius (red arrows) and two right-handed screw

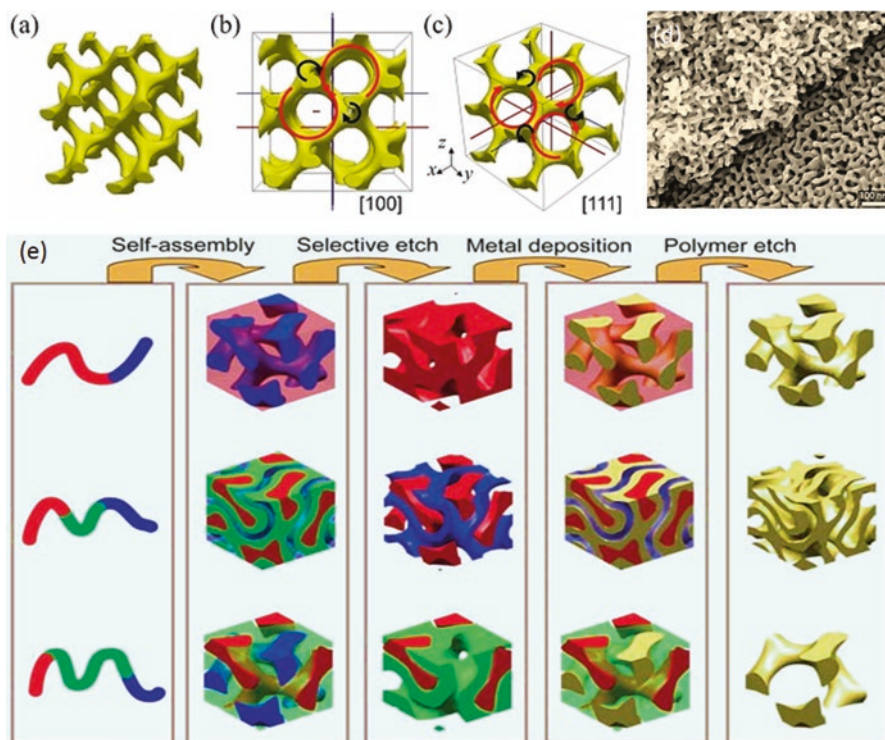


Fig. 6.6 Gyroid metamaterials (Oh and Hess 2015; Wiesner 2016): (a) unit cell of gyroid; (b) [100] direction; (c) [110] direction; (d) gold gyroid fabricated using block copolymer self-assembly method; and (e) illustration of fabrication methods

helices with a smaller radius (black arrows) along the [100] direction, while it has right-handed screw helices with a larger radius (red arrows) and left-handed screw helices with a smaller radius (black arrows) along the [111] direction.

The gyroid structure has been investigated very intensively with both dielectric and metallic forms. A negative refractive index has been theoretically predicted in a metallic gyroid; 3D optical metamaterials have been fabricated with self-assembly technique; and the circular dichroism of the metallic gyroid has been analyzed using its band structure. On the other hand, a dielectric gyroid structure shows a strong circular dichroism due to its bandgap, and it can be used as a circular polarizing beam splitter (Oh and Hess 2015).

6.3.5 *Nonlinear Chiral Metamaterials*

Nonlinear chirality would lead to intensity-dependent optical activity and nonlinear magnetoelectric responses. In general, nonlinear chirality is very weak. To overcome this, two approaches can be used (Oh and Hess 2015): (a) using a very strong light source and (b) exploiting local field enhancement, for example, surface-enhanced Raman spectroscopy and nonlinear plasmonics. The light–matter interaction and chirality in metamaterials are very important for optical wavelengths. For instance, an enhanced ultrafast nonlinear response from a gold gyroid metamaterial results in plasma frequency shift, which causes a dramatic enhancement in reflection and absorption upon the injection of a short pulse of pump light (Oh and Hess 2015).

6.4 Chiroptical Effects

6.4.1 *Extrinsic Chirality*

Optical activity can be observed even when the structures are intrinsically achiral in geometry (Fig. 6.7). Such extrinsic chirality arises from the mutual orientation of the achiral metamaterials and the incident beam. As shown in Fig. 6.7a, using asymmetric split rings, strong circular dichroism and birefringence indistinguishable from those of chiral 3D materials have been observed. The underlying mechanism is the simultaneously induced electric and magnetic dipoles that are parallel to each other. The oblique incidence is crucial for observing extrinsic chirality, because it breaks the mirror symmetry for any plane containing the wave vector (propagating direction). Extrinsic chirality can also induce a large circular dichroism in individual single-walled carbon nanotubes, with the degree of polarization reaching 65%. Moreover, electromagnetic chirality can occur in 1D patterned composites whose components are achiral. A schematic diagram is given in Fig. 6.7b. Electromagnetic waves propagate through a 1D metamaterial whose unit cell is obtained by stacking

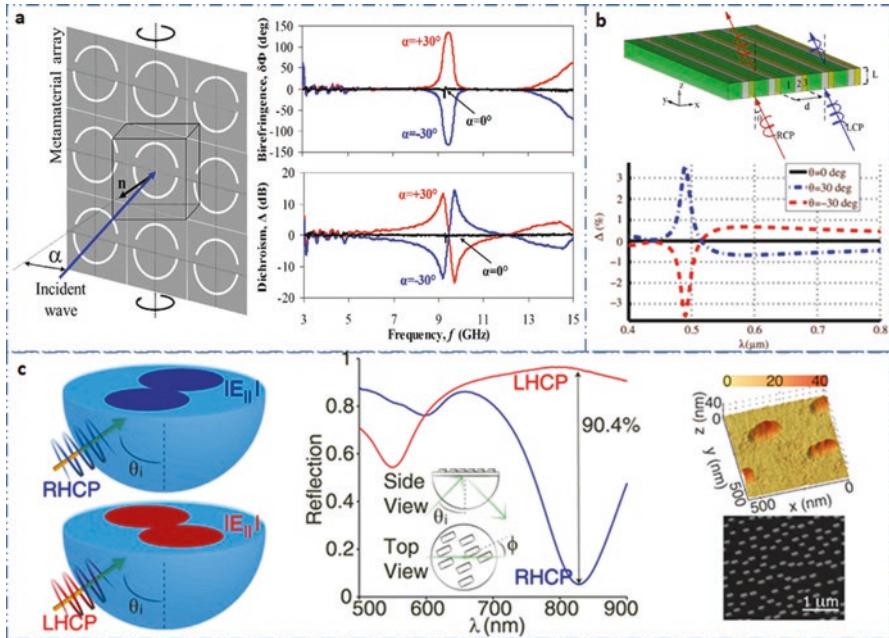


Fig. 6.7 Extrinsic chirality (Wang et al. 2016): (a) planar metamaterials based on an array of asymmetrically split rings manifest optical activity and circular dichroism at oblique incidence of light; (b) one-dimensional multilayer metamaterials show chirality in the epsilon-near-zero regime. The bottom panel depicts the optical activity of such a slab; (c) a randomly arranged anisotropic metasurface exhibits a near-complete photon spin selectivity under evanescent excitations. The left panels show the in-plane electric field amplitudes. The middle panel depicts the reflection spectra. The right panels are the AFM and SEM images of the elongated gold nanoparticles

layers of different media of different thickness along the x-axis. In the epsilon-near-zero regime, the nonlocal effect can be comparable or even greater than the local linear part of the dielectric response and results in enhanced chiroptical responses. Extrinsic chirality in anisotropic plasmonic metasurfaces can be greatly boosted by interaction with evanescent excitations. Figure 6.7c schematically illustrates the process in which the incoming light of opposite handedness impinges onto an array of gold nanoparticles. When illuminated slightly above the critical angle, no transmission is allowed. For incident wavelengths close to the plasmonic resonance of the nanoparticles, the metasurface can efficiently absorb the LCP light, while the other spin state is almost totally reflected. The effect of photon spin selectivity originates from the mutual orientation of the achiral metasurface, so-called extrinsic chirality, and highly depends on both the incident angle and the relative orientation of the nanoparticle. Almost perfect selectivity ($\sim 90\%$) of the incident photon spin has been observed at visible frequencies. Since polarization manipulation has intriguing applications in photonics, the enhanced chiroptical effects from evanescent waves may pave a new way for efficient on-chip chiroptical devices (Rizza et al. 2015; Wang et al. 2016).

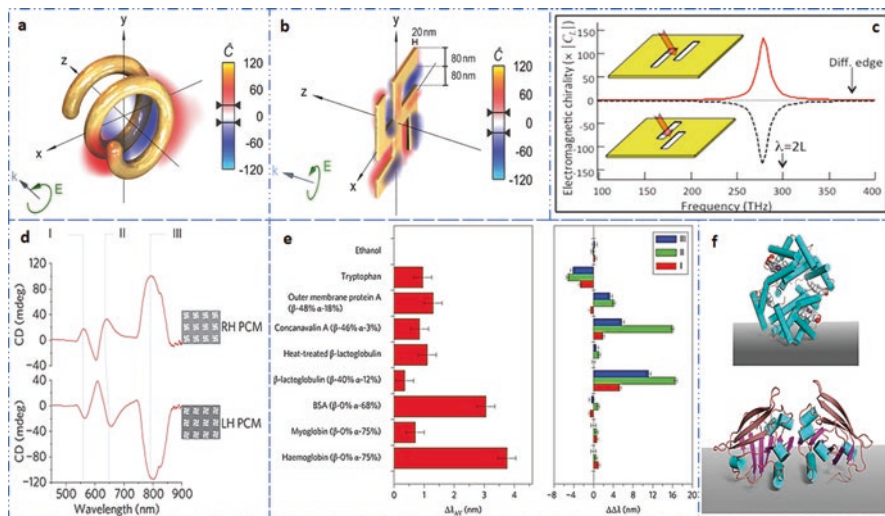


Fig. 6.8 Superchiral field (Hendry et al. 2010; Wang et al. 2016): optical chirality enhancement for (a) a left-handed helix and (b) a planar gammadion with left-handed circularly polarized light; (c) local electromagnetic chirality in the center of nanoslit pairs, 1 nm above the transmission interface of the array. Solid and dashed lines represent the two enantiomers; (d–f) superchiral field-based biosensing; (d) CD spectra of left-handed/right-handed planar chiral metamaterials; (e) the averaged resonance shift (*left*) and difference in resonance shifts (*right*) between right-handed and left-handed planar chiral metamaterials on adsorption of chiral biomolecular layers; (f) hemoglobin (*top*) and β -lactoglobulin (*bottom*) molecules adopt different geometries upon adsorption due to their secondary structures (α -helix, cyan cylinders, β -sheet, ribbons)

6.4.2 Superchiral Fields

The enhancement of the chiral field in the near-field region, known as the superchiral field, may provide a method for detecting the handedness of a single molecule. Plasmonic nanostructures, whose geometry directly influences the distributions of their near fields, can be utilized to generate chiral fields with strong optical chirality. This strong optical chirality exists not only in 2D and 3D chiral structures under circularly polarized illuminations but also in achiral structures illuminated by linearly polarized light. For example, Fig. 6.8a shows the optical chirality of a left-handed helix with left-handed circularly polarized light. The absolute values of optical chirality are much smaller for the nonmatching configurations, in which the same structure is illuminated with the opposite spin state. Planar gammadion also exhibits a similar behavior for circularly polarized light, as illustrated in Fig. 6.8b. However, the gammadion shows both positive and negative optical chirality with similar strength, while for the helix the values corresponding to the nonmatching configuration are much smaller. Moreover, in gammadion structures, regions with enhanced optical chirality are at the same position and have same signs for both spin states. Therefore, a change of incident polarization cannot provide a large change in

the optical chirality at a certain position, which makes this design less practical in applications (Wang et al. 2016).

Interestingly, the chiral near fields can also be formed in achiral structures. For example, optical chirality occurs in the near field of nanoslit pairs illuminated with linear polarized light (Fig. 6.8c). Superchiral fields for biosensing have been investigated by employing gold gammadion arrays working at visible and near-infrared frequencies. As shown in Fig. 6.8d, three resonant modes exist in this planar chiral metamaterial. The spectra of the left-handed and right-handed gammadions are mirror images of each other. By coupling the incident light into localized surface plasmon resonances of the gold nanostructures, the local chiral field is greatly enhanced, and thereby molecules adsorbed on the surface of the chiral metamaterials will strongly influence the resonant wavelength. The property of resonance shifts is caused by the change in the refractive index, which is determined by the chirality of the molecules and that of the fields. According to the first line in Fig. 6.8e, almost no shift is observed for an achiral adsorption such as ethanol. Specifically, large dissymmetry is observed in the difference in resonance shifts of tryptophan and β -sheet proteins. The measured results also provide indirect information on the geometry of chiral molecules, which can be used to explain the asymmetric difference in the resonance shifts. As shown in Fig. 6.8f, biomacromolecules rich in α -helices are more isotropically distributed at the interface, while the β -sheet proteins result in anisotropic aggregation in lateral directions (Hendry et al. 2010; Wang et al. 2016).

6.5 Typical Applications of Chiral Metamaterials

6.5.1 Chiral Metamaterial Sensors

Sensor abilities of a chiral metamaterial based on split ring resonators with double splits (SRDS) have been demonstrated in X-band range. The resonance frequency of the chiral metamaterial based SRDS sensor is linearly related to the permittivity and the thickness of the sensor layer which creates a suitable approach for sensing environment and organic parameters. When the sensor layer is filled with the related material, changes in the tissue temperature, sand humidity, and calcium chloride density lead to resonance frequency changes. Therefore, many other sensing applications can be realized by using SRDS-based chiral MTM sensor such as pressure, temperature, humidity/moisture, and density sensing (Karaaslan and Bakir 2014).

6.5.2 Nonlinear Optics in Chiral Metamaterials

The application of chirality in biochemical engineering is not limited to the linear regime; chiroptical effects in second-harmonic generation (SHG) are typically orders of magnitude larger than their linear counterparts. In the second-harmonic

process, two photons at a fundamental frequency are annihilated into a single photon at twice the frequency. This response can be described by a nonlinear polarization, which can be written in the electric dipole approximation as (Wang et al.):

$$P_i^{NL}(2\omega) = \chi_{ijk}^{(2)} E_j(\omega) E_k(\omega) \quad (6.3)$$

where ω is the angular frequency, $\chi_{ijk}^{(2)}$ is the second order susceptibility tensor, E is the electric field and i, j , and k are the Cartesian indices. SHG only exists in noncentrosymmetric materials or matter that lacks inversion symmetry. Thus chiral metamaterials are naturally suitable for SHG because all chiral structures are intrinsically noncentrosymmetric.

The chirality can be distinguished with linearly polarized light regardless of the polarization direction and the polarization state of the second-harmonic light. The linear response in chiral metamaterials is reciprocal; the nonlinear ones are nonreciprocal. In the nonlinear regime, however, the SHG-CD does change its sign. Moreover, the separation distance of neighboring units can be optimized to enhance the macroscopic circular dichroism in the second-harmonic field (Fig. 6.9a). Strong SHG-CD signals have also been observed in twisted-arc structures that lack the fourfold rotational symmetry. An image of the “GT” logo has been created by a point-by-point calculation of the SHG-CD (Fig. 6.9b). In addition, anisotropic SHG-CD measurements in fourfold symmetric G-shaped nanostructures have demonstrated that both the value and the sign of the CD response are highly dependent on the incident angles of the fundamental illuminations. The SHG probe can thereby also serve as an extremely sensitive probe of the structural symmetry, allowing to distinguish between chirality and anisotropic effects. Chiroptical effects in the second-harmonic field have also been investigated in anisotropic achiral structures. Figure 6.9c shows the measured circular dichroism in the second-harmonic field. Blue circles show the measured SHG-CD for the sample with the curvature of nanowires pointing down. The SHG-CD increases as the incident angle becomes larger. The situation is reversed when the sample is rotated by 180 degrees (red circles). Specifically, the achiral structure of curved nanowires has shown more than 50% visibility by exploiting the extrinsic chirality in the second-harmonic field (Wang et al. 2016).

6.5.3 Chiral Light–Matter Interactions

The enhancement of chiral light–matter interaction has been attempted in chiral metamaterials, while superchiral fields are used to overcome the problem of weak chiroptical signals in nature. Various nanostructures are developed to enhance chiroptical signals, such as plasmonic structures, dielectric nanoparticles, and negative-index metamaterials. The interaction between quantum emitter and chiral metamaterials (two enantiomers) has been experimentally investigated, as shown in

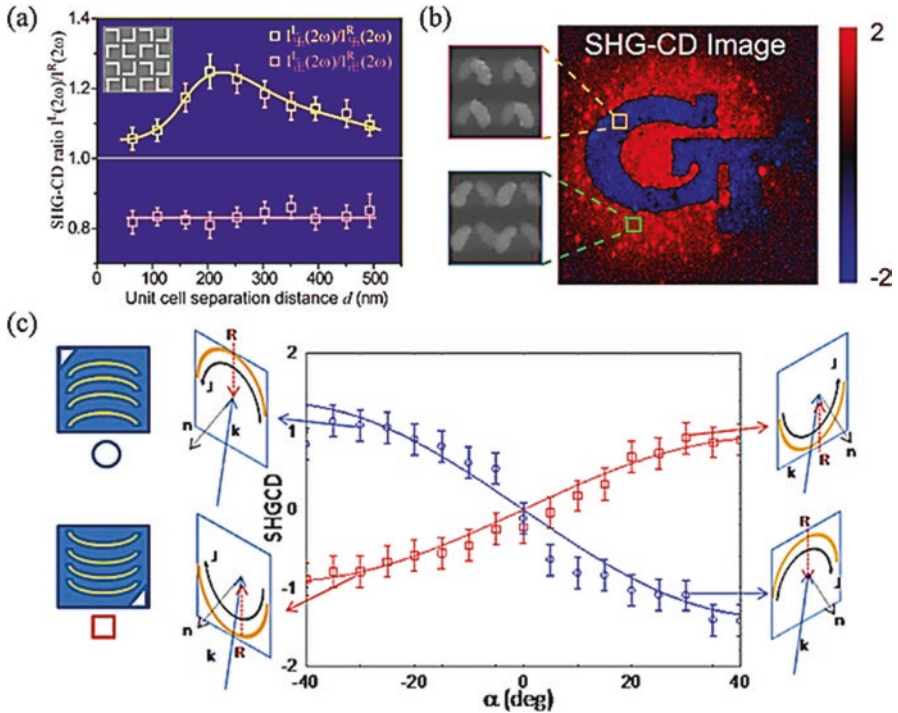


Fig. 6.9 Chiroptical effects in the second-harmonic regime (Wang et al.): (a) SHG-CD from two chiral centers (gammadions with opposite handedness) as a function of the gap size; (b) SHG-CD image (right panel) patterned logo based on twisted-arc structures and the SEM images of the two enantiomers (left panels); (c) SHG-CD of the sample with curved nanowires for 0° (blue circles) and 180° (red squares) orientation of the sample

Fig. 6.10a, b. Achiral quantum dots occupied the entire space around the upper arc and only a slight part of the lower arc. In the linear regime, the circular dichroism of the arc metamaterials reached as high as 50% at the wavelength of resonance (~ 780 nm), which led to the highest contrast of the transmission images of the chiral metamaterials. The light confinement at the resonant wavelength was largely boosted and thereby implied a chiral-selective enhancement in nonlinear light–matter interaction. These manifest the potential for applications in chiral-selective imaging, sensing, and spectroscopy (Wang et al. 2016).

Apart from the enhancement of quantum emitters, other applications are chiral-selective optoelectronics, catalysis, and photochemistry. In the photoemission process, light absorption in solids can produce hot carriers whose energies are larger than those of thermal excitations at ambient temperatures. Hot electrons generated from light absorption in a metal can be emitted over a Schottky barrier to produce current. Properly designed plasmonic nanostructures may greatly enhance light absorption and provide valuable control over the emission of the hot electrons in practical applications. Chiral plasmonic nanostructures enable disparate light

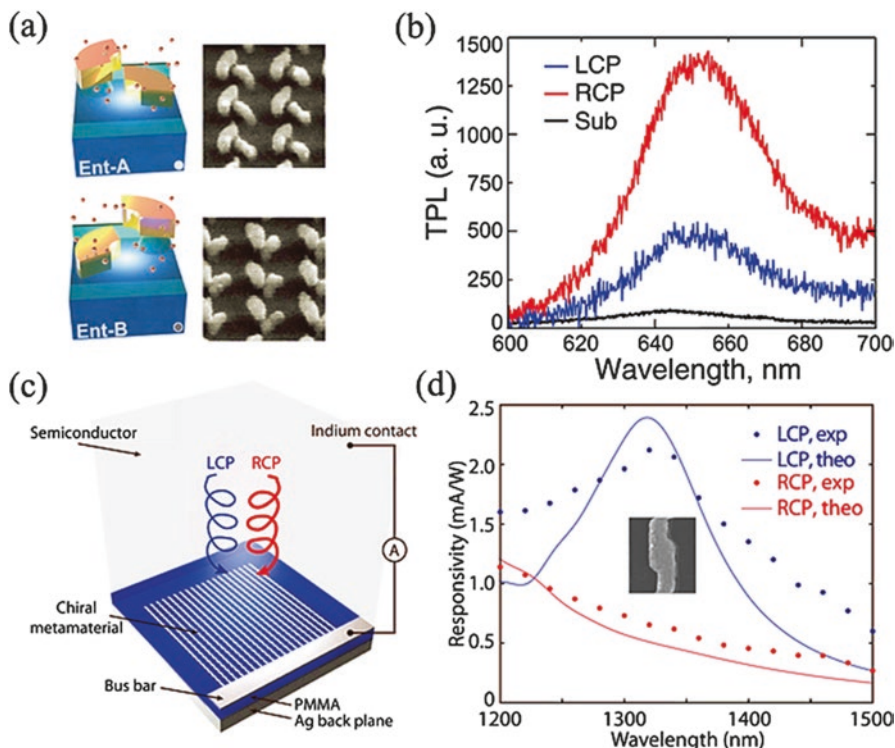


Fig. 6.10 Chiral light – matter interactions (Wang et al. 2016): (a) enantiomer A (*top*) and enantiomer B (*bottom*) of the twisted-arc chiral metamaterial – quantum dots fill the volume mostly surrounding the region around the upper arc; (b) two-photon luminescence profile at 800 nm under different input circular polarizations for enantiomer A; (c) a circularly polarized light detector consisting of a chiral metamaterial with a semiconductor that serves as a hot-electron acceptor; (d) experimentally measured (*dots*) and theoretically calculated (*solid curve*) photo responsivity spectra under LCP (*blue*) and RCP (*red*) illumination for left-handed metamaterials

absorption for different circular polarizations and result in chiral-responsive hot-electron devices. Figure 6.10c, d shows an ultracompact device for circularly polarized light detection. The designed chiral metamaterial consists of Z-shaped silver stripes on top of a dielectric spacer and an optically thick silver backplane. The chiral metamaterial acts as a perfect LCP light absorber at the resonant wavelength, and it reflects nearly 90% of the light of the other spin state. The simulated circular dichroism ($CD = ALCP - ARCP$) reaches as high as 0.9, promising enhanced discrimination between LCP and RCP in photodetection. In addition, a Schottky barrier is formed by integrating a semiconductor layer (n-type silicon) on top of the chiral plasmonic structure. Photoresponse spectra match well with the measured absorption spectra and demonstrate peak photo responsivity of the resonant state up to 2.2 mA/W^{-1} . The corresponding quantum efficiency reaches as high as 0.2%. This efficiency is two times that of chiral organic semiconductor transistors.

Furthermore, large circular dichroism gives rise to a significant distinction in photocurrents for the two spin states, with a polarization discrimination ratio of 3.4 and a difference in photo responsivity of 1.5 mA W^{-1} (Yang et al. 2013; Wang et al. 2016).

6.5.4 Active Chiral Metamaterials

Active control over the chirality of metamaterials has the potential of serving as a key element of future optical systems such as polarization-sensitive imaging and interactive display. Achieving active control over chiral metamaterials involves the reconfiguration of the metamolecule from a left-handed enantiomer to a right-handed counterpart and vice versa. In the terahertz regime, the generation of charge carriers via an optical pump in silicon has been utilized to actively switch the overall handedness of chiral structures. A pulsed laser working at 800 nm is utilized to excite electron–hole pairs across the 1.12 eV bandgap of silicon. Under the illumination of a 500 mW pump laser, the photoconductivity of silicon can be as high as $50,000 \text{ S m}^{-1}$. This feature enables all-optical switching of the handedness in chiral metamaterials in the THz regime. An all-optical tunable chirality has also been realized in a double-layer metamaterial, which consists of a nonlinear nano-Au: polycrystalline indium tin oxide layer between two L-shaped nanoantennas in the building block (Zhu et al. 2015). A 45-nm shift of the peak in the circular dichroism spectrum has been observed under a 40 kW cm^{-2} weak pump. This work opens up the possibility for ultralow-power and ultrafast all-optical tunable chirality at visible frequencies (Wang et al. 2016).

Switchable chirality can also be achieved by microelectromechanical systems. For example, a planar spiral structure is vertically deformed into its three-dimensional counterparts once a pneumatic force is applied (Fig. 6.11a). The pneumatic force is supplied through air channels with the pressure source of N_2 gas regulated by a pressure injector. Enantiomer switching is realized by selecting the deformation direction, which allows the alteration of the polarity of the optical activity without changing the spectral shape (Kan et al. 2015). To eliminate the cross-polarization conversion from birefringence, spiral arrays with C_4 symmetry have been further developed. A polarization rotation of up to 28 degrees has been experimentally observed, which provides a compact polarization modulator in the THz regime (Wang et al. 2016).

Phase-change materials, whose refractive index can be modified by temperature, voltage, or light pulses, have been integrated with chiral metamaterials to dynamically control the properties of metamaterials. For example, chirality can be controlled with a layer of phase-change material $\text{Ge}_3\text{Sb}_2\text{Te}_6$ that is sandwiched between two stacked nanorods (Fig. 6.11b). Such sandwich structures can ensure an optimum interaction between $\text{Ge}_3\text{Sb}_2\text{Te}_6$ and the plasmonic near field. A thermally induced transition from the amorphous state to the crystalline state occurs when the phase-change layer is heated up to the transition temperature (160°C) and leads to

a change in refractive index from $3.5 + 0.01i$ to $6.5 + 0.06i$. A giant spectral shift of around 20% at mid-infrared frequencies can occur when the phase transition happens. The wavelength tunability has also been utilized to obtain a reversal in the sign of the circular dichroism. Thermal switching of the handedness at a fixed wavelength is realized by cascading an active right-handed chiral dimer with a passive left-handed one. In the amorphous state, the strong positive CD signals from the active right-handed chiral dimer dominate and make the entire structure right-handed. In the crystalline state, the CD peak red shifts and the signals from the passive left-handed chiral dimer determines the entire chirality of the cascade system. These findings pave a new way toward thermal-controlled polarization modulation in the mid-infrared region and may find potential applications in thermal imaging and detection (Yin et al. 2015; Wang et al. 2016).

DNA-directed assembly is a viable method for the controlled arrangement of plasmonic nanostructures, thus offering reconfigurable chirality. As shown in Fig. 6.11c, two gold nanorods are hosted on a reconfigurable DNA template, which consists of two connected bundles folded from a long single-stranded DNA scaffold.

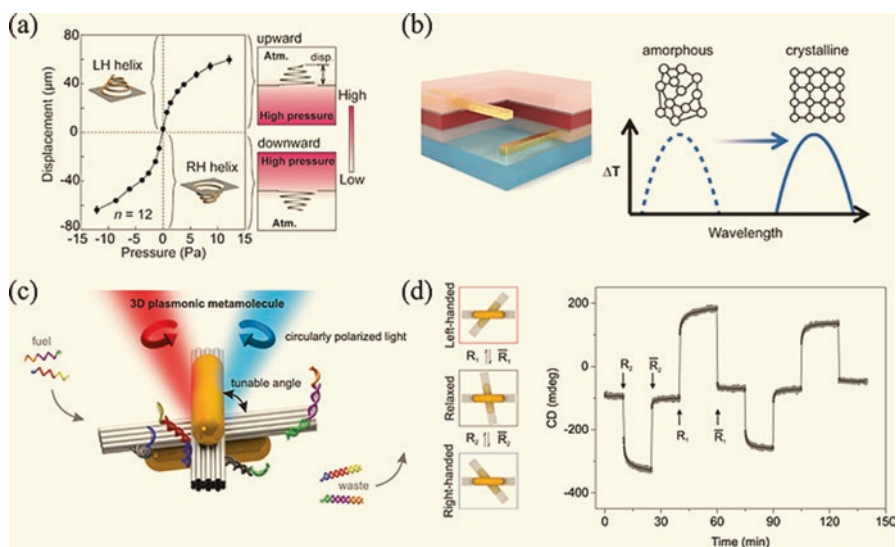


Fig. 6.11 Active chiral metamaterials (Wang et al. 2016): **(a)** displacement of the spiral structure with respect to the applied pressure of N_2 gas. The sign of the pressure is positive when the pressure is applied to the bottom chamber, resulting in left-handed spirals and vice versa; **(b)** active chiral plasmonic dimer stack consisting of 50 nm phase-change material $\text{Ge}_3\text{Sb}_2\text{Te}_6$ (red) with two 10 nm ZnS/SiO_2 layers (gray) sandwiched between gold nanorods embedded in PC403 (light red). The right panel depicts the shift of CD signal when the amorphous-to-crystalline phase transition occurs; **(c)** schematic diagram of the reconfigurable chiral metamolecules based on DNA self-assembly. Two gold nanorods are hosted on a reconfigurable DNA origami template consisting of two connected bundles, which subtends a tunable angle. **(d)** Measured CD signals of the plasmonic metamolecules over time at a fixed wavelength of 725 nm. The plasmonic metamolecules can be driven to either handedness by adding removal or return strands

The relative angle between nanorods can be controlled by two DNA locks that extended from the sides of the DNA origami bundles. By adding designed DNA fuel strands, the 3D metamolecules can be switched between different conformational states, thus giving distinct CD spectra. Both of the DNA locks are open in an initially relaxed state. In the left cyclic process, a removal strand is added to dissociate the DNA strand from the arm through a branch migration process. Unreactive waste is produced during this process. The two DNA bundles are joined together, and therefore a left-handed system is established. With the addition of a return strand, the DNA lock is opened again through a second branch migration process. Hence, the system returns to its relaxed state. Figure 6.11d presents the measured CD signal over time between three distinct states: relaxed, left-handed, and right-handed. The wavelength here is fixed at 725 nm. This CD signal clearly describes the cycling between three states of this system. The combination of plasmonics with DNA technology provides a versatile platform for designing active devices and may advance the development of smart probes for life science and biochemistry (Kuzyk et al. 2014; Wang et al. 2016).

In addition, it is important to determine what kind of chiral structures are suitable for practical applications. Since many biologically active molecules and proteins are chiral, bio-inspired and biocompatible chiral devices with performance that is superior to existing technologies are greatly needed. This in turn will significantly advance developments in biochemistry, biophotonics, and other interdisciplinary areas (Wang et al. 2016).

References

- Hendry E, Carpy T, Johnston J, Popland M, Mikhaylovskiy RV, Laphorn AJ, Kelly SM, Barron LD, Gadegaard N, Kadodwala M (2010) Ultrasensitive detection and characterization of biomolecules using superchiral fields. *Nat Nanotechnol* 5:783–787
- Kan T, Isozaki A, Kanda N, Nemoto N, Konishi K, Takahashi H, Kuwata-Gonokami M, Matsumoto K, Shimoyama I (2015) Enantiomeric switching of chiral metamaterial for terahertz polarization modulation employing vertically deformable MEMS spirals. *Nat Commun* 6:8422
- Karaaslan M, Bakir M (2014) Chiral metamaterial based multifunctional sensor applications. *Prog Electromagn Res* 149:55–67
- Kuzyk A, Schreiber R, Zhang H, Govorov AO, Liedl T, Liu N (2014) Reconfigurable 3D plasmonic metamolecules. *Nat Mater* 13:862–866
- Li Z, Mutlu M, Ozbay E (2013) Chiral metamaterials: from optical activity and negative refractive index to asymmetric transmission. *J Opt* 15:023001 (1–13)
- Lindell IV, Sihvola AH, Tretyakov SA, Viitanen AJ (1994) *Electromagnetic waves in chiral and bi-isotropic media*. Artech House Publishers, Boston
- Oh SS, Hess O (2015) Chiral metamaterials: enhancement and control of optical activity and circular dichroism. *Nano Convergence* 2:24 (1–14)
- Panpradit W, Sonsilphong A, Wongkasem N (2011) Chirality control in metamaterials by geometrical manipulation. *2011 Int Conf Electromagn Adv Appl* 2(d):540–543
- Park HS, Kim T-T, Kim H-D, Kim K, Min B (2014) Nondispersive optical activity of meshed helical metamaterials. *Nat Commun* 5:5435 (1–7)
- Pendry JB (2004) A chiral route to negative refraction. *Science* 306:1353–1355

- Rizza C, Di Falco A, Scalora M, Ciattoni A (2015) One dimensional chirality: strong optical activity in epsilon-near zero metamaterials. *Phys Rev Lett* 115:057401
- Tretyakov S, Nefedov I, Sihvola A, Maslovski S, Simovski C (2003) Waves and energy in chiral nihility. *J Electromagn Wave Appl* 17:695–706
- Wang B, Zhou J, Koschny T, Kafesaki M, Soukoulis CM (2009) Chiral metamaterials: simulations and experiments. *J Opt A Pure Appl Opt* 11:114003 (1-10)
- Wang Z, Cheng F, Winsor T, Liu Y (2016) Optical chiral metamaterials: a review of the fundamentals, fabrication methods and applications. *Nanotechnology* 27:412001 (1-20)
- Wiesner U (2016) Metamaterials. https://wiesner.mse.cornell.edu/res_optics.htm. Accepted on November 30, 2016
- Yang Y, da Costa RC, Fuchter MJ, Campbell AJ (2013) Circularly polarized light detection by a chiral organic semiconductor transistor. *Nat Photon* 7:634–638
- Yin X, Schäferling M, Michel A-K U, Tittl A, Wuttig M, Taubner T, Giessen H (2015) Active chiral plasmonics. *Nano Lett* 15:4255–4260
- Zhang S, Zhou J, Park Y-S, Rho J, Singh R, Nam S, Azad AK, Chen H-T, Yin X, Taylor AJ, Zhang X (2012) Photoinduced handedness switching in terahertz chiral metamolecules. *Nat Commun* 3:942
- Zhu Y, Hu X, Chai Z, Yang H, Gong Q (2015) Active control of chirality in nonlinear metamaterials. *Appl Phys Lett* 106:091109

Chapter 7

Plasmonic Metamaterials and Metasurfaces

7.1 Plasmonic Meta-atoms and Their Interactions

Plasmonic metamaterials are based on meta-atoms made from metallic nanostructures whose optical response is governed by the particle plasmon resonances they support. When an electric field is applied to a metallic particle, the conduction electrons are displaced from their equilibrium position with respect to the core ions, causing a polarization of the particle and a depolarizing field that acts as a restoring force. In a time-varying external field, this collective motion can be described as a Lorentzian oscillator, with its characteristic peak in the displacement amplitude (polarizability) around the resonance frequency accompanied by a π phase shift over the spectral width of the resonance. It is this resonant phase behavior that is the basis of many phase gradient metasurface devices (Meinzer et al. 2014).

For very small particles whose dimensions are far below the subwavelength, in particular nanoparticles, the electric field penetrates the whole volume of the particle, polarizing it completely, thereby resulting in a dipolar response whose resonant frequency depends on the material property, particle shape, and its dielectric environment. In other words, plasmon oscillates locally around the particle, and hence it is called localized surface plasmon resonance. Since the electrons are displaced from their equilibrium state, the redistribution tendency of surface charge applies a restoring force on the disordered electrons and results in oscillation with a certain frequency, known as plasmon resonance frequency. Therefore, a field builds up inside the particle while establishing a dipolar field on the outer surface of particle. This has drew attention to plasmonic nanoparticles with strongly enhanced near field around the nanoparticles which considerably increase their absorption and scattering cross section (Hedayati et al. 2014).

On the other hand, when the particle dimensions are larger, retardation becomes important; furthermore, when the size is more than twice the skin depth, the electric field acts primarily on the surface electrons giving rise to higher-order multipole resonances. For these larger particles, the plasmon resonance is even more sensitive

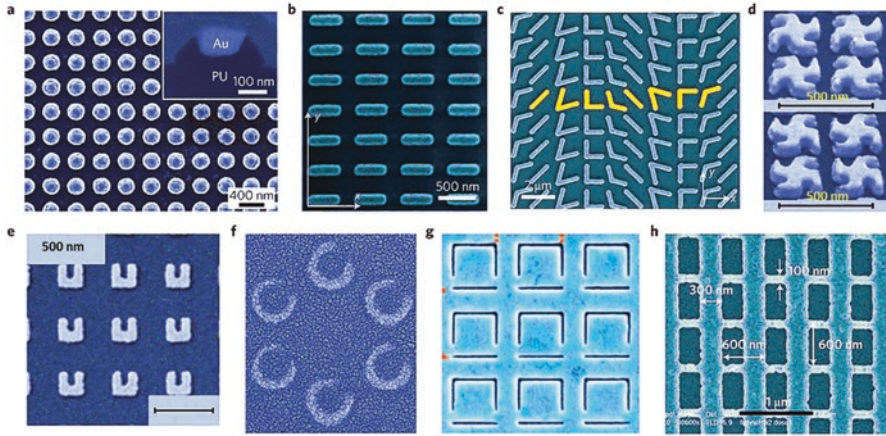


Fig. 7.1 Meta-atoms and metasurface fabrication techniques (Meinzer et al. 2014): (a) nanodisks fabricated by template stripping; (b) rod antennae fabricated by nanoimprint; (c) a metasurface composed of different V-shaped antennae fabricated by electron beam lithography (EBL); (d) double-layer right-handed (*top*) and left-handed (*bottom*) gammadions forming a chiral metamaterial fabricated by EBL; (e) split-ring resonators fabricated by EBL; (f) SRR with an inner diameter of 108 nm and an outer diameter of 188 nm, fabricated by nanosphere lithography; (g) inverse asymmetric SRR fabricated by ion beam milling 25-nm-wide slits into a gold film resulting in a 495×495 nm meta-atom, which is arranged on a square lattice with a period of 731 nm; (h) double fishnet structure fabricated by nanoimprint

to the size and shape of the particle. All these particles can be used to form plasmonic meta-atoms and metasurfaces. Figure 7.1 shows a variety of fabrication techniques that have been used to produce plasmonic meta-atoms and metasurfaces. As shown in Fig. 7.1a, spherical particles exist for ellipsoids for which the resonant frequency further depends on the orientation of the particle, relative to the driving field. Another meta-atom is metal nanorod with subwavelength dimensions (Fig. 7.1b), which, to a first approximation, acts as a dipole antenna that supports a half-wavelength resonance along its principal axis. One can use this basic antenna element to build up more complex meta-atoms. For example, folding a nanorod along its middle creates a V-shaped antenna (Fig. 7.1c) where the two lowest-order eigenmodes in terms of symmetric and antisymmetric charge density distributions. However, the magnetic moment for a V-shaped antenna is weak, and it is more common to use C- or U-shaped split-ring resonators (SRRs, Fig. 7.1e, f). To achieve a negative-index material, fishnet structure (Fig. 7.1h) is formed with long wires to give a metallic response. When two meta-atoms are brought into close proximity, two near-field coupled meta-atoms are coupled dipoles that exhibit hybridization, creating a geometrical asymmetry (Fig. 7.1g). The resulting mode exhibits a very small net dipole moment and couples only weakly to optical fields. Consequently, the associated resonance exhibits low radiative losses and thus a narrow linewidth, making it interesting for sensing applications or for coupling to excitonic materials.

In addition, spatially and spectrally overlapped electric and magnetic field components can be designed to couple, enabling near fields to take on a chiral character (Fig. 7.1d). This can ultimately result in chiroptical far-field effects like optical activity or circular dichroism far stronger than anything observed in natural materials (Meinzer et al. 2014).

Different periodic arrays of plasmonic meta-atoms may result in change to the response (Meinzer et al. 2014): (a) the proximity of nearest neighbors will lead to a change in the field distribution around a particle, thereby altering its polarizability; (b) for arrays of appropriate period, the possibility exists for coherent interactions between many particles, from which new collective modes emerge. When the array period is of order the wavelength of the particle resonance, neighboring particles may interact coherently, leading to collective modes known as surface lattice resonances (SLRs). Array structures that support plasmon modes may be used for light harvesting and harnessed to make light-emitting devices such as LEDs and lasers. Metasurface is an alternative approach dealing with one- and two-dimensional (1D and 2D) plasmonic arrays with subwavelength periodicity. Due to their negligible thickness compared to the wavelength of operation, metasurfaces can (near resonances of unit cell constituents) be considered as an interface of discontinuity enforcing an abrupt change in both the amplitude and phase of the impinging light (Pors and Bozhevolny 2013).

7.2 Plasmonic Metamaterials Implementing Negative Refraction and Negative Refractive Index

Engineering the dispersion of SPPs provides an alternative approach to realize negative refraction and negative refractive index. For instance, there are two bound SPP modes in a two-dimensional (2D) metal–dielectric–metal (MDM) slab waveguide, which originate from the coupling and hybridization of the SPP mode at each individual metal–dielectric interface when the thickness of the dielectric layer is small. For the high-frequency, antisymmetric SPP mode (between the surface plasmon resonance frequency and the bulk plasmon frequency), the dispersion curve exhibits a negative slope, leading to negative group velocity ($v_g = d\omega/dk$). In contrast, the phase velocity ($v_p = \omega/k$) is positive. As a result, the energy and phase fronts propagate in opposite directions; this mode thus behaves as if it has a negative refractive index. On the other hand, the low-frequency, symmetric SPP mode (below the surface plasmon resonance frequency) appears to have a positive refractive index, as its group and phase velocities are simultaneously positive. Utilizing these properties, negative refraction is obtained at visible wavelengths by cascading two MDM waveguides. The Au-Si₃N₄-Ag waveguide is designed to sustain a single negative-index mode, while the Ag-Si₃N₄-Ag waveguide is tailored to support propagation of only positive index modes within the same wavelength range (Fig. 7.2a). The left column of Fig. 7.2b shows the scanning electron microscope (SEM) image of the fabricated structure to demonstrate in plane negative refraction, which was made by

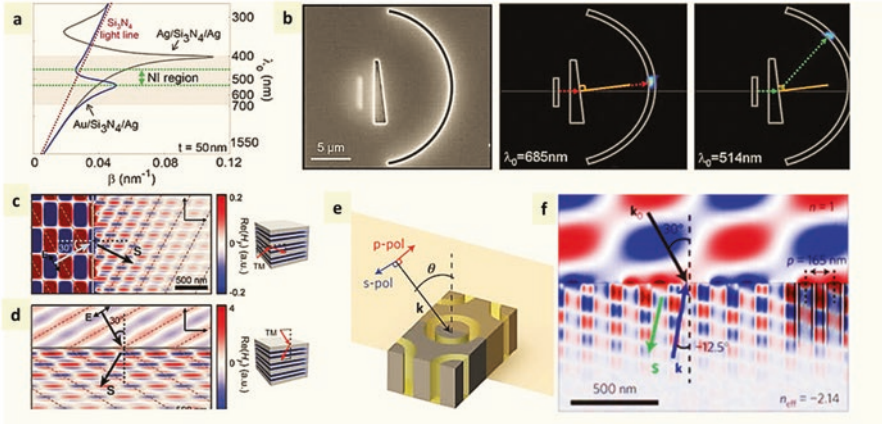


Fig. 7.2 Plasmonic metamaterials implemented negative refraction and negative refractive index (Yao and Liu 2014): (a) dispersion curves for SPPs in an Ag-Si₃N₄-Ag and an Au-Si₃N₄-Ag waveguide when the thickness of Si₃N₄ is 50 nm. (b) Left column—the fabricated device at the output side. Central and right columns—illumination at $\lambda_0 = 685$ nm and 514 nm, showing positive refraction and negative refraction of SPPs, respectively. (c, d) Field plot of the Hy component showing negative refraction of light ($\lambda_0 = 400$ nm), which is incident from air into a 3D metamaterial made of an array of MDM waveguides. The arrows show the unit-cell-averaged direction of the time-averaged Poynting vector. The illuminated interface is normal and parallel to the waveguides in (c, d), respectively. Gray dashed lines indicate incident and refracted wave fronts. (e) Unit cell of a NIM consisting of a hexagonal array of subwavelength coaxial waveguide structures. (f) Negative refraction of light ($\lambda_0 = 483$ nm) at the interface between air and a metamaterial made of an array of Ag-GaP-Ag coaxial plasmonic waveguides. The period of the waveguide array is 165 nm, the thickness of the GaP annular channel is 25 nm, and the inner Ag diameter is 75 nm

applying a sequence of thermal evaporation and focused ion milling steps to both sides of a suspended Si₃N₄ membrane. The input slit at the backside is revealed by electron transparency. In the prism region, the SPPs exhibit negative group velocity for the thickness of the Si₃N₄ equal to 50 nm, while the rest region only sustains SPPs with positive group velocity. The semicircular slit works as an output coupler. At $\lambda_0 = 685$ nm, the position of the output spot indicates positive refraction at the prism's interface with a refraction angle $\theta = +0.1^\circ$. The output-spot position shifts upward when λ_0 is reduced to 514 nm, indicating negative refraction of SPPs with a refraction angle $\theta = 43.7^\circ$. Given the incident angle equal to 7° , Snell's law yields an effective index ratio for SPPs, which is +0.01 and -5.57 at $\lambda_0 = 685$ nm and 514 nm, respectively (Yao and Liu 2014).

By stacking an array of MDM waveguides, a metamaterial can be made with a 3D negative refractive index at visible frequencies. The unit cell is designed as a pair of strongly coupled MDM waveguides, in which eigenmodes resemble even and odd superpositions of the antisymmetric mode in the individual MDM waveguide. The odd superposition exhibits a negative mode wave vector as well as a

negative coupling coefficient, resulting in negative refraction of both phase and energy for the transverse magnetic (TM) polarized light. The constant frequency contour can be almost spherical by tailoring the dielectric layer thickness between the unit cells. Therefore, wave propagation in such a 3D metamaterial can be described by an isotropic negative refractive index. Figure 7.2c and 7.2d show the H_y component when a TM-polarized plane wave ($\lambda_0 = 400$ nm) is incident from air into the metamaterial under two different conditions, that is, from the side and top of the waveguides, respectively. The arrows indicate the calculated time-averaged Poynting vector S , while the gray dashed lines indicate the incident and refracted wave fronts. Not only the wave fronts but also the energy is refracted negatively with $n = -1$ for light incident on both interfaces. In addition to the negative refractive index, near-zero refractive index has also been demonstrated in the planar MDM waveguide and the transformed crescent plasmonic structure in the optical domain (Verhagen et al. 2010; Yao and Liu 2014).

Similar to the planar MDM plasmonic waveguide, a coaxial MDM waveguide geometry can also support an antisymmetric SPP mode that has a negative refractive index (Fig. 7.2e). Moreover, the negative-index mode is accessible from free space, independent on polarization and incident angle. An array of coupled plasmonic coaxial waveguides functions as a NIM working in the 450–500 nm spectral range with a figure of merit $FOM = |\text{Re}(n)/\text{Im}(n)| \sim 8$. Figure 7.2f plots the H_y component for a TM-polarized light ($\lambda_0 = 483$ nm) incident at 30° . The phase front is clearly refracted in the negative direction with an angle of -12.5° with respect to the interface normal, and the wave indeed propagates backward from the finite-difference time-domain (FDTD) simulation (Burgos et al. 2010; Yao and Liu 2014).

In addition, various attempts have been made to achieve isotropic NIMs by utilizing the Mie resonance of core–shell nanostructures. From the Mie theory, a particle can support both electric and magnetic multipolar modes, and the electromagnetic scattering and extinction efficiencies of a particle originate from the contribution from all the modes. The magnetic dipole resonance is generally much weaker than the fundamental electric dipole mode, but it can be significantly enhanced in a structure made of high-permittivity materials, which include semiconductors such as silicon and germanium. Some properly designed core–shell structures exhibit negative refractive indices by overlapping the electric and magnetic resonance within the same spectral range. The metallic core provides the electric plasmon response, while the semiconductor shell is responsible for the strong magnetic resonance with negative permeability. Both core–shell nanowires and core–shell nanoparticles can implement NIMs operating in the near-infrared regime. Because both electric and magnetic responses are obtained from a single constituent, no special requirement is needed for the lattice arrangement of inclusions. In particular, NIMs constructed by core–shell nanoparticles exhibit isotropic and polarization-independent properties, owing to the spherical symmetry of the constituents (Yao and Liu 2014).

7.3 Plasmonic Metasurfaces

Metasurfaces are a kind of 2D metamaterials, which can tailor the in-plane phase front with an extremely thin slab consisting of judiciously designed plasmonic structures. By patterning plasmonic nanostructures and engineering the spatial phase distribution within the metasurfaces, exotic optical phenomena and optical components can be achieved, including negative refraction or reflection, as well as ultrathin focusing or diverging lenses.

Metasurfaces can overcome the challenges encountered in bulk metamaterials, while their interactions with the incident waves can be still sufficiently strong to obtain very useful functionalities. At microwave and terahertz (THz) frequencies, the design of metasurfaces can take advantage of subwavelength metallic resonators such as split-ring resonators (SRRs) and a variety of elements typically used in frequency selective surfaces. Abrupt and controllable changes of optical properties are achieved by engineering the interaction between light and an array of optical scatterers called optical antennas or plasmonic nanostructures, which can take a variety of forms, including metallic or dielectric micro-/nanoparticles, apertures formed in metallic films, and their multilayer structures. The most critical feature of metasurfaces is that they provide degrees of freedom in designing spatial inhomogeneity over an optically thin interface. Arrays of antennas with subwavelength separation between adjacent elements can have spatially varying structural features or material compositions. Thus, metasurfaces are able to introduce a spatially varying electromagnetic or optical response (i.e., scattering amplitude, phase, and polarization) and mold wave fronts into shapes that can be designed at will (Chen et al. 2016).

Therefore, metasurfaces exhibit three unique advantages over bulk metamaterials in controlling light propagation with extraordinary abilities (Yao and Liu 2014): (a) the reduced dimension could also reduce both loss and cost, which arises from ohmic loss of metals and fabrication complexity, respectively. (b) The designs of nanoantennas are diverse, thus, allowing one to adopt different candidates for different applications, where the requirements on wavelength, polarization, and efficiency may vary. (c) The planar metasurface can be readily integrated with other on-chip or quasi-planar optical devices. This is highly desirable for miniaturized photonic systems. Unlike conventional lenses with bulk volume and complex surface curvature, a metasurface-based lens could be ultrathin, flat, and aberration-free.

The physical realization of an interface with continuous phase shifts can be constructed by an array of plasmonic nanostructures with varied geometries and subwavelength separations. Similar to the long-wavelength counterparts of transmission arrays and reflectarrays in frequency selective surfaces, the spatially varied plasmonic nanostructures play the role of resonators to engineer the in-plane phase shifts, which eventually determine the directions of the refracted and reflected beams. Figure 7.3a shows the SEM micrograph of a metasurface consisting of gold nanoantennas with a V shape. By breaking the geometrical symmetry, a V-shaped antenna gives different responses to the different polarization components of the incident light, providing a wide range of degrees of freedom to modify the phase

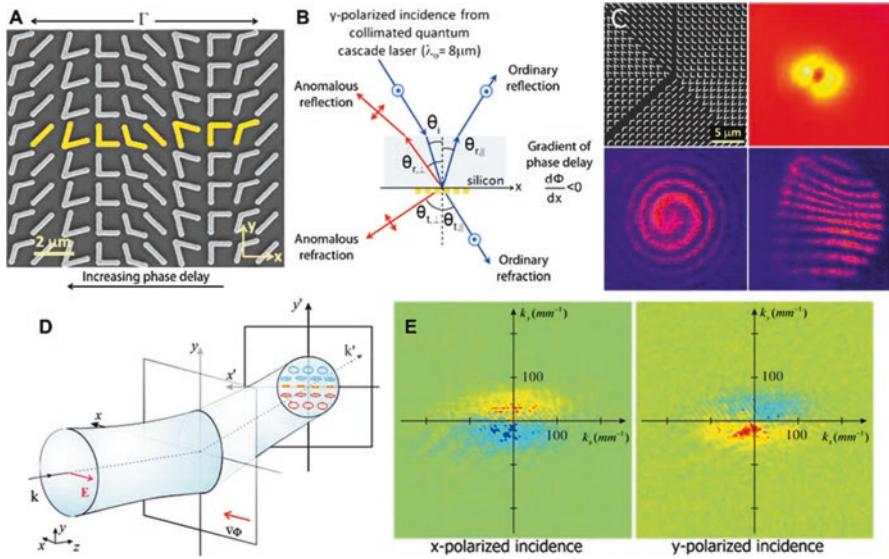


Fig. 7.3 Representative metasurfaces and their phase shifts (Yao and Liu 2014): (a) metasurface consisting of a V-shaped plasmonic nanoantenna array. (b) Metasurface-induced anomalous reflection and refraction, in comparison to the ordinary reflection and refraction. (c) Properly engineered metasurface creates an optical vortex with a topological charge of one. Starting from the top left, the four images in the clockwise direction show the SEM image of the sample, the far-field intensity distribution of the vortex beam, the fringe pattern created by the interference of the vortex and a Gaussian beam tilted with respect to it, and the spiral pattern created by the interference of the vortex and a co-propagating Gaussian beam. (d) Transverse polarization splitting from a metasurface with a phase retardation along the +x direction and (e) its experimental evidence—red and blue indicate the right and left circular polarizations, respectively

distribution and the state of the scattered light at the interface. The V-shaped nanoantennas are arranged periodically along the x direction (period $11 \mu\text{m}$), and the angle between the axis of symmetry of each unit cell and the x -/ y -axis is fixed to be 45° . For an x - or y -polarized incidence, these antennas can provide cross-polarized scattered light, with equal amplitudes and constant phase difference between neighbors along the x -axis. For the scattered light, the cross-polarized component exhibits anomalous reflection and refraction due to the phase discontinuity across the interface, while the other component simply follows the standard laws, resulting in ordinary propagation. Figure 7.3b plots the schematic of an experimental setup with y -polarized incidence (Aieta et al. 2012; Yao and Liu 2014).

Metasurfaces have been used for far-field beam shaping. Because phase shifts are controlled by the arrangement of plasmonic nanoantennas, the wave front of the scattered light can be shaped in an almost arbitrary manner. For example, optical vortices or vortex beams with orbital angular momentum (OAM) can be generated as an optical field propagating with its wave front twisted around the beam axis like a corkscrew, which promises direct applications in detection and optical tweezers

for rotating or trapping small particles. The vortex beams have infinite states characterized by an integer called topological charge, which represents the number of twists of the wave front as light propagates a distance of one wavelength. Because different topological charges correspond to different speeds of information manipulation, vortices are expected to be applied in signal processing such as encoding and multiplexing. The creation of vortex beams is commonly achieved by using spiral phase plates, computer-generated holograms, q-plates, or other modulators, which are bulky and rely on the surface geometry and refractive index profile. In contrast, metasurface can easily generate such beams with a proper phase distribution by patterning nanoantenna arrays. The top left panel of Fig. 7.3c shows an example of the fabricated plasmonic metasurface to create vortex beams at mid-infrared with a topological charge of one. The array is divided into eight sectors occupied by one constituent element each, rendering, in turn, a $\pi/4$ phase delay in the clockwise direction. Using such a structure, vortex beams can be excited upon normal illumination of linearly polarized light. The resulting beam has a uniform intensity except the singularity at the center, which appears as a bright ring in the top right panel. The helical wave front of the vortex is revealed by its interference with copropagating Gaussian beams parallel and tilted with respect to it, as shown by the spiral and fringe patterns at the bottom of Fig. 7.3c, respectively (Yu et al. 2011; Yao and Liu 2014).

In addition to OAM, the spin angular momentum (SAM) is another fundamental property of light. In a circularly polarized light beam, each photon carries a SAM of $\pm \hbar$ directed along the beam axis. Here, \hbar is the reduced Planck constant, and the positive (negative) sign is adopted for left (right) circular polarization. When the light beam is propagating along a curved trajectory, the evolutions of polarization state (spin) and light trajectory (orbital motion) will affect each other. This optical spin-orbit interaction, in analogy to its electronic counterpart, is normally weak, requiring the measurement sensitivity of displacements at the angstrom level. A rapid phase gradient along a metasurface can dramatically enhance the optical spin-orbit interactions when photons pass through the metasurface, giving rise to clearly observable changes to the trajectories of light besides the anomalous refraction along the phase gradient. This is the so-called helicity-dependent transverse displacement or photonic spin Hall effect (SHE). For an incidence of linear polarization, its components of opposite helicities will be split and accumulated at the opposite half spaces of the anomalously refracted beam, as schematically depicted in Fig. 7.3d. Experimentally, the helicity of the anomalously refracted light cannot be observed directly, as shown in Fig. 7.3e (Yin et al. 2013; Yao and Liu 2014).

Another feature of plasmonic metasurfaces is the ability to control optical surface waves, such as SPPs, in the near-field regime. Conceptually, one can manipulate the propagation of light and SPPs with the transformation optics approach as they both obey Maxwell's equations. However, the physical realization of transformation optical devices still relies on either bulk metamaterials or dielectrics in most cases, which leads to intrinsic limitations on the size and cost of the devices. However, metasurfaces can efficiently mold SPPs. When the patterned plasmonic nanostructures of a metasurface interact with light, part of the re-radiative energy is

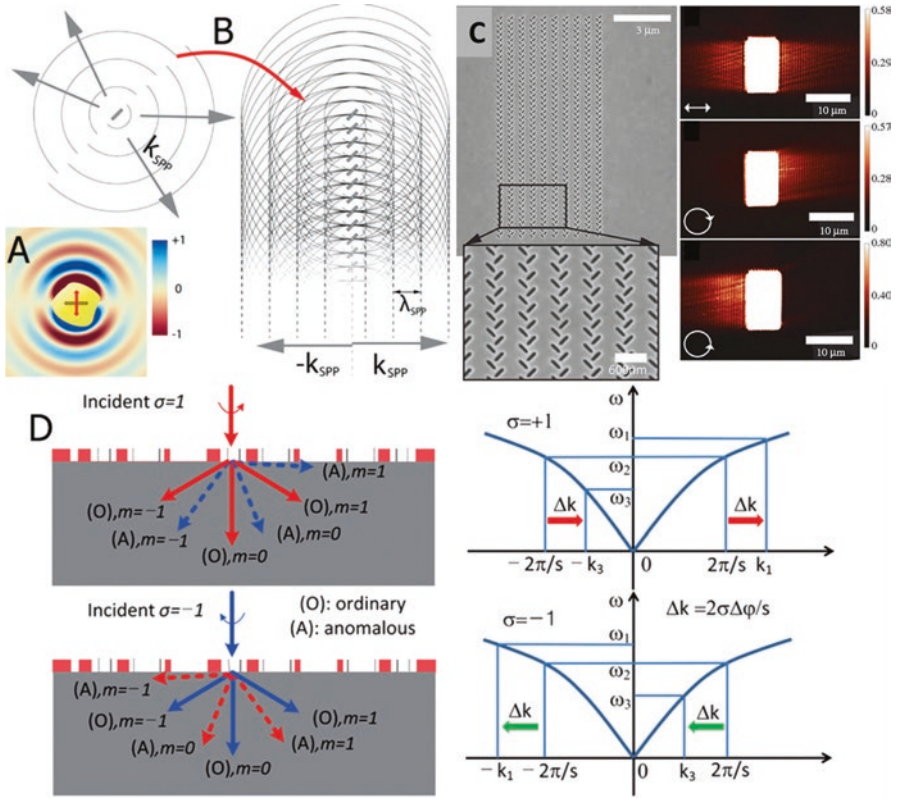


Fig. 7.4 Control of optical surface waves (Yao and Liu 2014): (a) a narrow aperture in a gold film selectively scatters light polarized perpendicular to its orientation. (b) SPPs emitted from an array of closely spaced subwavelength apertures interfere constructively along planes parallel to the column. (c) Metasurface consisting of multiple parallel column pairs enables polarization-controlled directional coupling of SPPs. Linearly polarized light generates two SPP beams symmetrically propagating to both sides of the structure, while in contrast, the right (*left*) circularly polarized light is converted to SPPs propagating to the right (*left*) side of the structure only. (d) Anomalous diffraction of right (*left*) circularly polarized light adds an extra momentum toward the right (*left*), leading to asymmetric excitation of SPPs

converted to SPPs. In other words, the plasmonic nanostructures function as SPP emitters. By controlling the relative phase among the emitters via modifying the geometry of the nanostructures or the polarization state of the incident light, unidirectional excitation of SPPs can be achieved. For example, an aperture array—the complementary structure of the nanoantennas—has been used to excite directional SPPs. As shown in Fig. 7.4a, a single subwavelength aperture milled into a gold film resonantly interacts with light that is polarized along the long axis of the aperture, producing an equivalent dipole oriented along the short axis, as represented by the red arrow in the figure. The dipole excites SPPs, which display a symmetric radiation pattern. Then, in Fig. 7.4b, the SPPs generated from a column of apertures with

the same orientation interfere constructively along the planes parallel to the column, giving rise to plane-wave-like SPPs that propagate symmetrically away from the structure. By placing a second parallel column consisting of apertures oriented orthogonally to those in the first column, the total intensities of the left-going and right-going SPPs can be controlled by the helicity of the incident light and the separation of the two columns of apertures. The left panel of Fig. 7.4c illustrates the SEM image of a metasurface with multiple column pairs to launch polarization-controlled SPPs. The right panels show that a linearly polarized light normally incident from top generates SPP beams of almost equal intensity to both sides of the structure, while in contrast, the right (left) circularly polarized light is converted to SPPs propagating to the right (left) side of the structure only. The different orientations of the apertures between a column pair are essential. Near-field interference can be also induced on a flat interface by a circularly polarized dipole, whose vertical and horizontal component owns an odd and even parity of spatial frequency spectrum, respectively, resulting in an asymmetric profile of SPPs (Lin et al. 2013; Yao and Liu 2014).

An alternative metasurface stemming from the phase discontinuity mechanism consists of an aperture array, which can provide a phase gradient as a dipole antenna array does. This structure is able to control anomalous light propagation depending on the polarization state. When light illuminates on such an interface, the diffraction equation needs to be modified by taking into account the effect of the phase shifts (Yao and Liu 2014):

$$\sin(\theta_t)n_t - \sin(\theta_i)n_i = m\lambda_0/s + \sigma \cdot \lambda_0 \nabla \Phi / \pi \quad (7.1)$$

where θ_t and m are the angle and order of diffractions, respectively, s is the lattice constant of the array, and σ is a coefficient of helicity taking $1/-1$ for the left/right circular polarization. Figure 7.4d compares the ordinary and anomalous refraction and diffraction of two helicities at normal incidence. While the ordinary diffraction orders lie symmetrically about the surface normal, the anomalous ones are shifted sideward together with the refracted light in accordance with the helicity of the incidence. This asymmetric profile enables one side of the array to gain a larger wave vector, which leads to efficient excitation of SPPs. In contrast, the wave vector is smaller on the other side (shifted closer to the light line), and the SPP excitation condition is not satisfied (Huang et al. 2013; Yao and Liu 2014).

Among the growing family of metasurfaces, the symmetry property of nanoantennas is a possible gateway leading to highly efficient plasmonic sources and spin-controlled photonic devices. Hyperbolic metasurface inherits the superior ability of its 3D counterpart in terms of large photonic density of states. Therefore, they are promising for on-chip lasing and quantum information applications. Furthermore, improvements for tunability, loss, and so forth are always needed in plasmonic metamaterials (Yao and Liu 2014).

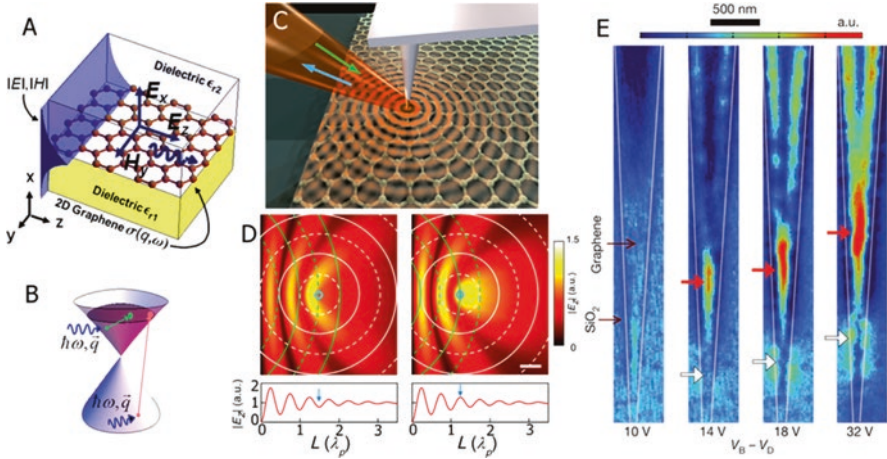


Fig. 7.5 Graphene based plasmonics (Yao and Liu 2014): (a) SPPs in graphene. (b) Electronic band structure of graphene. The green and pink arrows represent the intra- and interband transitions, respectively. (c) Experimental configuration to launch and detect SPPs on graphene based on near-field scanning optical microscopy (NSOM). A sharp metallic tip illuminated by an infrared laser is used to locally excite SPPs, and the near-field SPP signal can be scattered by the tip into the far field and detected. (d) *Top* panels show the snapshots of destructive (*left*) and constructive (*right*) interference of plasmon waves underneath the tip (*blue circles*). The *bottom* panels are the profiles of electric field amplitude underneath the tip versus its distance to the *left* edge. The scale bar is half wavelength of SPPs. (e) Near-field amplitude images showing the switching of graphene plasmons when a backgate voltage is applied. *Red* and *white arrows* denote the positions of resonant local plasmon modes on a tapered graphene ribbon

7.4 Graphene-based Plasmonic Metamaterials

Graphene, a monolayer of carbon atoms arranged in a honeycomb lattice, can support surface plasmons to confine light strongly while potentially maintaining small losses at terahertz and infrared frequencies because of its unique electronic property. Moreover, the mechanical, electronic, optical, and even thermal properties of graphene are highly tunable via chemical doping and electrical gating. These are favorable features for developing graphene-based tunable plasmonics and metamaterials.

Theoretically, surface plasmons can exist in a material with mobile charge carriers whose conductivity is predominantly imaginary. This is equivalent to a material, such as a noble metal, of which the real part of electric permittivity is negative. Graphene is an atomically thin semiconductor, whose electron density, and thus the plasma frequency, is much lower than that of bulk noble metals. As a result, graphene satisfies the requirements of supporting SPPs as a bulk metal does, whereas its operating frequencies reside at terahertz and infrared regimes, much lower than that of metals at visible and ultraviolet. Because of the 2D nature of the platform, graphene surface plasmons exhibit exponential field decay into the surrounding dielectric layers on both sides of the graphene sheet (Fig. 7.5a). Indeed, graphene

plasmonics resemble plasmons in the 2D electron gases (2DEGs) (Hwang and Sarma 2007).

As a zero-gap semiconductor, graphene can be doped to high density of charge carriers by either chemical methods or electrical gating which provides an in situ access to tune the electronic and optical properties of graphene layers. Figure 7.5b illustrates one valley of the electronic band structure of graphene, where the intra- and interband transitions are represented by the green and pink arrows, respectively. A sufficiently high level of doping leads to a larger value of Fermi energy E_F . The absorption of photons with energy less than $2E_F$ is forbidden due to the Pauli blocking. Therefore, doping can suppress the absorption losses introduced by the interband transition and compels SPPs toward higher frequencies. Because the charge carriers in graphene are massless, Dirac electrons and the excitations are essentially confined in the transverse dimension; graphene plasmons are expected to provide much smaller wavelengths (about 200 nm at infrared frequencies) and thereby much stronger light–matter interaction. Such an exceptional confinement is not possible in conventional SPPs supported by noble metals at the same frequency range. Direct spatial mapping of graphene plasmons has been performed based on the scattering-type near-field scanning optical microscopy (NSOM) at infrared frequencies. High-resolution imaging of the real-space profiles of propagating and standing surface plasmons are achieved. Figure 7.5c shows the configuration of the experimental setup. Plasmons with high in-plane momenta are excited by illuminating a sharp atomic force microscope (AFM) tip with a focused infrared beam, as indicated by the green arrow. The near-field amplitude profiles are obtained from the backscattered light beam (blue arrow). Various characteristics of SPPs can be observed from the resulting images. For instance, the plasmon interference patterns are given by the simulated near-field amplitude profiles in Fig. 7.5d. Because of the presence of the graphene/substrate boundary at $L = 0$, interference occurs between the tip-launched plasmons (white circles) and the reflected plasmons (green circles), giving rise to different standing wave patterns when the tip is located at a different distance from the edge, as denoted by the blue circles and arrows, respectively (Fei et al. 2012).

A unique property of graphene plasmonics is that the plasmon wavelength is determined by the carrier density, implying that the characteristics of graphene plasmons can be tuned and sophisticated functionalities achieved by simply varying the gate bias. Figure 7.5e shows the plasmonic switching by electrical gating, where tapered graphene ribbons are deposited on a SiO_2 substrate with a Si backgate. With a sufficiently large and increasing backgate voltage V_B , which causes larger carrier density and Fermi energy, the two local plasmon modes shift toward regions with a larger ribbon width due to the corresponding increase in plasmon wavelength. Therefore, graphene gate can be effectively tuned and the graphene plasmonics can be used to control and switch optical signals at the nanoscale (Chen et al. 2012; Yao and Liu 2014).

In addition to doping and gating, geometry patterning is an alternative approach to tune the optical properties of graphene, rendering a variety of graphene-based plasmonic and metamaterial structures at infrared wavelengths. As a representative

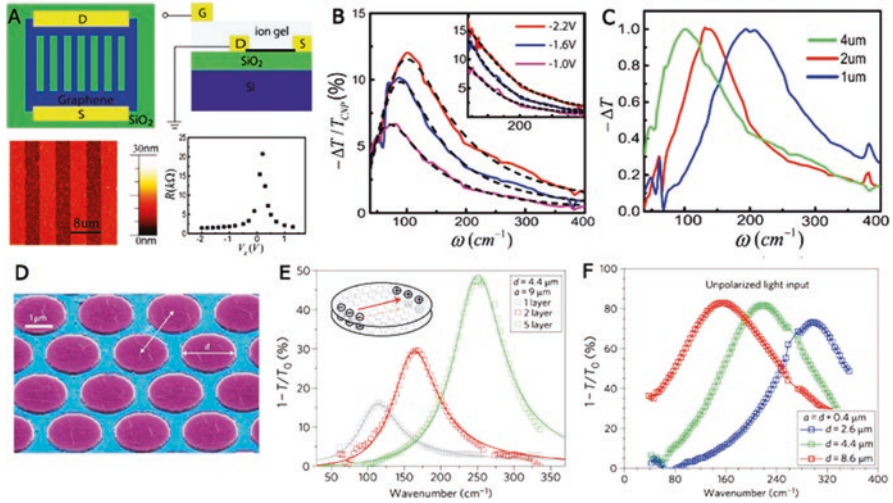


Fig. 7.6 Graphene-based metamaterials and metadevices (Yao and Liu 2014): (a) graphene microribbon array. Four panels in the clockwise direction show the top-view, side-view, gate-dependent electrical resistance trace, and the AFM image of a sample with the grapheme ribbon width of 4 μm and the period of 8 μm . (b) Control of the absorption of graphene plasmons via electrical gating. The graphene ribbon array is the same as in (a), and the polarization is perpendicular to the graphene ribbon. For comparison, the inset shows the corresponding spectra for terahertz radiation polarized parallel to ribbons. In this case, the absorption strength increases with carrier concentration (bias voltage), but the spectral shape remains the same. (c) Spectra of change of transmission with different microribbon widths (1, 2, and 4 μm). (d) SEM image and (e) extinction spectra of patterned graphene/insulator stacks with varied numbers of graphene layers. (f) Tunable terahertz filters using stacked graphene devices with different diameters of the stack. The total number of graphene layers is fixed at five

example, a gated graphene microribbon array is shown in Fig. 7.6a. The widths of ribbon and gap are identical and varied from 1 to 4 μm , which is much smaller than the wavelength of incidence and enables efficient excitation of plasmon resonances. Owing to the anisotropic nature of configuration, the microribbon array responds differently to incident light with polarization perpendicular and parallel to the ribbons. In Fig. 7.6b, the spectra of perpendicular polarization exhibit a distinctly different Lorentz line shape because the plasmon excitations correspond to carrier oscillations across the width of microribbons. While the carrier concentration n increases with increasing gate voltages, the absorption peak not only gains strength but also shifts to a higher energy, in accord with the $n^{1/4}$ scaling signature of massless Dirac electrons (Fig. 7.6b). For comparison, the inset of Fig. 7.6b depicts the absorption spectra for parallel polarization at three different gate voltages. In this case, the optical response originates from mobile charge carrier oscillation similar to that in a graphene monolayer, which can be described by Drude model and changes only in amplitude with increasing gate voltage. In both cases, the absorption at plasmon resonances reaches the level of over 12% for gate voltage greater

than 2 V. Compared with the 2.3% absorption by a single layer of pristine graphene, such a substantial absorption implies strong light plasmon couplings in the patterned graphene ribbons. For polarization perpendicular to the ribbons, changing the width of the ribbon is an alternative way to tune the plasmon resonance frequency. Figure 7.6c shows the change of normalized transmission with different ribbon widths w , in which the carrier concentration is fixed to be $1.5 \times 10^{13} \text{ cm}^{-2}$. Theoretical derivations based on quasi-static description suggest that the plasmon resonance scales as $w^{-1/2}$, a characteristic behavior of 2DEGs. Further engineering, such as broadening the ribbon width and adjusting the filling ratio, can be performed to achieve tunable plasmon resonance ranging from 1 to 10 THz. The strong dependence of polarization may not be a desirable property in practical applications. Graphene/insulator stacks, in a circular shape and arranged in a high-symmetry order, can circumvent such a disadvantage. More importantly, the number of the stacked layers significantly influences the plasmonic resonance frequency and amplitude. Figure 7.6d shows the SEM image of an array of microdisks arranged in a triangular lattice, where two parameters, the diameter of disks d and the lattice constant a , determine the configuration of the stack array in the transverse dimension. In Fig. 7.6e, the extinction spectra of the samples are plotted for one-, two-, and five-layer samples, respectively. With the increasing number of graphene layers, both the resonance frequency and peak intensity increase significantly because of the strong Coulomb interaction between adjacent layers, which is drastically different from the simple addition of carrier concentration in conventional 2DEG lattices. On the other hand, unlike resonances in graphene monolayer owning a weak $n^{1/4}$ carrier density dependence, plasmons in the stack structure show a strongly enhanced dependence on carrier concentration. The resonance amplitude and frequency are proportional to n and $n^{1/2}$, respectively. The latter scale stands for conventional 2DEGs. As a result, the resonance frequency and amplitude of the graphene plasmons can be effectively tuned in the stacked microdisks, promising great potential in THz photonic applications (Ju et al. 2011; Yan et al. 2012).

By adjusting the in-plane geometrical parameters while maintaining a large filling factor, which is defined as microdisk area over total area, a peak extinction as high as 85% can be achieved (red curve in Fig. 7.6f). The device functions as a tunable, polarization-independent plasmonic notch filter, and the peak value in the spectra corresponds to an extinction ratio of ~ 8.2 dB. Because of the extraordinary electronic properties and great tunability, graphene is regarded as a competitive candidate for many applications, such as absorbers, nanoantennas, and waveguides. To further improve the performance of graphene-based devices, besides manipulation on graphene itself, like gating and patterning, the hybridization of graphene and other conventional plasmonic nanostructures or metamaterials can be used to generate a wide range of tunable optical devices at terahertz and infrared frequencies (Yan et al. 2012; Yao and Liu 2014).

Consequently, the combination of graphene physics and plasmonics generates a versatile new platform for applications in the terahertz and optical regime. By maintaining the advantages of conventional plasmons, graphene-based devices are able to improve the performance of nanoantennas, broadband absorbers, and (bio)

chemicals, while by keeping the ultrathin and highly tunable properties, they also have the potential to be used as building blocks of new emerging materials, such as hybrid metamaterials and metasurfaces (Yao and Liu 2014).

7.5 Self-assembled Plasmonic Metamaterials

Nanoscale self-assembly of metallic nanoparticles with a variety of shapes (such as sphere, rod, cube, plate, pyramid, star, cage, core-shell, etc.) can be achieved through optimized wet chemical synthesis techniques. As shown in Fig. 7.7, the geometry, facet, or even inner structure of the nanoparticles could be rationally controlled, providing a complete, ingenious toolbox to construct complex metamaterials (Tan et al. 2011). The interactions between nanoparticles, in addition to their size and shapes, play an important role in the resulting self-assembled geometry. These interactions include van der Waals forces, electrostatic forces, capillary forces, and molecular surface forces after decorating the surface of nanoparticles with various chemical functionalities. The magnitude and direction (i.e., attractive or repulsive) of these forces as well as their working distances (i.e., long range or short range) are distinctly different. The intricate balance of these interactions gives

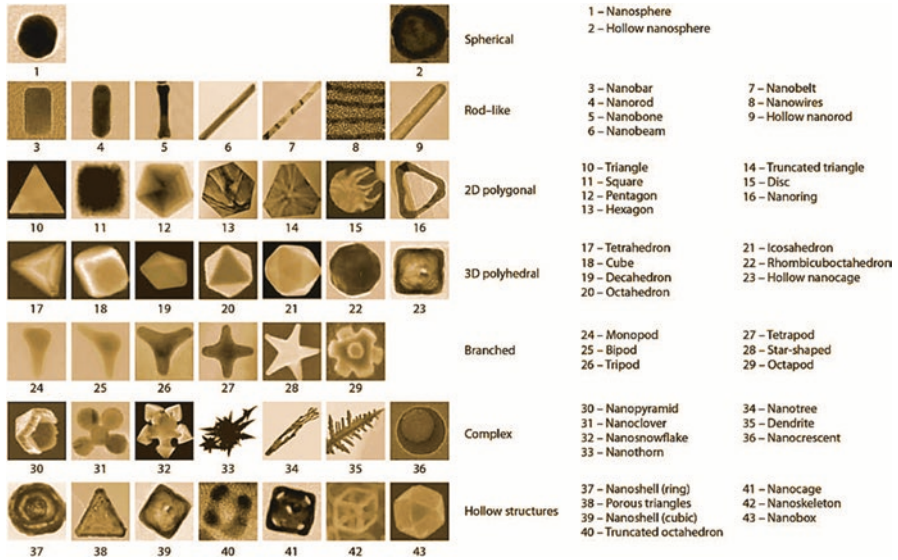


Fig. 7.7 Metallic nanoparticles in different shapes, dimensions, and geometries, which serve as building blocks to self-assemble plasmonic metamaterials. The geometric order of the nanoparticles gradually increases from left to right in each row in terms of aspect ratios, number of sides, facets, or branches (Tan et al. 2011)

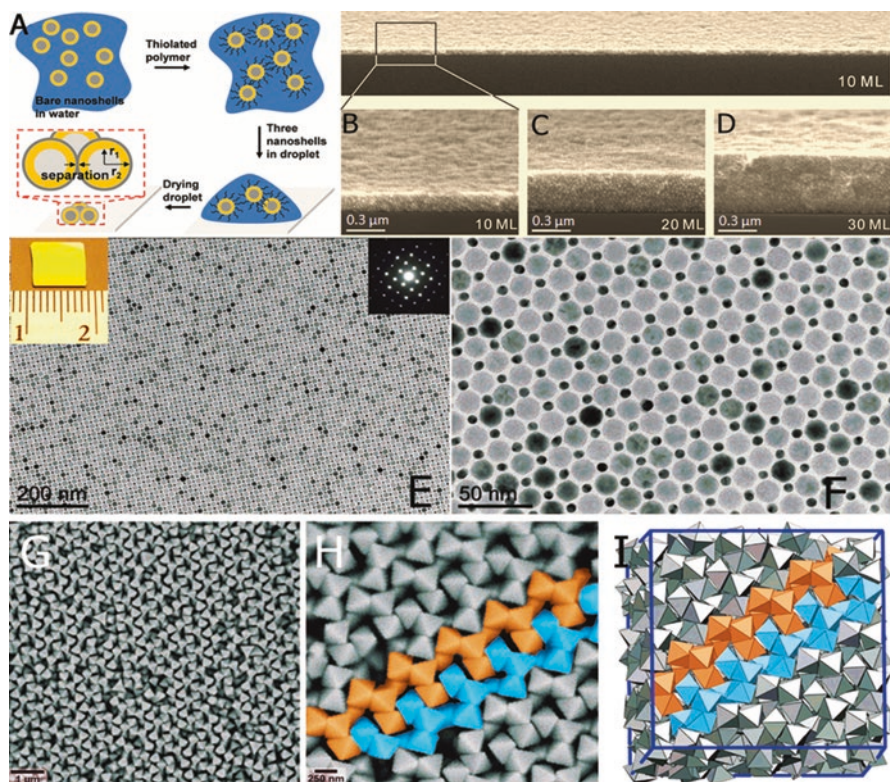


Fig. 7.8 Self-assemble plasmonic metamaterials (Yao and Liu 2014): (a) procedures to assemble plasmonic clusters. (b–d) SEM micrographs of layer-by-layer assembled 3D supercrystals made of Au nanoparticles (diameter 6 nm). (e) TEM image of an AB-type binary superlattice monolayer self-assembled from 16.5 nm Fe_3O_4 and 6.4 nm Au nanoparticles. The upper left inset shows a photograph of a SiO_2/Si wafer coated with such a superlattice, and the upper right inset shows the small-angle electron diffraction pattern. (f) High magnification TEM image of the monolayer in (e). (g–i) Self-assembled Ag octahedral. (g) SEM micrograph showing the octahedron supercrystal. The lattice consists of tetramer motifs (h) and forms spontaneously in Monte Carlo simulations of octahedra with depletion attractions (i)

rise to the spontaneous organization of nanoparticles into a relative stable structure at a thermodynamic equilibrium state, where the Gibbs free energy of the entire system is minimum (Yao and Liu 2014).

Figure 7.8a shows the polymer-coated nanoshells are assembled into clusters by slowly drying a droplet of the core–shell nanoparticles on a hydrophobic substrate. A trimer, consisting of three core–shell nanoparticles, supports a magnetic dipole mode that originates from the induced in-plane current loop. A 3D tetrahedral cluster can support isotropic magnetic resonances. Furthermore, Fano resonance is observed in a heptamer plasmonic cluster that is composed of seven identical elements. The overall dipole moment of the outer hexagon is similar in magnitude but

opposite in sign with respect to the dipole moment of the central core–shell nanoparticle, leading to strong destructive interference of their radiating fields and the asymmetric line shape (Fan et al. 2010; Yao and Liu 2014).

DNA-guided assembly is an alternative, viable method for controllable arrangement of nanoparticles of different size and composition. The unique and specific Watson–Crick base pairing of DNA, that is, adenine–thymine (A–T) and guanine–cytosine (G–C), offers systematically and precisely programmable hydrogen bonding. The length and the mechanical strength of DNA strands can be finely and widely tuned over a large range. All of these merits enable DNA as a superior interface to regulate the interactions between nanoparticles and produce desired self-assembly hierarchy with judicious structural and sequence design. Moreover, DNA-origami technique even allows pattern designs in an almost arbitrary manner. The key is to use specific short single-stranded DNA as “staple” to direct the folding of a long single strand into the desired shape (Rothmund 2006; Yao and Liu 2014).

For large-area self-assembled plasmonic metamaterials, different approaches have been developed. Figure 7.8b–d show a method for synthesizing 3D plasmonic crystals over an area $> 1 \text{ cm}^2$ consisting of gold and silver nanoparticles. Janus nanoparticles, which have solvent-phobic top surface and solvent-philic bottom surface, form close-packed monolayers based on layer-by-layer (LbL) assembly from suspensions of thiolate-passivated gold or silver colloids. Such plasmonic crystals exhibit strong transverse (intralayer) and longitudinal (interlayer) near-field coupling. Furthermore, large-area superlattices with two or three types of nanostructures promise a new route for designing metamaterials with rationally tunable properties by adjusting the chemical composition, size, and stoichiometry of the constituents. Figure 7.8e, f show the self-assembly and transfer of macroscopic, long-range ordered superlattices made of binary or ternary nanocrystals using the liquid–air interfacial assembly approach, which result in monodisperse Ag nanocrystals with well-defined polyhedral shapes, including cubes, truncated cubes, cuboctahedra, octahedra, and truncated octahedra. The particle shape provides an additional handle to twist the structure of assembled patterns, when the polyhedra are self-assembled into long-range ordered superstructures. In addition, monodisperse Ag polyhedra, coated with polyvinylpyrrolidone (PVP), assemble into large, dense supercrystals by gravitational sedimentation. Unlike cubes and truncated octahedra, octahedra in their densest lattice packing show only incomplete face-to-face contact, and the equivalent faces of neighboring octahedra either do not lie in a common plane. Unadsorbed PVP polymer in solution will induce attractions between particles, leading to new structures that are not governed solely by packing efficiency of hard shapes. As shown in Fig. 7.8g, h, a lattice of octahedra with intriguing helical motifs is generated, if extra PVP is added to the solution immediately before sedimentation. Higher amounts of PVP result in less Minkowski lattice and more helical lattice. This characteristic is confirmed by Monte Carlo simulation (Fig. 7.8i). The large degree of face-to-face contact in the latter reflects significant attractive forces (Dong et al. 2010; Henzie et al. 2011).

7.6 Application Perspective

7.6.1 Optical Nanocircuits and Nanoantennas

7.6.1.1 Optical Nanocircuits

In electronics, basic functionalities are synthesized by “lumped” circuit elements, such as resistors, inductors, capacitors, and transistors; and more complex operations are obtained by combining them in large circuits. The metatronics—metamaterial-inspired optical circuitry—aims at similarly modularizing the nanoscale optical response with “lumped optical nanocircuits,” providing the necessary concepts to move upward in the “design stack” from the level of nanoparticles and nanoclusters to more complex nanophotonic devices and systems (Monticone and Alù 2014).

At the basis of this modularization is the concept of optical impedance, which is defined, for a subwavelength nanoparticle, as the ratio of the local potential difference $V = |\mathbf{E}| l$ and the flux of displacement current $I_d = -i\omega\epsilon_0\epsilon |\mathbf{E}|S$ through the nanoparticle, where \mathbf{E} is the local electric field vector, l the length of the nanoparticle along the electric field, S its transverse cross section, and ϵ its relative dielectric constant. The optical impedance so defined is an intrinsic characteristic of the nanoparticle, independent of the surrounding environment, similar to its electrical counterpart. Therefore, a dielectric nanosphere of radius a corresponds to a nanocapacitance (Monticone and Alù 2014):

$$C_{sph} = \pi a \epsilon_0 \text{Re}[\epsilon] \quad (7.2)$$

whereas a plasmonic nanosphere is modeled as a nanoinductance (Monticone and Alù 2014):

$$L_{sph} = \left(-\omega^2 \pi a \epsilon_0 \text{Re}[\epsilon]\right)^{-1} \quad (7.3)$$

For a lossy particle, an equivalent nanoresistor is also added. The optical response of a subwavelength plasmonic nanosphere can then be quantitatively predicted by the simple nanocircuit model shown in Fig. 7.9a (right), composed of a nanoinductor representing the particle, connected in parallel with a nanocapacitor associated with the surrounding dipolar fringe fields ($C_{\text{fringe}} = 2\pi a \epsilon_0$), all driven by a current source representing the applied field. The nanocircuit model correctly predicts the occurrence of a resonance for subwavelength plasmonic particles, as the nanoinductor resonates with the capacitive fringe fields; conversely, small dielectric particles cannot resonate due to their purely capacitive optical impedance.

Optical nanocircuits obey Kirchoff’s circuit laws if retardation effects can be neglected (quasi-static regime), allowing to directly translate and transplant the simple and elegant design rules of electrical circuits to optical frequencies. Moreover, the interplay of scattering zeros and poles in plasmonic structures, which

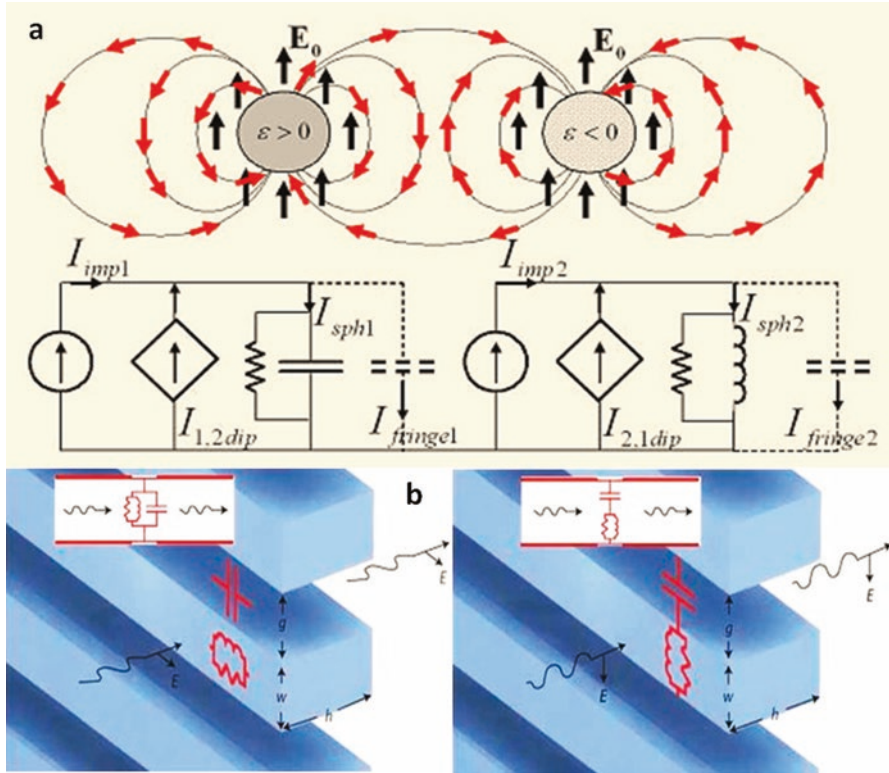


Fig. 7.9 Optical lumped nanocircuits (Monticone and Alù 2014): (a) optical nanocircuit models of a dielectric (left) and a plasmonic nanoparticle (right). Black arrows denote the incident electric field, whereas red arrows represent the electric dipolar fringe field from the nanospheres. (b) Subwavelength grating of parallel plasmonic rods realizing a 2D optical nanocircuit with stereo functionality, namely, the incident field polarization (or direction) selects the effective optical connection (series or parallel) between the nanoelements

determines anomalous scattering effects, finds a natural framework in the context of optical nanocircuits. Indeed, introducing new independent reactive elements in a circuit, such as new nanoparticles in a cluster or array, increases the order of the circuit and adds new complex zeros and/or poles to its response. By suitably designing the position of these zeros and poles on the complex frequency plane, following well-established design rules of electrical filters, it may be possible to implement advanced filtering functionalities at optical frequencies (e.g., Chebyshev or Butterworth filters) based on lumped nanocircuit elements (Pozar 2011).

As shown in the 2D optical nanocircuit of Fig. 7.9b, different incident illuminations select different effective optical connections between the nanoelements of this “stereo-nanocircuit,” which may be exploited for parallel processing of multiple flows of information through a single nanostructure. Optical nanocircuit concepts have also been used in the design and tuning of optical nanoantennas and

metasurfaces and have provided useful physical insights to model several composite nanostructures, including circuit-based microcavity lasers, nanoparticle clusters, and nanorings, as well as to envision all-optical metamaterial circuit boards (Alù and Engheta 2009; Walther et al. 2010).

7.6.1.2 Optical Nanoantennas

Plasmonic optical antennas are defined as devices able to efficiently couple localized sources or guided waves at the nanoscale to far-field radiation and, by reciprocity, to convert the impinging radiation from the far field into subwavelength localized or guided fields. Due to their plasmonic nature, however, optical nanoantennas exhibit novel and interesting phenomena not encountered at lower frequencies. In fact, as frequency increases above the GHz range, into the THz region and beyond, the conduction properties of metals change dramatically, due to the finite electron density of states and their significant kinetic inductance that cause the electrons to respond to electromagnetic excitation with increasing phase lag, introducing a frequency-dispersive permittivity (typically Drude dispersion) with small negative real part, and associated plasmonic effects. As a result, the fields penetrate the plasmonic nanoantennas inducing a flow of displacement current $\mathbf{J}_d = -i\omega\mathbf{D} = -i\omega\epsilon_0\epsilon\mathbf{E}$, which, at sufficiently high frequency, becomes dominant over conduction effects. The plasmonic modes of the nanoantenna guide the oscillating displacement current, leading to extreme field enhancement and localization, which can be exploited to boost weak optical nonlinearities and enhance spontaneous emission from quantum dots and fluorescent molecules. Generally, a vast range of applications may largely benefit from the strong and peculiar light–matter interactions enabled by plasmonic nanoantennas, including solar energy harvesting, infrared absorbers for thermal detectors, wireless on-chip communications, as well as optical microscopy, spectroscopy, and sensing (Biagioni et al. 2012; Monticone and Alù 2014).

Despite the relevant differences between RF and optical frequency ranges, the theoretical background and antenna concepts established at RF can be at least partially applied to the design and modeling of optical nanoantennas. The concept of optical impedance of a plasmonic nanoantenna also developed within the framework of optical nanocircuit theory. The design and operation of a plasmonic nanoantenna can use the concept of optical impedance, which allows tuning and matching the nanoantenna in analogy to an RF radiator. Consider a linear dipole antenna, formed by two linear arms separated by a small gap (Fig. 7.10a, b). Its radiation/scattering properties and frequency response can be systematically optimized and tuned by using proper “loading” techniques. As depicted in Fig. 7.10a (left), a linear RF antenna is loaded at its gap with lumped circuit elements that, by changing the antenna input impedance, allow to operate at a given frequency or to achieve a good match to a specific feeding network, without the need of modifying the antenna’s physical properties, such as its length. Optical nanocircuits open the same possibilities for optical nanoantennas (Fig. 7.10a, right), fully translating the systematic design methodologies of conventional low-frequency radiators. The complex optical

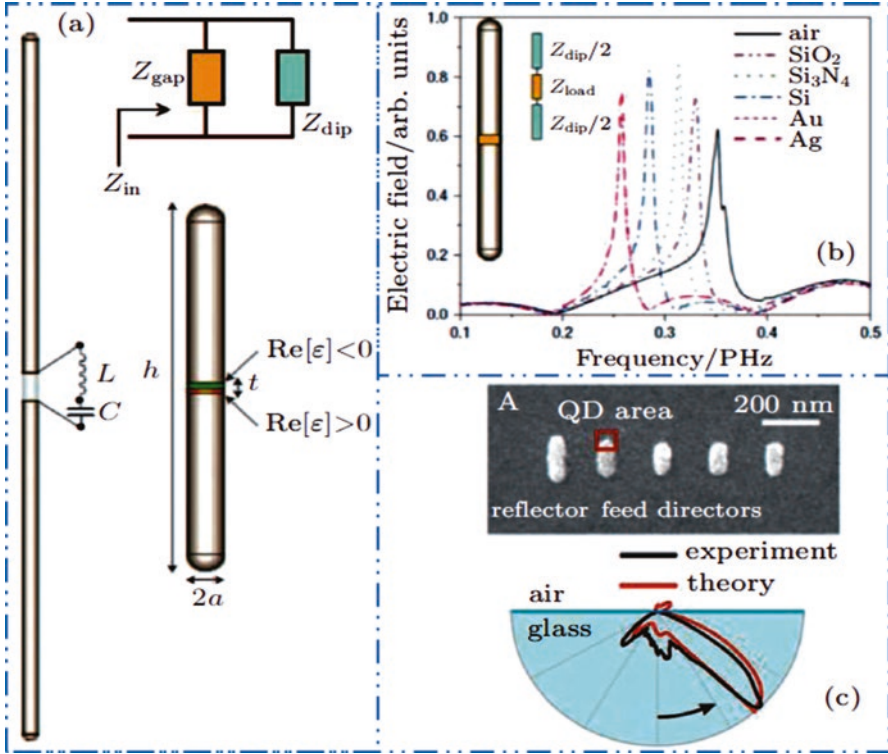


Fig. 7.10 Optical lumped nanoantennas (Monticone and Alù 2014): (a) RF dipole antenna (*left*) loaded with lumped circuit elements at its feeding gap and, analogously, a plasmonic dipole nanoantenna (*right*) loaded with optical nanocircuits. The *top inset* shows the circuit model of the antenna input impedance. (b) Tuning of the nanoantenna resonance by “gap loading” with different realistic materials. (c) Example of advanced optical nanoantenna: Yagi-Uda nanoarray (SEM image) driven by a quantum dot, exhibiting a highly directional radiation pattern (*bottom panel*)

input impedance of the nanoantenna, $Z_{\text{in}} = R_{\text{in}} - iX_{\text{in}}$, is defined, within the framework of optical nanocircuit theory, as the ratio of the applied voltage at the gap and the induced flux of displacement current across the dipole terminals (R_{in} and X_{in} represent, respectively, the antenna input resistance and reactance). As sketched in the inset of Fig. 7.10a, this input impedance can be interpreted as the parallel combination of the dipole intrinsic impedance Z_{dip} and the gap impedance Z_{gap} . While the former is assumed to be a fixed property of the nanoantenna geometry and surrounding environment, the latter can be engineered to a large extent by loading the gap with different materials. For a cylindrical gap of height t , radius a , and permittivity ϵ , excited by an electric field parallel to its axis, the gap impedance is given by (Monticone and Alù 2014):

$$Z_{\text{gap}} = \frac{it}{\omega\epsilon_0\epsilon\pi a^2} \quad (7.4)$$

which is inductive (capacitive), for negative (positive) values of $Re[\varepsilon]$. Therefore, by filling the gap with dielectric or plasmonic materials or their proper series or parallel combination, the input impedance of the nanoantenna can be tailored to a large degree, based on this nanocircuit model. In analogy with RF radiators, it is possible to tune the resonance of the nanoantenna at the desired frequency ω_0 by properly designing the nanoload such that the overall reactance is compensated, i.e., $Im[Z_{\text{gap}}(\omega_0)] = -Im[Z_{\text{dip}}(\omega_0)]$, as shown in Fig. 7.10b. Besides, the nanoantenna input resistance at resonance can also be fully controlled, which determines the impedance matching of the nanoantenna to a given feeding system, such as an optical transmission line or a quantum dot, maximizing the power delivered to the far field from nanoscale sources and vice versa (Alù and Engheta 2009).

Nanoantennas composed of a single nanoparticle or paired elements (e.g., nanodimers, nanobowties) are electrically small and, therefore, exhibit a weakly directive radiation pattern (with directivity of about 1.76 dB, typical of small dipole antennas) and a dominant electric dipole response. In order to increase the directivity of the emitted radiation and design a more interesting scattering response, collections of several closely spaced nanoparticles can be considered. For example, clusters and rings of plasmonic nanoparticles can be designed to tailor the flow of displacement current, supporting higher-order multipolar scattering patterns and tailored interference between plasmonic modes. This results in a more interesting temporal and spatial response of plasmonic nanoantennas, with moderately directive radiation patterns and sharper scattering resonances. A particularly interesting example of optical nanoantenna is the

Yagi–Uda array configuration in Fig. 7.10c. Drawing inspiration from its popular RF counterpart, the design consists of a nanoantenna element driven by a localized optical source (e.g., a quantum dot), whose radiation is then directed and shaped by the neighboring parasitic nanoelements. The resulting radiation pattern has much higher directivity compared to individual nanoantennas, particularly appealing for enhanced radiation from single-photon quantum sources, with potential for narrow-angle beam steering of nanoscale optical emission. In addition, very large arrays of nanoantennas are particularly well suited to realize three-dimensional (3D) metamaterials and two-dimensional (2D) metasurfaces, as their very short resonance length is ideal to achieve strong resonant optical response at the nanoscale while keeping a deeply subwavelength separation between neighboring elements. The very small array period prevents the onset of grating lobes, realizing a locally homogeneous effective response that enables anomalous optical effects (Novotny 2007; Monticone and Alù 2014).

7.6.2 Functional Metasurfaces

Metasurfaces have many different applications depending on their constitutive materials and geometry. Nevertheless, all metasurface-based devices can be classified as broadband, wideband, and narrowband according to their frequency

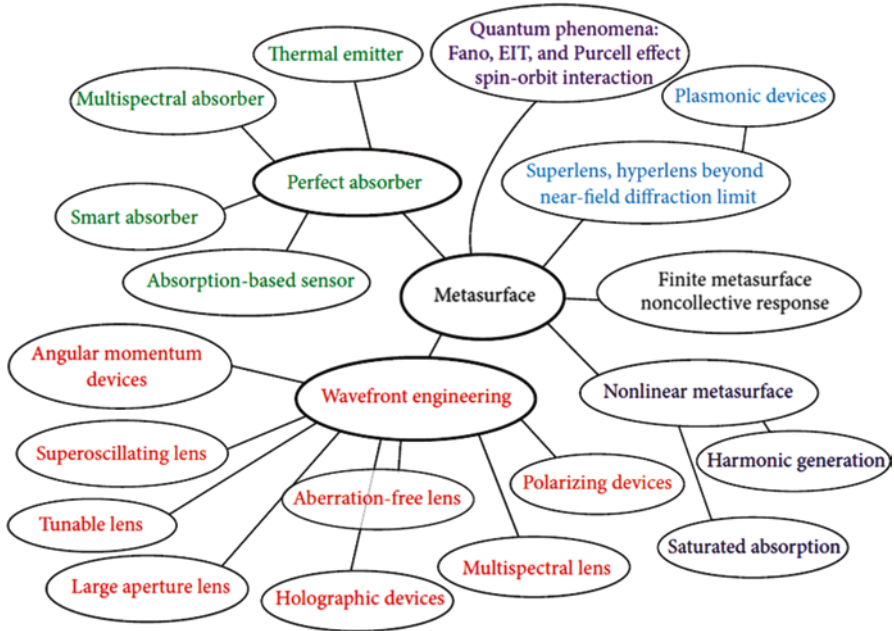


Fig. 7.11 Application perspective and future trends of metasurface and metadevices (Luo et al. 2015)

responses. The typical case of narrowband application is the Fano resonance. One of the most important aspects of Fano resonance is the sharp resonance peak accompanied with strong local field enhancement, which is the basis of many applications, such as biological sensing and nonlinear photonics. For broadband and multiband applications, the dispersion of metasurface can enable superresolution imaging beyond the diffraction limit, high-performance color filter, broadband absorbers, and polarizers. Wideband metasurfaces can be used in many applications such as reflect array antennas, beam-steering antennas, radar cross-section reduction, and electromagnetic cloaking (Luo et al. 2015; Li et al. 2016).

Figure 7.11 shows current application perspective and future trends of metasurface and metadevices. In general, functional metasurfaces need better performances. For example, current flat lenses suffered from the strong chromatic dispersion. Although these devices are thin, lightweight, and capable of working at a wide range of frequencies, the focus lengths would vary as the change of operational wavelength. Another drawback of these metasurfaces is that efficiencies are typically very low, especially for the devices based on geometric phase. In addition, another huge challenge for the successful application of metasurfaces is how to fabricate large-area metasurfaces fast and low cost (Luo et al. 2015).

7.6.3 Plasmonic Metamaterials for Sensing

Plasmonic metamaterials and metasurfaces exhibit unique features of tight field confinement and strong field enhancement and are very sensitive to the changes of refractive index of the dielectric media in the vicinity of metal structures. As a result, they can be used to design miscellaneous structures for sensing purposes through which observable changes of corresponding quantities, such as a shift in resonance, a variation in field intensity, or an offset in angle, are expected. Therefore, plasmonic metamaterials and metasurfaces not only provide a label-free, real-time access to probe biological components at nanoscales but also lead to an extremely high resolution. Both propagating and localized SPPs have been applied for biochemical or biomedical applications. They each have unique advantages while facing their own problems. For approaches based on propagating SPPs, a detection sensitivity exceeding 10^{-5} refractive index units (RIU) has been achieved. However, this target is still challenging for analytes with very small size or selective nanoarchitectures. As to localized SPPs, by altering the size, shape, and chemical components of the plasmonic structures, a device of this kind owns great tunability and adaptability, whereas it suffers a sensitivity of at least one order of magnitude lower (Yao and Liu 2014).

Plasmonic metamaterials hold a new promise for biosensing with unprecedented sensitivity and specificity. On one hand, it inherits the feature of metamaterials that the operation frequency can be widely tuned to bind the characteristic vibrations of biomolecules, and the spectral line shape can be engineered to be very sharp to obtain higher sensitivity. On the other hand, the plasmonic nanostructures serve as building blocks to keep the merit in adaptability, ensuring that the device satisfies the selective requirements in different applications (Tetz et al. 2006; Yao and Liu 2014).

References

- Aieta F, Genevet P, Yu N, Kats MA, Gaburro Z, Capasso F (2012) Out-of-plane reflection and refraction of light by anisotropic optical antenna metasurfaces with phase discontinuities. *Nano Lett* 12:1702–1706
- Alù A, Engheta N (2009) All optical metamaterial circuit board at the nanoscale. *Phys Rev Lett* 103:143902
- Biagioni P, Huang JS, Hecht B (2012) Nanoantennas for visible and infrared radiation. *Rep Prog Phys* 75(2):024402
- Burgos SP, de Waele R, Polman A, Atwater HA (2010) A single-layer wide-angle negative-index metamaterial at visible frequencies. *Nat Mater* 9:407–412
- Chen J, Badioli M, Alonso-González P, Thongrattanasiri S, Huth F, Osmond J, Spasenovic M, Centeno A, Pesquera A, Godignon P, Zurutuza A, Camara N, Abajo JGD, Hillenbrand R, Koppens F (2012) Optical nano-imaging of gate-tunable graphene plasmons. *Nature* 487:77–81
- Chen H-T, Taylor AJ, Yu N (2016) A review of metasurfaces: physics and applications. *Rep Prog Phys* 79:076401
- Dong A, Chen J, Vora PM, Kikkawa JM, Murray CB (2010) Binary nanocrystal superlattice membranes self-assembled at the liquid-air interface. *Nature* 466:474–477

- Fan JA, Wu C, Bao K, Bao J, Bardhan R, Halas NJ, Manoharan VN, Nordlander P, Shvets G, Capasso F (2010) Self-assembled plasmonic nanoparticle clusters. *Science* 328:1135–1138
- Fei Z, Rodin AS, Andreev GO, Bao W, McLeod AS, Wagner M, Zhang LM, Zhao Z, Thiemens M, Dominguez G, Fogler MM, Neto AHC, Lau CN, Keilmann F, Basov DN (2012) Gate-tuning of graphene plasmons revealed by infrared nano-imaging. *Nature* 487:82–85
- Hedayati MK, Faupel F, Elbahri M (2014) Review of plasmonic nanocomposite metamaterial absorber. *Materials* 7:1221–1248
- Henzie J, Grünwald M, Widmer-Cooper A, Geissler PL, Yang P (2011) Self-assembly of uniform polyhedral silver nanocrystals into densest packings and exotic superlattices. *Nat Mater* 11:131–137
- Huang L, Chen X, Bai B, Tan Q, Jin G, Zentgraf T, Zhang S (2013) Helicity dependent directional surface plasmon polariton excitation using a metasurface with interfacial phase discontinuity. *Light: Science and Applications*, 2(3), [e70]. DOI:10.1038/lsa.2013.26
- Hwang E, Sarma SD (2007) Dielectric function, screening, and plasmons in two-dimensional graphene. *Phys Rev B* 75:205418
- Ju L, Geng B, Horng J, Girit C, Martin M, Hao Z, Bechtel HA, Liang X, Zettl A, Shen YR, Wang F (2011) Graphene plasmonics for tunable terahertz metamaterials. *Nat Nanotechnol* 6:630–634
- Li Y, Zhang J, Zhang Y, Chen H, Fan Y (2016) Wideband, co-polarization anomalous reflection metasurface based on low-Q resonators. *Applied Physics A* 122:851
- Lin J, Mueller JPB, Wang Q, Yuan G, Antoniou N, Yuan X-C, Capasso F (2013) Polarization-controlled tunable directional coupling of surface plasmon polaritons. *Science* 340:331–334
- Luo X, Pu M, Ma X, Li X (2015) Taming the electromagnetic boundaries via metasurfaces: from theory and fabrication to functional devices. *Int J Antennas Propag* 2015:1–80
- Meinzer N, Barnes WL, Hooper IR (2014) Plasmonic meta-atoms and metasurfaces. *Nat Photonics* 8:889–898
- Monticone F, Alù A (2014) Metamaterials and plasmonics: from nanoparticles to nanoantenna arrays, metasurfaces, and metamaterials. *Chin Phys B* 23(4):047809
- Novotny L (2007) Effective wavelength scaling for optical antennas. *Phys Rev Lett* 98:266802
- Pors A, Bozhevolnyi SI (2013) Plasmonic metasurfaces for efficient phase control in reflection. *Opt Express* 21:27438
- Pozar DM (2011) *Microwave engineering*. Wiley, New York
- Rothmund PW (2006) Folding DNA to create nanoscale shapes and patterns. *Nature* 440:297–302
- Tan SJ, Campolongo MJ, Luo D, Cheng W (2011) Building plasmonic nanostructures with DNA. *Nat Nanotechnol* 6:268–276
- Tetz KA, Pang L, Fainman Y (2006) High-resolution surface plasmon resonance sensor based on linewidth-optimized nanohole array transmittance. *Opt Lett* 31:1528–1530
- Verhagen E, de Waele R, Kuipers L, Polman A (2010) Three-dimensional negative index of refraction at optical frequencies by coupling plasmonic waveguides. *Phys Rev Lett* 105:223901
- Walther C, Scalari G, Amanti MI, Beck M, Faist J (2010) Microcavity laser oscillating in a circuit-based resonator. *Science* 327(5972):1495–1497
- Yan H, Li X, Chandra B, Tulevski G, Wu Y, Freitag M, Zhu W, Avouris P, Xia F (2012) Tunable infrared plasmonic devices using graphene/insulator stacks. *Nat Nanotechnol* 7:330–334
- Yao K, Liu Y (2014) Plasmonic metamaterials. *Nanotechnol Rev* 3(2):177–210
- Yin X, Ye Z, Rho J, Wang Y, Zhang X (2013) Photonic spin Hall effect at metasurfaces. *Science* 339:1405–1407
- Yu N, Genevet P, Kats MA, Aieta F, Tetienne J-P, Capasso F, Gaburro Z (2011) Light propagation with phase discontinuities: generalized laws of reflection and refraction. *Science* 334:333–337

Chapter 8

Metamaterials Inspired Frequency Selective Surfaces

8.1 Evolution of Frequency Selective Surfaces

Frequency selective surfaces (FSSs) have a long pedigree and are used for a number of applications including antenna reflectors, radomes, radar absorbent materials, and composite metamaterials (Mackay et al. 2014). The theory governing the use of frequency selective surfaces (FSSs) has evolved directly from the diffraction grating used in optics. The filtering properties of a frequency selective surface were discovered in 1786, when David Rittenhouse noted that some colors of a light spectrum were suppressed when he observed a lamp through a silk scarf (Brito 2010). Pedantically, a single FSS should be a thin surface defined by a pattern of conductor or resistive material on a planar or curved surface with some structural support, usually a dielectric layer. Certainly, multiple FSS structures may be, and often are, constructed using multiple dielectric layers and/or FSS embedded within some composite. In addition, an FSS may also feature non-thin components such as inductors, capacitors, diodes, and transistors which are bonded to the surface. Often these are referred to as circuit analogue structures. The FSS may feature deliberate loss, as part of a radar absorbing material, or may be designed to be as lossless as possible. They may be active, featuring amplification structures, semi-active featuring biased diodes, and so on, or completely passive. There may be connecting structures, such as vias, between FSS, or each FSS may be electrically isolated. They may also comprise arrays of fully three-dimensional elements, such as the calthroops. It may become difficult to decide what to call such structures and how they fit in with antenna array definitions, two- or three-dimensional metamaterials, dichroic surfaces, etc. (Mackay et al. 2014).

The operation mechanism of traditional FSSs is based on the resonant elements: aperture and patch. When a plane wave illuminates an array of metallic elements, it excites electric current on the elements. The amplitude of the generated current depends on the strength of the coupling of energy between the wave and the elements. The coupling reaches its highest level at the fundamental frequency where

the length of elements is a $\lambda/2$. As a result, the elements are shaped so that they are resonant near the frequency of operation. Depending on its distribution, the current itself acts as an electromagnetic source, thus producing a scattered field. The scattered field added to the incident field constitutes the total field in the space surrounding the FSS. By controlling the scattered field (designing elements), therefore, the required filter response is produced which can be seen in the spectrum of the total field. Although the geometry of the elements has a critical influence on the filtering behavior, there are other parameters that can affect the frequency response. This could be the choice of the parameters of the substrate supporting the elements of the FSS and also its inter-element spacing. The substrate affects both the frequency of operation and the bandwidth of the response. A smaller inter-element spacing is usually preferred. However, the spacing can also change the bandwidth; a larger spacing in general produces a narrower bandwidth (Bayatpur 2009).

FSSs can be seen as electromagnetic filters that are normally realized using periodic structures formed by arrays of conducting elements on a dielectric substrate or by periodic aperture elements in a conducting sheet. Figure 8.1 shows typical element types and equivalent circuits used in the FSS unit cell (Fallahi 2010, Costa et al. 2014), including center linked or N-pole, type of loop, interior solid or plate type, and combinations of the others elements.

Group 1: Center connected or N-poles, such as dipole, three-legged element, the Jerusalem cross, and the square spiral. For instance, the tripole element consists of three concentric, thin monopoles which share a common point (the center). They can be packed tightly to reduce the inter-element spacing and, therefore, enhance the bandwidth. The Jerusalem cross consists of two crossing dipoles

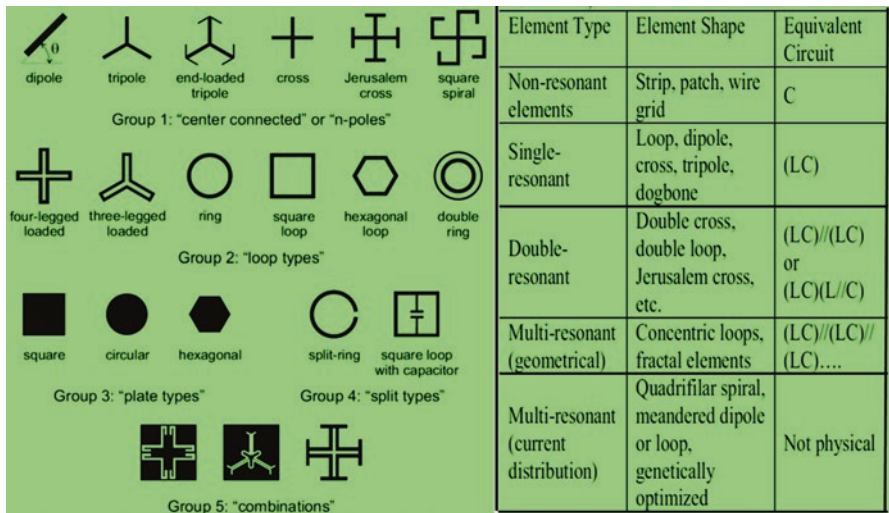


Fig. 8.1 Typical element types and equivalent circuits used in the FSS unit cell (Fallahi 2010; Costa et al. 2014)

which are loaded with small, orthogonal sections at their ends. In comparison with the tripole array, the Jerusalem FSS exhibits a better stability as the angle of incidence is changed from normal to 45° , both in terms of response characteristics, i.e., bandwidth and harmonics.

Group 2: Loop types such as the three- and four-legged loaded elements, the circular loops, and the square and hexagonal loops. For instance, the four-legged element is made up of two meandered, half-wave dipoles. A half-wave dipole can be similar to a shorter dipole which is loaded with a reactance; the overall reactive impedance of the dipoles has to be zero at the resonance. Comparably, hexagonal element has a better harmonic performance and a better scan stability.

Group 3: Solid interiors or plate types. (a) Array of metallic patches in the shape of a circular disk, square, rectangular, etc., which is usually used as reflecting arrays; (b) array of slots on a metallic plate in the form of circle, square, etc., which is often transparent. Since the traditional design of patches (holes) dimensions must be close to $\lambda/2$ in this approach, such elements usually suffer from issues of angle dependence and early onset of grating lobes, and thus, they are not too favorable for filter designs. However, such patch arrays can be adapted with metamaterials to get better performance.

Group 4: Split types, which have been widely used for metamaterials design.

Group 5: Combinations. Any combination of the elements belonging to any of these groups can also construct a new element, and this list is endless.

In order to decrease the sensitivity of the FSS response to the oblique angles of the incident wave, the unit cell size should be miniaturized. This is especially important when the FSS is used in close proximity to the radiation source. Therefore, metamaterials inspired FSSs have been developed based on miniaturized elements. These types of FSSs operate based on a different principle that allows superior performance over the traditional structures. Instead of using fully resonant elements as the unit cell of the FSS, nonresonant unit cells with small dimensions are used. These miniaturized elements act as lumped capacitors or inductors and are arranged in a way that they couple to the incident electromagnetic wave. In this way, the electrical size of the unit cells is decreased to less than $1/4$ and even in some cases smaller than $1/10$ (Ebrahimi 2016).

The most common metamaterial FSS types take the form of planar, periodic metal, or dielectric arrays in 2D space. Frequency behavior of an FSS is determined by the geometry of the surface unit cell provided that the surface size is infinite. FSSs were originally introduced as spatial filters and since that they have been employed in a variety of other applications including metamaterial applications (Brito 2010). The widespread areas of their application include hybrid radomes in airborne applications, dual- or multiband dichroic (Cassegrain) reflectors, circuit analog absorbers, electromagnetic interference (EMI) shielding, diplexers and polarizers, band-pass windows for metallic radomes or energy-saving windows, phase screens for beam steering in antenna arrays, and high-impedance surfaces

(HISs) or electromagnetic bandgap (EBG) resonators for directivity and gain enhancements of antennas (Haghzadeh and Akyurtluu 2016).

8.2 Design of Metamaterial-Based Miniaturized-Element Frequency Selective Surfaces

Metamaterial-based miniaturized FSS can also basically be divided into two types: the band-pass FSS (mesh type) and the band-stop FSS (patch type). The FSS structures may further be classified as follows (Narayan and Jha 2015): infinite periodic FSS structure, cascaded FSS or multilayered FSS structure, finite periodic and electrically large FSS structure, and curved FSS (CFSS) structure.

Frequency selective surfaces have been designed using different techniques such as perturbation, multi-element unit cells, multi-resonant unit cells, composite unit cells, and genetic algorithm design techniques and using complementary structures (Mudar and Behdad 2010). Various configurations such as ring, patch, square loop, strip, and slot shapes have been used to design the FSS layer. Fractal structures constituting the unit cells of frequency selective surfaces have shown to be capable of providing multiband operation (Bao et al. 2006).

The initially designed miniaturized-element FSS consists of a periodic array of metallic patches backed by a wire mesh having the same periodicity much shorter than the wavelength. The array of patches constitutes a capacitive surface and the wire mesh, a coupled inductive surface (Fig. 8.2), which together act as a resonant structure in the path of an incident plane wave. Due to a high external coupling coefficient, such a primitive single-pole design has shown to have a poor selectivity and a high insertion loss. To remedy this major shortcoming, two cascaded surfaces with proper coupling were devised to obtain a band-pass response with much better performance. However, large electrical separation remained an issue as regards fabrication, mounting, and again producing angle of incidence dependence to some extent.

In the next stage, the design of the miniaturized-element FSS was modified and improved to overcome the performance and the assembly through designing loop-wire FSS, which produces a high-Q, high-order, band-pass characteristic using just a single-substrate screen. The periodicity, moreover, is reduced by at least a factor of two, making the unit cell dimensions as small as $\lambda_0/12$. These improvements that are achieved include (Bayatpur 2009): (a) the loop surface behaves as notch filter capable of producing a transmission zero; (b) both electric and magnetic mutual coupling are established between the two surfaces using a very thin substrate. A lumped capacitor can be inserted in the gap between the loops to avoid issues related to fabrication of capacitance values beyond what can be achieved by air gaps. The loop-wire design exhibits not only a better frequency selectivity, compared to the first generation, but also a much better insensitivity to incidence angle.

In another effort, the tunability of this class of frequency selective surfaces was studied. The basic idea was to interconnect loops with lumped varactors. These

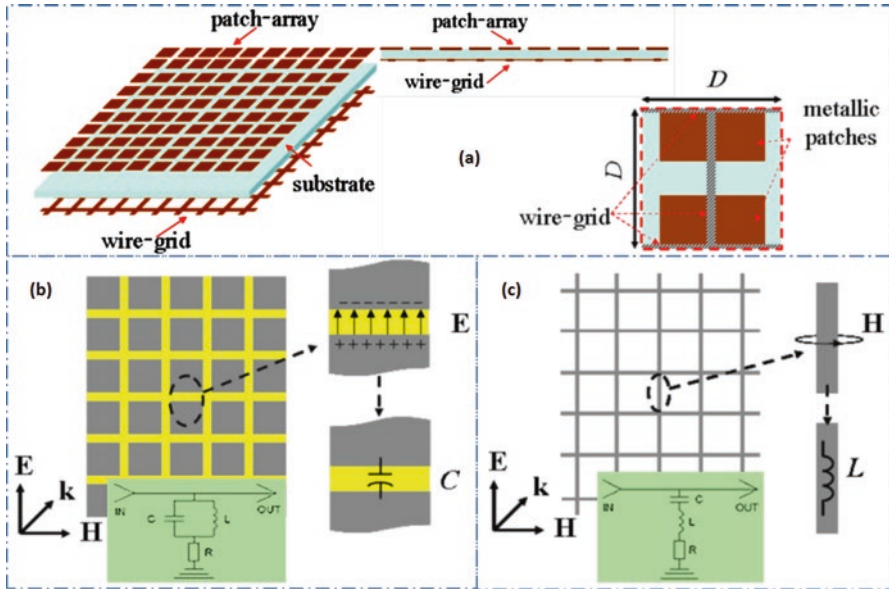


Fig. 8.2 Design of miniaturized capacitive junctions and inductive traces (Bayatpur 2009): (a) the patch-wire miniaturized-element FSS; (b) upon incidence of a plane wave on patch array, the electric field creates positive and negative charges on the edges of the two adjacent patches, thus producing a gap capacitor; (c) in a wire grid, parallel wires that are normal to the magnetic field act as inductors

varactors are placed in series and can be biased with a very-high-voltage DC power supply. The structure shows a great potential for wide tuning range with a negligible loss of performance. As the varactors are changed, the transmission zero frequency on one side or both sides can be tuned. In a way, a metamorphic frequency response can be achieved by tuning the varactors. This metamorphic behavior refers to two totally different modes of operations: band-stop and band-pass. The band-pass behavior of the response can also be reconfigured for single- or multiband, without introducing frequency harmonics of the response. In addition to two completely different modes of operation, the center frequency as well as the bandwidth of the response can be tuned independently (Bayatpur 2009).

The next generation of the miniaturized-element FSS was designed with the intension of improving the frequency selectivity without increasing the fabrication complexity. For this design a two-sided substrate having a periodic array of loops on either side was devised (Fig. 8.3a). For this design, the loop array on one face was translated in both x and y directions by half a period. This allows establishment of proper electric magnetic mutual coupling between the two surfaces. The loops on each surface have the ability to create a transmission zero. Placing two such transmission zeros on either side of the passband frequency produces much improved frequency selectivity and out-of-band rejection. Similar to loop-wire structure, the loop-loop surface can also be tuned by placement of varactors in the gaps between

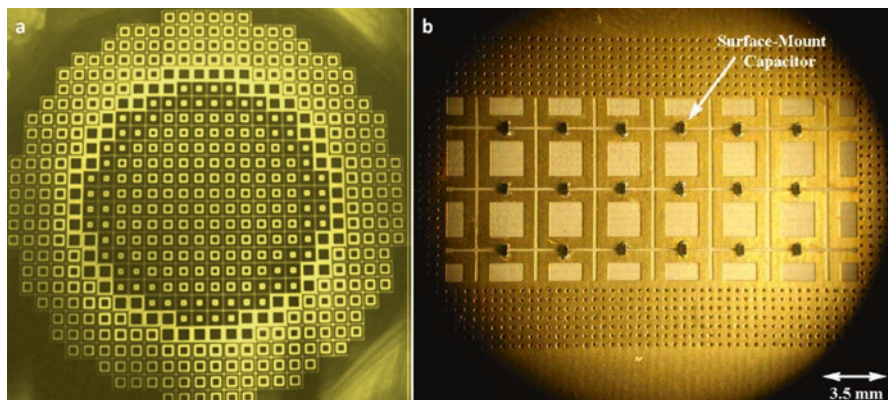


Fig. 8.3 The loop-wire miniaturized-element FSS (Bayatpur 2009, Edalati and Sarabandi 2014): without (a) and with a surface-mount capacitor (black boxes, b)

the loops (Fig. 8.3b). Next, the multipole characteristics of the miniaturized-element FSSs were considered. Being the standard approach of creating a multipole filter, cascading previously designed single-band surfaces used to construct multipole structures. Simply, a few FSS layers were stacked along with dielectric spacers between the layers. These designs were then further improved, in terms of selectivity and number of metal faces, by designing a single-sided loop-wire FSS which was used as building blocks of stacked, multipole FSS structures (Bayatpur 2009).

8.3 Printed Flexible and Reconfigurable Frequency Selective Surfaces

Frequency selective surfaces are traditionally fabricated with printed circuit board (PCB) manufacturing process on rigid substrates, which usually results in heavy and nonconformal panels. In many modern applications of FSS in radomes, microwave antennas, or electromagnetic shielding, there is an ever-growing demand for flexible, low-cost, lightweight, and conformal frequency selective surfaces. Therefore, all printed, flexible, and reconfigurable frequency selective surfaces have been developed and fabricated with emerging printed flexible electronics approaches.

Figure 8.4a illustrates the design for an all-printed, flexible, and reconfigurable miniaturized-element ($\lambda/10$) FSS, where its resonance frequency can be tuned and its mode of operation can be varied (Haghzadeh and Akyurtlua 2016). The metamaterials inspired FSS has two loop-wire layers that are directly printed on both sides of a 25.4- μm -thick polyimide Kapton sheet. The interdigitated capacitors (IDCs) and barium strontium titanate/cyclic olefin copolymer (BST/COC) dielectrics are designed for frequency tuning. The conductive features can be printed using an

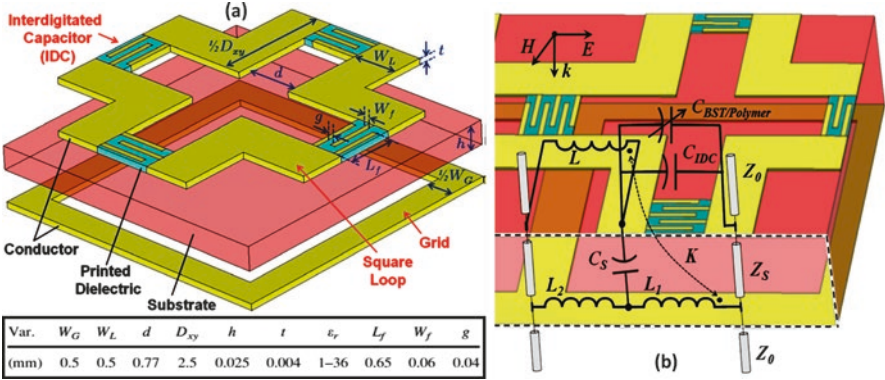


Fig. 8.4 Illustration of an all-printed, reconfigurable miniaturized-element, loop-grid frequency selective surface (Haghzadeh and Akyurtlua 2016): (a) unit cell model with semi-lumped interdigitated capacitors (IDCs) additively filled with a printed dielectric; (b) Equivalent circuit model of the unit cell

Aerosol Jet printer with a nano-silver ink and depositing dielectrics using a fluid dispensing printer with BST/COC.

Figure 8.4b shows an equivalent circuit model for one unit cell of the FSS structure. The bottom wire grid is modeled with two purely inductive elements, L_1 and L_2 , since the strips support the electric currents generated by the incident wave. Their inductive values are dependent on the grid strip width and length and independent of polarization due to the inherent symmetry. The square loops on the top are modeled with a combination of inductive and capacitive elements. For a given linearly polarized normal-incident plane wave, the sides of the square loop parallel to the electric field store magnetic energy since these traces carry the excited electric currents. This inductive behavior is modeled by a loop inductance, L . The inductance of a strip, L_i , can be expressed as (Haghzadeh and Akyurtlua 2016):

$$L_i = \mu_0 \frac{D}{2\pi} \ln \left(\frac{1}{\sin \left(\frac{\pi w}{2D} \right)} \right) \tag{8.1}$$

where D is the length of the strip and w is the width.

On the other hand, the adjacent sides of the successive loops perpendicular to the electric field store electric energy in the gap between them since positive and negative charges are built up on these edges. This capacitive behavior of the gap is modeled by the gap capacitance, C_g , which can be given by a first-order approximation (Haghzadeh and Akyurtlua 2016):

$$C_g = \varepsilon_0 \varepsilon_{\text{eff}} \frac{2S}{\pi} \ln \left(\frac{1}{\sin \left(\frac{\pi d}{2S} \right)} \right) \quad (8.2)$$

where S is the facing side length of two adjacent loops, d is the spacing between them, and ε_{eff} is the effective dielectric constant due to the substrate.

It can be seen that the array of square loops constitute a series L - C (band-stop) circuit. There are also two types of interactions between the top and bottom layers that are intensified due to a very thin substrate. First, the encircling magnetic fields induced by currents flowing in the strips of wire grid couple to the traces of square loops and induce electric currents that consequently generate a magnetic field that couples back to the grid strips. This mutual inductive coupling is modeled by the mutual inductance, K . Second, the accumulated charges on the sides of the square loops (perpendicular to the electric field of the incident wave) establish an electric field (normal to the substrate) at the locations where strips of the loops and the wire grid overlap. This interaction results in displacement currents between the layers (similar to a capacitive junction) and is modeled as the substrate capacitance, C_s . Finally, the presence of a semi-lumped IDC in the gap between the adjacent loops results in an increased capacitive coupling between them and is modeled by the IDC capacitance, C_{IDC} , and $C_{\text{BST/Polymer}}$. This capacitance depends on the dimensions of the IDC fingers, the gap between them, and the dielectric constant of the printed dielectric between the fingers. The IDC capacitance for the dielectric filled IDC, C_{IDC} , has an in-plane capacitance part, C_{ip} , and a parallel-plate capacitance part, C_{pp} , that is (Haghzadeh and Akyurtlua 2016):

$$C_{\text{IDC}} = C_{\text{ip}} + C_{\text{pp}} \quad (8.3)$$

The in-plane part, C_{ip} , is due to the fringing electric fields passing through the substrate as well as air, which can be calculated using Eq. (8.2). The parallel-plate capacitance, C_{pp} , is due to the fact that the IDC fingers (especially when the lines are thick) constitute vertical parallel plates with air or printed BST/COC dielectric in their overlapping, meandered area. It can be expressed as (Haghzadeh and Akyurtlua 2016):

$$C = \varepsilon_0 \varepsilon_r \frac{t}{g} \left((n-1)(L_f - g) + nW_f \right) \quad (8.4)$$

where ε_r is the relative permittivity of air or the printed BST/COC dielectric, n is the number of IDC fingers, g is the gap between them and the pad base, and t , L_f , and W_f are the thickness, length, and width of the IDC fingers, respectively.

The interdigitated capacitor (IDC) is designed for tuning the frequency response, which can be filled with any printable dielectric of choice. As shown in Fig. 8.4, this

planar, semi-lumped capacitive element is printed between every two adjacent square loops on one side of the surface. Changing the dielectric constant of the printed dielectric will modify the capacitance of the IDCs, the coupling between the adjacent square loops, and consequently, the resonance frequency of the FSS. In order to obtain a printable dielectric with the ability to significantly change its dielectric constant, a multiphase ferroelectric–polymer composite has been used, such as suspending micro- or nano-sized particles of barium strontium titanate ($\text{Ba}_x\text{Sr}_{1-x}\text{TiO}_3$) in cyclic olefin copolymer (COC) matrix. The relative permittivity of composites made of randomly and homogeneously distributed micro/nanoparticles in polymer matrices can be calculated by (Whittow et al. 2014):

$$\log \varepsilon_r = \log \varepsilon_p + s(1-k)v_b \log \left(\frac{\varepsilon_b}{\varepsilon_p} \right) \quad (8.5)$$

where ε_r , ε_b , and ε_p are the relative permittivity values of BST/polymer composite, pure bulk BST, and pure polymer, respectively, and v_b is the volume fraction of BST. The fitting constant, k , represents the level of dispersion. A value of $k = 0.3$ represents a well-dispersed ceramic–polymer composite, and any value greater than 0.3 means a less dispersed ceramic–polymer mixing. In order to account for the effects of Ba mole fraction (x) in the relative permittivity of paraelectric $\text{Ba}_x\text{Sr}_{1-x}\text{TiO}_3$, s is introduced as the ratio of Ba mole fraction of BST particles (x) to 0.7 (the maximum Ba mole fraction for a paraelectric phase BST).

The FSS can be fabricated with printed electronics technologies that vary from conventional flexography, offset, gravure, and screen printing to direct-write printing technologies such as ink-jet printing, micro-dispensing, direct deposition, and Aerosol Jet printing. Figure 8.5 shows Aerosol Jet printed flexible and reconfigurable FSS (Haghzadeh and Akyurtluu 2016): (a) FSS with no IDCs; (b) FSS with air-filled IDCs, corresponding to $\varepsilon_r = 1$; (c) FSS with BST/COC filled IDCs using 25 vol. % loading of $\text{Ba}_{0.5}\text{Sr}_{0.5}\text{TiO}_3$, corresponding to $\varepsilon_r = 6$; (d) FSS with BST/COC filled IDCs using 70 vol. % loading of $\text{Ba}_{0.67}\text{Sr}_{0.33}\text{TiO}_3$, corresponding to $\varepsilon_r = 36$; (e) reflection |S11| (dB) as a function of frequency (GHz); and (f) printed sample of a flexible FSS with enlarged images of interdigitated capacitors that can be filled with a printed dielectric for tuning purposes. The dielectric filled IDC design as an adjustable capacitive coupling element between the square loops of the FSS enables not only shifting the resonance frequency of a first order band-pass filtering but also switching the mode of operation from a first order to a dual band. These tuning behaviors are achieved by printing different BST/COC dielectric inks with different dielectric constants on IDCs of choice. The dielectric constant of the dielectric inks can be modified from 6 to 36 by changing the BST loading as well as the stoichiometry of the BST particles. This approach is time- and cost-efficient since it avoids multiple design iterations and lengthy prototype fabrication of FSS structures required to reach the targeted performance. It can be used in many applications for flexible printed RF and microwave devices, where there is a need to fine-tune or alter the final performance of a system.

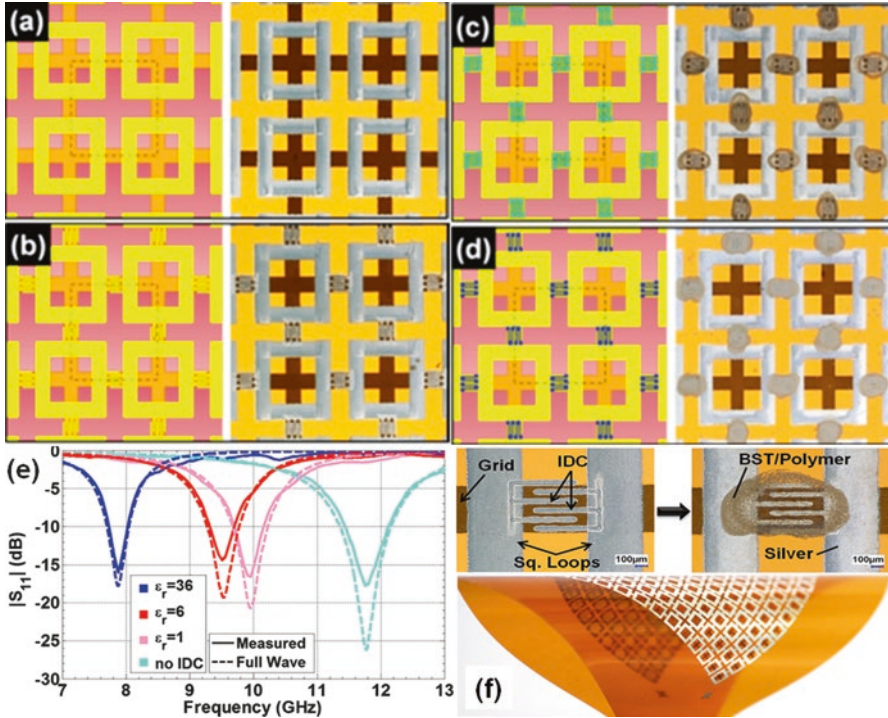


Fig. 8.5 All-printed flexible and reconfigurable FSS (Haghzadeh and Akyurtlua 2016): (a) FSS with no IDCs; (b) FSS with air-filled IDCs, corresponding to $\epsilon_r = 1$; (c) FSS with BST/COC filled IDCs using 25 vol. % loading of $\text{Ba}_{0.5}\text{Sr}_{0.5}\text{TiO}_3$, corresponding to $\epsilon_r = 6$; (d) FSS with BST/COC filled IDCs using 70 vol. % loading of $\text{Ba}_{0.67}\text{Sr}_{0.33}\text{TiO}_3$, corresponding to $\epsilon_r = 36$; (e) reflection $|S_{11}|$ (dB) as a function of frequency (GHz); (f) printed sample of a flexible FSS with enlarged images of interdigitated capacitors that can be filled with a printed dielectric for tuning purposes

8.4 Metamaterials Inspired FSS Antennas and Circuits

Metamaterial frequency selective surfaces can be used in designing reactive impedance surfaces in a form of an artificial magnetic conductor (AMC) and electromagnetic bandgap (EBG). The FSSs are an alternative to fixed frequency metamaterial where static geometry and spacing of unit cells determine its frequency response. FSSs have reflective characteristics with a certain phase and amplitude that allow frequency changes in a single medium and are not restricted to a fixed frequency response. This metamaterial FSS will be used as a ground plane for antennas in order to effectively suppress undesirable wave fluctuations, i.e., surface waves inside the substrate, while producing good radiation patterns. Frequency selective surfaces can be used as a superstrate to enhance the performance of a number of antennas. These superstrates offer the advantage of ease of fabrication with microstrip technology and reduced thickness as compared with those of the

dielectric type superstrates. The FSS can suppress its grating lobes, and as a result a high-gain antenna can be obtained (Brito 2010).

8.4.1 *Ultra-Wideband Antennas and Microstrip Filters*

Interference is a big issue for ultra-wideband (UWB, 3.1–10.6 GHz) communication systems. As UWB transmitters must not cause electromagnetic interference on any nearby communication systems, a solution to notch this band is needed (Brito 2010): (a) a parasite metamaterial SSR structure is inserted directly in the antenna's patch—one kind of SRR rings is made of metal-like copper, and the other is a slot-type SRR (CSSR) where the rings are slots on a nonmagnetic metal, which are etched in the foursquare patch—or (b) a microstrip UWB filter backed by the CSRR placed on its ground plane. The CSRR-based medium has the property of negative effective permittivity and can be used to reject unwanted frequency band. Due to the relatively high insertion loss for CSRR slots, the CSRR has a band-stop filtering property. Moreover, the band-notched frequencies can be varied by adjusting the length of C-shaped slot and the dimensions of CSRR independently.

The use of UWB systems needs efficient antennas to provide acceptable bandwidth requirements and radiation pattern characteristics throughout the designated UWB spectrum (Fig. 8.6a). It is generally accepted that for antennas to be classified as ultra-wideband, the requirement will be to satisfy minimum fractional bandwidths of at least 20% or 500 MHz or more (Allen et al. 2006).

8.4.2 *Microstrip Antennas with HIS Ground Plane*

The high-impedance surface (HIS) ground planes can provide planar solutions for antenna design. While a conductive sheet is useful as a reflector, it also has several drawbacks such as permitting the propagation of surface waves and a phase reversal for reflected plane waves. The presence of surface waves will result in the normal current that occurs on any electrical conductor. The HIS electromagnetic characteristics allow reducing the interactions between the antenna and its backward environment.

A low-profile broadband antenna can be made suspending over a HIS ground plane, as shown in Fig. 8.6b. The medium between the plate and ground plane is basically air or a substrate of very low relative permittivity. In contrary to other existing feeding structures, such as a direct microstrip line feed, an aperture in the ground plane is made with proximity coupling; a long and isolated coaxial probe feed is the chosen option for this antenna because of the large spacing and the very low relative permittivity in between the antenna and the ground plane. Furthermore, to compensate the large reactance due to the long probe in a broad frequency range, the antenna is off centered by 1.1 mm for matching purposes (Brito 2010).

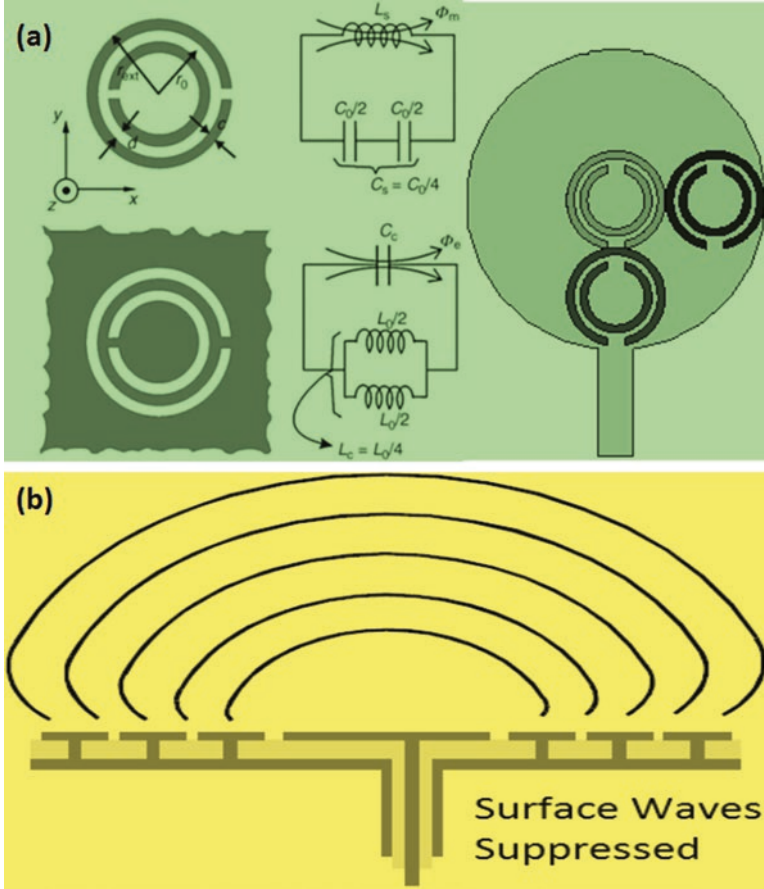


Fig. 8.6 Metamaterials inspired FSS antennas (Brito 2010): (a) ultra-wideband antennas and microstrip filters; (b) a patch antenna embedded in a high-impedance ground plane

8.4.3 Fabry–Pérot Antenna

Employing a patch-type FSS-cover with low-pass rather than band-stop response can obtain a stable response of reflectivity and reflection phase. The mushroom-type HIS has been used as base to suppress the lateral waves between the cover and base, which enlarges the directivity-bandwidth product and supports enough aperture efficiency. Fabry–Pérot antennas are designed by employing these techniques.

Fabry–Pérot Resonator (FPR) antennas have attracted significant attention in microwave and millimeter waves due to a number of attractive properties, such as low complexity, high directivity, and conformal deployment capability.

8.5 Metamaterials Inspired Microfluidic Sensors

Metamaterial resonators have attracted great attention in designing sensors. The split-ring resonators (SRRs) and complementary split-ring resonators (CSRRs) provide concentrated electromagnetic fields at their resonance with high-quality factor characteristic. These electromagnetic fields are very sensitive to the environment changes such as displacement, rotation, and dielectric property. Any change in these factors affects the resonance characteristics of the SRRs and CSRRs. Therefore, they can function as sensors with a compact footprint. Furthermore, integration of metamaterials and microfluidics has been used in the gigahertz (GHz) and terahertz (THz) spectral range for liquid sensing. Microfluidics enables the precise manipulation of fluid with a small volume inside a microchannel by utilizing the microelectromechanical systems (MEMS) technology. It also facilitates precise handling, sorting, and trapping of microsubstances suspended in liquid solution. By proper design of the flow resistance, a single particle trapping can be positioned at the desired area of the microfluidic device. Hence, by integrating microfluidic systems with metamaterials, it is possible to control the volume of the sample and the location of microsubstances without any chemical modification or additional handling. Moreover, the versatility of metamaterial resonator designs with the ease of microfluidic integration offers a new set of interesting functionalities for applications in the field of chemical and biological sensing (Shih et al. 2017).

Figure 8.7 shows two examples of metamaterials inspired microfluidic sensors (Ebrahimi 2016, Shih et al. 2017). One is the microstrip coupled CSRR sensor with the PDMS microfluidic channel (Fig. 8.7a). The CSRR is composed of a metallic capacitive plate that is connected through an inductive metallic path to the surrounding ground plane. The microfluidic channel is positioned along the lower edge of the CSRR, which is made of polydimethylsiloxane (PDMS). By adding the PDMS channel, the resonance frequency is shifted down with a small decrease of peak attenuation since a part of the CSRR is covered with the PDMS. The use of microfluidic channel enables the microfluidic sensing with a little amount of liquid sample where the cross section of the sensing area is smaller than $2 \times 10^{-5} \lambda_0^2$ and where λ_0 is the operational guided wavelength. The compact designs promise the potential of the designed sensors for integration in lab-on-a-chip technology.

Another example is microfluidic SRR sensor operating in the THz spectral region (Fig. 8.7b). The device consists of microfluidic channels integrated with trapping structures on top of a SRR structure to trap the microparticles in the most sensitive region of each unit cell, and the changes in the THz transmission response of the metamaterial are used to examine the type and quantity of the trapped microparticles. The split-ring resonator (SRR) structure is selected as the metamaterial resonator. The incoming THz wave with electric field polarized in the direction parallel to the SRR gap excites the fundamental inductive–capacitive (*LC*) resonance of the SRR, where a circulating current in the metallic ring confines a strong electric field in the gap region. The *LC* resonance frequency of the SRR is determined by the inductance (*L*) of the square metal ring and capacitance (*C*) of the gap region using

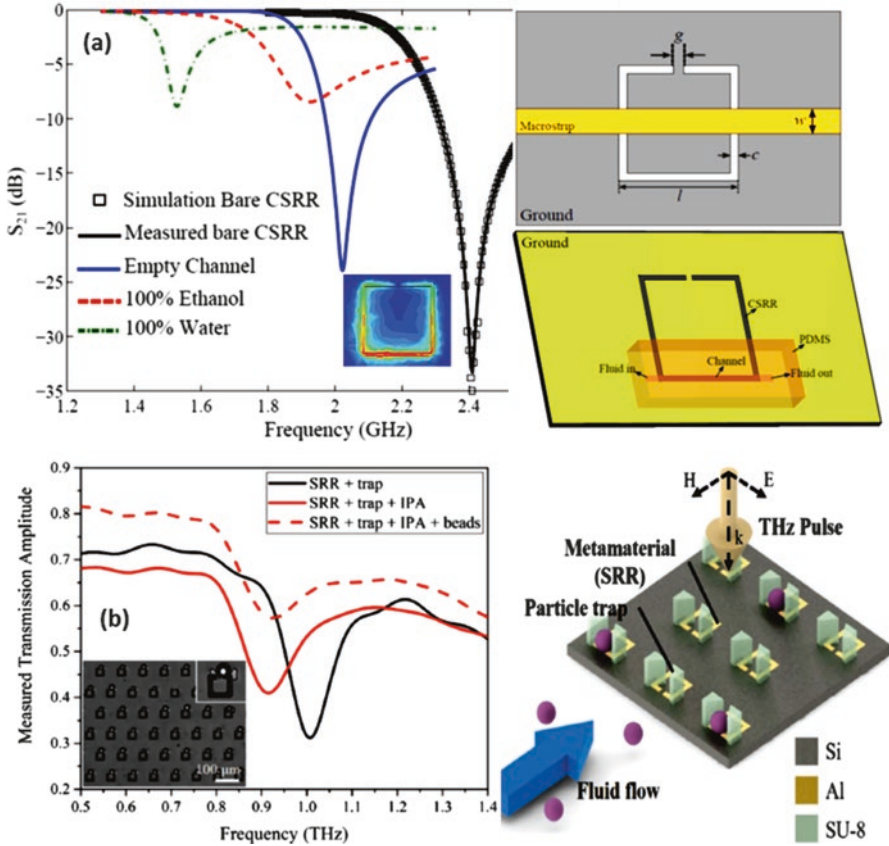


Fig. 8.7 Metamaterials inspired microfluidic sensors (Ebrahimi 2016, Shih et al. 2017): (a) the microstrip coupled CSRR sensor with the PDMS microfluidic channel; (b) microfluidic SRR sensor operating in the THz spectral region

the expression, $f_r = \frac{1}{2\pi} \sqrt{LC}$. Since C is a function of the permittivity, any changes in the dielectric property of the material positioned in the gap region will change its effective C , thereby resulting in a spectral shift of the LC resonance. In order to trap the microparticles at the capacitive gap of SRR geometry, a microfluidic system was integrated on top of the SRR structure. Quartz was selected as the substrate material to fabricate metallic resonator patterns as well as microfluidic structures because of its high transparency in the THz spectral region. SU-8 photoresist was chosen as the material for microfluidic structures for its capability of forming structures in microscale with a high aspect ratio. Moreover, the ultraviolet (UV) curable property of SU-8 allows easy and direct alignment of trapping structure fabrication on top of SRR patterns. Due to the predefined number of microparticles trapped in each SRR, the THz transmission response can provide both the qualitative and

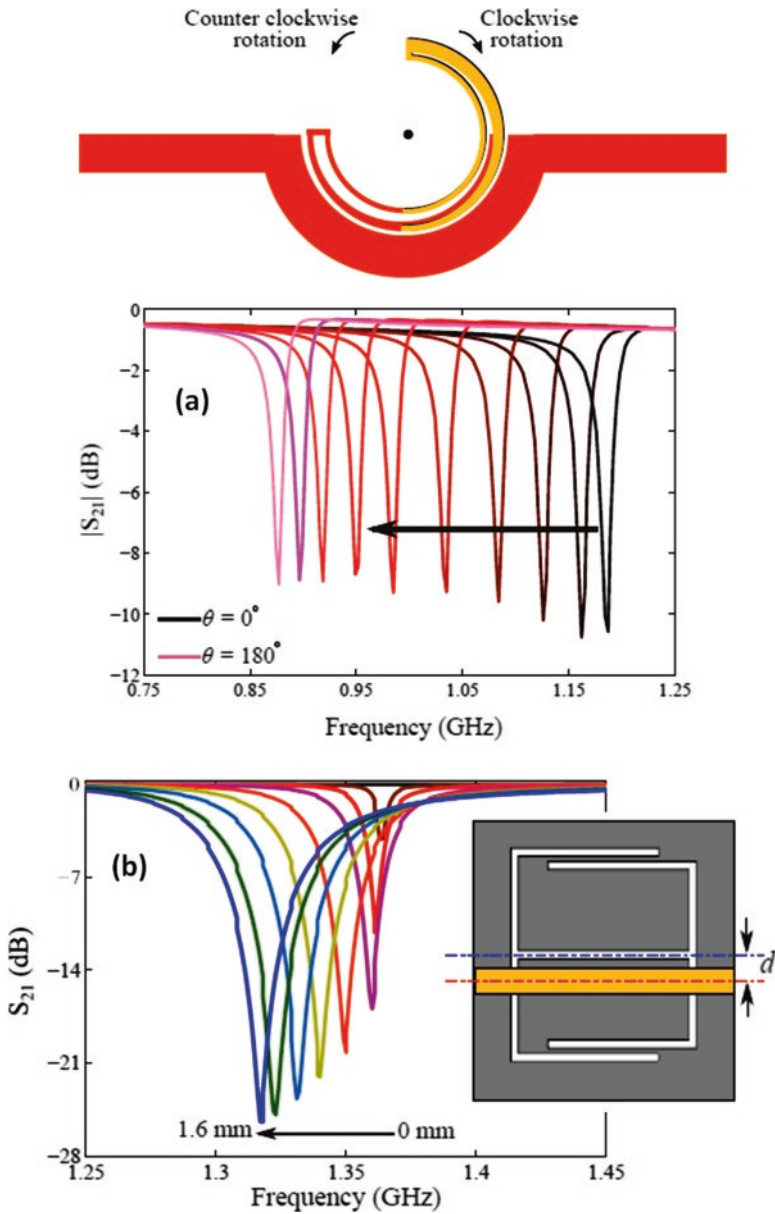


Fig. 8.8 Metamaterials inspired rotation and displacement sensors (Ebrahimi 2016): (a) rotation sensor; (b) CELC displacement sensor

quantitative estimation of the trapped particles in terms of their resonance frequency and the amplitude modulation, respectively. The maximum blue shift of 10 GHz is achieved for 15% particle trapping rate. The versatility of metamaterial resonator designs along with the selective trapping functionality of microfluidics

operating in the low-energy THz spectral range will open up new research opportunities focused on label-free detection, biomolecular sensing, and quantification of microparticles in the terahertz and infrared frequencies (Shih et al. 2017).

8.6 Metamaterials Inspired Rotation and Displacement Sensors

On resonance, metamaterials inspired SRR and CSRR resonators will provide localized electromagnetic fields that are very sensitive to variations in dielectric properties and their geometries. The sensitivity to the geometry can be used to design displacement and rotation detectors. For example, the rotation sensor is based on broadside coupled U-shaped resonators, where the rotation affects the coupling coefficient between them (Fig. 8.8a). A change in the coupling shifts the resonance frequency of the structure. This effect can be used to measure the rotation angle. The designed sensor operates in the low microwave frequency range with a compact size. A linear sensing characteristic is achieved by asymmetrically tapering the two resonators. It is shown that this new configuration can improve the dynamic range up to 180°. The rotation direction can also be detected (Ebrahimi 2016).

Another example is a displacement sensor by exploiting the symmetry property of a CELC resonator loaded with a microstrip line (Fig. 8.8b). The designed sensor provides a sensing range up to 1.6 mm. The sensitivity, linearity, and the dynamic range of the proposed sensor can be improved by optimization of the resonator or the microstrip line section (Ebrahimi 2016).

References

- Allen B, Dohler M, Okon E, Malik W, Brown A, Edwards D (2006) Ultra wideband antennas and propagation for communications. Radar and Imaging, Wiley-Blackwell
- Bao XL, Ruvio G, Ammann MJ, John M (2006) A novel GPS patch antenna on a fractal high-impedance surface substrate. *IEEE Antennas Wirel Propag Lett* 5:323–326
- Bayatpur F (2009) Metamaterial-inspired frequency-selective surfaces. PhD dissertation. University of Michigan, Ann Arbor
- Brito DB (2010) Metamaterial inspired improved antennas and circuits. PhD dissertation. Universidade Federal do Rio Grande do Norte, combined with Telecom ParisTech, Natal
- Costa F, Monorchio A, Manara G (2014) An overview of equivalent circuit modeling techniques of frequency selective surfaces and metasurfaces. *ACES J* 29(12):960–976
- Ebrahimi A (2016) Metamaterial-inspired structures for microwave and terahertz applications. PhD dissertation. The University of Adelaide, Australia
- Edalati A, Sarabandi K (2014) Reflectarray antenna based on grounded loop-wire miniaturized-element frequency selective surfaces. *IET Microw Antennas Propag* 8(12):973–979
- Fallahi A (2010) Optical design of planar metamaterials. PhD dissertation. Swiss federal Institute of Technology, Zurich

- Haghzadeh M, Akyurtlu A (2016) All-printed, flexible, reconfigurable frequency selective surfaces. *J Appl Phys* 120(184901):1–10
- Mackay A, Sanz-Izquierdo B, Parker EA (2014) Evolution of frequency selective surfaces. *FERMAT* 2(008):1–7
- Mudar AA, Behdad N (2010) Low profile, highly-selective, dual-band frequency selective surfaces with closely spaced bands of operation. *IEEE Trans Antennas Propag* 58(12):4042–4050
- Narayan S, Jha RM (2015) Electromagnetic techniques and design strategies for FSS structure applications. *IEEE Antennas & Propag Mag* 57(5):135–158
- Shih K, Pitchappa P, Manjappa M, Ho CP, Singh R, Lee C (2017) Microfluidic metamaterial sensor: selective trapping and remote sensing of microparticles. *J Appl Phys* 121:023102
- Whittow WG, Li Y, Torah R, Yang K, Beeby S, Tudor J (2014) Printed frequency selective surfaces on textiles. *Electron Lett* 50:916–917

Chapter 9

Nonlinear Metamaterials and Metadevices

9.1 Introduction

Nonlinear metamaterials began on the theoretical side of research before practical implementations started to appear. The theoretical approaches varied considerably and can be classified depending on the degree of approximations used and on the starting assumptions. On one pole, there are examples of metamicroscopic theory, where the analysis departs from the exact properties of the structure on the level of individual elements, often discussing a particular implementation method, and derives the corresponding effective medium parameters to describe the response of the entire metamaterial in terms of linear permittivity and/or permeability and nonlinear susceptibilities of one or several orders. On the opposite pole, theory relies on homogenized medium parameters, hypothetically assumed or retrieved from scattering, and then discusses a mixture, interplay, or perhaps further structuring of such media to obtain the overall nonlinear behavior. Most of the models reported in the field fall somewhere close to either of these two extremes, sometimes combining the advantages of each approach and using different degrees of generality (Lapine et al. 2014).

The practical implementations have had nonlinear metamaterials offer promising opportunities for enhancing and controlling nonlinear response. Many interesting and unique nonlinear phenomena have been demonstrated using metamaterials, illustrating the potential for structured metamaterials to support novel nonlinear response not easily realizable in conventional materials. The design of nonlinear metamaterials, as has been the case for their linear counterparts, is greatly facilitated by the introduction of a homogenization scheme, wherein effective nonlinear susceptibilities for a composite are determined, in addition to the linear permittivity and permeability. The homogenization approach allows the anticipated properties of the nonlinear metamaterial to be determined efficiently from simulations of the repeated metamaterial element (Larouche et al. 2015).

One of the advantages that have propelled the field of linear metamaterials is the expanded palette of available material response, including the capability of

implementing electric, magnetic, and magnetoelectric properties, even in the absence of inherently magnetic materials. The addition of magnetic response in metamaterials leads to a considerably rich and complex collection of phenomena, especially when magnetic nonlinearity is included. The issue of magnetoelectric coupling, in fact, arises naturally for nonlinear metamaterials, and thus nonlinear homogenization schemes must include and quantify a significantly larger set of nonlinear susceptibilities, the majority of which are negligible for conventional materials (Larouche et al. 2015).

Therefore, metamaterials offer an enormously expanded set of tools for the design of novel nonlinear optical media. With the inclusion of artificial magnetic response, which can readily be realized in artificially structured media, the number of potential nonlinear susceptibilities dramatically increases, allowing much more control over harmonic generation or wave mixing processes, as well as many other nonlinear phenomena, in particular, nonlinear magnetoelectric metamaterials, which hold great potential for new nonlinear physics and nonlinear metadvice optimization.

9.2 Implementation Approaches to Manufacture Nonlinear Metamaterials

Many practical approaches have been developed to manufacture nonlinear metamaterials and inspired functional metadevices, including insertion of nonlinear elements, nonlinear host medium, local field enhancement, nonlinear transmission lines, intrinsic structural nonlinearity, nonlinearity based on liquid crystals, as well as utilization of quantum and superconducting elements.

9.2.1 *Insertion of Nonlinear Elements*

Macroscopic nonlinearity for electric or magnetic fields has been created with nonlinear insertions in the resonant meta-atoms of metamaterials. Nonlinear insertions are most suitable for implementations in microwave and lower THz ranges and offer consistently high nonlinearities with nonlinear modulation (exceeding 10% of the linear signal) with a few watt power applied.

The nonlinear response of metamaterials with nonlinear components is defined by the properties of the particular insertions, as shown in Fig. 9.1a. The nonlinear split-ring resonators with varactor diodes have both nonlinear conductivity and nonlinear capacitance. Such properties lead to a complicated mechanism of the nonlinearity in the resonators, which is mainly caused by rectification of the induced current in the structure. The drawback of the nonlinear response of those structures is that the quality of the metamaterial resonance is degrading at higher powers. This can be resolved by using heterostructure barrier varactors (HBV), which have

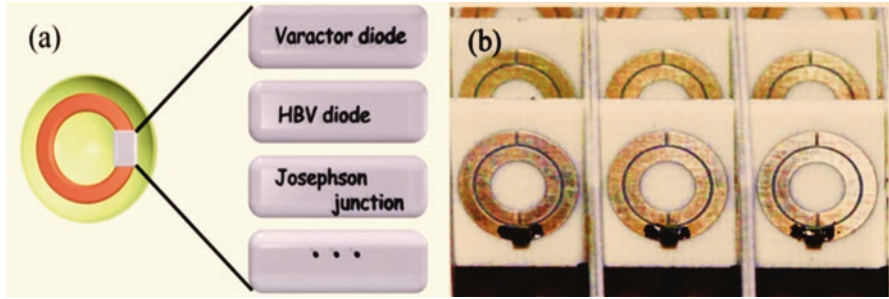


Fig. 9.1 Metamaterials with insertion of nonlinear elements (Lapine et al. 2014): (a) schematics of a meta-atom with various possible nonlinear insertions, including a varactor diode, a hetero-structure barrier varactor (HBV) diode, a Josephson junction, and other possible diodes. (b) Metamaterial made of split-ring resonators with varactor diodes

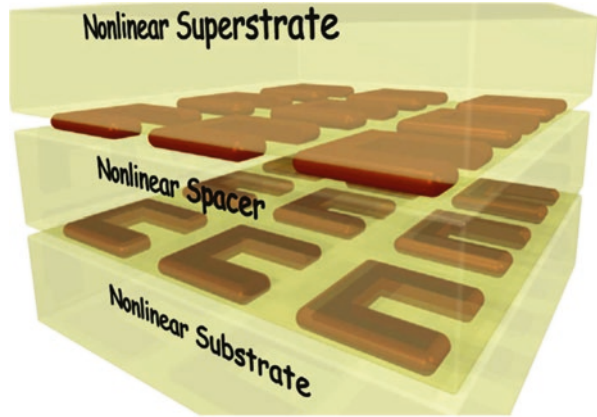
symmetric dependence of its capacitance on applied voltage, and in such structures the strength of the resonance increases with the increase of the electromagnetic wave intensity. More exotic types of inclusions are quantum dots, used along with nanoring chains, or Josephson junction-employed superconducting metamaterials (Lapine et al. 2014).

Bulk two-dimensional metamaterials with varactor inclusions (Fig. 9.1b) demonstrate several nonlinear effects predicted for metamaterials, including harmonic generation and dynamic tunability. Nonlinear insertions in metamaterials not only introduce the nonlinear response to the whole structure, but they can also be used for creating meta-atoms with completely new functionality, which cannot be achieved in linear structures. In particular, it was shown that the asymmetric nonlinear meta-atom can exhibit nonreciprocal transmission of electromagnetic waves, the so-called electromagnetic diode effect, which has been utilized in transmission line structures (Lapine et al. 2014).

9.2.2 Nonlinear Host Medium

Making metamaterials using nonlinear insertions is almost impossible for optical frequencies. In optical structures it appears more feasible to use either nonlinear substrates, superstrates, or dielectric spacing layers in multilayered metal-dielectric structures as schematically shown in Fig. 9.2. These approaches are closely related to the idea of making nonlinear metamaterial by embedding meta-atoms into nonlinear host media (Zharov et al. 2003). Enhancement of the local electric fields near small metal components leads to the possibility of improving the nonlinear response of matter. Such an improvement would be of paramount importance, since the nonlinearities found in natural optical materials are weak and limit possible applications. Both the dielectric and the magnetic properties may become nonlinear in such structures, providing an additional degree of freedom for engineering the nonlinear

Fig. 9.2 Achieving nonlinear response of a metamaterial by using nonlinear substrate and/or nonlinear spacer layer and/or nonlinear superstrate (Lapine et al. 2014)



response of materials. With this approach, however, it is not only possible to depart from a weak conventional nonlinearity of the host materials, achieving a stronger effect by appropriate structural arrangements, but also to have a much higher impact on the properties of host media, by affecting electronic properties through enhanced light–matter interaction. That is, the nonlinear response of metamaterials is valuable both for employing a conventional nonlinearity on a different scale (often converting microscopic electric nonlinearity into macroscopic magnetic one) and for boosting the nonlinear response by supplying much more intense fields to the host material (Lapine et al. 2014).

One of the specific approaches to create tunable and nonlinear host metamaterials is to infiltrate a metamaterial structure with liquid crystals. Liquid-crystal infiltration is quite attractive because of their tunable optical anisotropy and strong orientational nonlinearity. Importantly, liquid crystals offer several different approaches to realize tunability: by changing temperature, by applying external electric or magnetic field, or even all optically by employing their nonlinear-optical response. All-optical control of fishnet metamaterials infiltrated with E7 nematic liquid crystals is shown in Fig.9.3 (Minovich et al. 2012). A fishnet structure was fabricated using gold and MgF_2 layers deposited on a glass substrate (Fig. 9.3a), filled with the liquid crystal (LC) completely (Figs. 9.3b, c). This interplay between the impact of the optical fields and the biasing electric field on liquid-crystal reorientation demonstrates an interesting mechanism of electrically controlled optical nonlinearity in metamaterials, promising, for example, reconfigurable cloaking devices (Zheludev and Plum 2016).

The use of nonlinear host materials is most appropriate for THz, infrared, and optical implementations, typically providing nonlinear response stronger than in traditional nonlinear optics, thanks to the local field enhancement and genuine combination of the components. For instance, split-ring resonators on semiconductor substrates based on GaAs have been designed to achieve tunability via photoexcitation and superstrates with carbon nanotubes, graphene, or liquid crystals to exhibit dynamically tunable responses.

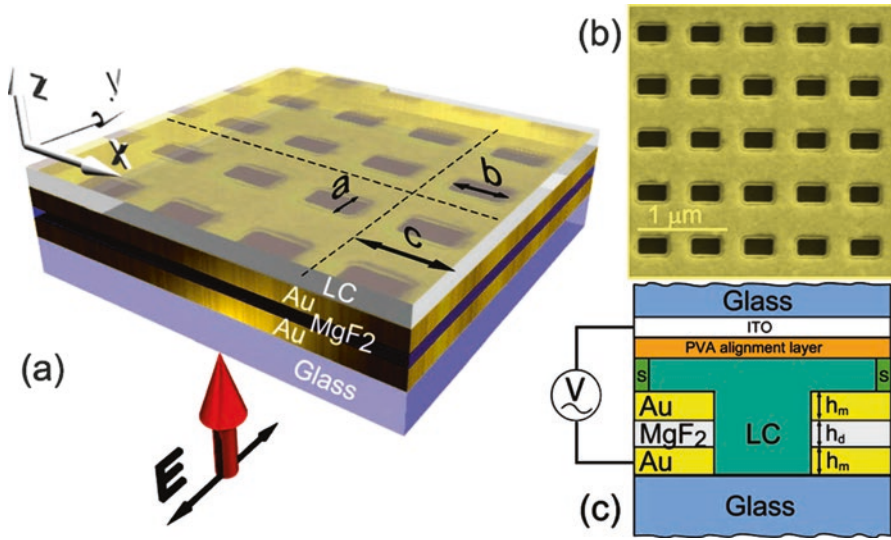


Fig. 9.3 Nonlinearity based on liquid crystals (Minovich et al. 2012): (a) schematic of the fishnet metamaterial structure infiltrated with nematic liquid crystal. (b) Scanning electron microscope image (*top view*) of the fabricated fishnet metamaterials. (c) Side view of the liquid-crystal cell

9.2.3 Local Field Enhancement

There may be two ways to enhance a nonlinear response of a conventional nonlinear material without actually changing its nature (Lapine et al. 2014): One is the use of a metamaterial structure to increase the local field in the area where nonlinearity is placed and thus to enhance the nonlinear response. The other is to make such a structural arrangement which would improve the efficiency of a specific nonlinear process, e.g., via better phase-matching conditions.

As shown in Fig. 9.4, substantial efforts for the local field enhancement have been performed with T-shaped nanoparticle pairs (top), L-shaped particles, nanorods, and more complex patterns. A particularly important role in the nonlinear processes in such structures is played by the local field effects, and important distinctions between surface and bulk nonlinearity contributions should be taken into account. With metal patterns of more complex, chiral geometry, nonlinear effects may come into play for various chiro-optical effects and result, in particular, in efficient second-harmonic generation enabled by symmetry breaking.

The diverse range of various local field enhancement techniques employs traditional nonlinearity of conventional materials in combination with unusual properties granted by metamaterial design, which boosts nonlinearity and provides new functionality. However, special care should be taken with regard to the side effects of using high power with metallic structures, which can cause excessive heating and complicate the observed spectra with the effects of thermal expansion or even damage the samples (Valev et al. 2013).

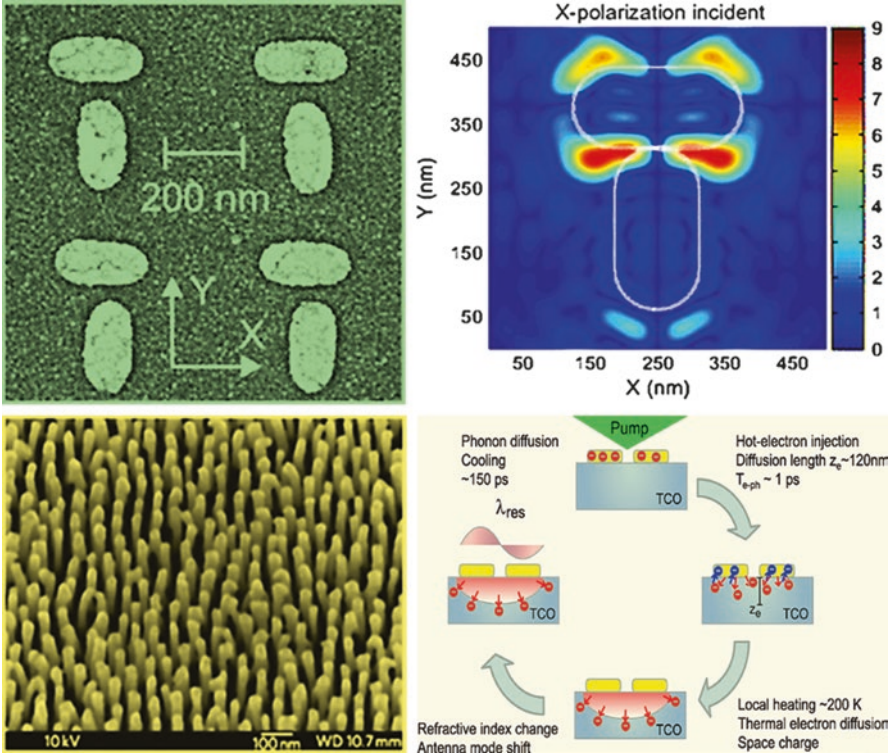


Fig. 9.4 Examples of metamaterials where local field enhancement is used to boost nonlinear processes (Lapine et al. 2014): T-shaped pairs of elongated nanoparticles and polarization-specific second-harmonic enhancement; fabricated nanorod “forests”; emergence of the nonlinear response upon hybridization of nanoparticles with transparent conducting oxides

9.2.4 Nonlinear Transmission Lines

Various nonlinear effects in left-handed transmission lines (LH TLs) have been studied. Usually, the nonlinearity is added to the structure by replacing capacitors with varactor diodes, which are shown as $C(V)$ in Fig. 9.5a. In a left-handed transmission line, each unit cell contains series capacitance and shunt inductor; in addition, any realistic transmission line has shunt capacitance and serial inductance (see L_s and C_s in Fig. 9.5a), which are tailored along with the main components to achieve a desirable dispersion. The resulting TLs have frequency bands of negative and positive phase velocities, as shown in Fig. 9.5b, and are called composite right-left-handed (CRLH) transmission lines. CRLH TLs have dispersion properties very similar to those of ideal metamaterials, and therefore, they offer an ideal model system for studying and verifying fascinating effects predicted for metamaterials. As an additional degree of freedom, the varactors can be also biased by dc voltage to control their capacitance. Furthermore, the possibilities to engineer dispersion of

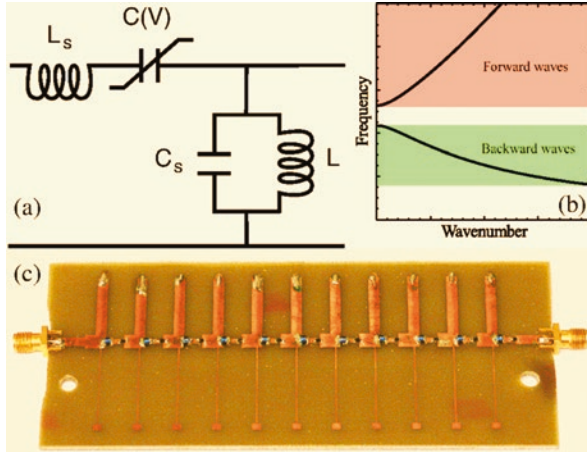


Fig. 9.5 Nonlinear transmission line (Somerville et al. 2011; Lapine et al. 2014): (a) schematics of a CRLH transmission line with nonlinear capacitance $C(V)$. (b) Dispersion of the CRLH TL showing the bands of frequencies where forward or backward modes are supported. (c) Nonlinear dual band CRLH TL with phase matching of zero phase velocity waves

waves in transmission lines allow one to obtain exotic regimes of phase matching between forward and backward waves, between two backward waves, and even between two waves with zero phase velocities. A dual band CRLH TL supporting such unique regimes of phase matching is shown in Fig. 9.5c (Somerville et al. 2011).

Nonlinear CRLH TLs have shown a rich variety of possible nonlinear phenomena. For example, the amplitude-dependent harmonic generation allows generation of short pulses with very sharp slopes. Another potential application of nonlinear CRLH TLs is in tunable leaky-wave antennas. Because of the ability to change the phase velocity of waves in tunable CRLH TLs between negative and positive values, in the leaky-wave regime, it becomes possible to steer the radiated beam over a large range of angles. All in all, nonlinear transmission lines offer easy implementation and practical functionality, being most useful for one-dimensional waveguides or two-dimensional surface arrays. They make high nonlinearity (with the strength of nonlinear modulation potentially comparable with linear signal) at low power (a fraction of watt to a few watts) available for the microwave frequency range (Lapine et al. 2014).

9.2.5 Intrinsic Structural Nonlinearity

An exotic way to provide nonlinearity to metamaterials relies on their internal structure rather than the properties of the materials or components. This involves a specific design that allows coupling between phenomena of different physical nature, so that the electromagnetic response is altered by mechanical or thermal effects.

Such an approach essentially brings new degrees of freedom into metamaterial design and opens a wide range of possibilities. Possible drawbacks are relatively slow response time and high power required for operation, which may cause excessive heating (Lapine et al. 2014).

9.2.6 Nonlinear Metamaterials with Quantum and Superconducting Elements

Quantum metamaterials in a broad sense are artificial electromagnetic composites which (i) comprise of quantum coherent elements with desired parameters, (ii) have quantum states that can be directly controlled, and (iii) maintain global coherence for the duration of time, exceeding the traversal time of a relevant electromagnetic signal. Without the properties (ii) and (iii), the system is essentially equivalent to a classical metamaterial made of intrinsically quantum meta-atoms. This is also valid for the so-called superconducting metamaterials—the most feasible candidates for the realization of quantum metamaterials (Lapine et al. 2014).

Quantum metamaterials offer a radically new paradigm for data processing and quantum information technologies and implementations for practical devices such as electro-optical modulators. Superconducting metamaterials may not only provide a dramatic reduction of losses but also allow access to the extreme sensitivity of the superconducting state to external stimuli such as heat, electric and magnetic fields, light, current, and mechanical stress.

9.3 Nonlinear Responses and Effects

The most prominent features of nonlinear metamaterials are the availability of exceptionally strong nonlinearities (sometimes exceeding 10% nonlinear modulation), the translation of microscopic electric nonlinearity into a macroscopic magnetic one, and the possibility of efficient dispersion engineering.

9.3.1 Nonlinear Self-Action

Nonlinear self-action is associated with the “first harmonic,” where, by virtue of nonlinear properties, the linear parameters of metamaterials are affected. This may result in switching of a metamaterial between different states, leading to bistable and multistable behavior, and can also provide continuous tuning of the linear properties with power. These effects are normally closely connected.

The conceptual origin of bistability in resonant structures relies on the fact that the frequency of the resonance may shift with the change of applied power, and if the dependence is sufficiently strong, the resonance effectively “bends,” yielding nonstable configurations. This results in jumps between different branches of the multivalued response function, which can be observed with varying amplitude or frequency, so that for a given input intensity, two output intensity levels can be observed. Bistability phenomena were mostly treated from a theoretical or numerical perspective. Nevertheless, magnetoelastic metamaterials permitted direct experimental observation of rotational bistability in a metamaterial with an internal mechanical degree of freedom, where the SRRs, connected through elastic feedback, were allowed to twist with respect to each other. Moreover, a system of three resonators, which are both electromagnetically and mechanically coupled, will offer much more sophisticated nonlinear dynamics in the mechanical and electromagnetic response, leading to nonlinear self-oscillations and chaotic behavior (Lapine et al. 2014).

Contrary to multistability, tunability is a much more practical outcome of nonlinear self-action. With tunable nonlinear metamaterials, one aims to control and adjust the linear properties with power, and this is a clear target for applications. At the same time, tuning the nonlinear properties themselves is also an interesting point to consider. Tunability of electronic structures is relatively straightforward to realize with the help of additional biasing circuits which control the properties of nonlinear elements. Thus, inserting an externally biased varactor into an SRR allows its resonance frequency to be shifted with applied voltage, while incorporating varactors into a leaky-wave antenna, designed as a transmission line metamaterial, results in its radiation angle and beam width being tunable with electronics. On the other hand, self-tunability can be achieved with incident electromagnetic waves, making a direct use of nonlinearity. Having a nonlinear resistance results in a drop in transmission with the increasing power, while using a nonlinear capacitance shifts the resonance frequency, permitting a metamaterial slab to be tuned between transmission, absorption, and reflection. Apart from the use of nonlinearity to tune metamaterial properties with power, other tuning approaches can be employed to modify the nonlinear response, for example, by applying structural tuning to control the nonlinear properties of symmetric and antisymmetric modes in the varactor-loaded coupled resonators (Hannam et al. 2012). In addition, nonlinearity in metamaterials often leads to nontrivial time-dependent processes and gives rise to a number of instability scenarios.

Nonlinear chirality has been studied with insertion of a chiral electromagnetic diode, which is a direct analog of an electronic diode. A convenient planar design of the canonical spirals is shown in Fig. 9.6, which offers a great potential for engineering of the electric, magnetic, and chiral properties of the nonlinear metamaterials. Another approach to obtain power-dependent chirality relies on structural nonlinearity, which can be achieved with flexible helices for metamaterials, whereby multiturn helices appear to be particularly useful, as they show both a stronger chirality and a stronger nonlinear response. The chirality of each helix directly depends on its pitch, so the mechanical contraction commencing with increasing power

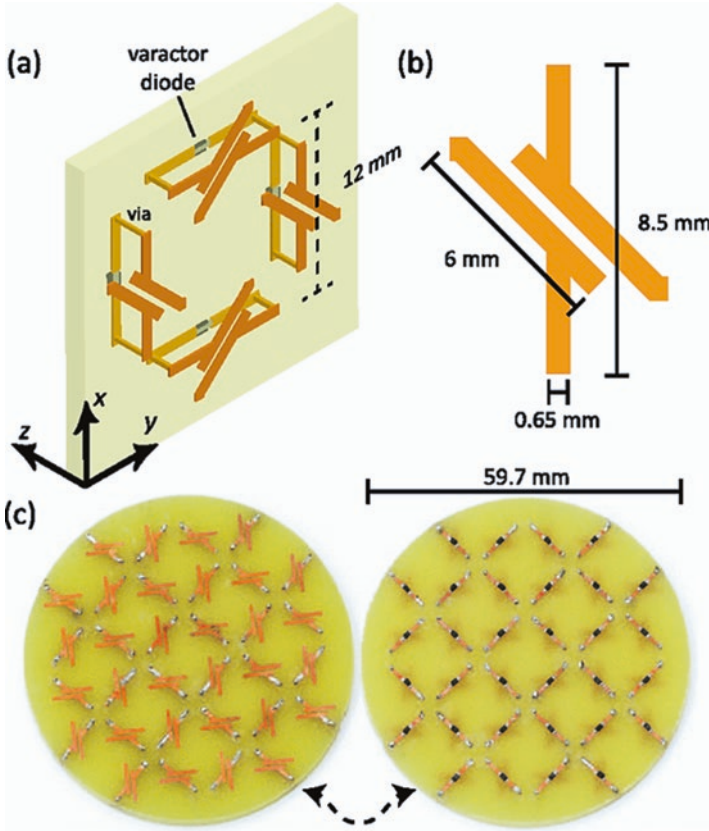


Fig. 9.6 Nonlinear chirality (Lapine et al. 2014): (a) metamaterial unit cells each consisting of two nonlinear particles; (b) details of one side of the nonlinear particle, with (c) photographs of the two sides of the fabricated sample

decreases the chirality coefficient. This may lead to interesting behavior related to the wave propagation inside the bulk samples of such metamaterials, leading to nonlinear polarization rotation and formation of dynamic domains with different chirality inside the initially homogeneous metamaterial (Lapine et al. 2014).

9.3.2 Frequency Conversion and Parametric Amplification

Harmonic generation and parametric amplification are two of the most widely used nonlinear effects. These processes involve energy exchange between waves of different frequencies, and this becomes possible due to nonlinear properties of the media supporting the interacting waves. In metamaterials, due to nontrivial linear and nonlinear properties, these processes are significantly different as compared to natural dielectrics (Lapine et al. 2014).

9.3.2.1 Harmonic Generation

Second-harmonic generation, also known as frequency doubling, is the generation of an electromagnetic wave with a frequency twice that of the incident wave. In metamaterials, because of the narrow frequency band, where the index of refraction is negative, the interaction of the fundamental frequency and second harmonics takes place for the waves with energy propagating in opposite directions, for which exact phase matching can be achieved. Such interaction of a backward fundamental frequency (FF) wave and a forward second-harmonic (SH) wave leads to second-harmonic generation in the reflected wave, and for the case of the semi-infinite metamaterial, it will form a second-harmonic reflecting mirror. Using the freedom of metamaterial engineering, it is possible to enhance the nonlinear interaction by using double-resonant metamaterials. The effective nonlinear susceptibility is proportional to the product of linear susceptibilities at the interacting frequencies. As a result, a metamaterial containing resonators of two types, with resonant frequencies differing by a factor of two, can lead to a significant enhancement of the second-harmonic generation. Third-harmonic generation and higher-order effects have also been studied in microwave and optical ranges.

In optics, most metamaterials have one or a few layers with metallic inclusions, and their properties are often dominated by surface plasmon polaritons or localized plasmons when the metamaterial structure contains individual metallic nanoparticles. Rather than the nonlinear response of dielectrics, in plasmonic structures, the nonlinearity is dominated by the response of free electrons in metals. In particular, the efficiency of the SHG process depends on the symmetry of the nanostructures, and a seemingly small difference in the arrangement of the nanoparticles can lead to a dramatic change in the second-harmonic generation. At the same time, with an appropriate combination of centrosymmetric and noncentrosymmetric arrays, SHG can be dramatically enhanced via plasmonic interactions (Czaplicki et al. 2013).

Hyperbolic metamaterials also offer curious implications for second-harmonic generation: for example, in layered media, a generated signal can be trapped and phase locked under the cone of a pump (de Ceglia et al. 2014).

9.3.2.2 Parametric Amplification and Loss Compensation

Parametric amplification is the process of amplifying a signal wave by using a high-power pump from which energy is transferred to the signal via nonlinear interaction. Since metamaterials typically rely on using metallic or high-index materials, significant attenuation of electromagnetic waves due to dissipation is often encountered. For this reason, parametric amplification has been used as a means of compensating losses in negative-index materials with demonstrations mostly performed in the microwave range, including transmission lines, magnetoinductive arrays, as well as ring resonators, bulk SRR structures, and cavities (Lapine et al. 2014).

9.3.2.3 Phase Matching

The freedom in metamaterial design provides a route to dispersion engineering or built-in quasi-phase matching. Phase matching has been done via a specific design relying on metamaterial arrays with dual resonances, assembled as two subsystems of resonators with different resonant frequencies. Alternative options for phase matching are offered with the harmonic generation in reflection, available in nonlinear metamaterials with negative refraction—the so-called nonlinear-optical mirror. It is also possible to achieve automatic phase matching in metamaterial arrays, where the parameters can be adjusted so as to achieve matching conditions on a single dispersion curve. Then, dispersion engineering, owing to unique linear properties of metamaterials, may play a significant role for phase matching, particularly if the effective wavelength in the medium becomes extremely large so that no phase is accumulated over the interaction length (Suchowski et al. 2013).

Quasi-phase matching in metamaterials can be realized by the design of splitting resonators embedded in a semiconductor with the gaps filled with silicon. The photosensitivity of silicon inclusions is then used to tune the resonance of the meta-atoms by imposing a spatially periodic intensity pattern of laser illumination, adjusted to modulate the resonance strength to achieve phase matching via periodic perturbation. The ease of metamaterial design for microwaves also allows direct application of standard phase-matching principles, such as periodic poling (Rose et al. 2011).

9.3.2.4 Phase Conjugation

Phase conjugation is a specific four-wave mixing process which aims to compensate any distortion of a signal propagating through a medium, by effectively reversing the wave front in the reflected signal. Apart from the phase conjugation, four-wave mixing processes in nonlinear nanostructures have been investigated to imitate negative refraction in planar systems or to provide high conversion efficiency when using with plasmonic nanoantennas (Maksymov et al. 2013).

9.3.2.5 Stimulated Raman Scattering

Another specific process which depends on the third-order nonlinear susceptibility is the scattering of propagating waves by optical phonons, known as Raman scattering. In metamaterials, apart from the likely requirement to consider the corresponding phenomena at lower frequencies than optical ones, some peculiarities of stimulated Raman scattering can be expected in cases where negative refraction is involved. The choice of having a negative index for the Stokes component is quite natural with the resonant origin of negative parameters, as it avoids severe complications with having the pump wave in the vicinity of the metamaterial resonance (Lapine et al. 2014).

9.3.2.6 Nonlinear Subwavelength Lenses

Metamaterial superlens offers subwavelength focusing along with evanescent field enhancement, which can be improved with the use of quadratic nonlinearity, where a microwave superlens, assembled with nonlinear SRRs, is designed to be opaque for the fundamental while being negatively refracting for the second harmonic. This device provides a second-harmonic image, whereas the original source could be screened. A similar effect occurs when a negatively refracting linear layer is combined with a conventional nonlinear slab. Nonlinear imaging is also suggested with hyperbolic metamaterials with the second-harmonic signal generated from a pair of sources resolved, while the sources are indistinguishable at the fundamental frequency. The impact of nonlinearities on the focusing performance of Lüneburg (gradient) lenses has also been investigated (Mattheakis et al. 2012).

9.3.3 Surface Effects

Surface plasmon polaritons are widely used in sensing applications with the ability to design structures supporting surface modes with desired properties, such as polarization, localization, and wavelength. Surface waves can be either forward or backward, i.e., their phase fronts propagate either with or against the energy flow, respectively. Such behavior is possible because the energy flows in negative-index materials and dielectrics are in opposite directions (Fig. 9.7a) and their balance determines the direction of the total energy flow. To add one more possibility for manipulating the properties of surface guided waves, it may be considered that the materials forming the interface are nonlinear (Shadrivov et al. 2004). In particular, this will allow the dispersion of the waves to be controlled, so that the type of the waves can be switched between forward and backward by adjusting the wave intensity (Fig. 9.7b). In other words, such tuning can allow changing the sign of the group velocity. In a particular point, when the group velocity vanishes, the energy flowing in the negative-index medium is compensated by that in the dielectric. Nonlinear change of the dispersion is also crucially important for the propagating temporal surface plasmon solitons, the spreading of which is determined by the wave dispersion (Shadrivov et al. 2004).

Another type of nonlinear surface waves is related to the nonlinear Tamm state. Such waves are localized due to the bandgap of the periodic structure and can exist at surfaces which do not support linear surface modes (Lapine et al. 2014).

A beam reflected from an interface between two media experiences a lateral displacement from its position, because each of its plane-wave components acquires a different phase shift. The lateral shift is called the Goos–Hänchen effect, and it is usually much smaller than the beam width. However, larger beam shifts may occur in either layered structures supporting surface waves, which are able to transfer energy along the interface, or at nonlinear interfaces, where the higher power of the incident beam may result in nonlinear surface wave excitation. Surface waves are

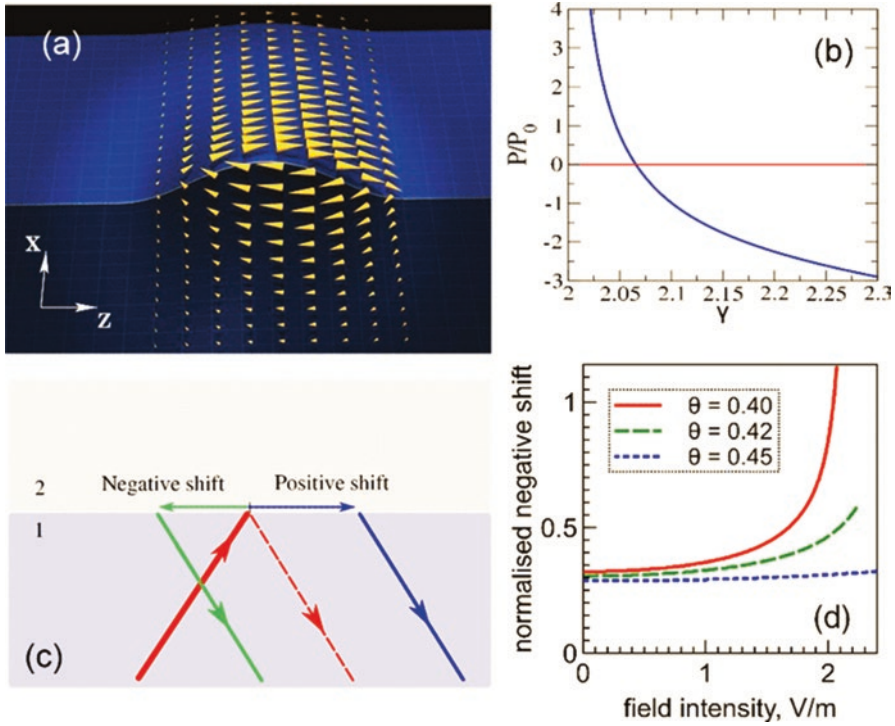


Fig. 9.7 Nonlinear surface waves and Goos-Hänchen (Shadrivov et al. 2004; Lapine et al. 2014): (a) energy flow diagram in a pulse propagating along the surface between a negative-index metamaterial and a positive-index dielectric; (b) example of the normalized energy flow in the surface mode as a function of the wave number; (c) schematic of negative and positive Goos-Hänchen shifts at the reflection from the interface between two media; (d) dependence of the nonlinear Goos-Hänchen shift on the incident field intensity at various incident angles

not excited at a single interface between linear media, because the phase-matching condition of the incident (propagating) and surface (localized) waves is not satisfied. The Goos-Hänchen shift can be either positive or negative (Fig. 9.7c) depending on the type of the wave excited. In particular, a negative beam shift can be observed at the interface between linear dielectric and nonlinear negative-index material due to the nonlinearity; the effect depends on the intensity of the incident wave, as shown in Fig. 9.7d (Zhang et al. 2008).

In the Otto configuration for the excitation of nonlinear surface waves, the beam shift becomes bistable as a result of the resonant excitation of the surface waves. The wave intensity affects the resonant phase-matching condition for the wave excitation, thus providing a bistable response for the angle of incidence close to the resonance condition. Additionally, the Goos-Hänchen shift affects the group delay of the pulses scattered on finite slabs of negative-index metamaterial (Lapine et al. 2014).

9.3.4 *Nonlinear Guided Waves and Solitons*

For guided waves, nonlinear effects may not only change the properties of guided modes and introduce symmetry breaking effects, but they may also lead to the creation of new families of waves, such as spatial or temporal solitons. Spatial solitons are electromagnetic beams, whose diffraction is arrested by the nonlinear self-focusing, while temporal solitons are pulses whose dispersion broadening is compensated by nonlinear self-action effects. The models employed for the study of the nonlinear guided waves in metamaterials can be divided into two major categories (Lapine et al. 2014): (a) discrete approach, treating metamaterial as an array of coupled nonlinear resonators, and (b) assuming that metamaterial is a homogeneous effective medium with specific dielectric permittivity, magnetic permeability, as well as nonlinear response. Metamaterials are strongly affected by dissipation, which should not be neglected in realistic models. As a result, stable temporal solitons do not exist in a pure form, but instead soliton-like pulses or dissipative solitons can form due to the presence of nonlinearity. As an example, soliton-like pulses can be generated by continuous waves in metamaterials with resonant nonlinearity.

9.3.5 *Discreteness Effects*

In general, the response of a metamaterial is not simply given by the sum of the responses of individual resonators but also depends on the interaction between the resonators within the system, which can be particularly sophisticated when the near-field interaction is involved. A standard theoretical approach for analyzing the properties of metamaterials is based on the effective medium approximation when the structure is treated as a homogeneous medium being characterized by effective macroscopic parameters. However, with finite size, as well as with larger wave vectors, metamaterials demonstrate their discrete nature and strong nonlocal effects, so they should be described as arrays or lattices of resonant elements (Lapine et al. 2014).

Discreteness effects are essential for parametric amplification in coupled magnetoinductive waveguides. In that case phase-matching conditions can be satisfied by tailoring the dispersion characteristic of magnetoinductive waves, governed by discrete structure. Nonlinear physics of discrete metamaterials can be studied using coupled nonlinear equations describing nonlinear magnetoinductive waves, with the modification by taking into account both electric and magnetic near-field coupling between the neighboring sites. (Rosanov et al. 2011).

Besides, nonlinear effects in active metamaterials, tunable metamaterials, nonlinear plasmomics, and nonlinear acoustic metamaterials have also been explored. Nonlinear metamaterials will bring unique functionalities by allowing the engineering of artificial media and the nonlinear response of such media to create a new paradigm of metadevices, with varied nonlinear effects such as nonlinear selfaction,

parametric interactions, and frequency conversion, which will boost the development of various methods for achieving tunable, switchable, nonlinear, and sensing functionalities of metamaterials.

9.4 Applications of Nonlinear Metamaterials Toward Functional Metadevices

Many research and application areas have turned to artificial and composite materials, with homogenizable metamaterials representing an extension of such composites into the electromagnetic domain. In particular, the inclusion of nonlinear elements has caused metamaterials research to spill over into the field of nonlinear optics. Through appropriate design of their constituent elements, nonlinear metamaterials are capable of supporting an unprecedented range of interactions, promising nonlinear devices of novel design and scale.

9.4.1 *Controlling Light with Nonlinear Metamaterials*

Nonlinear metamaterials can find many useful applications, e.g., for super-resolution and transformation optics. Many efforts have been made to achieve tunability of the metamaterial properties, either externally or by employing their nonlinear response. At microwave frequencies, it is relatively easy to design a tunable nonlinear meta-atom as a split-ring resonator (SRR) loaded with a varactor diode that operates in either bias-free or biased regimes and subsequently creates a bulk nonlinear magnetic metamaterial allowing a power-induced control of the wave transmission. Moreover, such artificial nonlinear media allow the demonstration of many interesting phenomena accessible at low powers such as a nonlinear-optical mirror (Kivshar 2014).

On other hands, second-harmonic generation (SHG) from nanostructured metallo-dielectric metamaterials with an engineered quadratic nonlinear response provides extreme local field enhancements. This can be achieved through metamaterial-based nonlinear photonic crystals (NLPCs) to enhance the collective nonlinear phenomena to a level that is orders of magnitude larger than those of natural nonlinear materials. In NLPCs, the quadratic nonlinear coefficient $\chi^{(2)}$ is modulated in one-, two-, or three-dimensional periodic or quasiperiodic patterns, which affect the nonlinear generation process. In addition to generating an efficient nonlinear signal, they can be used to prevent walk-off of the interacting beams and enable the adjustment of other aspects of the interaction such as the direction of the generated beams and their spatial shape. Moreover, NLPCs can be used for active metadevices and the efficient generation of entangled photon pairs. Merging the power of NLPCs to control nonlinear interactions with the potential of metamaterials for artificial optical manipulation can control nonlinear interactions in metamaterials. It can also be used to achieve

efficient quasi-phase-matched nonlinear interactions, which can increase the total conversion efficiency by orders of magnitude in order to develop nonlinear metamaterials that are viable for device applications (Segal et al. 2015).

The SRR-based NLMPCs are constructed based on utilizing the geometry of the SRRs to set the phase of the locally generated second harmonic (SH) at the level of each SRR meta-atom with respect to the phase of the fundamental harmonic (FH) (Fig. 9.8). For an FH beam polarized along the base of the SRR, the generated SH currents are mostly cross-polarized with respect to the polarization of the incident FH beam and are asymmetric with respect to the base of the SRR (Fig. 9.8b). A mirror inversion of the SRR with respect to its base will therefore have a minimal effect on the FH beam but will induce π phase shifts on the SH currents and the locally generated SH radiation (Fig. 9.8d). To construct a one-dimensional periodic NLMPC, the orientation of the SRRs is inverted with a period Λ , which leads to periodic inversion of the effective $\chi^{(2)}$ (Fig. 9.8a). Figure 9.8c shows the simulated near-field radiation pattern of the FH and SH for the case of uniform SRR arrays and NLMPCs, respectively. The near-field patterns of the FH are uniform in both cases, whereas the near-field patterns of the SH are uniform for the case of uniform arrays and have the desired π phase shift for the NLMPC. This leads to the simulated far-field emission patterns shown in Fig. 9.8e, f, respectively (and illustrated in Fig. 9.8a), demonstrating that the SH emission can be controlled and directed by the NLMPC (Segal et al. 2015).

The exceptional ability of NLMPCs to control the direction of the nonlinear emission can also be used to focus the nonlinear emission directly from the NLMPC and in this way can lead to huge intensity improvements of the nonlinear signal, even from two-dimensional NLMPCs. Figure 9.9 shows a design of NLMPC that acts as a nonlinear binary-phase Fresnel zone plate (FZP). Adjacent zones of the NLMPC-based FZP consist of SRRs with mirror inversion symmetry (Fig. 9.9a) and generate SH with opposite phase. The focus of the nonlinear lens was set to be 1 mm away from the sample. The diameter of the SH at the focus was 7 μm , and its intensity was 73-fold higher than the intensity of the generated SH at the surface (Fig. 9.9b–e). This agrees reasonably well with simulation results, which predict an intensity enhancement of about 150-fold. The difference can be attributed to the fact that the exciting FH field was Gaussian instead of flat (as in the simulation). Although the SH emission is strongly modified by the lens, the direction of the FH beam is unaffected. In addition, the SH radiation patterns involve strongly focused and defocused forward and backward emission, which can be used for various nonlinear illumination schemes (Segal et al. 2015).

In addition, by designing an NLMPC-based ultrathin (30 nm) nonlinear FZP, an enhancement of the SH intensity of almost two orders of magnitude can be achieved without the need for an external lens. This potentially provides a wide range of opportunities for the creation of integrated, ultracompact, nonlinear optical devices such as frequency converters, all-optical switches, scanners, and optical amplifiers with potentially unique control schemes. These can also be combined with photonic and plasmonic waveguides for the construction of advanced active photonic circuitry (Rose et al. 2011; Segal et al. 2015).

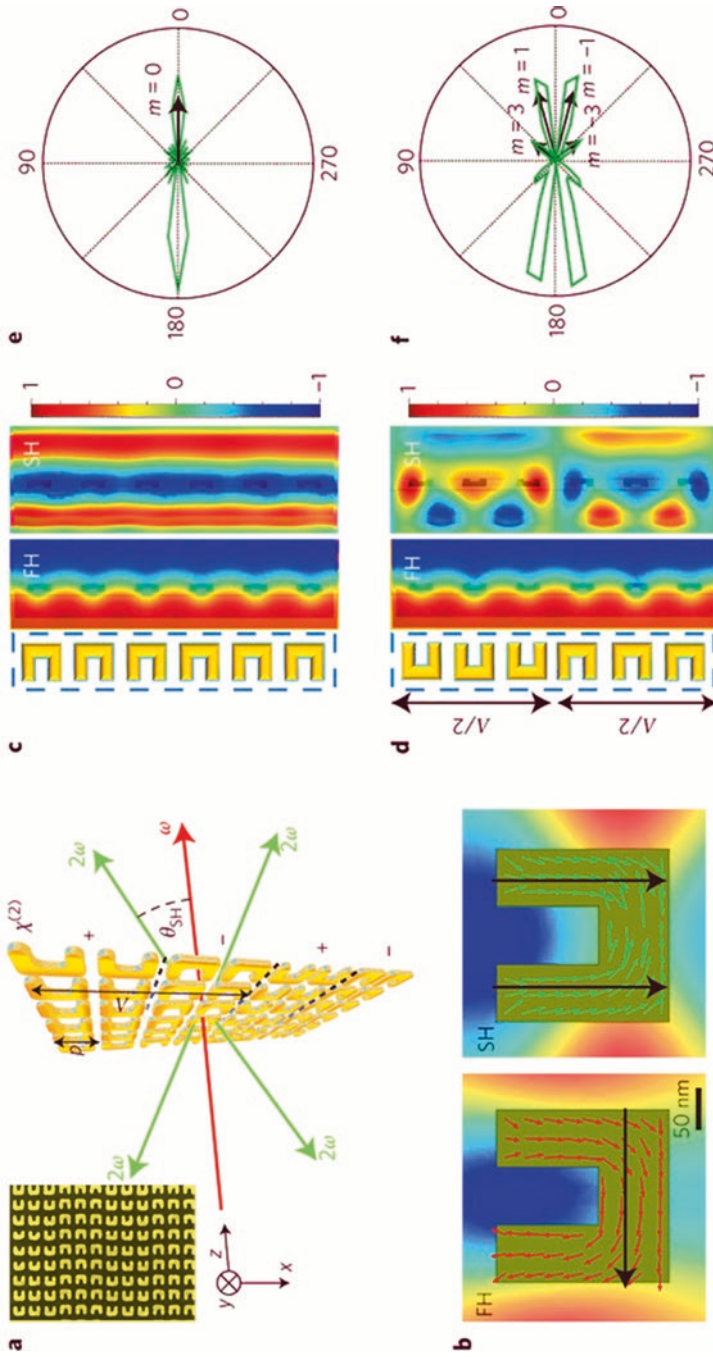


Fig. 9.8 Manipulating the direction of nonlinear emission by NLMPCs (Segal et al. 2015): (a) NLMPC with one-dimensional modulation of $\chi^{(2)}$ (Λ is the modulation period and p is the SRR period); (b) calculated FH surface currents and generated SH currents. *Black arrows* mark polarization of the FH beam, the average polarization of the SH currents and emitted radiation. Color scale shows the near-field radiation 100 nm from the SRRs (same color key as in c and d). (c, d) Simulated near field of the FH and emitted SH for uniform arrays (c) and for the NLMPC ($\lambda_{FH} = 1300$ nm; $p = 400$ nm; and $\Lambda = 2400$ nm); (d) the phase of the SH emission from the NLMPC is flipped due to the inverted SRRs, while the FH radiation maintains a constant phase; (e, f) far-field SH emission from uniform array and NLMPC, respectively. SH emission patterns are not symmetric with respect to the vertical meridian due to emission to different media (air on the right and glass on the left)

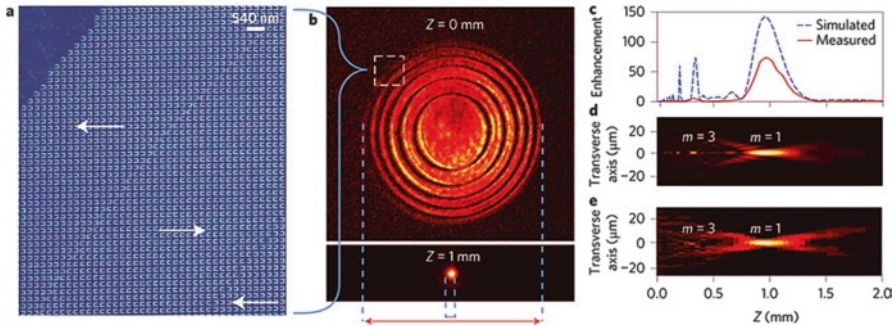


Fig. 9.9 Nonlinear Fresnel zone plate (FZP) from NLMP (Segal et al. 2015): (a) zoomed scanning electron micrograph of a part of the FZP showing mirror inversion of the SRRs in adjacent zones that radiate SH with opposite phases. Arrows mark the effective $\chi(2)$ direction; (b) recorded normalized images of SH (600 nm wavelength) at $Z = 0$ and $Z = 1$ mm; (c) SH intensity enhancement with respect to SH intensity generated on the surface of the nonlinear FZP lens; (d, e) Beam propagation simulation (d) and experimental results (e) of transverse focusing of SH by the nonlinear lens (m denotes focusing order)

Indeed, the ability to control the local material properties by applying light patterns may lead to unprecedented flexibility in confining, guiding, or redirecting the flow of electromagnetic radiation. This will make it possible to fabricate dynamically tunable structures such as lenses and waveguides, as well as fully reconfigurable cloaking meta-device (Kivshar 2014).

9.4.2 Nonlinear Terahertz Metadevices

Nonlinear terahertz (THz) metamaterials can confine the electric or magnetic field to subwavelength dimensions, yielding pronounced field enhancement. This enables functional meta-device development using the phenomena such as field-induced phase transitions, ultrafast field emission of electrons, electromigration, and electroluminescence. In general, nonlinear THz metamaterials can be realized by integrating subwavelength resonators with transition metal oxides, semiconductors, or any other nonlinear dielectric medium. Semiconductors such as GaAs and InAs have been mostly used. It is also possible to exclusively employ semiconductors to create plasmonic devices at THz and infrared frequencies. The plasma frequency of semiconductors can be tuned by adjusting the doping level, providing a path toward THz plasmonic semiconductor metamaterials (PSMM). The response of PSMM can be tailored via structure and geometry and can be modulated using, as examples, electric, magnetic, and thermal stimuli. Importantly, semiconductors exhibit large nonlinearities at THz frequencies enabling nonlinear plasmonics and providing a key capability for terahertz circuits and systems (Seren et al. 2016; Zhao et al. 2016).

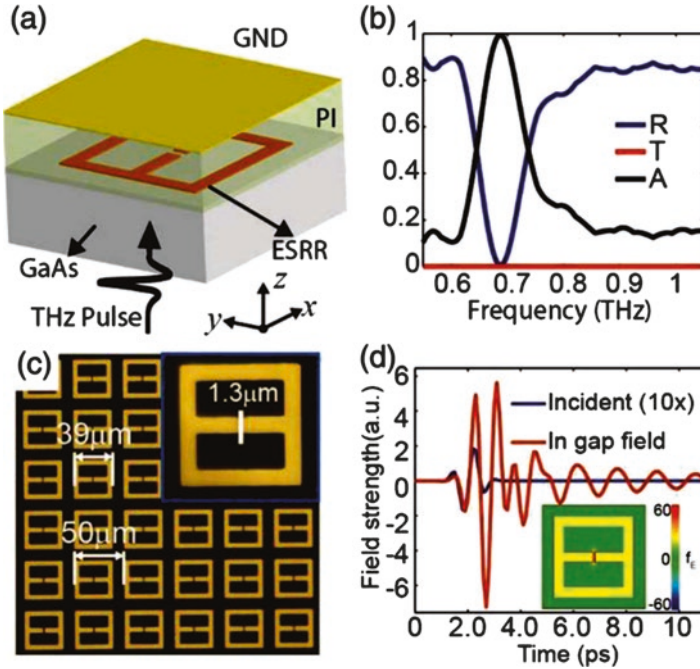


Fig. 9.10 Nonlinear terahertz metamaterial perfect absorber (MPA, Zhao et al. 2016): (a) schematic of the MPA on the GaAs substrate; (b) simulated transmission (T), reflection (R), and absorption (A) spectra; (c) microscope image of the ESRR array of the MPA (inset, closeup view of a unit cell); (d) simulated time-domain field strength of the incident THz pulse ($10\times$) and the electric field in the middle of the capacitive gap (inset, the 2D map of the electric field enhancement factor (fE))

One example of the nonlinear THz MPA is shown in Fig. 9.10, which consists of an array of electric split-ring resonators (ESRRs) on the semi-insulating GaAs (SIGaAs) substrate, a polyimide (PI) spacer, and a gold ground plane (GND, Fig. 9.10a). When the THz pulse impinges on the metamaterial from the GaAs substrate, a fraction of the electromagnetic (EM) wave will be reflected due to the induced currents in the ESRR. The remaining portion will be transmitted into the spacer layer, which will be totally reflected by the GND after traveling in the PI spacer. Multiple reflections occur in the spacer. For each metamaterial structure, an optimized spacer thickness can be found to cancel out the reflection due to the destructive interference. At the same time, the transmission is blocked by the ground plane. As a result, the EM wave is absorbed by the MPA at these frequency bands. For instance, near-perfect absorption at 0.7 THz can be achieved (Fig. 9.10b) with the metamaterial structure shown in Fig. 9.10c. According to the simulation results shown in Fig. 9.10d, the peak field in the 1.3 μm capacitive gap is enhanced by a factor of 30 in comparison to the incident field. In the MPA structure, multiple reflections of the THz pulse in the spacer layer induce surface currents in the ESRRs. On resonance these currents add constructively, resulting in a higher field

enhancement in the capacitive gaps than for the case of single-layer ESRRs. The intense in-gap electric field can induce electron tunneling and/or impact ionization (IMI) in the semiconductor substrate, modifying the electronic properties of the substrate in the vicinity of the gap. This, in turn, changes the EM response of the MPA (Zhao et al. 2016).

Furthermore, nonlinear terahertz devices have also been fabricated utilizing plasmonic semiconductor metamaterials (PSMM). While the PSMM absorbers with a GaAs substrate demonstrate the feasibility of creating metamaterial saturable absorbers and optical limiters, it is desirable to eliminate the substrate to achieve real perfect absorption. As shown in Fig. 9.11, substrate-free PSMM absorbers have been made using n-InAs film grown on an AlAsSb sacrificial layer grown via MBE

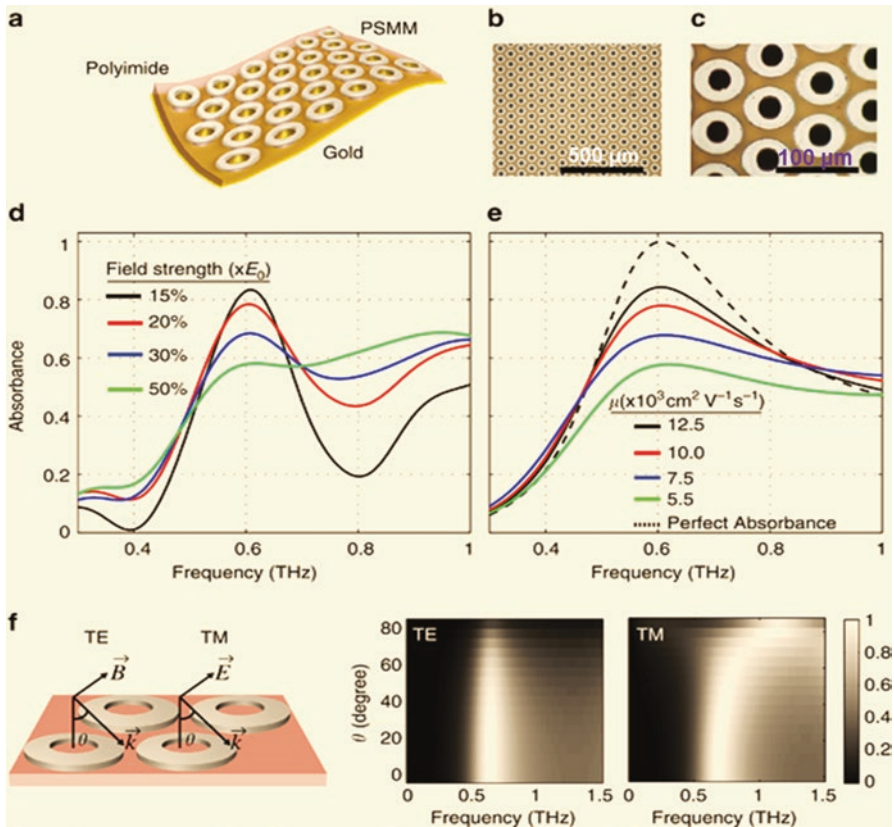


Fig. 9.11 Plasmonic semiconductor metamaterial absorber on flexible substrate (Seren et al. 2016): (a) representative sketch of the flexible semiconductor-based metamaterial absorber; (b) microscope image of the fabricated flexible absorber; (c) closeup image of the rings. Rings have 30 μm outer and 15 μm inner radius on average with 72.7 μm hexagonal symmetry; (d) terahertz-time-domain spectroscopy measurements showing the absorbance for increasing field strength; (e) simulated absorbance spectra for Drude models with varying mobility and effective mass; (f) simulated absorbance spectra of substrate-free absorber as a function of incidence angle (θ) for TE and TM polarized THz light

on a SI-GaAs substrate. This substrate-free device is optimized to act as a saturable THz absorber (Seren et al. 2016).

In addition, PSMMs are of potential use in applications that include ultrafast THz optics and as protective layers from strong resonant electromagnetic fields. The ability to create flexible nonlinear devices further facilitates applications since these PSMMs can conformally adhere to curved surfaces. PS resonators complement existing metallic structures, such as split ring resonators, providing alternative fabrication strategies to create active materials with reduced local field enhancement and correspondingly higher damage thresholds. Geometries other than disk and ring arrays (for example, dimers or bowties) can also be employed to obtain useful functionality. Finally, the doping level and defect density in InAs can be engineered to control the resonance frequency, strength, and response time of MM devices. In principle, even higher mobility materials (e.g., InSb or two-dimensional electron gases) will yield even sharper plasmonic resonances (Seren et al. 2016).

9.4.3 Control of Quantum Dot Emission

The control of spontaneous emission in photonic structures relies on enhanced light–matter interactions due to strong field enhancement and large interaction times. Therefore, nanostructured plasmonic materials have been used for this purpose owing to their high field localization and good coupling to free space. Particularly, the strong local-field enhancement near metallic structures can be used to manipulate spontaneous emission properties of quantum emitters and opens up the way to a broad range of applications such as quantum information devices, efficient lasers, and solar energy harvesting. Spontaneous emission control of fluorescent molecules and quantum dots (QDs) has been implemented using metallic substrates or small spherical metal nanoparticles. On the other hand, the opportunity of achieving loss reduction and gain in plasmonic structures using quantum emitters is particularly promising for optical metamaterials where the step to practical applications is significantly hindered by inherent and strong energy dissipation in the metal. Overcoming this major obstacle would lead to novel functional materials based on the possibility of tailoring not only the electric but also the magnetic properties of light at optical frequencies. This opens up new functionalities such as negative refractive index, chirality and subwavelength imaging, active metamaterials, and quantum metamaterials (Kivshar 2014).

Efficient polarization-dependent control of spontaneous emission of quantum dots (QDs) has been demonstrated through coupling to selected metamaterial modes (Fig. 9.12). By superimposing two orthogonal modes of equal strengths at the wavelength of QD-photoluminescence, emission control via sharp differences in the interaction of QDs with magnetic and electric modes of the split-ring resonator metamaterial can be done. Spontaneous emission control in QD-metamaterial systems has paved the way toward loss-compensated metamaterials, quantum metamaterials, and metamaterial nanolasers (Decker et al. 2013).

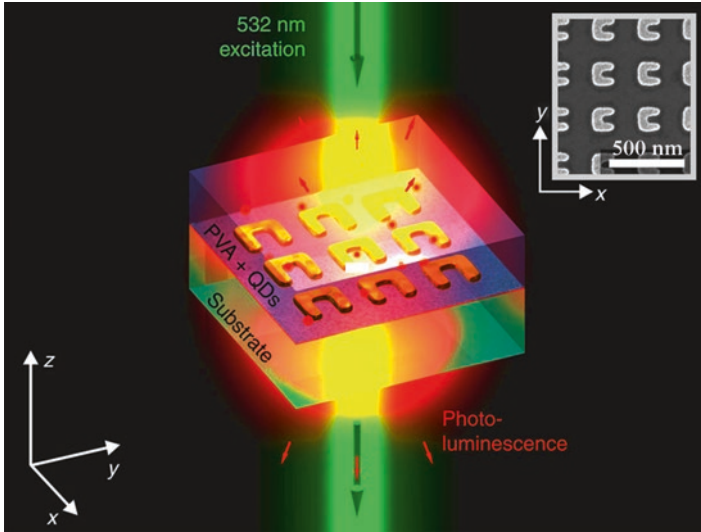


Fig. 9.12 A magnetic SRR metamaterial processed on a glass substrate is covered by a 200-nm-thin PVA layer containing QDs. The sample is excited by 532-nm CW laser from the top with a $\times 100$ objective (NA = 0.9). The measured spot size was ~ 800 nm. The QD PL is then collected from the bottom. The inset shows a scanning electron micrograph of a sample without the QD-containing PVA layer (Decker et al. 2013)

9.4.4 Metamaterial RF Limiter

An RF limiter is a circuit device which is typically used to protect sensitive electronics (such as a low-noise amplifier) from high-power signals and surges. The metamaterial RF limiter has a different topology than that of a circuit-based limiter: it can be designed as a screen, to be placed around a device or system requiring protection from high signals. In contrast, circuit-based limiters must be plugged into the RF electronics of the system needing protection.

The base metamaterial particle selected to form the metamaterial RF limiter is a complementary electric inductive–capacitive (CELC) resonator, as shown in Fig. 9.13. A CELC is a planar metamaterial and thus well suited for constructing an RF limiter sheet. As the complement of an electric inductive–capacitive resonator, a CELC exhibits high reflection and absorption except at its resonant frequency f_0 while exhibiting high transmission at f_0 . The CELC also includes a large, continuous ground plane as part of each unit cell. The PIN diodes are used to shorten the interiors of the CELCs at high power, preventing them from resonating and thus decreasing transmission. At low power, the diode presents a large resistance across the gap. At high power, the diode presents a very small resistance, effectively shorting the interior of the unit cell to the ground plane. Shorting a CELC in this way destroys the resonance, decreasing the transmission of the metamaterial. The performance of the metamaterial RF limiter is similar to that of a traditional circuit

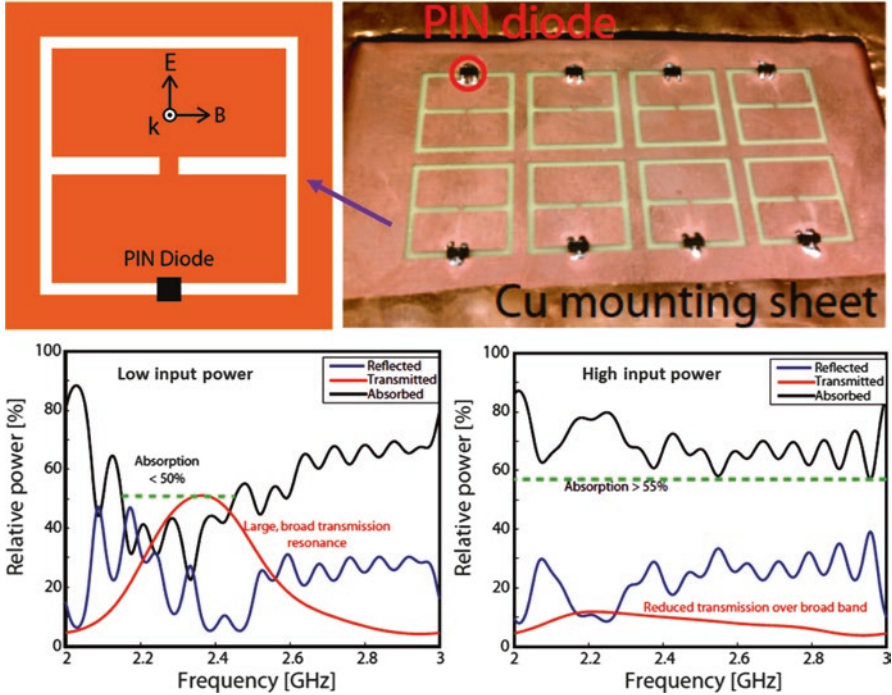


Fig. 9.13 Metamaterial RF limiter and its power analysis at different input power levels (Katko 2014)

limiter but in the form of an easily deployable sheet. Nevertheless, a metamaterial can be designed to mimic an essential nonlinear function of a circuit by embedding a particular type of nonlinear device in a metamaterial unit cell (Katko 2014).

9.4.5 Metamaterials-Based Energy Harvesting

A generalized energy harvesting process is to generate electrical energy from its surroundings using special conversion mechanism. The environmental energy sources may include kinetic energy in the form of vibrations and noises, electromagnetic radiation, thermal energy, and so on. In practice, an energy harvesting device has to be closely tuned to its power source in order to achieve high conversion efficiency, which depends strongly on the conversion medium. With their unique nonlinearity and tenability, metamaterials have been introduced into designing innovative conversion media for high-performance energy harvesting.

Phononic crystals have been used for vibration elastic wave broadband and low-frequency vibroacoustic energy harvesting (VAEH). According to basic properties of phononic crystals, phononic bandgaps have the ability of forbidding elastic

waves from propagating within specific frequency ranges. So as long as vibration or acoustic frequencies fall in the bandgap, the strongly localized energy can be converted into electrical energy using photonic crystals. Moreover, a phononic crystal can have several bandgaps simultaneously, which may be an advantage in practice. On the other hand, the central frequency of any bandgap depends on the lattice constant of a phononic crystal. Large lattice constant leads to low-central frequency, so the whole size of a phononic crystal has to be large for low-frequency vibroacoustic energy. This property may hinder phononic crystals from low-frequency vibroacoustic energy harvesting due to the limitations of space and intensity in many engineering applications (Chen et al. 2014).

Acoustic metamaterials can be designed to exhibit nontraditional physical behaviors such as negative stiffness, mass, and Poisson's ratio. These unique abilities of acoustic metamaterials have been used to enhance vibroacoustic energy harvesting. Similar to the mechanism of phononic crystals, bandgap is also the basis of acoustic-based broadband vibroacoustic energy harvesting. However, there are two different principles (Chen et al. 2014): (a) acoustic superlens can be used to concentrate vibroacoustic energies; (b) local resonance can be used to localize vibroacoustic energies by setting defects. Compared to phononic crystals, acoustic metamaterials with small size can generate low-frequency band, so they are more applicable for low-frequency vibroacoustic energy harvesting.

In addition, electromagnetic metamaterials (EM)-based wireless power transmission (WPT) has been explored to enhance the performance of microwave wireless power transmission (MWPT) and wireless power transmission (WPT) using coupled magnetic resonance (CMR). The microwave spectrum is defined as electromagnetic energy ranging from approximately 1 GHz to 1000 GHz in frequency. A complete MWPT system consists of three essential parts: converting DC energy to microwave power, capturing the microwave power by antennas, and converting the captured power to DC output power. In particular, the rectifying antenna called rectenna is one of the key components affecting the performance of a MWPT system. Optimal design of RF antennas with metamaterials can enhance EM-based MWPT. Metamaterials have also been used to change near-field characteristics in WPT systems with CMR, which is very different in MWPT systems. The traditional WPT efficiency drops steeply as a function of the distance between the coils, as well as a function of the resistive load. To address these issues, metamaterials are being introduced to enhance WPT with CMR because they possess peculiar electromagnetic properties, such as negative refractive index and evanescent wave amplification. These properties make themselves enhance the evanescent near field and eventually improve the power transfer efficiency (Kurs et al. 2010; Chen et al. 2014).

Metamaterials have also been used for thermal energy harvesting and improving the efficiency of the solar light absorbing. Besides, metamaterials-based multifunctional structures with energy harvesting abilities have been developed, such as load-bearing composite materials and structures with integrated functionalities of sensing, actuation, and energy transduction and multifunctional piezoelectric self-charging structures where piezoelectric devices are combined with thin-film lithium batteries and a layer of supporting substrate layer in order to simultaneously harvest

energy, store energy, and carry structural load. For example, it is a promising way to harness engineering structural vibrations by simultaneously mitigating them. Moreover, harvested useable energy can provide power for online sensing and diagnostic capabilities. Another example is creating multifunctional negative effective mass structures by implementing acoustic metamaterials at the structural scale, in which active control could be coupled with the energy harvesting subsystem to make the structure self-sustaining and self-regulating (Chen et al. 2014).

9.4.6 Nonlinear Metamaterials for Holography

A hologram is an optical element storing phase and possibly amplitude information enabling the reconstruction of a three-dimensional image of an object by illumination and scattering of a coherent beam of light, and the image is generated at the same wavelength as the input laser beam. Plasmonic metasurfaces have been used to generate holograms for various applications, where a target image is digitally processed and the phase pattern of the hologram is calculated using numerical methods for light propagation/diffraction. The image is reconstructed by a reading laser beam that illuminates the storage medium. In standard computer-generated holography, the image is formed at the same wavelength of the reading laser beam. Nonlinear phase control can be built in plasmonic metasurfaces and demonstrate THG holograms where the image is formed at a wavelength different from the reading beam, as illustrated in Fig. 9.14. The high-density storage enabled by sub-micron nanoantennas, especially in multilayered structures, may lead to holograms with very high resolution, such as V-shaped gold antennas and metallic rods of varying aspect ratio and orientation angle. Nonlinear phase control has been

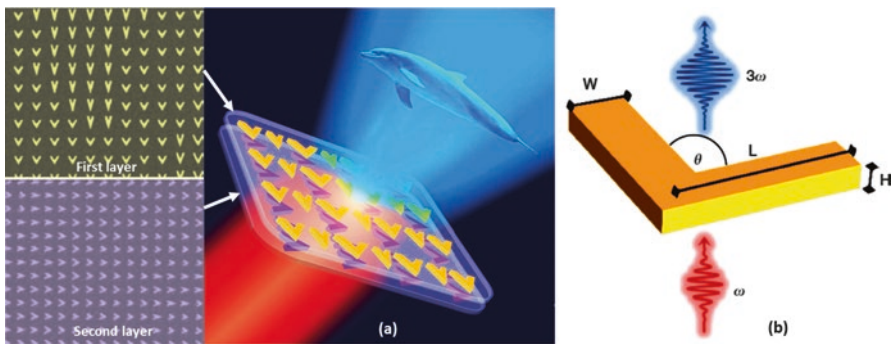


Fig. 9.14 Schematic of a multilayer nonlinear metamaterial hologram (Almeida et al. 2016): (a) when the hologram is illuminated by an infrared laser, it generates a holographic image of an object at the third-harmonic frequency in the blue; (b) dimensions of the V-shaped gold antennas for local control of the phase of the nonlinearity. The free parameters are the arm length L and the angle θ between the arms. $H = 30$ nm and $W = 40$ nm are constant for all antennas

demonstrated for second-harmonic generation in arrays of metallic split-ring resonators, third-harmonic generation (THG) in cross-shaped metallic nanoparticles for circularly polarized light, and four-wave mixing in metallic thin films (Almeida et al. 2016).

References

- Almeida E, Bitton O, Prior Y (2016) Nonlinear metamaterials for holography. *Nat Commun* 7:12533
- Chen Z, Guo B, Yang Y, Cheng C (2014) Metamaterials-based enhanced energy harvesting: a review. *Physica B* 438:1–8
- Czaplicki R, Husu H, Siikänen R, Mäkitalo J, Kauranen M, Laukkanen J, Lehtolahti J, Kuitinen M (2013) Enhancement of second-harmonic generation from metal nanoparticles by passive elements. *Phys Rev Lett* 110:093902
- de Ceglia D, Vincenti MA, Campione S, Capolino F, Haus JW, Scalora M (2014) Second-harmonic double resonance cones in dispersive hyperbolic metamaterials. *Phys. Rev. B* 89(7):075123
- Decker M et al (2013) Dual-channel spontaneous emission of quantum dots in magnetic metamaterials. *Nat Commun* 4:2949
- Hannam KE, Powell DA, Shadrivov IV, Kivshar YS (2012) Tuning the nonlinear response of coupled split-ring resonators. *Appl Phys Lett* 100:081111
- Katko AR (2014) Functional metamaterials for nonlinear and active applications using embedded devices. PhD dissertation, Duke University
- Kivshar YS (2014) Tunable and nonlinear metamaterials: toward functional metadevices. *Adv Nat Sci Nanosci Nanotechnol* 5:013001
- Kurs A, Moffatt R, Soljacic M (2010) Simultaneous mid-range power transfer to multiple devices. *Appl Phys Lett* 96(2010):044102
- Lapine M, Shadrivov IV, Kivshar YS (2014) Colloquium: nonlinear metamaterials. *Rev Mod Phys* 86(3):1093–1123
- Larouche S, Rose A, Smith DR (2015) A constitutive description of nonlinear metamaterials through electric, magnetic, and magnetoelectric nonlinearities. In: Shadrivov IV et al (eds) *Nonlinear, tunable and active metamaterials*. Springer International Publishing, Switzerland
- Maksymov I, Miroshnichenko A, Kivshar Y (2013) Cascaded four-wave mixing in tapered plasmonic nanoantenna. *Opt Lett* 38:79
- Mattheakis M, Tsonis G, Kovanis V (2012) Luneburg lens waveguide networks. *J Opt* 14:114006
- Minovich A et al (2012) Liquid crystal based nonlinear fishnet metamaterials. *Appl Phys Lett* 100:121113
- Rosanov N, Vysotina N, Shatsev A, Shadrivov I, Powell D, Kivshar Y (2011) Discrete dissipative localized modes in nonlinear magnetic metamaterials. *Opt Express* 19:26500
- Rose A, Huang D, Smith D (2011) Controlling the second harmonic in a phase-matched negative-index metamaterial. *Phys Rev Lett* 107:063902
- Segal N, Keren-Zur S, Hendler N, Ellenbogen T (2015) Controlling light with metamaterial-based nonlinear photonic crystals. *Nat Photonics* 9:180–184
- Seren HR et al (2016) Nonlinear terahertz devices utilizing semiconducting plasmonic metamaterials. *Light: Science & Applications* 5:e16078
- Shadrivov I, Sukhorukov A, Kivshar Y, Zharov A, Boardman A, Egan P (2004) Nonlinear surface waves in left-handed materials. *Phys Rev E* 69:016617
- Somerville WRC, Powell DA, Shadrivov IV (2011) Second harmonic generation with zero phase velocity waves. *Appl Phys Lett* 98:161111
- Suchowski H, O'Brien K, Wong ZJ, Salandrino A, Yin X, Zhang X (2013) Phase mismatch-free nonlinear propagation in optical zero-index materials. *Science* 342:1223

- Valey VK et al (2013) Nanostripe length dependence of plasmon-induced material deformations. *Opt Lett* 38(13):2256–2258
- Zhang L-J, Chen L, Liang C-H (2008) Goos-Hänchen shift at the interface of nonlinear left-handed metamaterials. *J ElectromagnWaves Appl* 22:1031
- Zhao X et al (2016) Nonlinear terahertz metamaterial perfect absorbers using GaAs. *Photon Res* 4(3):A16–A21
- Zharov AA, Shadrivov IV, Kivshar YS (2003) Nonlinear properties of left-handed metamaterials. *Phys Rev Lett* 91:037401
- Zheludev NI, Plum E (2016) Reconfigurable nanomechanical photonic metamaterials. *Nat Nanotechnol* 11:16–22

Chapter 10

Acoustic Metamaterials and Metadevices

10.1 Historical Perspective and Basic Principles

The study of electromagnetic and acoustic waves is an endeavor that dates back centuries. Acoustic metamaterial (AMM) research was originally motivated by parallel developments in electromagnetics, such as negative refraction and cloaking. The emergence of acoustic metamaterials resolved the sample size problem that electromagnetic metamaterials faced and further introduced new functionalities not found previously, such as pentamode materials (exotic materials that only resist one mode of deformation, analogous to how fluids only resist volumetric change). Moreover, the advancement of computer simulation and additive manufacturing technologies has helped drive rapid advances in AMMs (Haberman and Norris 2016).

Acoustic metamaterials can be used to manipulate acoustic waves that are governed by Newton's law of motion, the fluid continuity equation, and the thermodynamic equation of state (for adiabatic process). The acoustic wave equation in a homogeneous medium absent of a source is given by (Ma and Sheng 2016):

$$\nabla^2 P - \frac{\rho}{\kappa} \frac{\partial^2 P}{\partial t^2} = 0 \tag{10.1}$$

where P is pressure and the two constitutive parameters are the mass density ρ and the bulk modulus κ . The speed of sound v is given by $\sqrt{\kappa / \rho}$. In an acoustic metamaterial, the two constitutive parameters can take unusual values when considered in the effective medium sense (e.g., negative, zero, or close to divergent). If such unusual features arise from local resonances of the constituent components, then they are “narrow band” in character (i.e., occurring only in the vicinities of the resonant frequencies). Acoustic waves in fluids are longitudinal scalar waves. In contrast, electromagnetic waves are transverse vector waves with two polarizations. However, an analogy between the two can still be made easily, owing to their wave equations having the same mathematical form. The two constitutive parameters can

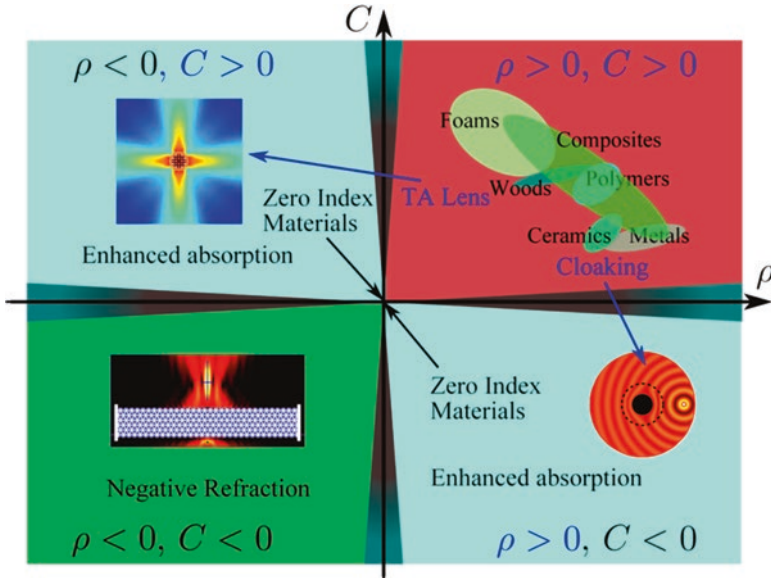


Fig. 10.1 The material design space for acoustic metamaterials—density (ρ) versus compressibility (C): Top right quadrant is the space familiar in normal acoustics. The other quadrants have one or both parameters with negative values. Negative density or compressibility can only be achieved dynamically. For instance, Helmholtz resonators driven just above their frequency of resonance lead to negative dynamic compressibility. The three devices shown employ the metamaterial effects of negative refraction, transformation acoustics (TA), and cloaking (Haberman and Norris 2016)

be mapped as $\rho \rightarrow \varepsilon$ and $\kappa \rightarrow 1/\mu$, where ε and μ are dielectric constant and magnetic permeability, respectively. This also indicates that the two types of waves share much (but not all) of the underlying physics. Therefore, electromagnetic/optical metamaterials and the related intriguing phenomena, such as negative refraction, superlensing, and cloaking, have developed hand in hand with their counterparts in acoustic metamaterials.

Figure 10.1 displays the design space of AMMs, a range that includes negative values for both density and compressibility. The effective density and compressibility provide a helpful way to view the overall response of an engineered structure as an effective medium rather than using the impedance of a complex system. This is consistent with the metamaterial paradigm that seeks to expand the available parameter space available for designing acoustic systems and devices to control acoustic waves (Haberman and Norris 2016).

10.2 Dynamic Negative Density and Compressibility

Many AMM devices are based on negative acoustic density and/or compressibility (inverse of bulk modulus). The speed of sound, more precisely the phase speed, is the square root of the bulk modulus divided by the density. If either quantity is

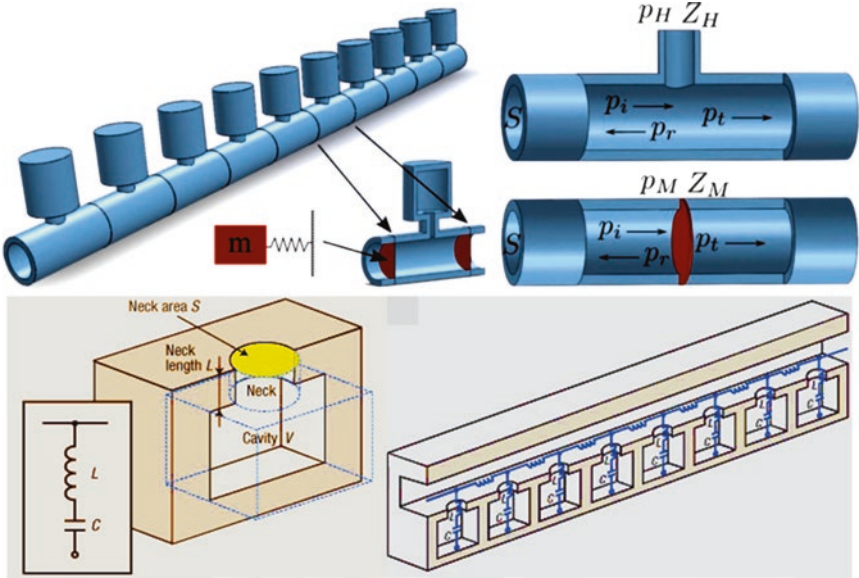


Fig. 10.2 An acoustic duct with alternating membrane masses and Helmholtz resonators. The resonances of the two elements produce negative effective density and effective compressibility in certain frequency ranges. Simultaneously negative density and compressibility, a “double-negative material,” can be obtained by matching the resonances (Haberman and Norris 2016; Ma and Sheng 2016)

negative, then the phase speed is imaginary, corresponding to exponential decay, and hence no transmission. When both acoustic parameters are negative, the phase speed is again a real-valued number, implying wave propagation, although with a twist: the energy and phase velocities are in opposite directions. Negative inertia can be thought of as an out-of-phase time harmonic motion of a moving mass. As shown in Fig. 10.2, the Helmholtz resonators are defined by impedances that relate acoustic pressure (p) with volumetric flow velocity (U), according to $p_M = Z_M U_M$ and $p_H = Z_H U_H$. The effective density and compressibility can be calculated by (Haberman and Norris 2016):

$$\rho_e = \rho + \frac{2SZ_M}{(-i)\omega b} \tag{10.2}$$

$$C_e = C + \frac{1}{2(-i)\omega bSZ_H} \tag{10.3}$$

where ω is the radial frequency, b is one-half the period length, ρ and C are the fluid density and compressibility, respectively, and S is the duct cross section. A membrane attached to the sides of the duct behaves as a mass (m) constrained by a spring (Fig. 10.2) with $Z_M = -i\omega m[1 - (\omega/\omega)^2]/(2S)^2$ and therefore acts as a high-pass filter. In this way, negative effective inertia has been demonstrated in a periodic array

of membranes in air by observing transparency above 735 Hz and very low transmission below that (Lee et al. 2009). By contrast, the low-frequency absorber with impedance $Z_M = -i\omega m [1 - (\omega/\omega_0)^2]^{-1}/(2S)^2$ is a low-pass device whose cutoff frequency $\omega_0/2\pi$ can be made very low (400 Hz) by increasing the mass of the internal oscillator (Liu et al. 2000). By selecting the resonance frequencies properly, it is possible to simultaneously achieve negative density and negative compressibility over a finite range of frequencies. Therefore, the phase and energy propagation directions are then opposite. This situation is known as negative group velocity (group and energy propagation velocities are almost always the same, except in the case of large absorption).

AMMs take advantage of negative properties in a variety of ways, including radiation/sensing in leaky wave antennae (LWAs) and focusing in phononic crystals. LWAs are one dimensional transmission line devices, like the duct as shown in Fig. 10.2, designed to radiate sound into a surrounding fluid much like a long flute-like instrument with the sound emanating from the tone holes. The coupling to the exterior fluid is particularly strong if the compressibility element is an open hole. LWAs provide the possibility to refract acoustic waves at different angles using the frequency-dependent phase speed within the waveguide. Positive and negative effective properties allow the angle to range over 180° , from the forward direction with phase and energy velocities aligned to the negative direction where the energy in one direction in the fluid couples with the LWA wave with the phase velocity in the opposite direction. The LWA performs just as well sensing incident acoustic waves as it does radiating, which is a consequence of acoustic reciprocity under time reversal. The LWA property to discriminate direction using frequency therefore allows directionality detection of incoming sound using a single microphone in place of beamforming using multiple sensors (Esfahlani et al. 2016; Haberman and Norris 2016).

If both effective density and compressibility become zero at the same frequency, then the phase speed remains real as this frequency is crossed because the properties are double positive on one side and double negative on the other. Such zero-index materials provide infinite phase speeds (zero index), which allows for devices that can steer acoustic energy in unusual ways, such as unidirectional transmission and cloaking (Ma and Sheng 2016).

10.3 Membrane-Type Acoustic Materials

Decorated membrane resonators (DMRs) constitute a class of acoustic metamaterials that can display both mass and bulk modulus frequency dispersions, as well as double negativity, over certain frequency ranges. Typically, its effective frequency regime falls within the audible range of 50–2000 Hz. As shown in Fig. 10.3a, a flexible elastic membrane that is submillimeters thick and several centimeters wide is fixed on a rigid rim. A uniform prestress is applied to provide the proper restoring force for oscillations. A rigid platelet is attached to the center of the membrane, whose mass is set by the desired resonant frequencies. This structure may be

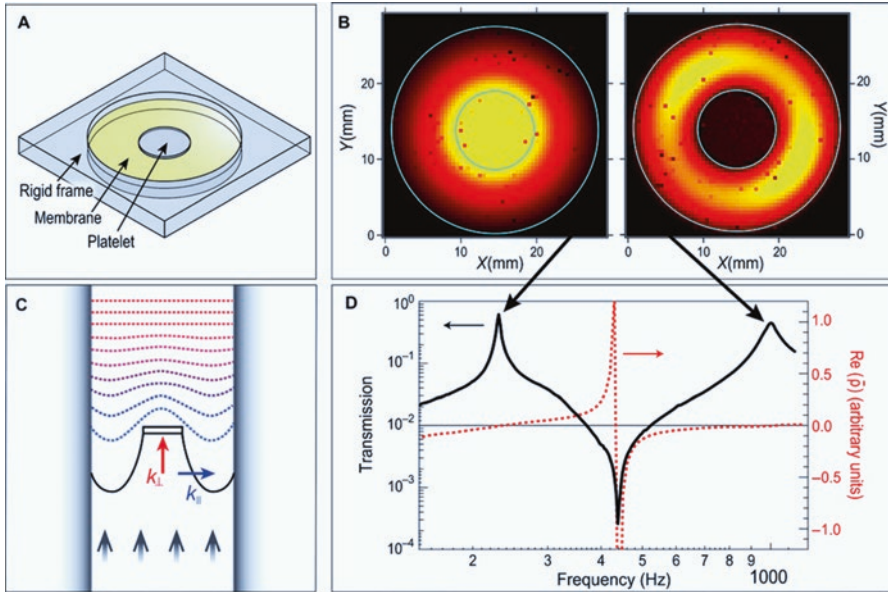


Fig. 10.3 Single membrane with negative effective mass density (Ma and Sheng 2016): (a) A schematic drawing of a typical decorated membrane resonator (DMR); (b) Out-of-plane displacement amplitude of the low-frequency eigenmodes (measured with a laser Doppler vibrometer) of two DMRs—light yellow indicates a large normal displacement amplitude, whereas darker colors indicate small or no normal displacement. Cyan circles delineate the edge of the membrane and the position of the platelet; (c) A schematic illustration indicating that, as a result of the deep-subwavelength size of the DMR, the large in-plane wave vectors only contribute to evanescent waves (blue dashed lines), owing to the fact that the lateral fast variations of the up-and-down displacements tend to cancel each other in air and the net amplitude decays exponentially as a result. (d) Measured amplitude transmission coefficient of a DMR (black solid curve, left axis) and the real part of the calculated effective mass density r (red dashed curve, right axis)

modeled as a spring-mass oscillator by simply regarding the central platelet as the mass and the membrane as the spring (also with a small mass). The response of a DMR to an incident acoustic wave is characterized by its normal displacement profile. Because of the membrane's small thickness, the DMR's low-frequency eigenmodes are dipolar in symmetry, as the compressive oscillations of the membrane are necessarily in the high-frequency regime. Typically, two eigenmodes can be found below 1 kHz. Their normal displacement profiles are shown in Fig. 10.3b. The dipolar symmetry of the resonances implies that the scattering characteristics of the DMR can be reflected in the frequency variation of the effective mass density ρ_e . Figure 10.3c shows a schematic illustration indicating that, as a result of the deep-subwavelength size of the DMR, the large in-plane wave vectors k_{\parallel} only contribute to evanescent waves (blue dashed lines), owing to the fact that the lateral fast variations of the up-and-down displacements tend to cancel each other in air and the net amplitude decays exponentially as a result. The far-field propagating wave is determined by the k_{\perp} of the surface-averaged component of the normal displacement

(red dashed lines). In the system, the DMR (black) is blocking a one-dimensional waveguide, and a planar sound wave impinges from the bottom. As shown in Fig. 10.3d, measured amplitude transmission coefficient of a DMR (black solid curve, left axis) and the real part of the calculated effective mass density ρ_e (red dashed curve, right axis). In the frequency regime between the two resonant peaks, a particular point is known as the antiresonance, where ρ_e diverges in conjunction with a change in sign. When that happens, the impedance also diverges, and the wave would be totally reflected. Such characteristic enables the realization of super-thin lightweight reflective panels, which excel at blocking low-frequency noise. Near-zero ρ_e has also been utilized to achieve supercoupling, which allows an almost perfect transmission through small channels under normal incidence. The negative sign, however, is a reflection of Newton's third law: reaction opposes applied force. A negative ρ_e in the low-frequency limit has been identified for liquid foam, which could be modeled as an array of flexible membranes (Pierre et al. 2014; Ma and Sheng 2016).

The single membrane's small thickness will result in very high frequency vibrations along its thickness direction. To lower the caused monopolar resonant frequencies, two membranes can be coupled to form a new DMR, as shown in Fig. 10.4a. This structure has two dipolar eigenmodes similar to those of a single DMR; therefore, the characteristics of ρ_e are largely preserved. As two membranes oscillate against each other, three-mode vibration profiles are produced (Fig. 10.4b).

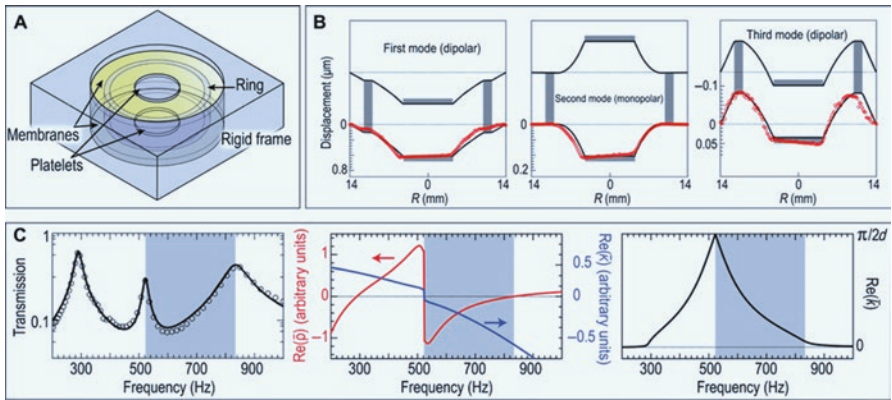


Fig. 10.4 Coupled membranes giving rise to both mass and modulus dispersions (Ma and Sheng 2016): (a) Schematic DMR with two coupled membranes. Two identical membranes decorated with platelets are placed closely together, sealing a layer of gas in between. A rigid ring is added for extra tunability. (b) Normal displacement profiles of three low-frequency eigenmodes. Red symbols delineate the measured profiles using the laser vibrometer, whereas the black solid curves are the results of finite-element simulations. (c) *Left*: The transmission coefficient of the structure shown in (a). Here, the circles denote the measured result, and the solid curve indicates the calculated result. *Middle*: Effective mass density. *Right*: The real part of the effective wave vector. The total thickness of the DMR is $2d$. Double negativity is seen in the region shaded in gray

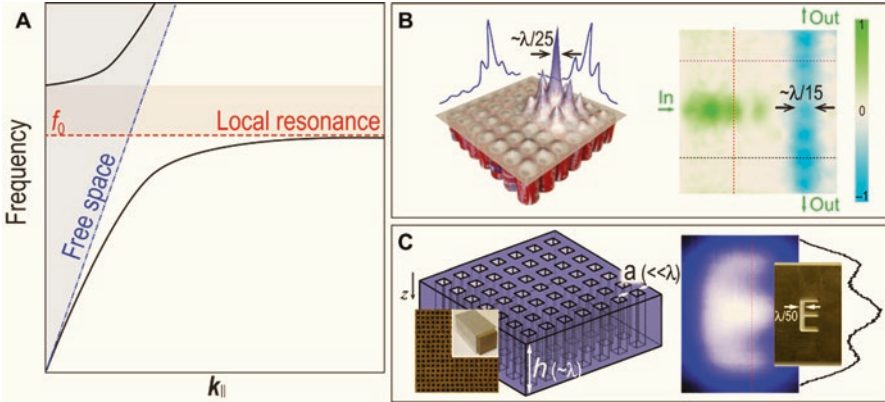


Fig. 10.5 Superresolution with local resonances (Ma and Sheng 2016): (a) The type of dispersion relation that is commonly used for superresolution and deep-subwavelength focusing with acoustic metamaterials; (b) Superresolution focusing (*left*; showing the pressure distribution) and subwavelength wave guiding (*right*; showing the normalized pressure amplitude) achieved by using a two-dimensional array of air-filled cavity resonators (soda cans)—the resonances of the soda cans yield a dispersion; (c) A two-dimensional array of subwavelength waveguides is shown on the *left*, which can support Fabry-Pérot resonances that have flat dispersions to achieve superresolution imaging (*right*)—*light color* represents stronger pressure intensity

The DMR undergoes compressive/expansive motions, with its volume pulsating but with the center of mass remaining stationary under the new mode, which leads to an effective bulk modulus that is frequency dispersive (Fig. 10.4c, middle). The effective bulk modulus reaches zero at the monopolar eigenfrequency and turns negative on the higher-frequency side of this mode. The dipolar and monopolar modes in this DMR are separately tunable. Even though the effective density is large at around 520 Hz (Fig. 10.4c, middle), a transmission peak is observed (Fig. 10.4c, left). The maximum $\text{Re}(\bar{\kappa})$ can reach $\pi/2d$ at the monopole eigenfrequency (Fig. 10.4c, right), where $2d$ is the total thickness of the coupled DMR. Given the small thickness of the DMR, this is much larger than the wave vector allowed in free space (i.e., $k \leq 2\pi/\lambda$). Such large wave vectors can, in principle, be utilized for a wide range of functionalities such as subdiffraction focusing (Ma and Sheng 2016).

The exotic constitutive parameter values enabled by the acoustic metamaterials, such as DMRs, have expanded the horizon of acoustic wave manipulation. Figure 10.5 demonstrates superresolution with local resonances (Ma and Sheng 2016): (A) The type of dispersion relation that is commonly used for superresolution and deep-subwavelength focusing with acoustic metamaterials. Here, the blue dotted-dashed line is the “sound line” (i.e., the dispersion of acoustic wave in the homogeneous background medium), and the red dashed line is that of the local resonance with eigenfrequency f_0 . Coupling between the two induces anticrossing in the vicinity of f_0 and gives rise to the dispersion delineated by the two black curves. The region shaded in gray is a bandgap. In free space, only the \mathbf{k} components within the blue-shaded region are accessible. However, for the lower branch, the \mathbf{k} components much larger than those available in free space (the blue-shaded region)

become accessible. (B) Superresolution focusing (left; showing the pressure distribution) and subwavelength wave guiding (right; showing the normalized pressure amplitude) achieved by using a two-dimensional array of air-filled cavity resonators (soda cans). The resonances of the soda cans yield a dispersion, as shown in (A). (C) A two-dimensional array of subwavelength waveguides is shown on the left. The thickness of the lens h is the same as the operating wavelength in air (not drawn to scale in this schematic drawing). These waveguides can support Fabry-Pérot resonances that have flat dispersions, which are useful for achieving super-resolution imaging. More specifically, owing to the longitudinal nature of acoustic waves, Fabry-Pérot resonances can be realized in waveguides with cross-sectional dimensions $\ll \lambda$, but which can have a length on the order of a wavelength or more. These resonances have almost-flat dispersions in which the magnitude of \mathbf{k} can significantly exceed that of free space. By placing an array of these waveguides in the near field of the source, with each waveguide being capable of picking up highly localized disturbances and then conveying this information to the targeted locations, acoustic images with subwavelength sharpness can be achieved (Zhu et al. 2011). In the imaging result shown on the right, light color represents stronger pressure intensity. The object is in the shape of the character “E” (inset). The stroke width of “E” is $\sim 1/50$. The lens is placed close to the object, and an image is formed on the other side, where the shape “E” can be recognized.

Acoustic superlens and hyperlens can be realized with perfect imaging as shown in Fig. 10.6. In the top of Fig. 10.6a, a slab of doubly negative medium can bring diverging waves into two foci: one inside the slab and the other one outside. On the

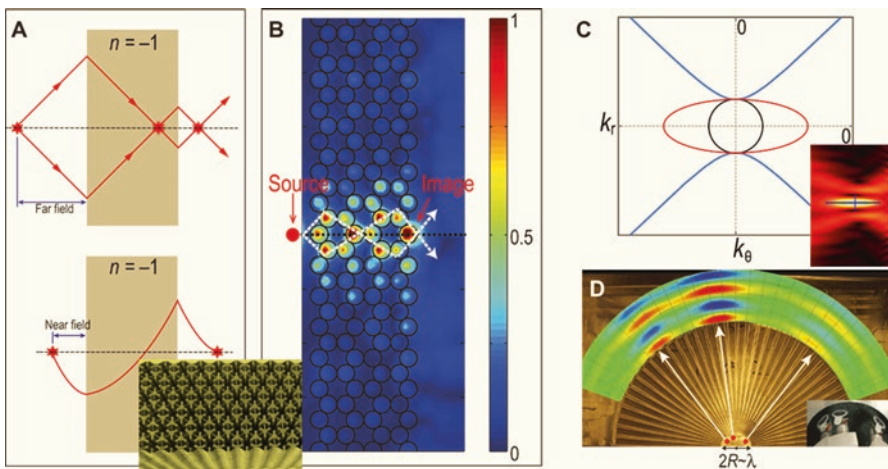


Fig. 10.6 Acoustic realizations of superlens and hyperlens (Ma and Sheng 2016): (a) *Top*: A slab of doubly negative medium can bring diverging waves into two foci: one inside the slab, and the other one outside. *Bottom*: The same slab can amplify evanescent waves, thereby theoretically enabling the formation of a perfect image. (b) Experimental demonstration of the imaging capability of an acoustic superlens. (c) Three distinctive equipfrequency contours. (d) The strong anisotropy in k_r and k_θ , such as that indicated by the red ellipse in (c)

bottom, the same slab can amplify evanescent waves, thereby theoretically enabling the formation of a perfect image. Figure 10.6b shows experimental demonstration of the imaging capability of an acoustic superlens. Here, cavity resonators (soda cans, represented by black circles) are arranged into a honeycomb lattice. It is clearly seen that the near field is sustained and even amplified by the metamaterial slab. Negative refraction and the consequent foci are delineated by white dashed arrows. The normalized pressure intensity field is displayed as a color map. The source (red dots) had an amplitude full width at half maximum of $\lambda/5$, whereas the measured image size is $\lambda/15$. Figure 10.6c shows three distinctive equifrequency contours. The black circle represents that of a homogeneous material. Anisotropy can distort the contour into an ellipse (red), in which a large k_r can be accessed. However, if the material's parameter has different sign, then the contour becomes hyperbolic (blue curves). Figure 10.6d shows the strong anisotropy in k_r and k_θ , such as that indicated by the red ellipse in (C), used for superresolution imaging. Here, the fan-like structure has stripes alternating between air and brass. The effective mass is highly anisotropic. The center circle of the device has a diameter of about one wavelength, in which three sound sources are closely placed with subwavelength separations, represented by the red dots. An image of the sound sources is also shown in the lower-right inset. Red/blue represents positive/negative pressure, with the three clearly resolved regions being representative of the magnified image of the three sound sources (Li et al. 2009; Kaina et al. 2015).

10.4 Transformation Acoustics and Metadevices with Spatially Varying Index

The advent of acoustic metamaterials has greatly expanded the allowed values of the constitutive parameters. A generalized way to appreciate the implied capabilities afforded by this new freedom is through transformation acoustics, such as acoustic cloaking, zero-index medium, and acoustic black hole and illusion metadevices.

An acoustic cloak is a shell surrounding an object so that sound incident from any direction passes through and around the cloak, making the cloak and the object acoustically “invisible.” Figure 10.7 shows a pyramidal structure rendered a region of space three wavelengths in diameter invisible to sound. Active cloaking, on the other hand, uses sound sources to cancel the incident wave. It is closely related to active noise control and anti-sound which creates a zone of silence, although unlike cloaking, the sound is generally not required to be non-radiating. The acoustic cloak is expected to be use for improving noise reduction, sound absorption, architectural acoustics, environmental acoustics, and defense underwater sound control (Norris 2015).

Zero-index medium (ZIM) can also be used for cloaking. From the point of view of transformation acoustics, an area/volume occupied by such materials is equivalent to a point with a measure of zero but expanded in space. As a result, the wave field inside such materials will not undergo any change and, therefore, must be constant.

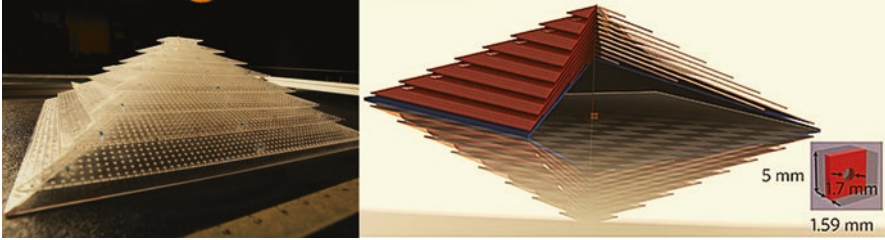


Fig. 10.7 Pyramidal acoustic carpet cloak (Zigoneanu et al. 2014)

This also means that the outgoing wave front is determined by the shape of the ZIM's boundary. Hence, a scatterer placed inside a ZIM is hidden, in the sense that it generates no scattered wave if viewed from the outside. However, ZIM cloaking can only happen with normal incidence. Moreover, a ZIM's functionality is highly sensitive to the nature of defects (Ma and Sheng 2016).

Besides cloaking, transformation acoustics also proves to be a powerful tool for designing a wide range of acoustic functionalities. Opposite to the functionality of a cloak, which detours the incident wave around a scatterer, a device can be designed to guide the incident wave into the core region without being scattered. By placing absorbing agents in the core region, these acoustic “black holes” can display absorption performance independent of the incident angle. A number of different acoustic “illusions” also demonstrate the power of transformation acoustics. For instance, an acoustic wave front rotator is designed to be capable of rotating a planar wave front, which created an illusion of the incident angle. Similarly, this design can be used to alter the radiation directivity of a sound source that is enclosed inside. Some other examples, such as aberration correction, radiation collimation, and reshaping, have been demonstrated (Ma and Sheng 2016).

10.5 Space-Coiling and Acoustic Metasurfaces

Acoustic waves are longitudinal in character. Hence, acoustic waveguides have no cutoff frequency. This feature has to be exploited to design space-coiling, which essentially forces sound waves to propagate through passages that are much longer than their external dimension. An example is shown in Fig. 10.8a. The color indicates the phase of the propagating sound wave. The coiled-up passage introduces a large phase delay $\Delta\phi = k_0 L$, where k_0 is the wave number in the background fluid and L is the “acoustic path.” Historically, similar structures have found applications in bass woofers that were sometimes called folded horn speakers, a name that aptly describes the enclosure design. By adjusting the total length of the passage, the apparent phase and group velocities can be tuned and hence the effective index and the dispersion relation. With proper design, such structures can be used for many novel effects, such as the negative-refracting prism (Fig. 10.8b), near-zero-index

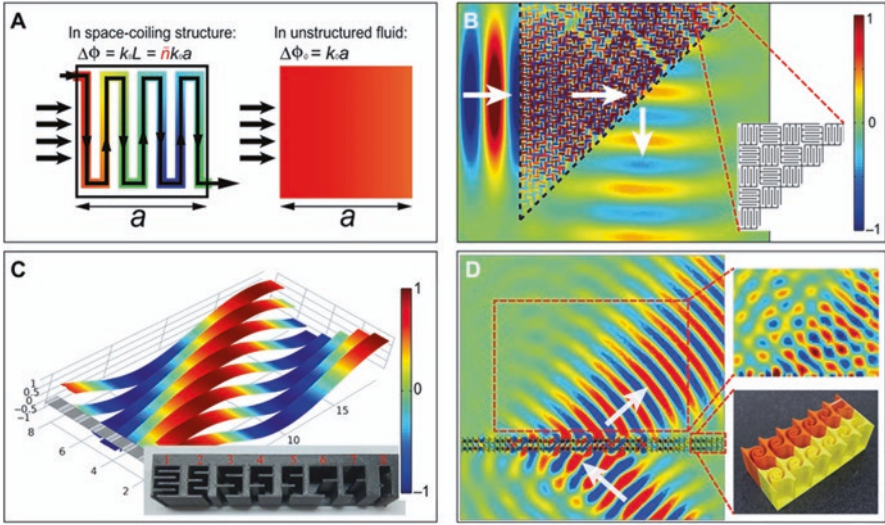


Fig. 10.8 Space-coiling and acoustic metasurfaces (Ma and Sheng 2016): (a) An example of the space-coiling structure and the relevant sound pressure field inside; (b) Negative-refracting prism; (c) A design of reflective acoustic metasurface that is capable of generating phase changes up to 2π ; (d) A design of the metasurface that generates negative refraction for the transmitted wave. *Left:* The simulation result (*white arrows* delineate incident and refracted beam directions). *Right:* The experimentally measured pressure map (*red and blue* represent positive pressure and negative pressure, respectively) (*top*) and a photographic image of a section of the actual sample (*bottom*)

cloaking, and Dirac-like dispersion. As shown in Fig. 10.8b, space-coiling unit cells are assembled into a prism. Sound incidents from the left, and encounters of negative refraction as it emerges from the prism, are indicated by white arrows. Red/blue represents positive/negative pressure. Because of its effectiveness and ease of implementation, the space-coiling design has demonstrated multi-functionalities including zone-plate focusing, one-way transmission, high transmission, and high absorption (Liang et al. 2013; Ma and Sheng 2016).

Space-coiling structures are particularly effective for constructing acoustic metasurfaces. These are essentially acoustic phase arrays with subwavelength thickness, which are capable of generating an abrupt phase shift (up to 2π) across a single layer. This phase shift supplies the incident wave with an extra momentum, thereby causing it to reflect/refract at an “abnormal” angle. Figure 10.8c shows a reflective geometry design in which part of the incident wave can enter the coiled channels, which are designed in such a way that the reflected wave would acquire a laterally varying phase delay so that a nonspecular reflected beam can appear. The wave front of the latter can be identified by the red ridge in Fig. 10.8c (red and blue represent positive pressure and negative pressure, respectively). The metasurface is shown on the lower left, and the wave is incident normally on the surface. The ridge of red stripe sections indicates the emergence of a reflected wave at a nonspecular angle (inset: implementation of a slightly modified space-coiling

design of the metasurface, with a lateral gradient of phase delays). One drawback of the space-coiling structures is the large impedance mismatch to the incident wave. That can mean some challenges for the transmission configuration because, in addition to phase shifts, impedance matching is also required to achieve optimal results. An improved impedance matching by adding horn-like designs is shown in (Fig. 10.8d). Resonances can also be used to improve coupling. However, these exotic functionalities are dependent on the conditions of the incident wave such as the beam shape, incident angle, and source geometry and position (Li et al. 2014; Ma and Sheng 2016).

10.6 Acoustic Absorption

Acoustic absorption is important for both noise mitigation and interior acoustic optimization. Absorption performance for a relatively broad range of frequencies mainly depends on (a) an effective means for dissipation through friction using porous materials such as sponges, mineral wools, fiber glass, and cotton as sound-absorbing materials and (b) impedance matching by enhancing coupling of the incident acoustic energy with the absorbers—gradient index is a standard method used to improve absorption performance. For example, porous materials are prepared with spatially varying filling density, and blocks of absorbing materials are cut into wedge or conical shapes to improve impedance matching (for high-frequency sound, this also adds the benefit of a diffusor). In addition, resonances can also be advantageous because they are usually accompanied by high energy density and improved impedance matching. Microperforated panels with back cavities constitute an example along this line (Maa 1998; Arenas and Crocker 2010).

However, acoustic metamaterials can provide effective absorption in the low-frequency regime. Figure 10.9 demonstrates acoustic absorption by DMRs. Large absorption can be achieved with elastic membranes of submillimeter thickness, decorated by asymmetrically shaped rigid platelets. Because of the contrast in flexural rigidity at resonances, a large energy density can be concentrated within small regions near the perimeter of the rigid platelets. These regions have lateral dimensions that are much smaller than the relevant wavelength. Hence, the high energy densities and perfect impedance matching can be simultaneously attained. Figure 10.9a (left) shows numerically simulated elastic bending energy density of a soft membrane decorated with rigid platelets, delineated by blue curves. Light color represents high energy density. The energy is highly concentrated in the small areas along the perimeters of the platelets and along the sample boundary. On the right, a photographic image of such a membrane absorber is shown. Fig. 10.9b shows total absorption of low-frequency sound at multiple frequencies using hybrid resonances. The left panel shows the absorption coefficient of a three-unit membrane metasurface (structure shown in the right inset). The markers are measured data, and the solid curve represents simulation. The membrane metasurface unit cell comprises a stretched membrane decorated with a rigid platelet, backed by a thin layer of sealed

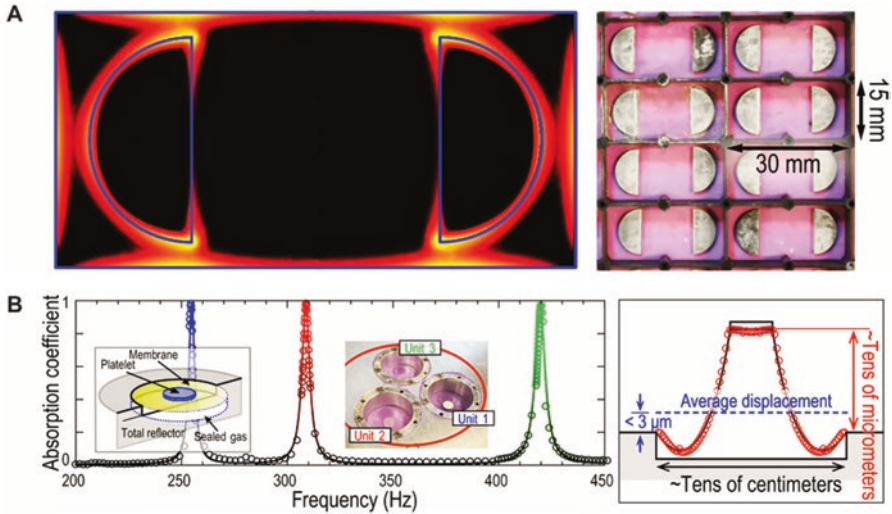


Fig. 10.9 Acoustic absorption by DMRs (Ma and Sheng 2016): (a) *Left*: Numerically simulated elastic bending energy density of a soft membrane decorated with rigid platelets, delineated by blue curves. Light color represents high energy density. The energy is highly concentrated in the small areas along the perimeters of the platelets and along the sample boundary. *Right*: A photographic image of such a membrane absorber. (b) Total absorption of low-frequency sound at multiple frequencies using hybrid resonances. The *left panel* shows the absorption coefficient of a three-unit membrane metasurface (structure shown in the *right inset*). The *right panel* of (b) shows the vibration profile of the membrane at the hybrid resonant frequency

gas (thickness expressed in centimeters). The hybrid resonance structure is fabricated on top of a hard reflecting surface (left inset). The right panel of Fig. 10.9b shows the vibration profile of the membrane at the hybrid resonant frequency. Red markers represent experimentally measured data. The surface-averaged normal displacement (blue dashed line; not drawn to scale) matches the amplitude of the incident sound—an indication of impedance matching. However, the normal displacement can be much larger locally, suggesting a very large energy density in the form of the deaf component that couples only to evanescent waves (Ma et al. 2014).

Total absorption can be realized by two degenerate resonators, in which a monopolar resonator and a dipolar resonator, both deep subwavelength in scale and resonant at the same frequency, are placed closely together so that the incident wave perceived the two as a single unit. At resonance, the average impedance of the two subunits perfectly matched the air so that the incident wave generated no reflection, whereas the different symmetries of the two resonators caused the transmitted wave to be cancelled. That resulted in total absorption. So far, the high absorption achieved by acoustic metamaterials remains within narrow frequency bands. It complements well the acoustic absorption of the traditional approaches in the low-frequency regime, where machine-generated noise can be an important source (Ma and Sheng 2016).

10.7 Active Acoustic Metamaterials

Acoustic metamaterials can be tuned and reconfigured for their versatility and broadened application potentials. Certain nonlinear processes can introduce multistable configurations that are controllable by external means, such as static force loading. This was exploited to add tunability to metamaterials. Examples have been demonstrated with ordered granular chains/crystals and buckling elastomers. Piezoelectric elements, which have long been used for acoustic-electric transducers, can display an acoustic response that is variable under different external electric controls. Schemes based on the electrical control of resonant frequencies in membrane-type metamaterials have been realized (Xiao et al. 2015).

Besides reconfiguration, powered devices are also exploited to achieve more exotic functionalities such as asymmetric scattering. These functionalities are partly derived from the controlling electronics. For example, a nonreciprocal acoustic device is constructed, in which an electronic frequency converter is loaded onto a piezoelectric membrane, which gave it a nonlinear response that can up-convert the frequency of the incident sound. A Helmholtz resonator is then connected to one side of this membrane to filter the incident sound, leaving the up-converted frequency unaffected. This combination results in the strong asymmetric transmission of acoustic energy. Moreover, an electronically controlled loudspeaker as a gain component is used to compensate for the energy that is lost to an absorber. This allows the realization of anisotropic transmission resonance (Ma and Sheng 2016): for incidence from both sides, transmission reached almost unity, but because of the asymmetrically positioned gain and loss components, reflections are highly asymmetric.

10.8 Emerging Directions and Future Trends

10.8.1 *Nonlinear Acoustic Metamaterials*

The use of nonlinear effects is an emerging area of acoustic metamaterial research. Elevated material nonlinearity has been achieved using several mechanisms, including buckled structures, patterned holes in soft media, active elements, and granular media. Nonlinear acoustic media opens the door to the reconfigurable AMM, in which the medium (actively or passively) can be altered in a way that fundamentally changes its dispersive properties. Analogues are deployable structures used in aerospace applications or the everyday example of a deployable structure, the umbrella. An umbrella is highly compliant and dense (i.e., contained in a small volume) before expanded into its “usable” configuration. When deployed, however, the structure is considerably stiffer and less dense. A reconfigurable metamaterial is one that employs similar structural concepts on the subwavelength scale to produce a material that can control acoustic waves in dramatically different ways depending on the configuration (Haberman and Norris 2016).

10.8.2 Nonreciprocal Acoustic Devices

Nonreciprocal AMM devices exhibit exciting potentials, such as the ability to hear but not be heard, sensors that can transmit and receive at the same time, or sensors that have different transmit and receive patterns. The first such device exploited material nonlinearity to generate nonreciprocal acoustic wave behavior. Other nonreciprocal acoustical systems followed, including a linear device that employed momentum field biasing via fluid motion in a resonant cavity and another that modulated the material properties using electrically active components (Popa and Cummer 2014).

Reciprocity can be formulated for most systems supporting wave propagation (acoustic, electromagnetic, elastodynamic) using the Onsager–Casimir principle of microscopic reversibility. The challenge of creating media and devices displaying nonreciprocal behavior is thus to violate microscopic reversibility. For example, fluid flow is used to induce momentum field bias coupled with a resonant cavity. Another means to break reciprocity is to violate some assumptions of the Onsager–Casimir principle. Nonreciprocal transmission can thus be induced by breaking linearity or time invariance (Haberman and Norris 2016). Incorporation of nonlinearity into acoustics can also create nonreciprocal transmission, in addition to reconfigurability and high-intensity focusing. Systems whose property (e.g., effective mass) is temporally modulated are also able to display nonreciprocity (Wang et al. 2015).

10.8.3 Elastic and Mechanical Metamaterials

Acoustic metamaterials have also influenced the study of structural elastic waves. Cloaking, negative refraction, and subdiffraction focusing are demonstrated in thin plates. Investigations on resonant elastic metamaterials reveal fascinating possibilities such as negative shear modulus and superanisotropy. The mitigation of the destructive effects of seismic waves has also been explored with a rectangular array of boreholes drilled into the ground surface that showed the clear effect of blocking low-frequency surface vibrations. Three-dimensional printed pentamode mechanical metamaterials represent a novel type of structural material in which rigidity is maintained through point contacts between the tips of the elongated structural elements. Because bending and rotational motions about these point contacts encounter much smaller resistances, these structures consequently can have a bulk modulus that is much larger than the shear modulus, leading to the interesting characteristic that the compression and transverse vibrations are essentially decoupled (Ma and Sheng 2016).

10.8.4 Graphene-Inspired Acoustic Metamaterials

Graphene-inspired acoustic metamaterials have potentials to manipulate acoustic waves, dispersion relations that are similar to those found in a semiconductor electronic band structure known as the Dirac cone, featuring crossed linear dispersions

at a point in the reciprocal space. A Dirac-like dispersion located in the Brillouin zone center (G point, where $k \sim 0$) is related to a near-zero refractive index. Therefore, it can serve as a straightforward platform for the study of zero-index physics and relevant functionalities. In addition, Dirac-like dispersion is characterized by two (or more) states that can become degenerate, which indicates that they have different types of symmetry. The evolution of symmetry for these isolated bands may be characterized by geometric phases and/or topological entities such as the Chern number. For example, the symmetry of Bloch states is closely related to the geometric phases of the bands, and their direct observation is easier in macroscopic systems such as phononic crystals. Therefore, Dirac-like dispersion is usually a good starting point for the realization of relevant exotic physics, such as topological transition in photonic crystals, including the unique chiral edge modes that are immune to backscattering. Because acoustic waves are insensitive to magnetic fields, which are crucial elements in the appearance of the chiral edge modes in graphene, artificial gauge fields of various types may mimic the effect of magnetic fields in the context of acoustic metamaterials. Realizations of the chiral edge modes in mechanical systems have also appeared in systems such as a two-dimensional array of coupled pendula and an oscillator array consisting of spinning masses (Ma and Sheng 2016).

10.8.5 Acoustic Metamaterials with Characteristics Describable by non-Hermitian Hamiltonians

Acoustic metamaterials may play a role in the physics of non-Hermitian Hamiltonians, which describes systems with loss and/or gain. Originally studied in nuclear systems to explain phenomena such as the lifetime of excited states, real observable eigenstates have been shown to exist, despite the fact that the relevant eigenvalues may be imaginary. Intriguing phenomena related to exceptional points, at which two or more eigenstates coalesce when driven by a system parameter (such as loss), have found applications such as asymmetric reflection, single-mode lasing cavity, and loss-induced lasing revival in optical systems. Investigations in the context of acoustics have also started to appear (Fleury et al. 2015; Ma and Sheng 2016).

10.8.6 Future Trends

Acoustic metamaterials have expanded the capabilities of acoustic wave manipulation, encompassing ideas like negative refraction, superresolution, cloaking, enhanced absorption, nonreciprocity, active control, and material tunability. Present reliance on resonances implies frequency dispersions and narrow frequency bands in the effectiveness of acoustic metamaterials. Hence, broadening the frequency

range of operation of acoustic metamaterials is a direction for diverse applications. Acoustic metamaterials are also expected to affect ultrasonic acoustics, where countless applications (such as medical imaging) lie. New thinking such as “digitizing” metamaterials into binary units has already made some promised functionalities more accessible, such as actively controllable metasurfaces. Owing to the simplicity of the fabrication process (e.g., compared to those for electronic and display devices), the commercialization of some of the research results targeting old challenges such as noise abatement and selective perception in human audition may occur in the near future. Furthermore, acoustic metamaterials may be useful for protection against seismic waves (Giovampaola and Engheta 2014; Ma and Sheng 2016).

References

- Arenas JP, Crocker MJ (2010) Recent trends in porous sound-absorbing materials. *J Sound Vib* 44:12–17
- Esfahlani H, Karkar S, Lissek H (2016) Exploiting the leaky-wave properties of transmission-line metamaterials for single-microphone direction finding. *J Acoust Soc Am* 139:3259–3266. doi:10.1121/1.4949544
- Fleury R, Sounas D, Alù A (2015) An invisible acoustic sensor based on parity-time symmetry. *Nat Commun* 6:5905
- Giovampaola CD, Engheta N (2014) Digital metamaterials. *Nat Mater* 13:1115–1121
- Haberman MR, Norris AN (2016) Acoustic metamaterials. *Acoust Today* 12(3):31–39
- Kaina N, Lemoult F, Fink M, Lerosey G (2015) Negative refractive index and acoustic superlens from multiple scattering in single negative metamaterials. *Nature* 525:77–81
- Lee SH, Park CM, Seo YM, Wang ZG, Kim CK (2009) Acoustic metamaterial with negative density. *Phys Lett A* 373:4464–4469. doi:10.1016/j.physleta.2009.10.013
- Li J, Fok L, Yin X, Bartal G, Zhang X (2009) Experimental demonstration of an acoustic magnifying hyperlens. *Nat Mater* 8:931–934
- Li Y, Jiang X, Li R-Q, Liang B, Zou X-Y, Yin L-L, Cheng J-C (2014) Experimental realization of full control of reflected waves with subwavelength acoustic metasurfaces. *Phys Rev Appl* 2:064002
- Liang Z, Feng T, Lok S, Liu F, Ng KB, Chan CH, Wang J, Han S, Lee S, Li J (2013) Space-coiling metamaterials with double negativity and conical dispersion. *Sci Rep* 3:1614
- Liu Z, Zhang Z, Mao Y, Zhu YY, Yang Z, Chan CT, Sheng P (2000) Locally resonant sonic materials. *Science* 289:1734–1736. doi:10.1126/science.289.5485.1734
- Ma G, Sheng P (2016) Acoustic metamaterials: from local resonances to broad horizons. *Sci Adv* 2:e1501595. doi:10.1126/sciadv.1501595
- Ma G, Yang M, Xiao S, Yang Z, Sheng P (2014) Acoustic metasurface with hybrid resonances. *Nat Mater* 13:873–878
- Maa D-Y (1998) Potential of microperforated panel absorber. *J Acoust Soc Am* 104:2861–2866
- Norris AN (2015) Acoustic cloaking. *Acoust Today* 11(1):38–46
- Pierre J, Dollet B, Leroy V (2014) Resonant acoustic propagation and negative density in liquid foams. *Phys Rev Lett* 112:148307
- Popa B-I, Cummer SA (2014) Non-reciprocal and highly nonlinear active acoustic metamaterials. *Nat Commun* 5:3398
- Wang Q, Yang Y, Ni X, Xu Y-L, Sun X-C, Chen Z-G, Feng L, Liu X-P, Lu M-H, Chen Y-F (2015) Acoustic asymmetric transmission based on time-dependent dynamical scattering. *Sci Rep* 5:10880

- Xiao S, Ma G, Li Y, Yang Z, Sheng P (2015) Active control of membrane-type acoustic metamaterial by electric field. *Appl Phys Lett* 106:091904
- Zhu J, Christensen J, Jung J, Martin-Moreno L, Yin X, Fok L, Zhang X, Garcia-Vidal FJ (2011) A holey structured metamaterial for acoustic deep-subwavelength imaging. *Nat Phys* 7:52–55
- Zigoneanu L, Popa BI, Cummer SA (2014) Three-dimensional broadband omnidirectional acoustic ground cloak. *Nat Mater* 13:352–355

Chapter 11

Mechanical Metamaterials and Metadevices

11.1 Introduction

Building upon the success of electromagnetic and acoustic metamaterials, mechanical metamaterials have been developed for obtaining extraordinary or extreme elasticity tensors and mass-density tensors to thereby mold static stress fields or the flow of longitudinal/transverse elastic vibrations in unprecedented ways. With the advances in additive manufacturing techniques that have enabled fabricating materials with arbitrarily complex micro-/nano-architectures, the rationally designed micro-/nano-architecture of mechanical metamaterials gives rise to unprecedented or unusual mechanical properties that could be exploited to create advanced materials with novel functionalities. These unusual mechanical properties include negative Poisson's ratio, negative elasticity, negative stiffness, negative compressibility, and negative thermal expansion coefficient. Some extremal metamaterials are extremely stiff in certain modes of deformation, while they are extremely soft in other modes of deformation. Typical materials that have been developed include auxetic, ultra-lightweight, negative mass density, negative modulus, penta-mode, dilational, anisotropic mass density, origami, nonlinear, bistable, reprogrammable, and seismic shielding mechanical metamaterials.

Figure 11.1 shows examples of mechanical metamaterials (Christensen et al. 2015): (a) auxetic, (b) lightweight, (c) negative-parameter (i.e., negative mass density and/or moduli at finite frequency $\omega \neq 0$), (d) penta-mode, and (e) origami mechanical metamaterials. The left column shows a combination of the Milton map (bulk modulus B versus shear modulus G) and the Ashby map (one elastic modulus versus mass density ρ). The parameters are zero at the crossing of the three arrows, pointing into the positive directions. In each entry, ordinary solids (black) are compared with the corresponding metamaterials (red). The center column exhibits blueprints of (extended) unit cells highlighting characteristic structural elements, the right column optical, or electron micrographs of fabricated structures. These metamaterials can (a) be easily compressible, yet not easily deformable; (b) be

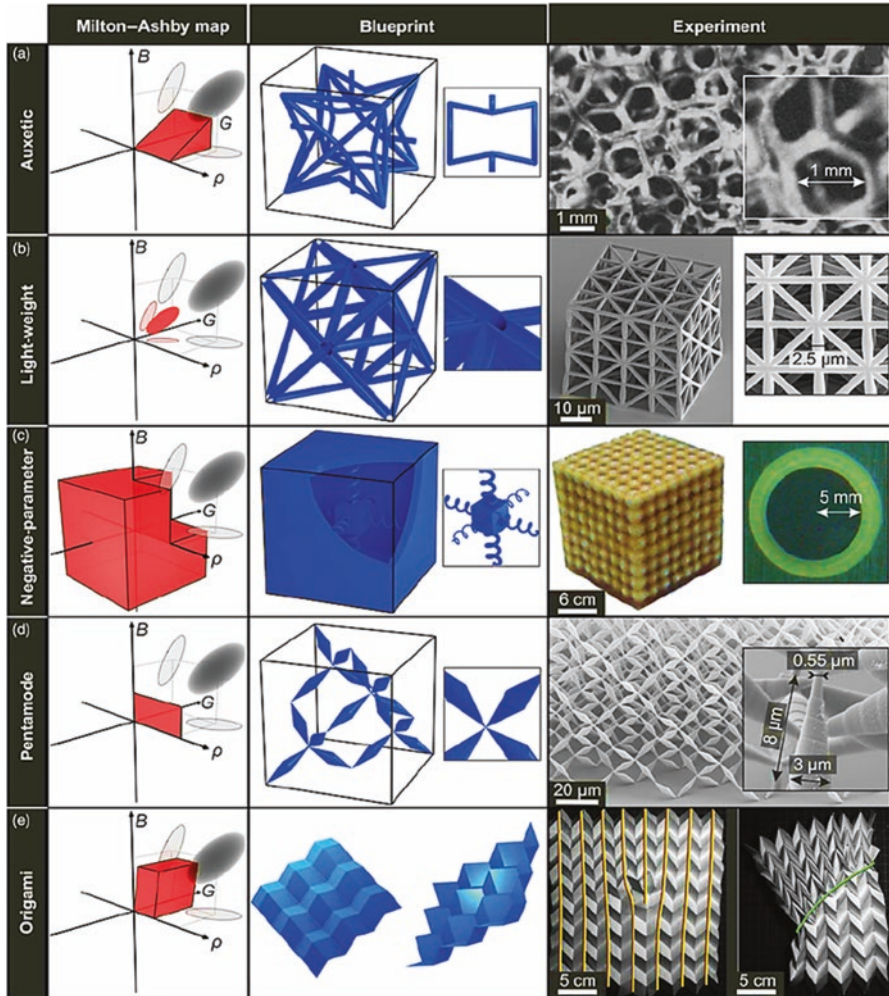


Fig. 11.1 Examples of mechanical metamaterials (Christensen et al. 2015): (a) auxetic, (b) light-weight, (c) negative-parameter (i.e., negative mass density and/or moduli at finite frequency $\omega \neq 0$), (d) penta-mode, and (e) origami mechanical metamaterials. The *left column* shows a combination of the Milton map (bulk modulus B versus shear modulus G) and the Ashby map (one elastic modulus versus mass density ρ). The parameters are zero at the crossing of the *three arrows*, pointing into the positive directions. In each entry, ordinary solids (*black*) are compared with the corresponding metamaterials (*red*). The *center column* exhibits blueprints of (extended) unit cells highlighting characteristic structural elements, the *right column* optical, or electron micrographs of fabricated structures

lightweight, yet ultrastrong; (c) exhibit complete bandgaps or support backward waves; (d) be easily deformable, but not easily compressible; and (e) be deployable, lightweight, bistable, and reprogrammable. Applications could be as (a) shock absorbers, (b) support structures, (c) reflectors or concentrators, (d) mechanical cloaks, and (e) structures for space missions.

Numerous analytical and computational methods have been developed for design of mechanical metamaterials. One analytical method is known as freedom, actuation, and constraint topologies (FACT), and it relies on design of flexure and screw elements to create unit cells and lattices with prescribed properties (Hopkins and Culpepper 2010a, b). The typical computational method is topology optimization (TO), which involves optimizing a unit cell's layout subject to an objective function and boundary conditions (Spadaccini 2015).

Physical realization of mechanical metamaterials requires a suite of fabrication processes with unique capabilities. Additive manufacturing (AM) methods are particularly well suited to the geometric complexity of these structures and lattices. For some attaining complicated features and geometries, some custom manufacturing techniques have also been developed, such as projection microstereolithography (PmSL), direct ink writing (DIW), and electrophoretic deposition (EPD). With these methods, three-dimensional micro- and nanoscale architectures can be generated with multiple constituent materials (polymers, metals, and ceramics) in the same structure (Spadaccini 2015).

11.2 Auxetic Mechanical Metamaterials

Auxetic mechanical metamaterials possess a negative Poisson's ratio. When stretched, they become thicker perpendicular to the applied force. This occurs due to their particular internal structure and the way this deforms when the sample is uniaxially loaded. Three well-established basic auxetic structures can be identified as reentrant structures, chiral structures, and rotating rigid structures. Other auxetic mechanisms exist as well, such as triangular network of shock absorbers, which axially deform and maintain their relative angles, and inherently auxetic double-helix yarn, which deforms through a reversal of the stiff, outer wrap and the more compliant, thicker core (Miller et al. 2009; Hou and Silberschmidt 2015).

Auxetic structures have since been widely applied in the development of novel products, such as running shoes, shape memory foams, and bioprotheses. This is not only for their unusual mechanical response, but auxetics also offer a route to attain extreme values of other material properties, like a higher indentation resistance, shear resistance, energy absorption, hardness, and fracture toughness. The ability to design a material with a structure that exhibits a desired set of mechanical properties, including a negative Poisson's ratio, has led to the development of auxetic mechanical metamaterials (Kolken and Zadpoor 2017).

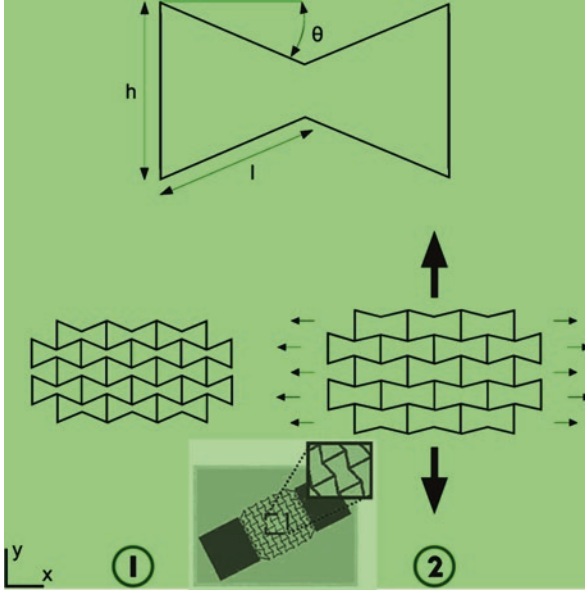


Fig. 11.2 Reentrant bow-tie structure with θ being the reentrant angle, h/l being the cell rib length ratio, and w being the thickness of the ribs (Kolken and Zadpoor 2017): (1) in rest. (2) Tensile loading in y-direction

11.2.1 Reentrant Structures

Reentrant structure generally has a negative angle for directed inward, such as the “bowtie” honeycomb as shown in Fig. 11.2. The deformation of the reentrant structure is dominated by the realignment of cell ribs (hinging), although deflection and axial deformation (stretching) of the cell ribs are also among the mechanisms responsible for the auxetic behavior (Smith et al. 2000).

11.2.1.1 Auxetic Foam

Porous materials are commonly used in vibration and noise control applications as they are known for their ability to dissipate acoustic waves propagating in their medium. Auxetic foams are a subset of porous materials, which consists of a solid phase (the frame or the skeleton) and a fluid phase that is the air or the fluid in pores. They can be produced from conventional low density open cell polymer foams by causing the ribs of each cell to permanently protrude inward, resulting in a reentrant structure. Auxetic foams are characterized by a negative Poisson’s ratio. They expand in all directions when only pulled in one.

Most of the differences between conventional and auxetic foams have been attributed to a change in the cell geometry, governed by the volumetric compression

ratio. Increasing the volumetric compression ratio usually gives rise to a relative minimum in Poisson's ratio, a decrease in Young's modulus (by a factor of 2), and an increase in shear modulus and toughness. However, polymeric foam in tension may experience an increase in Young's modulus at high volumetric compression ratios due to cell rib adhesion or interference. Auxetic foams may have higher yield strengths and energy absorptions than conventional foams of identical original density (Choi and Lakes 1995; Kolken and Zadpoor 2017).

11.2.1.2 Auxetic Honeycomb

Auxetic honeycombs refer to any array of identical reentrant cells which nest together to fill a plane or 3D space and exhibit a negative Poisson's ratio. While regular hexagonal cells show in-plane isotropy, reentrant hexagonal cells are highly anisotropic. They do, however, offer increased transverse Young's moduli and shear moduli as compared to regular hexagonal honeycombs. The transverse shear modulus showed significant dependence on the rib slenderness ratio (w/l), approaching the upper bound at small rib slenderness ratios. A linear relation could be obtained between the Young's modulus and Poisson's ratio, by changing the thickness of the added rib under small strain tension. The Poisson's ratio could even be tuned to positive values by changing the force constant of the added rib. Reentrant hexagonal honeycombs have been applied in the fabrication of filters with enhanced defouling properties and a Poisson's ratio of -1.82 (Alderson et al. 2000).

Besides the typical reentrant hexagonal honeycomb, several other geometries have been shown to deform according to the reentrant mechanism, as shown in Fig. 11.3. Figure 11.3a shows an auxetic arrowhead structure. Depending on the

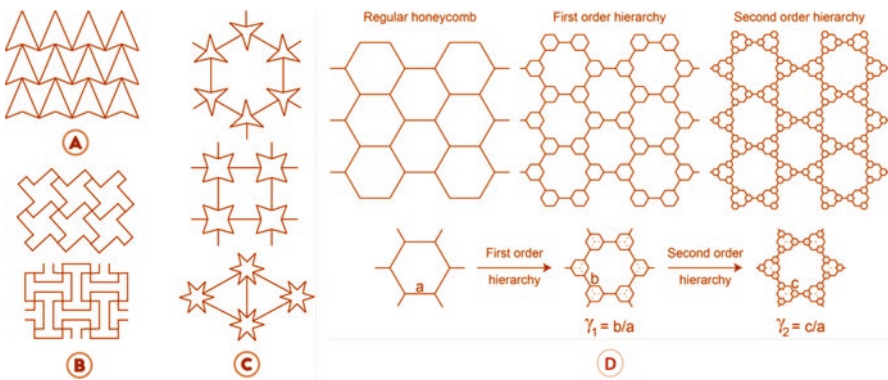


Fig. 11.3 Reentrant honeycomb structures (Mousanezhad et al. 2015; Kolken and Zadpoor 2017): (a) arrowhead; (b) Lozenge grid and square grid (from top to bottom); (c) STAR-3, STAR-4, and STAR-6 systems (from top to bottom); (d) the structural organization of the hierarchical honeycomb structure at each order of hierarchy (γ_i is defined as the ratio of the newly added hexagonal edge length (b for first order and c for second order of hierarchy) to the original hexagon's edge length (a)) (i.e., $\gamma_1 = b/a$ and $\gamma_2 = c/a$)

configuration of the arrowhead, compression will initiate the collapse of the triangles resulting in a transverse contraction with a Poisson's ratio of -0.8 to -0.92 (Larsen et al. 1997).

As shown in Fig. 11.3b, two auxetic geometries, introduced from the missing rib foam, refer to as the Lozenge grid and the square grid. Both structures exhibit an in-plane negative Poisson's ratio, with relative minima at -0.43 and -0.6 , respectively. Since the reentrant hexagonal honeycomb can be considered as a structure made from "arrow-shaped building blocks" and when the arrows are connected in such a way that their arms form "stars," structures with rotational symmetry of order $n = 3, 4,$ and 6 may be built (forming STAR-3, -4 and -6 systems, respectively) (Fig. 11.3c). Opening of the stars under uniaxial loading drives the auxetic effect, whereas the stiffness is governed by the applied force constants (Grima et al. 2005).

Figure 11.3d shows the structural organization of the hierarchical auxetic honeycombs at each order of hierarchy (γ_i is defined as the ratio of the newly added hexagonal edge length (b for first order and c for second order of hierarchy) to the original hexagon's edge length (a) (i.e., $\gamma_1 = b/a$ and $\gamma_2 = c/a$). Hierarchy-dependent elastic buckling introduced at relatively early stages of deformation decreases the value of Poisson's ratio as the structure is compressed uniaxially leading to auxeticity in subsequent stages of deformation. Hierarchical architecture is unique in exhibiting two different deformation modes for structures with different geometrical parameters when compressed along the same direction. An optimal design in terms of the lowest Poisson's ratio is achieved among the structures with first order of hierarchy, which interestingly corresponds to a point in which the buckling modes switch. The auxetic response can further be pronounced (i.e., lower Poisson's ratio) by introducing higher orders of hierarchy. The hierarchical honeycombs provide new insights into designing energy absorbing materials and tunable membrane filters (Mousanezhad et al. 2015).

11.2.1.3 Three-Dimensional Reentrant Structures

To ensure repeatability and enable to tune properties and unit cell geometry of the simple auxetic foams, 3D reentrant structures have been built using additive manufacturing techniques. Figure 11.4a shows a Ti-6Al-4 V reentrant structure manufactured using electron beam melting (EBM), which is a powder-based printing process in which an electron beam is used to selectively melt powder particles. After building each layer, the powder bed is lowered and a fresh layer of material (i.e. powder) is added. In such powder bed fusion systems, the parts may later be sintered or fused layer by layer to create the final structure. By maintaining the relative density of the structure and making its Poisson's ratio more negative, a higher strength and stiffness can be achieved. The same kind of structure can also be made using direct laser writing, optical lithography, and 3D printing (Kolken and Zadpoor 2017).

The buckling-induced pattern transformation seen in 2D soft structures has been extended to 3D in the form of "Bucklicrystals" (Fig. 11.4b, c). This term refers to the periodic arrangement of patterned spherical shells, which in response to a stimulus

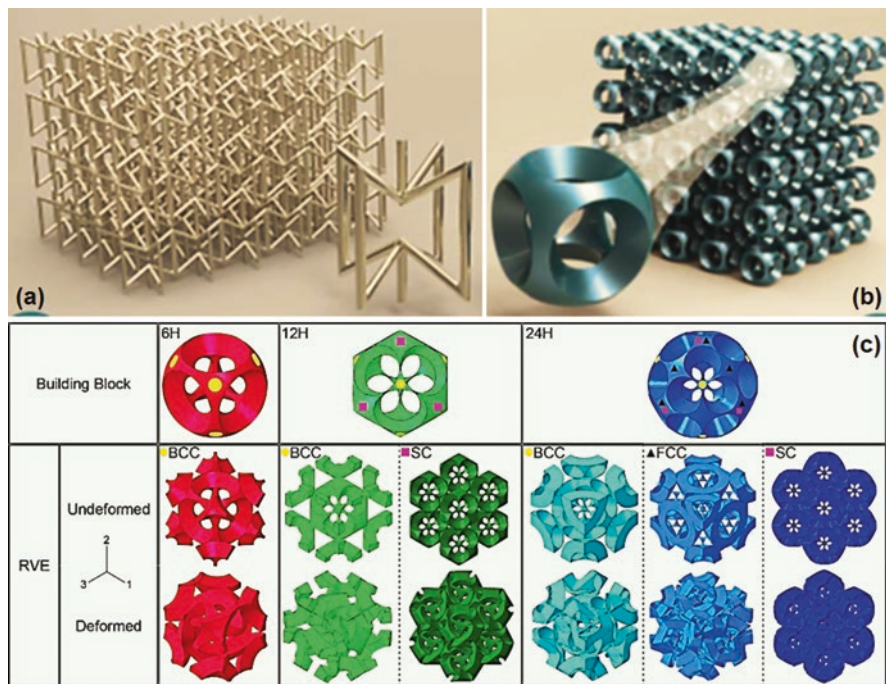


Fig. 11.4 Typical 3D reentrant structures (Babaee et al. 2013; Kolken and Zadpoor 2017): (a) a typical reentrant structure made of 3D reentrant hexagonal unit cells; (b) a 6-hole Bucklicrystal; and (c) gallery of Bucklicrystals—building blocks attached to the surrounding units using *yellow circles, black triangles, and magenta squares* for *bcc, fcc, and sc* packing configurations, respectively. *REV* representative volume elements

undergo an isotropic volume reduction. For this to happen, all ligaments should undergo a uniform first buckling mode. This implies patterns comprising of 6, 12, 24, 30, and 60 holes to be implemented in the building blocks. The 6-, 12-, and 24-hole Bucklicrystals show isotropic volume reduction, indicating a 3D NPR. In fact, the Poisson’s ratios exhibit a nonlinear response to strain: initially starting positive but finally reaching a negative plateau at large strains (−0.4, −0.2, and −0.5, respectively). Except for the 6-hole Bucklicrystal, all crystals retain their transversely symmetric behavior at large strains ($\epsilon = 0.3$) (Babaee et al. 2013; Kolken and Zadpoor 2017).

11.2.1.4 Auxetic Microporous Polymers

Auxetic microporous polymers have been shown to be highly anisotropic, with Poisson’s ratios as low as −12 (Caddock and Evans 1989). A schematic representation of the microstructure is shown in Fig. 11.5a, an interconnected network of

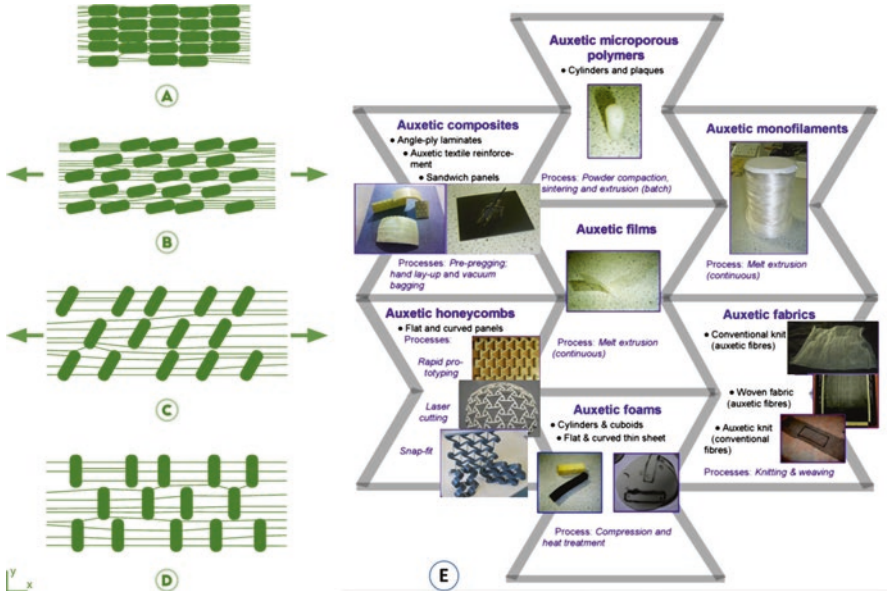


Fig. 11.5 Auxetic microporous polymers (Alderson 2017; Kolken and Zadpoor 2017): (a) nearly fully densified state; (b) tension in fibrils causes particle displacement; (c) rotation of the disk-shaped particles; (d) fully expanded condition; (e) examples of auxetic microporous polymer processes

disk-shaped particles and fibrils. During tensile testing, starting with a nearly fully densified material, the fibrils will cause a first expansion as they become taut and translate the particles (Fig. 11.5b). Secondly, the disk-shaped particles will start to rotate leading to the fully expanded form (Fig. 11.5c, d). A maximum NPR can be obtained at small strain values, primarily caused by the translation of the particles. The Poisson's ratio and stiffness are subsequently increasing with strain, upon rotation of the particles (Kolken and Zadpoor 2017).

As shown in Fig. 11.5e, for the production of auxetic ultra-high molecular weight polyethylene (UHMWPE), three distinct stages can be identified (Alderson 2017; Kolken and Zadpoor 2017): compaction of polymer powder, sintering, and extrusion through a die. This thermoforming route enabled the reproduction of the nodule-fibril microstructure observed in expanded PTFE. With improved processing route, many complex auxetic polymer products have been made.

11.2.2 Auxetic Chiral Structures

A typical auxetic chiral unit comprises a central cylinder encapsulated in tangentially attached ligaments, which is not superimposable on its mirror image. As shown in Fig. 11.6, the described basic unit can either be constructed right handed

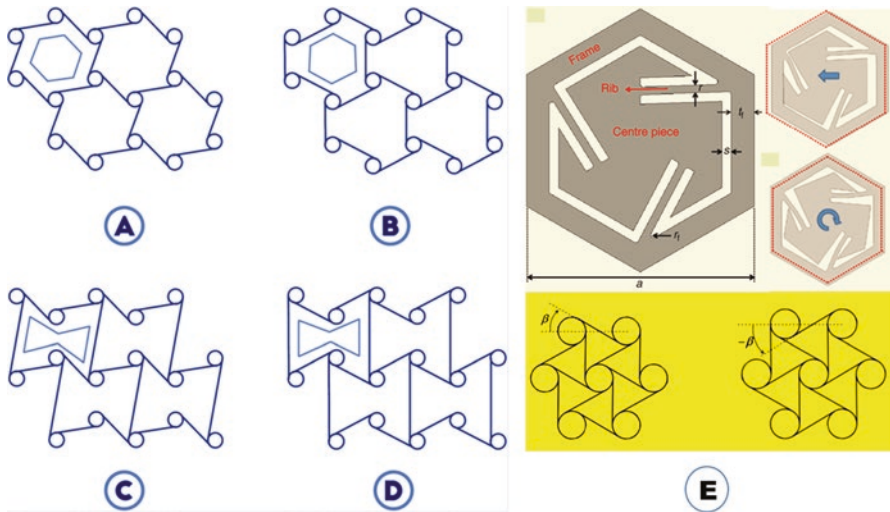


Fig. 11.6 Auxetic chiral structures (Lu and Hu 2016; Kolken and Zadpoor 2017): (a) trichiral honeycomb; (b) reentrant trichiral honeycomb; (c) anti-trichiral honeycomb; (d) reentrant anti-trichiral honeycombs; (e) trichiral lattice

or left handed, creating chiral or anti-chiral structures. Anti-chiral structures exhibit reflective symmetry, since their nodes are attached on the same side of the connecting ligaments. The cylinders will rotate under mechanical loading, causing the ligaments to flex. This results in folding or unfolding of the ligaments under tensile or compressive loadings, respectively. Depending on the geometrical features of the structure, this may result in a negative Poisson's ratio close to -1 . To create periodic chiral structures, the constraints of rotational symmetry should be obeyed. The number of ligaments attached to each node should therefore be equal to the order of rotational symmetry. Unless this constraint is relaxed, only five such structures can exist: trichirals, anti-trichirals, tetrachirals, anti-tetrachirals, and hexachirals. Meta-chiral structures may be created once this constraint is relaxed (Lu and Hu 2016; Kolken and Zadpoor 2017).

Three-dimensional chiral lattice structures have been made out of cubes and numerous deformable ribs. The effective Young's modulus and effective shear modulus depend on the number of unit cells per side while finally converging to a constant value. Increasing this number led to a decrease in stiffness, whereas an opposite effect is achieved by increasing the rib slenderness ratio. The Poisson's ratio could be tuned to negative values (-0.1393) with a sufficient number of cells (Ha et al. 2016).

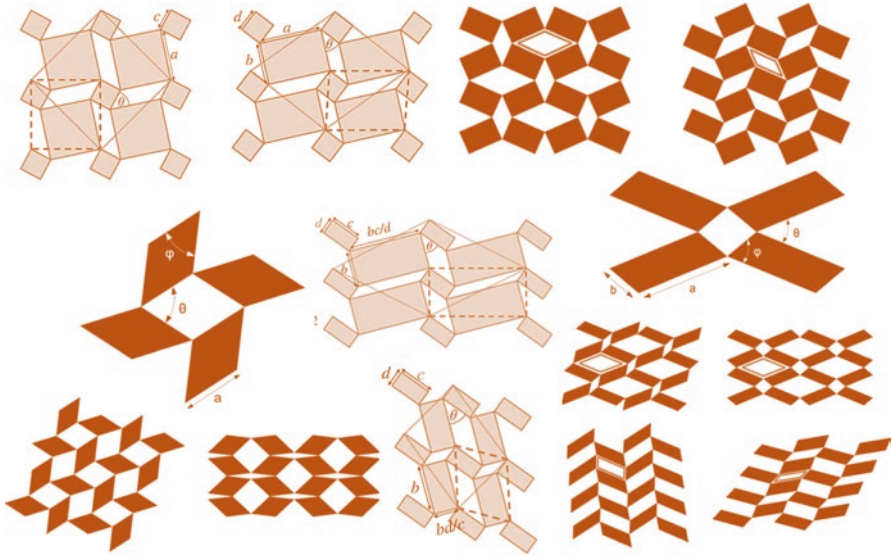


Fig. 11.7 Types of rotating auxetic structures (Grima et al. 2011; Kolken and Zadpoor 2017)

11.2.3 Rotating Rigid and Semirigid Auxetic Structures

An idealized rotating structure contains rigid squares connected through simple hinges. When loaded, the squares will rotate at the vertices, either expanding or contracting depending on the loading type. The concept has been widely implemented using squares, rectangles, triangles, rhombi, and parallelograms, as shown in Fig. 11.7 (Grima et al. 2011; Kolken and Zadpoor 2017).

11.2.4 Dilational Metamaterials

The relationship between the bulk modulus, B ; shear modulus, G ; and Poisson's ratio, ν , of isotropic materials can be written as follows (Zadpoor 2016):

$$\frac{B}{G} = \frac{\nu + 1}{3 \left(\frac{1}{2} - \nu \right)} \quad (11.1)$$

Both B and G are often assumed to be positive to ensure that the material is thermodynamically stable. For B and G to be positive, Poisson's ratio has to vary between -1 and 0.5 . In the case of $\nu = 0.5$, the bulk modulus is extremely high

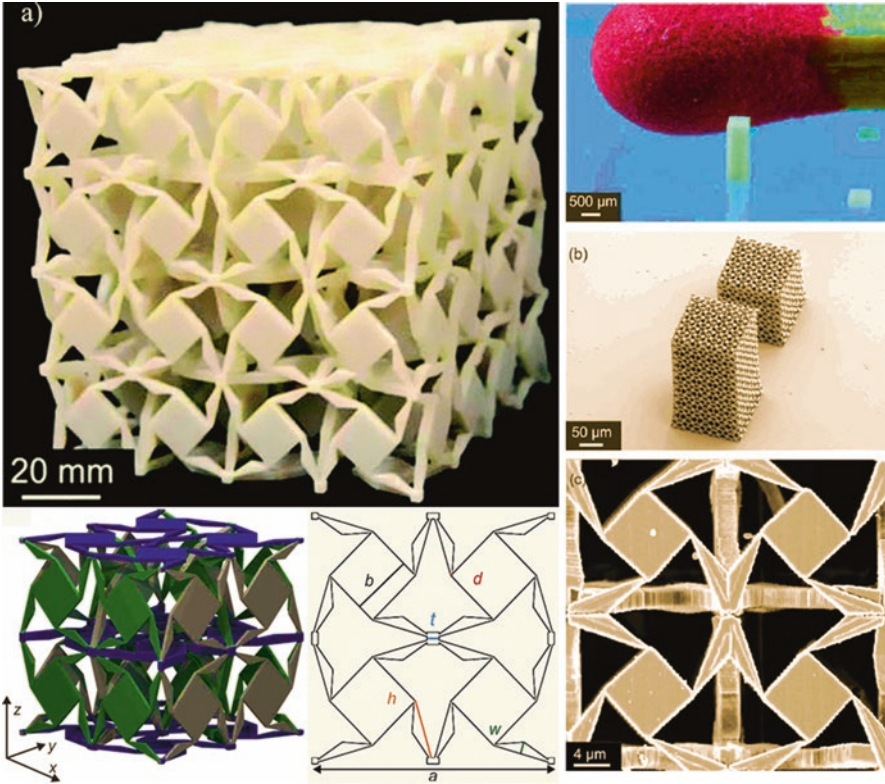


Fig. 11.8 Three-dimensional dilational elastic metamaterials realized at macroscopic (a) and microscopic (b, c) scales using additive manufacturing techniques (Bückmann et al. 2014)

and the shear modulus is extremely low, which is called penta-mode metamaterials (will be discussed in the next section). The opposite of this condition occurs when the Poisson's ratio value, $\nu = -1$. In this case, the bulk modulus is extremely small as compared to the shear modulus, and the extremal material is called a dilational material. That is, the shape of dilational materials remains the same regardless of how much deformation they undergo. It is only their size that changes. In other words, dilational materials are merely scaled as a result of deformation.

Various structures have been proposed for creating dilational metamaterials. Figure 11.8 shows a representative of three-dimensional dilational elastic metamaterials realized at macroscopic (a) and microscopic (b and c) scales using additive manufacturing techniques (Bückmann et al. 2014).

11.2.5 *Potential Applications of Auxetic Metamaterials*

Auxetic metamaterials have been applied in many applications including soft robotics, biomedicine, soft electronics, and acoustics. For instance, auxetic materials are currently used to achieve improved shock absorbance, synclastic curvature, and improved shear performance. These properties are especially useful in the automotive, defense, sports, and aerospace industries (Kolken and Zadpoor 2017).

Porous “smart bandages” have been introduced (bio)medical field to facilitate and monitor the wound healing process. A swelling may induce fiber stretching, which not only increases the breathability of the bandage but may also open up pores for the release of active pharmaceutical ingredients (APIs). The same concept could be applied to the design of smart stents, for the release of APIs during the “blow-up” phase. Hierarchical rotating rigid structures could be engineered to exhibit a variable pore size/shape upon loading. This behavior is not limited to stents and bandages, but could very well be applied in scaffolds and prostheses too. Even the agricultural industry could benefit from the controlled delivery of substances such as fertilizers. Although the auxetic effect is not limited to porous microstructures, it does offer great opportunities for the orthopedic industry where additively manufactured porous structures are often used. Their resemblance to cancellous bone enables their use as bone-substituting materials. When applied in prosthetic limbs or joints, they may counteract the variations in bone volume and hence prevent loosening. Subsequently, their synclastic curvature will allow the prosthesis to conform to the shape of the bone cavity. This may potentially improve the survival rate of prostheses and hence postpone the need for revision surgery (Kolken and Zadpoor 2017).

Auxetic materials have improved resistance against damage, as a result of their capability to distribute stress over a larger part of the material. In addition to negative Poisson’s ratio, useful properties of auxetic materials such as improved indentation resistance and better acoustic/vibration properties can be used for applications such as efficient membrane filter with variable permeability, fasteners, shape memory materials, and acoustic dampers.

11.3 Penta-Mode Metamaterials

Penta-mode metamaterials have:

- (a) Five very small eigenvalues, i.e., they are very compliant in five out of six principal directions
- (b) A very large bulk modulus, B , as compared to their shear modulus—the volume of penta-mode metamaterials does not change as a result of deformation
- (c) The Poisson’s ratio of the metamaterials is 0.5

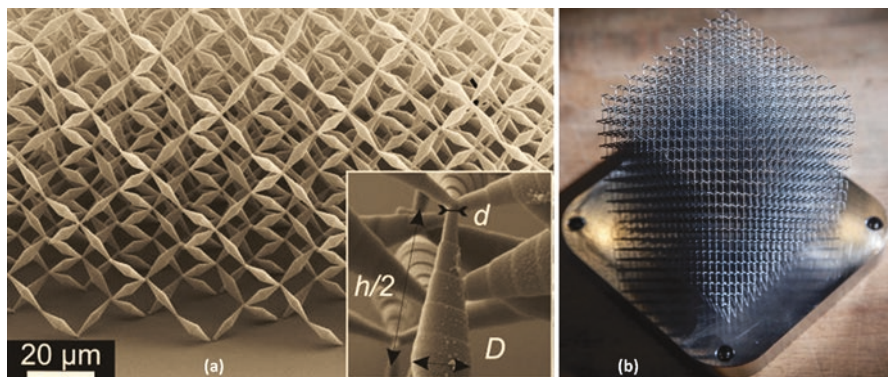


Fig. 11.9 A specific design of penta-mode metamaterials (a) and metallic penta-mode metamaterial based on the same design and manufactured with additive manufacturing technique (b) (Zadpoor 2016)

(d) Very small values of the shear modulus—ideal penta-mode metamaterials will immediately flow away, a behavior which is similar to fluids; therefore, penta-mode metamaterials are also called as “meta-fluids.”

A specific design of penta-mode metamaterials is shown in Fig. 11.9, in which beams with a specific type of variable cross section, i.e. two conical beams attached to each other at their bases, are arranged in a diamond-type lattice structure. This type of penta-mode lattice structure has been realized using 3D printing techniques. A completely different example of penta-mode materials is a gel that can be easily deformed in any given direction but strongly resists changes in volume under hydrostatic pressure. Other examples include granular materials (Milton 2013; Zadpoor 2016).

The mass density of penta-mode metamaterials could be decoupled from their stiffness. This is different from most porous materials and lattice structures where there is a power law relationship between the mass density and the elastic modulus of the structure. The specific properties of penta-mode metamaterials make them attractive for some applications. For example, they could be used for steering elastodynamic waves in specific directions so as to achieve the equivalent of optical cloaking for acoustic waves. The elastic modulus and mass density (or porosity) of penta-mode metamaterials can be changed independently from each other which makes them useful for extending the design space when designing porous tissue engineering scaffolds where the pore size and porosity have consequences in terms of cell attachment, cell nutrition/oxygenation, and rate of tissue regeneration. Moreover, by combining penta-mode metamaterials within the same lattice structure, one could make lattice structures with any positive definite elasticity tensor. This makes penta-mode metamaterials a general framework within which metamaterials can be designed and (additively) manufactured. This is particularly useful for realizing materials with complex distribution of mechanical properties. The complex

distribution of the mechanical properties may have resulted, for example, from application of topology optimization algorithms (Zadpoor 2016).

11.4 Ultra-Property Metamaterials

An ideal material for many structural applications would simultaneously possess two or more of the following properties (Zadpoor 2016): high stiffness, high strength, high toughness, and low mass density. Biological materials such as nacre can achieve high stiffness, high strength, and high toughness all at the same time due to their hierarchical and “staggered microstructure.” With the similar idea, ultra-property metamaterials have been developed with rationally designed architectures that give rise to ultra-stiff, ultra-strong, ultra-tough, and ultra-light properties.

Figure 11.10 shows different designs of ultra-light ultra-stiff metamaterials based on various types of repeating unit cells (Zadpoor 2016). For example, ultra-strong and ultra-light metamaterials are made from ceramics using two-photon lithography, atomic layer deposition, and oxygen plasma etching at the nanoscale. Despite being made from a brittle material, i.e., alumina, the nano-lattices exhibit

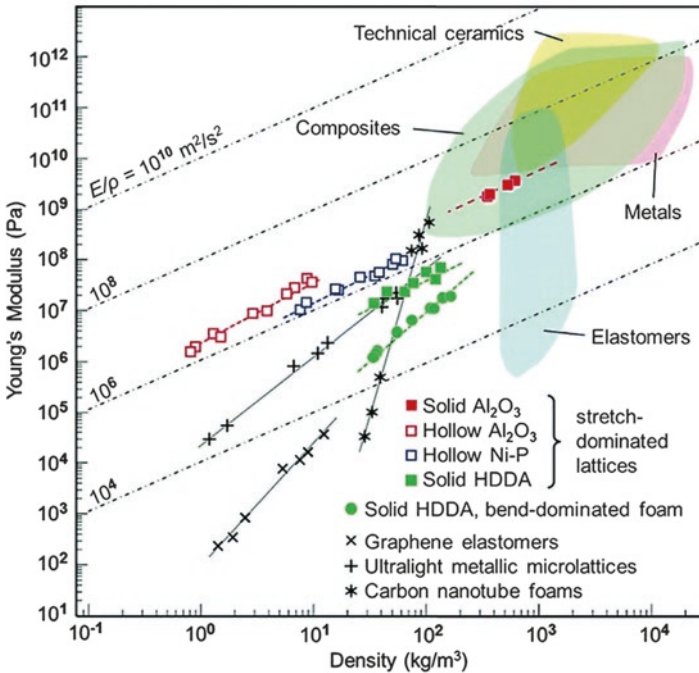


Fig. 11.10 Different designs of ultra-light ultra-stiff metamaterials based on various types of repeating unit cells (Zadpoor 2016)

recoverable deformation even when the metamaterials are compressed beyond 50% strain. The specific architecture of the lattices and the thickness to the radius ratio of the hollow tubes that made the nano-lattices were found to govern the mechanical behavior of those metamaterials (Fig. 11.1b). Another kind of metamaterials shows an almost constant stiffness per unit mass density even when the mass density was reduced by three orders of magnitude. This is a remarkable combination of high stiffness and low density that has been rarely observed elsewhere (Meza et al. 2014; Zheng et al. 2014).

11.5 Negative-Parameter Metamaterials

Negative effective parameters are allowed though at finite frequencies near local resonances. These can have small resonance frequencies equivalent to wavelengths much larger than the lattice constant of a periodic metamaterial structure. A negative mass density ρ means that an elastic body accelerates out of phase with respect to a harmonically varying driving force. For a negative bulk modulus B , the body would compress upon dynamic stretching. Combining $B < 0$ and $\rho < 0$ leads to the counterpart of double-negative or negative-index metamaterials in optics (Christensen et al. 2015).

For example, spherical metal cores coated with a compliant rubber shell, packed to a simple cubic lattice in a host material (Fig. 11.1c)—each core-shell unit forms a simple mass—and spring model, can exhibit a Mie-type resonance frequency far below the Bragg resonance frequency of the lattice. Depending of the order of these resonances, negative effective values of the mass density and/or of the elastic moduli can be accomplished. Combined with a negative mass density, the mechanical energy flow (Poynting) vector points into a direction opposite to that of the phase velocity vector. By combining dipolar-like and rotational resonances of the oscillating chiral center piece, a collective mode is induced that exhibits both negative effective mass density and negative longitudinal modulus (Christensen et al. 2015).

The most general definition of compressibility distinguishes between three types of compressibilities, namely, line, area, and volume compressibility. Negative compressibility basically means that a material expands in response to hydrostatic pressure. Depending on the number of dimensions along which the expansion occurs, the material may have a negative length, area, or volume compressibility. Crystals with negative line and area compressibility have been identified in methanol monohydrate, along with negative and anisotropic thermal expansion. In addition to crystals, a number of other systems exhibit negative compressibility that could be categorized into four major categories (Zadpoor 2016): (a) The geometry of cellular structures is the cause of negative compressibility. For example, hexagonal honeycombs show negative linear compressibility in 2D, while lattice structures made from an elongated hexagonal dodecahedron are 3D geometries that exhibit negative Poisson's ratio and negative compressibility. Tetragonal beam structures also show negative linear compressibility. (b) The combination of two materials with different

mechanical properties. An example of such an engineered material is a truss-type structure composed of multiple materials. (c) The negative compressibility is caused by specific constraints. (d) Negative compressibility is a property of the bulk material and not the way the geometry of the material is organized. Some applications have been proposed for materials with negative compressibility including protection of sensors and other sensitive instruments in deep ocean applications when compression needs to be avoided, study of muscles, and microelectromechanical systems.

Materials with positive stiffness deform in the direction of applied force and form a restoring force that tries to restore the original shape of the deformed material, thereby resisting deformation. Materials with negative stiffness, on the other hand, deform in a direction opposite to the direction of the applied force and form an assisting force, thereby assisting the deformation. Negative stiffness materials therefore experience larger deformations as compared to positive stiffness materials, when subjected to comparable loading conditions. That is the reason materials with negative stiffness are assumed to be unstable unless they are constrained. Materials with negative stiffness can, however, be combined with or embedded within positive stiffness materials or be otherwise constrained for stabilization. Many of the materials that exhibit negative stiffness are associated with some types of bistable (having two stable states) and snap-through behaviors. For example, materials that undergo volume-change phase transformation such as barium titanate or ferroelastic materials such as vanadium dioxide could show the negative stiffness behavior primarily due to their energy storing capability. In addition, other materials with the negative stiffness behavior, e.g., “discontinuous buckling” systems comprise buckled elements. One application of negative stiffness materials is achieving high damping and high stiffness at the same time. Another somewhat related application is the use of metamaterials for transformation acoustic applications such as acoustic cloaking. Many more applications of negative stiffness materials include vehicle vibration protection systems, seismic protection of structures, and railroad vibration isolation (Zadpoor 2016).

11.6 Mechanical Metamaterials with Tunable Negative Thermal Expansion

Materials with low coefficient of thermal expansion (CTE) are less sensitive to temperature changes and thus sought in several areas of engineering, such as precision instruments, scanning electron microscopes, flexible electronics, biomedical sensors, thermal actuators, and MEMS. Low CTE materials are also particularly crucial in aerospace components, such as space-based mirrors and satellite antennas, that are built on earth but operate in outer space where wide temperature swings may cause undesired shape and size shrinkage. Solid materials, such as Invar and other metallic alloys, with intrinsically low or negative thermal expansion exist and are

currently used despite their limitations. One of their drawbacks is the narrow range in which they can operate, which is problematic when large temperature swings, from -150 to 150 °C as in outer space, occur. The CTE of ceramics and other brittle solids, on the other hand, is low as well as insensitive to temperature variation; their brittleness, however, poses challenges because thermal stresses easily peak and lead to abrupt failure. In contrast, the ideal material would have CTE that could be tailored to vanish for the whole range of temperature it operates and would not be brittle, a condition currently unmet by all existing solids. One route to create a material with adjustable CTE is to engineer its structural architecture and purposefully tweak it to yield desired ranges of CTE, from positive to negative values including zero (Lehman and Lakes 2013).

Mechanical metamaterials have shown that the CTE of periodic materials can be tuned by purposefully designing the architecture of their repeating unit and proper selection of the constituent materials. It has been shown that low CTE can be obtained through a purely mechanical and thus temperature-independent mechanism, which can be in principle designed to make the material operate over a wide range of temperature. Existing mechanical metamaterials, however, have their limitations. The majority are two dimensional and can accommodate only in-plane thermal deformation. A handful are three-dimensional. Among those, some can generate a large range of CTE, i.e., their CTE tunability is high, but their structural efficiency, i.e., the specific stiffness and strength, is poor, since their architecture deform by bending when loaded, a deformation mechanism that is far from being structurally efficient. A very small set of architectures, on the other hand, are stretch dominated with high specific stiffness, but these concepts can generate only a narrow range of CTE and cannot yield a vanishing CTE. The trade-off between CTE tunability and structural efficiency has been explored. Figure 11.11 shows some examples to create a structurally efficient 3D architected material with highly tunable CTE including

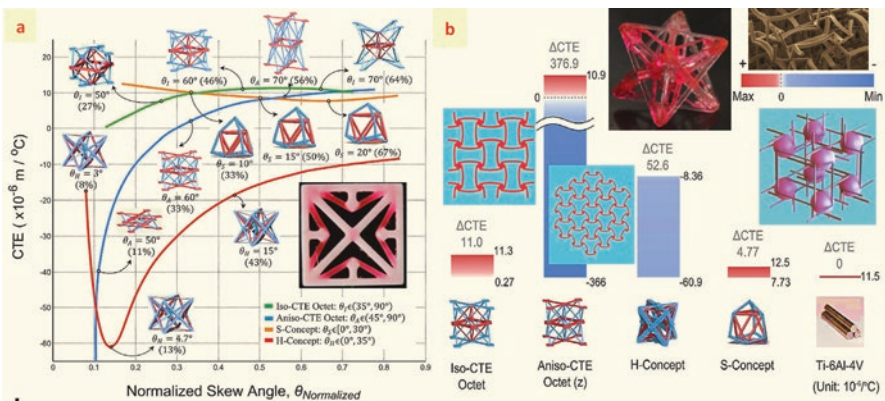


Fig. 11.11 Mechanical metamaterials with tunable thermal expansion (Xu and Pasini 2016): (a) thermal properties of the octet bi-materials and other mechanical metamaterials; (b) histogram showing the CTE tunability (ΔCTE) as well as the max and min CTE for some mechanical metamaterials compared to a low CTE solid material, i.e., Ti-6Al-4 V

negative, zero, or positive, with no loss in structural efficiency. The simplicity of the design and the ease in fabrication make this kind of bi-material architecture well suited for a wide range of applications, including satellite antennas, space optical systems, precision instruments, thermal actuators, and MEMS (Xu and Pasini 2016).

11.7 Active, Adaptive, and Programmable Metamaterials

Active, adaptive, and programmable metamaterials have been developed utilizing soft materials, large deformations, and instability. Various designs of mechanical metamaterials use clever combinations of these three concepts with rationally designed geometries that could, for example, harness the instability of soft materials in the nonlinear deformation range so as to achieve unprecedented or rarely seen properties and functionalities (Zadpoor 2016).

Active and programmable mechanical metamaterials have been emerged from research on the instability regimens of soft and patterned materials. Extreme levels of programmability based on blocks that could perform mathematical operations such as spatial differentiation, integration, and convolution have been achieved in electromagnetic metamaterials. Although the same level of programmability is yet to be shown for mechanical metamaterials, the idea of active and programmable metamaterials has spread to the mechanical metamaterials community too. Cellular solids made from soft materials and confined laterally are found to show some level of programmability in their mechanical behavior as well as multi-stability and “giant hysteresis.” Switching, activating, adapting, or regulating the mechanical behavior of metamaterials and their associated functionalities are the main purposes of another category of metamaterials. Prescribing and controlling the instability modes of metamaterials is the most widely used strategy for achieving those purposes. Two- and three-dimensional cellular soft solids are often used for regulating the instability behavior of materials (Fig. 11.12), because the geometry of the pores and their sizes could be used not only for changing the instability thresholds but also for regulating the instability types and patterns sometimes fully independent of the mechanical properties of the bulk material from which they are made. Various instability patterns and the way they break the applicable symmetries lead to distinct mechanical properties and functionalities. If the instability modes of a (multi-stable) metamaterial could be controlled or at least prescribe it through the rational design of the cellular structure, the functionality of the metamaterial and activate specific modes of instability would be controlled when required. That is the main idea behind the design of active/adaptive metamaterials which is often supplemented with other novel approaches such as coupled gyroscopes on a lattice or utilizing the so-called soft modes that function as possible building blocks for smart soft actuators (Janbaz et al. 2016).

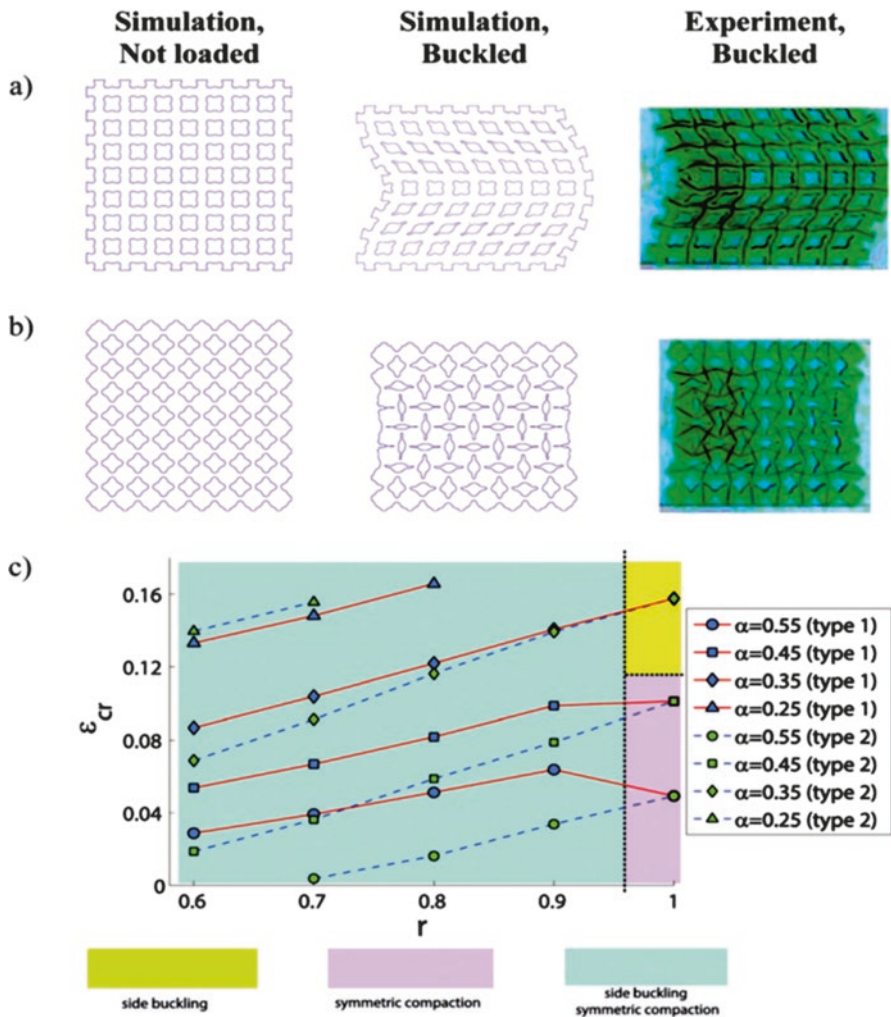


Fig. 11.12 Some design of cellular soft matter shows instability thresholds and instability patterns that could be fully controlled by geometry regardless of the mechanical properties of the bulk materials from which they are made (Janbaz et al. 2016): in this specific design, the instability patterns may be side buckling (a) or compaction (b) depending on the shape of the pores. An instability map could be used to relate various geometrical parameters to the instability patterns (c)

11.8 Origami-Based Metamaterials

Origami is the traditional Asian art of paper folding; kirigami additionally allows for introducing cuts into the paper. Today, by using free available computer programs such as “TreeMaker,” one can design the origami folding patterns of almost arbitrary complex three-dimensional structures—including origami (kirigami)

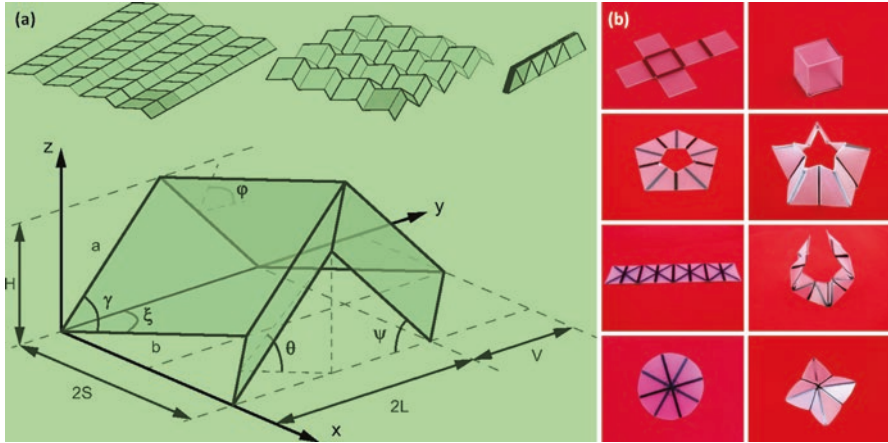


Fig. 11.13 Examples of origami-based metamaterials (Dickey et al. 2012; Schenk and Guest 2013): (a) the geometrical design of Miura-ori origami structures; (b) self-folding of flat polystyrene sheets into 3D objects by inducing localized heat shrink

mechanical metamaterials. Instead of paper, one can likewise start from a thin polymer sheet with indentations defining the creases or from rigid structures with hinges instead of the creases. Effectively, one can think of the creases as torsional Hooke's springs. Temperature-responsive polymer gels instead of paper are yet another option (Christensen et al. 2015).

Depending on the design of the crease and folding patterns, the resulting folded three-dimensional structure will have different geometries, mechanical properties, and functionalities. In rigid origami, for instance, the folding lines could be considered as kinematic joints. Figure 11.13 shows examples of origami-based metamaterials (Dickey et al. 2012; Schenk and Guest 2013). The shape of the folds of Miura-ori origami structures is determined by several geometrical parameters (Fig. 11.13a). Self-folding of flat polystyrene sheets into 3D objects can be done by inducing localized heat shrink (Fig. 11.13b).

Mechanical metamaterials created based on (some variants of) the Miura-folded origami have been, for example, shown to exhibit negative (in-plane) Poisson's ratios. Some variants of the Miura-ori origami have been used for developing reprogrammable mechanical metamaterials. Specific designs of Miura-ori origami tubes could be used for obtaining stiff and reconfigurable mechanical metamaterials. Origami-like structures have demonstrated some other features of mechanical metamaterials such as bistability and multi-stability. Therefore, combining the features of origami structures such as low weight, design flexibility, and alternative manufacturing possibilities with the anomalous properties shown by mechanical metamaterials is a promising area of research that is expected to deliver new categories of metamaterials and novel features not seen in other types of mechanical metamaterials.

Origami (kirigami) mechanical metamaterials could be used for different applications including self-folding robots, medical stents, active and deployable structures, and other areas related to mechanical metamaterials (Zadpoor 2016).

11.9 Mechanical Metamaterials as Seismic Shields

The regularity of earthquakes, their destructive power, and the nuisance of ground vibration in urban environments, all motivate designs of defense structures to lessen the impact of seismic and ground vibration waves on buildings. Low-frequency waves, in the range 1–10 Hz for earthquakes and up to a few tens of Hz for vibrations generated by human activities, cause a large amount of damage, or inconvenience; depending on the geological conditions, they can travel considerable distances and may match the resonant fundamental frequency of buildings. The ultimate aim of any seismic mechanical metamaterials and shields is to protect over this entire range of frequencies; the long wavelengths involved, and low frequency, have meant this has been unachievable to date. The preferable strategy is to attenuate seismic waves before they reach critical targets, additionally providing the means to protect distributed areas rather than individual structures. This approach can be implemented via seismic wave barriers made of mechanical metamaterials, including phononic crystals, locally resonant metamaterials, penta-mode lattices, 3D large-scale mechanical metamaterials, clamped seismic metamaterials, and many more other mechanical metamaterials due to their unusual behaviors, such as exceptional strength- and stiffness-to-weight ratios, excellent strain recoverability, very soft and/or very stiff deformation modes, auxetic behavior, phononic band-gaps, sound control ability, negative effective mass density, negative effective stiffness, negative effective refraction index, superlens behavior, localized confined waves, etc. These properties provide great potential to make them as components of new-generation seismic shields and dampers.

Figure 11.14 shows a seismic metamaterial device consisting of columns clamped to the bedrock surrounding the building to be protected. The structure atop a soil layer of finite thickness that overlays the bedrock; columns clamped to the bedrock puncture the soil layer and reach to the surface, or close to surface. The array of columns encircling the building to be protected.

11.10 Future Trends

The widespread availability of advanced 3D printing and additive manufacturing machines and services should enable researchers to realize the proposed theoretical concepts and experimentally observe the mechanical behavior of the resulting metamaterials, including the nonlinear range of deformations and soft metamaterials. Of particular importance are multimaterial 3D printing techniques that could start new

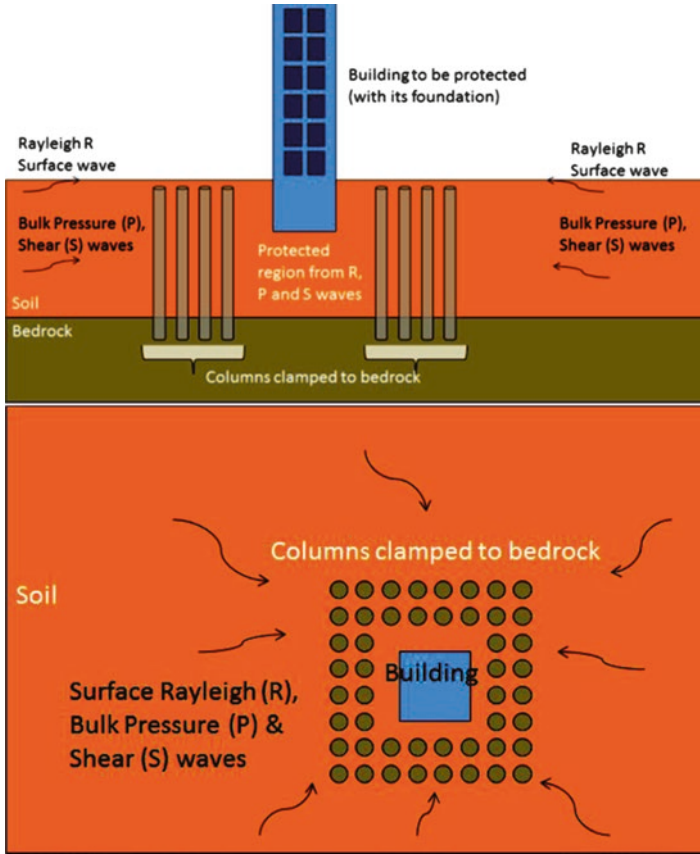


Fig. 11.14 The seismic metamaterial device consisting of columns clamped to the bedrock surrounding the building to be protected

paradigms in the design of mechanical metamaterials. For example, the spatial distribution of materials with different mechanical properties could be combined with rationally designed micro-architecture when designing mechanical metamaterials. Three-dimensional printing of soft materials could further enrich the possibilities for design and manufacturing of active, adaptable, and programmable metamaterials (Zadpoor 2016).

In addition to 3D printing, other design and production paradigms such as origami and kirigami would result in innovative mechanical metamaterials. In addition, the static, quasi-static, or specific types of dynamic behaviors of mechanical metamaterials have been widely explored. However, actual use of mechanical metamaterials for structural applications requires a thorough study of their fatigue behavior. Future research on mechanical metamaterials will give the widespread availability of advanced design techniques such as topology optimization and the ever increasing possibilities offered by a wide range of rapidly evolving additive manufacturing techniques (Zadpoor 2016).

References

- Alderson A (2017) Auxetic polymeric materials: expanding materials and applications. <https://www.iom3.org/sites/default/files/news-documents/alderson.pdf>. Accessed on 3/21/2017
- Alderson A, Rasburn J, Ameer-Beg S, Mullarkey PG, Perrie W, Evans KE (2000) An auxetic filter: a tuneable filter displaying enhanced size selectivity or defouling properties. *Ind Eng Chem Res* 39(3):654–665
- Babae S, Shim J, Weaver JC, Chen ER, Patel N, Bertoldi K (2013) 3D soft metamaterials with negative Poisson's ratio. *Adv Mater* 2013:1–6. doi:10.1002/adma.201301986
- Bückmann T, Schittny R, Thiel M, Kadic M, Milton GW, Wegener M (2014) On three-dimensional dilational elastic metamaterials. *New J Phys* 16:033032
- Caddock B, Evans K (1989) Microporous materials with negative Poisson's ratios – I. Microstructure and mechanical properties. *J Phys D Appl Phys* 22(12):1877
- Choi J, Lakes R (1995) Analysis of elastic modulus of conventional foams and of re-entrant foam materials with a negative Poisson's ratio. *Int J Mech Sci* 37(1):51–59
- Christensen J, Kadic M, Wegener M, Kraft O, Wegener M (2015) Vibrant times for mechanical metamaterials. *MRS Commun* 5:453
- Dickey M, Liu Y, and J Genzer (2012) Light-induced folding of two-dimensional polymer sheets. SPIENewsroom, 2012. <http://spie.org/newsroom/4530-light-induced-folding-of-two-dimensional-polymer-sheets>. Accepted on 3-28-2017
- Grima JN, Gatt R, Alderson A, Evans K (2005) On the potential of connected stars as auxetic systems. *Mol Simul* 31(13):925–935
- Grima JN, Manicaro E, Attard D (2011) Auxetic behaviour from connected different-sized squares and rectangles. *Proc R Soc A* 467:439–458
- Ha CS, Plesha ME, Lakes RS (2016) Chiral three-dimensional lattices with tunable Poisson's ratio. *Smart Mater Struct* 25(5):054005
- Hopkins JB, Culpepper ML (2010a) Synthesis of multi-degree of freedom, parallel flexure system concepts via freedom and constraint topology (FACT) – part I: principles. *Precis Eng* 34(2):259–270
- Hopkins JB, Culpepper ML (2010b) Synthesis of multi-degree of freedom, parallel flexure system concepts via freedom and constraint topology (FACT)-part II: practice. *Precis Eng* 34(2):271–278
- Hou X, Silberschmidt VV (2015) Metamaterials with negative poisson's ratio: a review of mechanical properties and deformation mechanisms. In: Silberschmidt VV, Matveenko VP (eds) *Mechanics of advanced materials -analysis of properties and performance*. Springer International Publishing, Switzerland pp 155–179
- Janbaz S, Weinans H, Zadpoor AA (2016) Geometry-based control of instability patterns in cellular soft matter. *RSC Adv* 6:20431–20436
- Kolken HMA, Zadpoor AA (2017) Auxetic mechanical metamaterials. *RSC Adv* 7:5111–5129
- Larsen UD, Signund O, Bouwsta S (1997) Design and fabrication of compliant micromechanisms and structures with negative Poisson's ratio. *J Microelectromech Syst* 6(2):99–106
- Lehman J, Lakes R (2013) Stiff lattices with zero thermal expansion and enhanced stiffness via rib cross section optimization. *Int J Mech Mater Des* 9:213–225
- Lu X, Hu G (2016) Elastic metamaterials making use of chirality: a review. *J Mech Eng* 62(7–8):403–418
- Meza LR, Das S, Greer JR (2014) Strong, lightweight, and recoverable three-dimensional ceramic nanolattices. *Science* 345:1322–1326
- Miller W, Hook P, Smith CW, Wang X, Evans KE (2009) The manufacture and characterisation of a novel, low modulus, negative Poisson's ratio composite. *Compos Sci Technol* 69(5):651–655
- Milton GW (2013) Complete characterization of the macroscopic deformations of periodic unimode metamaterials of rigid bars and pivots. *J Mech Phys Solids* 61:1543–1560
- Mousanezhad D, Babae S, Ebrahimi H, Ghosh R, Hamouda AS, Bertoldi K, Ashkan V (2015) Hierarchical honeycomb auxetic metamaterials. *Sci Rep* 5:18306

- Schenk M, Guest SD (2013) Geometry of Miura-folded metamaterials. *Proc Natl Acad Sci U S A* 110:3276–3281
- Smith CW, Grima J, Evans K (2000) A novel mechanism for generating auxetic behavior in reticulated foams: missing rib foam model. *Acta Mater* 48(17):4349–4356
- Spadaccini C (2015) Mechanical metamaterials: design, fabrication, and performance. In: *Frontiers of engineering: reports on leading-edge engineering from the 2015 symposium*. National Academies Press, Washington pp 85–98. <http://www.nap.edu/21825>
- Xu H, Pasini D (2016) Structurally efficient three-dimensional metamaterials with controllable thermal expansion. *Sci Rep* 6(34924):2016. doi:10.1038/srep34924
- Zadpoor AA (2016) Mechanical meta-materials. *Mater Horiz* 3:371–381
- Zheng X, Lee H, Weisgraber TH, Shusteff M, DeOtte J, Duoss EB et al (2014) Ultralight, ultrastiff mechanical metamaterials. *Science* 344:1373–1377

Chapter 12

Perspective and Future Trends

12.1 Emerging Metamaterials Capabilities and new Concepts

Based on what has occurred in RF and microwave metamaterials, the development of technology rooted in research on metamaterials occurs when the unique properties and attributes of these artificial materials systems are tailored to meet the needs of some specific application. In this way, metamaterials are not generally useful, but can be specifically configured to provide an engineered response when exotic, textured or dynamic properties are needed (Urbas et al. 2016).

12.1.1 *Virtual Photon Interactions Mediated by Metamaterials*

Thermal noise inside materials is the fundamental origin of blackbody radiation while quantum noise in vacuum lies at the heart of exotic phenomena such as the Lamb shift and Casimir forces. In order to manipulate the thermal and quantum fluctuations, metamaterials can be used to alter and control the zero point and thermal energy density inside materials for a range of applications including coherent thermal sources, thermos-photovoltaics, non-classical light sources and enhanced quantum interactions (Cortes and Jacob 2016).

The exchange of virtual photons between atoms or molecules can have measurable consequences, such as the collective Lamb shift of energy levels between multiple atoms. If the metamaterial can be engineered to alter this virtual photon interaction, many quantum electrodynamic effects can be enhanced even at large inter-molecular distances. Hyperbolic and ϵ -near-zero metamaterials have been used to achieve such long-range super-coulombic virtual photon effects. Long-range virtual photon interactions can induce entanglement between distant atoms and also help address the long-standing issue of scalability of qubits (Cortes and

Jacob 2016). In addition, all-dielectric metamaterials can be used for transparent subdiffraction photonics. All dielectric media can be explored in a host of interesting fundamental directions including quantum and thermal photonics and it can also pave the way for practical metadevices (Urbas et al. 2016).

A singular resonance can occur between plasmonic modes with positive and negative frequency in moving media made out of two metallic plates separated by a small gap, which can move relative to each other. A wave can appear as a positive photonic mode on one plate and be Doppler-shifted to a mode of equal-but negative-frequency on the other plate if the velocity of the plates and the size of the gap between them both have critical values. This situation gives rise to perfect coupling of waves of positive and negative frequency in the near-field region and a resonance with an infinite quality factor, which is fundamentally different from any resonance in stationary systems. This resonance leads to giant vacuum friction and is an important quantum phenomenon, which can occur at the nanoscale. The single-quantum emitters can be precisely positioned with atomic force microscope (Guo and Jacob 2014).

12.1.2 Routes to Aperiodic and Correlation Metamaterials

In the case of subwavelength structures with structurally complex geometries, such as systems with aperiodic positional order, the standard effective medium theory (EMT) will not be applicable. The distinctive symmetries (e.g. scale-invariance symmetry, local parity/reflection symmetry etc) embedded in deterministic aperiodic sequences significantly affect the metamaterial properties by establishing structural correlations that give rise to complex (i.e. generally multifractal) distributions of transmission gaps of varying widths at all wavelengths, irrespective of the optical thickness of the component layers. In addition, periodic/aperiodic positional ordering of subwavelength building blocks invariably introduces nanoscale nonlocal effects. This more general scenario is called as correlation metamaterials, meaning structures where positional order and correlation effects strongly influence their overall optical responses in the metamaterial limit. If properly engineered, nonlocal effects in such structures may result in a number of novel applications to nanoguiding and nonlinear signal generation especially with respect to anisotropic media with hyperbolic dispersion (Savoia et al. 2013).

Correlation metamaterials designed according to aperiodic mixing rules can expand concept well beyond the conventional EMT paradigm, providing access to additional degrees of freedom and opportunities. In particular, understanding the distinctive behavior of aperiodic metamaterials with structural resonances extending across multiple wavelength scales may advance fundamental science as well as engineering applications, especially in the important areas of multiplexed optical bio-sensing and enhanced nonlinear frequency conversion (Urbas et al. 2016).

There are multiple routes, not necessarily disconnected, that demonstrate the relevance of aperiodic order and positional correlations to metamaterial research.

One path originates from the systematic numerical optimization of specific metamaterials functions, such as broadband nanofocusing, negative refraction, reduced optical losses etc. Genetic optimization algorithms that have been successfully applied to the plasmonic nanoantennas and negative-index metamaterials, demonstrate optimal aperiodic designs. However, more efficient and accurate electromagnetic simulation tools capable of dealing with device-level complexity, large electric size parameters and localized nonlinearities are needed in order to fully leverage these powerful optimization techniques. Alternative routes towards the engineering of aperiodic media are provided by digital and coding, or programmable, metamaterials. It is possible to digitally synthesize optical structures that perform desired functions by properly sculpting only two material ‘bits’ into local functional units called metamaterial bytes. In contrast to traditional metamaterials, often constrained by log-range periodicity, digital metamaterials possess well defined structural units (i.e. the bytes) simply designed by mixing two material bits at the nanoscale. As a result, carefully designed local spatial ordering contributes to determine the effective properties of digital metamaterials, analogously to ordered sequences of ‘0 s’ and ‘1 s’ that convey information by their local position within more complex digital messages. On the other hand, in the related approach of coding metamaterials the resulting bytes do not even need to be described by effective medium parameters. Such metamaterials only rely on the presence of two types of unit cell with 0 and π phase responses, which can be controlled by field programmable gate arrays (FPGAs). Desired optical properties can be achieved by ‘programming’ two materials bits that display, when assembled into a specific pattern, the targeted responses. In particular, by dynamically programming the same metamaterial using different coding sequences it becomes possible to manipulate electromagnetic fields in very different manners and thus realize distinctly different functionalities. The third path to aperiodic order is that of quasicrystals and aperiodic tilings, which is called as the geometrical approach. This approach, which is rooted in geometry (e.g. fractal geometry and aperiodic point patterns) has been largely investigated in nanophotonics, where it led to numerous device applications to optical sensing, nonlinear optics, light sources, energy harvesting and solar cells. The geometrical approach leverages a large number of rigorous results on the relationship between the types of structural order displayed by a given system, its energy spectrum and wave transport properties. For example, enhanced transmission resonance through quasi-crystal arrays of subwavelength apertures; broadband transmission of terahertz radiation with enhanced efficiency through quasi-periodic grating structures; aperiodic patterns of Ag nanowires exhibit strong magnetic resonance with negative effective index at optical frequency (even stronger than their periodic counterparts). However, in order to drastically reduce the inherent optical losses of metal based components, it is highly desirable to implement future devices using all-dielectric materials within a scalable and cost-effective fabrication approach (Della and Engheta 2014; Urbas et al. 2016).

The engineering of all-dielectric aperiodic metamaterials with multiscale structural resonances induced by positional correlations has the potential to enable more efficient devices with controllable responses over multispectral ranges, at reduced

optical losses and featuring novel transport and scattering properties. However, in order to implement this vision, some challenges facing materials growth and device fabrication need to be overcome (Capretti et al. 2015; Urbas et al. 2016): (a) Low-loss and silicon compatible resonant materials, such as conductive oxides and nitrides, need to be developed to replace noble metals in the near-infrared and optical regime. (b) High-throughput and cost-effective fabrication techniques, such as three-dimensional fabrication of aperiodic nanostructures, need to be developed that can equally accommodate periodic and aperiodic designs with deep subwavelength features over large areas. If realized, these structures could additionally leverage strong chiral effects for the engineering of negative index and add new vistas to the powerful vision of digital metamaterials and transformation optics. Therefore, low-loss all-dielectric metamaterial structures with engineered nonlocal responses, geometrically determined electric/magnetic resonances, and enhanced nonlinearities may result in novel devices that operate across multiple spectral bands with unprecedented control of electromagnetic field localization and transport phenomena.

12.1.3 Mathematical Operations and Processing with Structured Metamaterials

Materials control waves, and as such they can, in principle, tailor, manipulate, redirect and scatter waves as required. In the field of metamaterials, the unprecedented possibility to design and engineer materials with desired material parameters temporally, spatially, locally and/or globally makes it possible to manipulate waves, e.g. electromagnetic and optical waves, in order to produce useful functionalities in devices and components. Moreover, metamaterials can bring a new vista for the next generation of wave-based functional nanostructures. For example, structured materials at the nanoscale may deform wave profiles in order to perform mathematical operations and computation, such as differentiation, integration and convolution, on incoming wave profiles. Handling modern audio and video data transmission and storage in a shrinking volume and at an increasing speed demands a new mindset and a disruptive methodology and approach. Metamaterials may offer an attractive possibility for a roadmap to address such a challenge. More specifically, computational metamaterials with the possibility to perform mathematical operations on incoming wave's profiles may potentially lead to a new paradigm for mathematical computation and signal processing with unprecedented speeds (Urbas et al. 2016).

Conventional digital computers are formed by clusters of numerous electronic 'circuit elements', functioning based on sophisticated algorithms and processing methodologies. It is interesting to explore whether optical metatronics may be a candidate for such a platform. Figure 12.1a shows the analogy between electronic signal processing and its optical metatronic counterpart. In electronics, a collection of circuits provides a processor with a desired transfer function affecting the

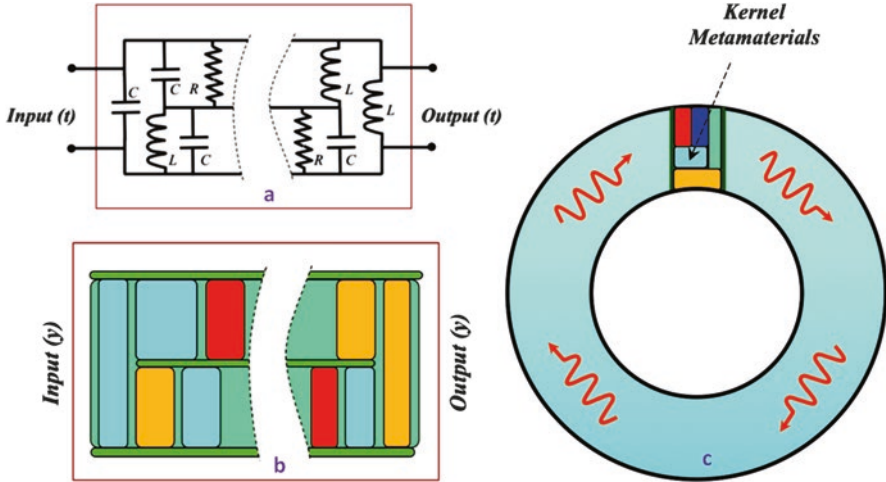


Fig. 12.1 Sketches of mathematical operations and processing with structured materials (Silva et al. 2014): (a) an electronic processor, formed by a collection of electronic circuit elements; (b) an optical metatronic processor, formed by various structured material blocks; and (c) concept for a future ‘equation solver’ using structured materials

temporal frequency contents of incoming signals. By analogy, the optical metatronic processor will be made of collections of nanomaterial structures, each acting as an optical circuit element but when arranged together functioning with a given spatial (and maybe also temporal) transfer function (i.e. desired spatial Green function) operating on an incoming wave, resulting in an output wave, whose spatial profile resembles the result of the desired mathematical operation on the profile of the incident wave (Fig. 12.1b). Two possible approaches for such metamaterial wave-based processors have been studied (Silva et al. 2014): (a) to design metasurfaces with required transfer functions in the spatial Fourier domain; (b) to engineer desired Green functions directly in the spatial coordinate domain, bypassing the need to perform spatial Fourier transform. In the former approach, one needs to utilize optical structures that perform spatial Fourier transform (such as conventional convex lenses or graded-index dielectric slabs and fibers) before adding the metasurfaces with desired transfer function (e.g. ik in the wavenumber k domain for the operation of spatial differentiation in the spatial coordinates), while in the latter there is no need for the spatial Fourier transformation, and thus much thinner structures such as multilayered metamaterial structures with thickness of the order of a few wavelengths can be designed to engineer the needed Green function. The concepts of ‘metamaterial analog computing’ and ‘wave-based signal processing’ by exploiting wave interactions with combinations and collections of material nanostructures may provide a transformative direction in signal processing at the nanoscale. This idea may also be augmented with the notion of ‘digital metamaterials’, in which two constituent material building blocks can be combined as ‘metamaterial bits’ to achieve a desired set of material parameters. The challenges to be overcome include

the need for high-precision nanofabrication, highly accurate characterization of material parameters, and structural and material stability in temperature-varying environments, etc. Moreover, such a wave-based processing platform will benefit tremendously from programmable architectures via reconfigurable materials (Urbas et al. 2016).

The next generation of near-field scanning optical microscopy (NSOM) with multiprobe systems, deeply subwavelength nanoscopy and other electron-beam-based characterization techniques such as cathodoluminescence (CL) microscopy and electron energy-loss spectroscopy (EELS) are all useful tools to address the need for future nanomaterial characterization and metrology. Another important element in the path to achieving ‘wave-based analog computing’ using metamaterials is the possibility of tunability and reconfigurability of constituent material elements forming such devices in order to perform different operations with the same material device. In integrated electronic circuits, the notion of field-programmable gate arrays (FPGAs), in which a user can program the circuit after construction in order to reconfigure it for a different functionality, has been proven to be a powerful concept in various applications of electronics. If FPGA-inspired metamaterials become a reality in the near future, numerous applications will emerge in the field of nanophotonics. For example, ‘programmable light-based analog computing at the nanoscale’ can perform different mathematical operations by reconfiguring its material constituents at will. Finally, one of the exciting future directions following wave-based analog computing will be to explore how such a system can be augmented to ‘solve equations’. If we start with the metamaterial structures that perform a mathematical operation such as differentiation or integration, by applying an appropriate feedback, one might be able to form an optical structure whose eigen solutions might be proportional to the solutions of a given differential or an integral equation, as shown in Fig. 12.1c. The concept of ‘informatic metamaterials’, may provide a transformative platform for mathematical computation and information processing at the nanoscale (Silva et al. 2014; Urbas et al. 2016).

12.1.4 Topological Effects in Metamaterials

Topological effects in metamaterials have been developed, including photonic topological insulators and optical topological phase transitions. Topological insulators represent an exotic state of quantum matter which cannot be characterized by symmetry alone and requires additional topological consideration for its complete understanding. In contrast to conventional insulating and conducting states of material, the topological insulators are insulating in the bulk, but allow for electronic transport to occur on their surface in the form of edge states, which is intimately related to their topological origin, as shown in Fig. 12.2a, b. The edge states are characterized by their spin being in one-to-one correspondence with their propagation direction or ‘spin locked’, which makes these modes insensitive to local defects, disorder and other structural imperfections. The latter property appears to be of

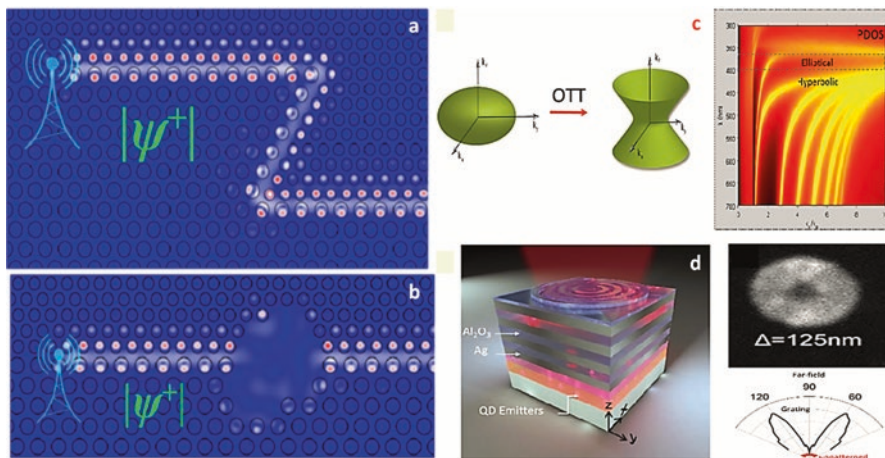


Fig. 12.2 Topological effects in metamaterials (Krishnamoorthy et al. 2012; Galfsky et al. 2015): Topologically protected propagation of light in photonic topological insulators (a) avoiding back-reflection at sharp corners and (b) avoiding formation of Fabry–Perot resonances in the cavity; (c) Optical topological transition in iso-frequency surface and the associated modification in photon density of states; (d) bullseye grating used for outcoupling high- k states along with observed emission and far-field emission pattern

immense value in electromagnetics, where an exotic state analogous to topological insulators has been emulated with the use of magnetic photonic crystals and bianisotropic metamaterials (Chen et al. 2014a).

Another topological concept—optical topological transition (OTT)—emerges in hyperbolic metamaterials. These structures are characterized by very unusual topology of their constant-frequency contours, which, in contrast to elliptical contours found in conventional dielectrics, assume hyperbolic shapes. However, the most interesting behavior takes place at the crossover between elliptical and hyperbolic topologies (Fig. 12.2c), where the mathematical singularity at the transition point manifests itself as a singularity in the photonic density of states (PDOS). This phenomenon has been used to demonstrate a large increase in spontaneous emission rate of a dipole emitter placed in the near field of the metamaterial. In addition, a transition between these two distinct topologies can be induced in a very unusual way when an external magnetic field is applied, leading to strongly nonreciprocal response and a unidirectional or ‘oneway’ character of the topological transition (Krishnamoorthy et al. 2012).

In practice, limitations of fabrication techniques used for structuring always lead to the presence of variations in geometrical parameters over the extent of the metamaterial, which is equivalent to the presence of both disorder and local defects. In many practical applications such structural imperfection may substantially degrade the performance of metamaterial-based devices, and, for instance, lead to broadening of artificial resonances and undesirable back-reflection. In the latter case the effect of disorder can be circumvented by using the property of topological

robustness. Bianisotropy, also referred to as magneto-electric coupling, can play a role analogous to the spin-orbital coupling for electrons in solids. This is a key ingredient of the quantum spin Hall effect (QSHE) topological state, which now can be implemented for photons. The systems that exhibit OTT are usually metal-dielectric structures where the dielectric constant along one or two of the directions can be made negative. In this context, one of the main issues is that of losses in metals. Nonmetallic plasmonic materials such as transparent conducting oxides are expected to partly address this issue. Another important challenge for metamaterials that undergo OTT is that of the severe phase mismatch between the high- k states in the metamaterials and free space. To alleviate this issue, grating and photonic hypercrystal structures have been used to efficiently outcouple the high- k states (Fig. 12.2d). The possibility of magnetization induced OTT allows one-way and nonreciprocal elements such as optical isolators and circulators. While there have been several reports of nonreciprocity in metamaterials relying on engineered resonances by making them narrowband, the use of OTT presents a broadband approach, which is crucial for wavelength multiplexing applications. Furthermore, the large PDOS in these systems also allow for miniaturization by enhancing naturally weak magneto-optical response (Galfsky et al. 2015; Urbas et al. 2016).

The realization of topological protected transport in metamaterials provides an attractive approach to alleviate some of the outstanding issues in these systems such as disorder-induced scattering. The OTT presents a new approach for broadband control of light-matter interaction and is expected to lead to practical device applications such as ultrafast LEDs and isolators (Urbas et al. 2016).

12.2 Manipulation of Metasurface Properties

12.2.1 *Functionally Doped Metal Oxides for Future Ultrafast Active Metamaterials*

Plasmonics has brought many radically new device concepts into optical technologies. This is not only due to the possibility of overcoming the major limitations related to the diffractive nature of light, but also because introducing metal constituents (exhibiting electric resonances) into the world of photonics allows for development of extraordinary engineered composite materials with effective optical properties distributed over a more extensive region of the electromagnetic parameter space (ϵ - μ space). However, metals including gold and silver have a very limited tenability of changing the material's optical properties and suffer from considerable losses. Alternative material platforms such as transition metal nitrides (TMNs) and transparent conductive oxides (TCOs) overcome such limitations intrinsic to gold and silver. The optical properties of TMNs (e.g. titanium and zirconium nitride-TiN, ZrN) resemble those of gold with a tailorable plasma frequency located in the visible-ultraviolet region. TMNs are robust, durable materials with exceptionally high

thermal, chemical and mechanical stability. They provide plasmonic performance similar to that of gold structures and they are good candidates for heat-assisted plasmonic applications such as thermophotovoltaics, heat-assisted magnetic recording and photocatalysis, due to their refractory nature. TCOs (e.g. aluminum-, gallium-, indium-doped zinc oxide-AZO, GZO, IZO, tin-doped indium oxide-ITO), on the other hand, are highly doped wide-band semiconductors with a plasma frequency typically located in the near-infrared range. In the near infrared, TCOs possess lower optical loss and a smaller magnitude of real permittivity (ϵ') compared to noble metals and nitrides. Because of these characteristics, TCOs allow one to access the ϵ -near-zero (ENZ) regime in the near infrared for both composite structures and bulk materials. In addition to this, complex oxides show a great dynamic tenability to alter the dielectric permittivity by either optical or electric excitation. Consequently, all these features make TCOs exceptionally promising for a new generation of active metamaterials and plasmonic devices (Maas et al. 2013; Guler et al. 2014).

Metasurfaces are effective for realizing numerous fundamental ultrathin optical components such as lenses, polarizers, beamsteerers, holographic plates, etc. As shown in Fig. 12.3, two basic approaches have been used for the design and realization of optical metasurfaces (Urbas et al. 2016): (a) nanoantennas (either made of metal or carved inside a metallic film); (b) gap plasmons. The first strategy relies on controlling the phase of a propagating wavefront using subwavelength metallic nanoantennas. This technique has the advantage of being implemented using standard electron beam lithography or ion beam milling including only one processing step, but has a limited efficiency. In other words, only a moderate percentage of the incident light is influenced by the presence of the nanopatterned antennas. The gap plasmon solution, in contrast, may maximize the desired optical efficiency at the

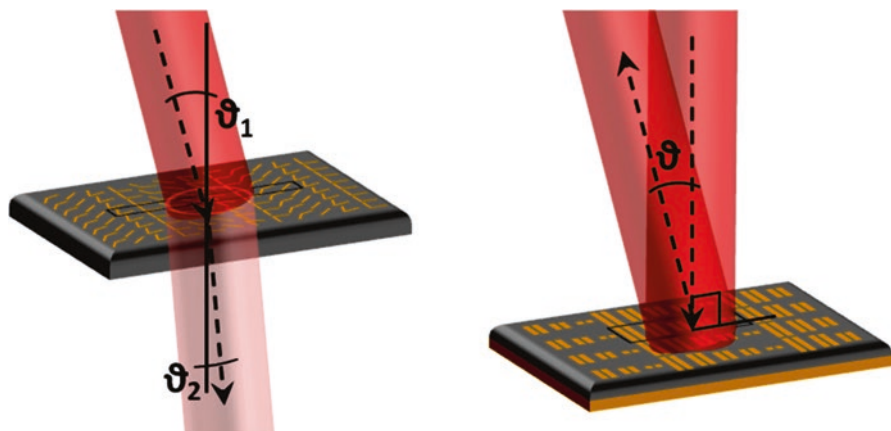


Fig. 12.3 Nanoantenna (left) and gap-plasmon (right) metasurfaces (Urbas et al. 2016): The schematic diagram depicts anomalous transmission and reflection plus the ‘efficiency versus flexibility’ trade-off typical of these structures

cost of a multilayer structure, higher losses and the impossibility of working in transmission.

For realization of metadevices related to the replacement of traditional noble metals (gold and silver) with CMOS-compatible materials, TCOs such as AZO and GZO can have significantly lower material losses (ϵ'') than silver at telecommunication wavelengths with the additional benefit of being nonstoichiometric materials, thereby providing the capability of tailoring the intrinsic plasma frequency in a wide range from the visible to the near infrared (e.g. ITO, 0.6–1.6 μm). What makes these materials special is their optical transparency and their ability to sustain very high doping levels without effective degeneration of their structure. The achievable intrinsic carrier concentration ($N \sim 10^{21} \text{ cm}^{-3}$) is very high compared to that of doped semiconductors (enabling metal-like properties in the NIR) and one order of magnitude smaller than that of noble metals ($N_{\text{gold}} = 5.9 \times 10^{22} \text{ cm}^{-3}$). Because of this moderately high concentration of free electrons, the absolute value of the real part of the dielectric permittivity is small, granting access to the ENZ regime, where the dynamic tunability of the optical properties is drastically enhanced together with the nonlinearities. In addition, high-quality TCO thin films can be deposited by numerous techniques (e.g. sputtering, laser ablation, aqueous chemical deposition, liquid film spray deposition etc.). Consequently, TCOs is promising to solve the problems which plague noble-metal-based metamaterials-CMOS compatibility, and tailorability together with dynamic tunability. On the other hand, gap plasmons could be used, which are inherently resonant and are thus more susceptible to the relative variation of ϵ . By optimizing the design/scheme of the metasurface as well as its material properties, large dynamic tuning and ultrafast recombination can be achieved to fabricate effective metasurfaces (Maas et al. 2013; Urbas et al. 2016).

As a result, highly doped semiconductor oxides appear to be key compounds for the realization of future tunable/active metadevices. As TCO films can be engineered to exhibit an ultrafast optical response, low loss and ENZ behavior over a wide wavelength range by controlling the material deposition, they have great potential to be used as novel plasmonic compounds for fabrication of flat metadevices (metalenses, holographic plates etc.) and switchable components (ultracompact modulators, routers, switches etc.).

12.2.2 *Optical Dielectric Metamaterials and Metasurfaces*

All-dielectric metamaterials (ADMs) can exhibit extremely small absorption loss if they are operated at frequencies below the constituent material's bandgap. Different from metallic metamaterial unit cells that are often complex, especially when a magnetic response is required, ADMs can be implemented with extremely simple geometries such as spheres and cubes. This allows easier scalability of the material and more isotropic properties, and greatly aids in the fabrication of thicker three-dimensional (3D) materials (Urbas et al. 2016).

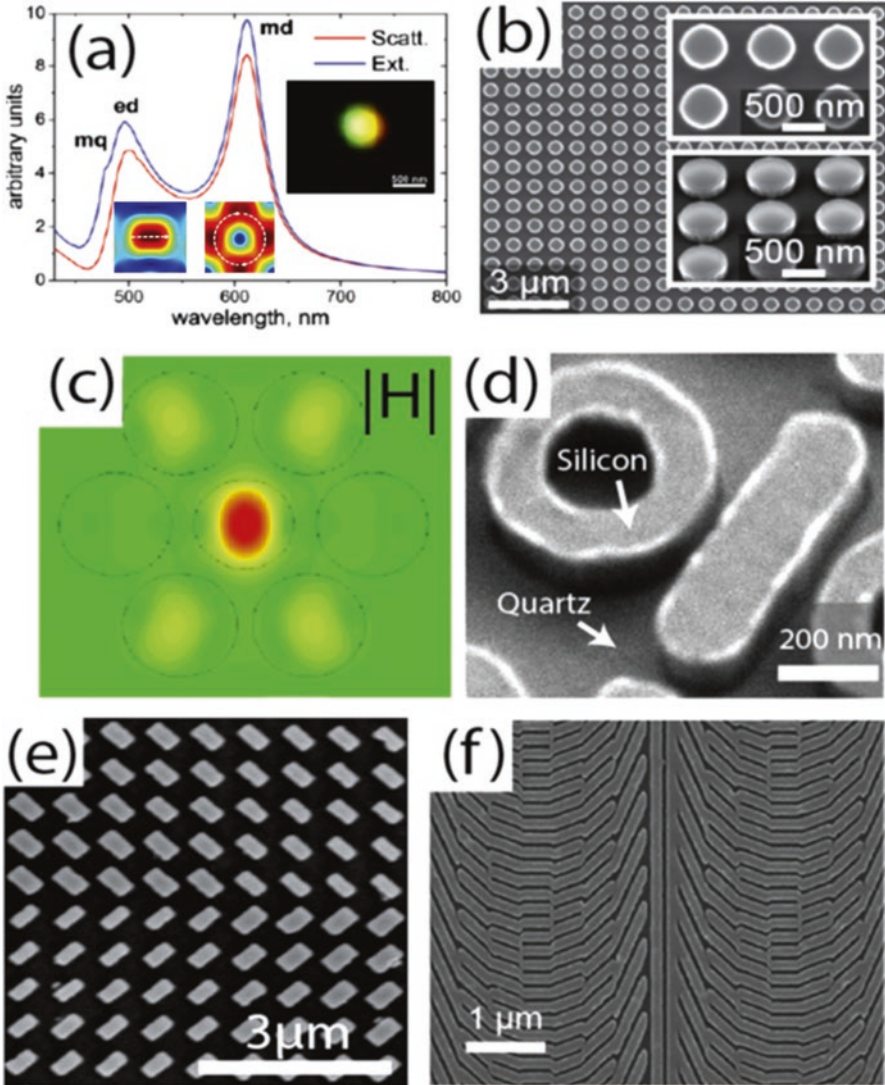


Fig. 12.4 All dielectric metamaterials and metasurfaces (Lin et al. 2014; Urbas et al. 2016): (a) Electric and magnetic modes in a Si sphere; (b) Si nanodisk-based metamaterials; (c) Fano-resonant Si oligomer; and (d) ring- and bar-based metamaterial implementations; (e, f) Metasurfaces for manipulating the phase of light

Figure 12.4 shows advances in some dielectric metamaterials and metasurfaces (Lin et al. 2014; Urbas et al. 2016): (a) Electric and magnetic modes in a Si sphere; (b) Si nanodisk-based metamaterials; (c) Fano-resonant Si oligomer; and (d) ring- and bar-based metamaterial implementations; (e, f) Metasurfaces for manipulating the phase of light. The dielectric metamaterials require that the constituent

dielectric must have a refractive index that is substantially larger than that of the surrounding medium, which is air in most cases. Since dielectric resonators act as cavities their size, and thus lattice period, is inversely proportional to the refractive index of the constituent material. In the short- to long-wavelength infrared regime small bandgap semiconductors such as germanium ($n \sim 4$), tellurium ($n \sim 5.5$) and silicon ($n \sim 3.5$) are viable options. For instance, in the telecommunications band silicon has been almost exclusively utilized to date. The real challenge lies in scaling dielectric metamaterials to visible frequencies due to the lack of high-index and wide-bandgap semiconductors. Choices are almost exclusively limited to III–V materials such as AlGaAs ($n \sim 3.8$) and GaP ($n \sim 3.4$). However, these materials are considerably more difficult to grow than Si.

Since semiconductors are often used as the constituent material, active control of ADM optical properties is an attractive application. There are several routes forward regarding the realization of active ADMs. In terms of tuning optical properties, one route is the use of high-quality-factor resonances combined with a relatively weak electro-optical effect. Achieving broadband control is potentially challenging as relatively large index changes within the unit cell must be achieved. Phase change materials such as VO₂ and chalcogenide glasses provide a potential solution, though thermal recovery time may limit the speed of the device. Controlling and enhancing light emission from ADMs is another interesting area. While light sources such as quantum dots can be incorporated within ADMs, it is potentially more interesting to use the resonator itself as the light source. Therefore, the potential for development of ADMs at infrared and visible frequencies is vast as many of the properties observed in plasmonic metamaterials are readily achievable in ADM variants with greatly reduced loss. Furthermore, the use of semiconductors as the constituent material provides a natural integration with active components and optoelectronic devices (Urbas et al. 2016).

12.2.3 *Beam Shaping with Metasurfaces*

Metasurfaces are able to transform an arbitrary incident optical wavefront into any desired transmitted wavefront. For example, metasurfaces have been designed to convert circularly polarized Gaussian beams into radially polarized Bessel beams, as shown in Fig. 12.5a. In addition, they have the potential to offer improved performance over conventional dielectric lenses since they can be designed to eliminate spherical and chromatic aberrations (Aieta et al. 2015).

Improving the efficiency of metasurfaces require lower-loss materials. Oxides and nitrides are promising alternatives to Au and Ag, since their plasma frequencies can be controlled, which could provide lower loss depending upon the application. Alternatively, patterning high-index dielectrics such as Si shows significant potential since these materials have extremely low loss. However, dielectric-based metasurfaces have yet to achieve the same degree of polarization control that plasmonic

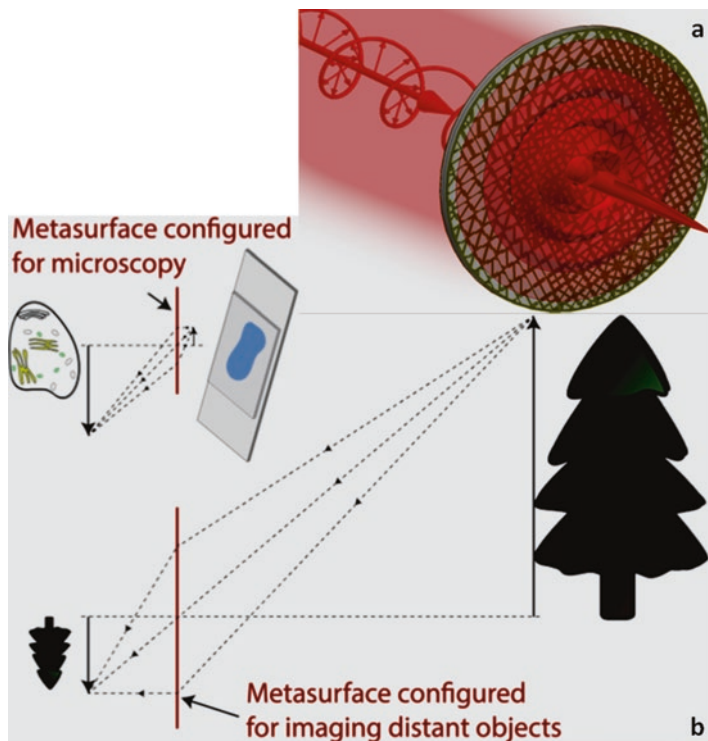


Fig. 12.5 Beam shaping with metasurfaces (Urbas et al. 2016): (a) Metasurfaces transform an arbitrary incident wavefront into any desired wavefront; (b) Reconfigurable metasurfaces could provide a wide range of optical transfer functions – a tunable metasurface could be reconfigured to focus on objects that are extremely close or far from an image sensor for microscopic and telescopic applications, respectively

metasurfaces offer. Reconfigurable metasurfaces have the potential to provide arbitrary optical transfer functions on demand. For example, a future smartphone camera consisting of reconfigurable metasurfaces may be capable of providing high-numerical-aperture lenses for diffraction-limited microscopy one instant and longer-focus lenses for imaging distant objects the next (Fig. 12.5b). Adding tunability to metasurfaces could also improve their performance. The beam generated by the metasurface could be monitored by a sensor, and this information fed back to tune the metasurface to reduce aberrations and improve the overall performance. This level of reconfigurability could be achieved using materials with an electronically controllable permittivity/sheet conductance such as liquid crystals and graphene, respectively. Alternatively, the physical geometry of the metasurface can be controlled by applying DC currents or voltages across the structure. Further, systematic design procedures need to be developed so that the metasurface's properties can be precisely controlled (Valente et al. 2015).

Therefore, optical metasurfaces offer unprecedented opportunities for tailoring optical wavefronts at will. They can offer a compact alternative to conventional optical components. Although promising, their performance, tunability and cost must be addressed before they become ubiquitous optical elements (Urbas et al. 2016).

12.2.4 Control of Emission and Absorption with Metamaterials

Electromagnetic absorption holds the key for taking a new optical technology to the realm of practical applications—from the anti-reflective coating to optimized narrow-band emitters for thermal photovoltaics to the ultralow-loss silica glass that led to the fiber-optical communication systems. With the wavelength-specific absorption and emission connected to each other by the Kirchoff law, the control of electromagnetic absorption becomes an essential element of a new optical material technology. Optical metamaterials offer the control of electromagnetic material response based on spatial patterning on a deeply subwavelength scale, thus offering freedom from the size limits of conventional optical technology. Furthermore, even a metasurface has a strong effect on the optical absorption and reflection (Yu and Capasso 2014).

Metamaterials with designed electromagnetic absorption and emission also offer the capability of dynamic control for the response of the device, which has many advantages for spectroscopic and imaging applications. However, while such devices have been fabricated for the terahertz frequency range, extending their performance to the optical domain, which implies increasingly more stringent requirements on the dimensions of the unit cell and material imperfections, remains a major challenge. Another capability that may be offered by the metamaterial approach to controlled emission and absorption is the potential to bridge the gap between the nanoscale quantum emitters (e.g. single atoms, organic dye molecules or quantum dots) and micrometer-scale optical wavelength. In the near field of a metamaterial, such an emitter can resolve the subwavelength details of the metamaterial unit cell, which allows the use of its geometry to optimize the resulting light–matter interactions. As a result, these quantum metamaterials may hold the key to a practical on-chip implementation of quantum optical communications and computations (Chen et al 2014a; Urbas et al. 2016).

Photonic hypercrystals and hyperbolic metamaterials with periodic spatial variation of dielectric permittivity on a subwavelength scale, that combine the features of optical metamaterials and photonic crystals, may help to address the challenge of coupling to quantum emitters. In fact, built-to-order metamaterial emitters and absorbers are entering the realm of practical devices and applications. Furthermore, it is likely that quantum metamaterial systems will become the key elements in future quantum information systems (Chen et al. 2014a).

12.2.5 Control of Far-Field Thermal Emission Properties through the use of Photonic Structures

Absorption and thermal emission lie at the center of many energy conversion processes. The advent of photonic structures such as metamaterials and photonic crystals provides new capabilities for controlling emission and absorption properties. Various kinds of metamaterial photonic structure, including photonic crystals, multilayer films, metal-insulator-metal structures, ϵ -near-zero (ENZ) and ϵ -near-pole (ENP) metamaterials, have been developed for the control of thermal emission and absorption properties. These structures enable thermal emission properties that are drastically different from those of conventional structures. For example, while thermal emission from conventional structures is typically thought of as spectrally broad and spatially incoherent, the use of photonic structures can lead to thermal emission that is spectrally selective, or spatially coherent. These novel capabilities of controlling thermal emission in turn have led to new potential application opportunities as in thermophotovoltaics and radiative cooling, where the capability for such spatial and spectral control of thermal emission is essential for enhanced performance in these applications. Overall, the use of metamaterial can lead to thermal emitters that are fundamentally different from conventional thermal emitters, and open new application possibilities in numerous areas such as energy conversion, imaging and sensing (Urbas et al. 2016).

12.3 Research Trends of Nonlinear, Active and Tunable Properties

12.3.1 Engineering Mid-Infrared and Optical Nonlinearities with Metamaterials

Nonlinear effects in optical materials are generally weak, yet they are of fundamental importance for frequency generation, optical sources, laser diagnostics, optical switching and modulation, integrated nanophotonic systems and much more. Due to the typically small extent of optical nonlinearities, high light intensities and long propagation distances are required to produce detectable nonlinear responses. Phase matching between pump and generated signals, as they propagate in the nonlinear material, becomes crucial, making nonlinear optical systems convoluted and not always practical. In order to enhance the optical nonlinear response, material substrates can be engineered at the quantum level to support very large nonlinear responses. Very large nonlinearities can be obtained around intersubband transitions in semiconductors, and they can be suitably engineered in n-doped multi-quantum-well (MQW) semiconductor heterostructures. Within this platform, by controlling the well and barrier width, the transition energy between electron subbands can be

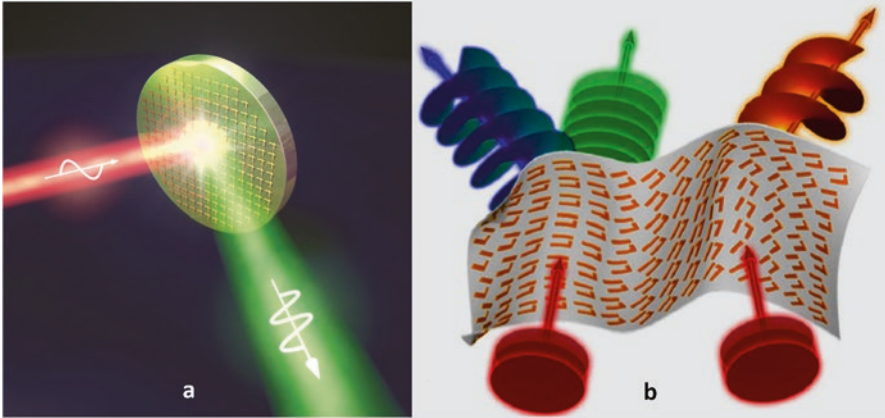


Fig. 12.6 examples of Engineering mid-infrared and optical nonlinearities with metamaterials (Lee et al. 2014; Gomez-Diaz et al. 2015): (a) A nonlinear mirror with high nonlinear conversion efficiency, based on a plasmonic metasurface loaded by a thin MQW substrate; (b) A metasurface with giant local nonlinear response may offer unique opportunities to pattern, redirect, steer and modulate the produced nonlinear wavefronts, opening a new paradigm for nonlinear optics

tailored to maximize nonlinear processes of choice. These subbands can also be electrically tuned with an applied voltage bias. These engineered substrates can be of fundamental relevance to overcome the current limitations of nonlinear optics, especially when applied to mid-infrared wavelengths, providing unique opportunities to tailor thermal emission, and in various military applications over a frequency range that lacks sources, detectors and various optical components (Urbas et al. 2016).

Figure 12.6a shows a nonlinear mirror with high nonlinear conversion efficiency, based on a plasmonic metasurface loaded by a thin MQW substrate. With a properly designed plasmonic metasurface resonant in the mid-IR range, the mirror is able to generate second-harmonic reflected waves at $4\ \mu\text{m}$ wavelength with very low input intensities, opening the possibility of engaging large nonlinear responses from weak mid-IR sources. The mirror produces about six orders of magnitude higher conversion efficiencies than natural nonlinear materials of similar thickness, achieved by the suitable combination of five parallel mechanisms (Lee et al. 2014): (a) proper coupling between the MQW resonance and the electromagnetic resonance sustained by the metasurface; (b) proper overlap of the resonant modes sustained by the metasurface within the MQW substrate at the fundamental and second-harmonic frequencies; (c) suitable conversion of the impinging transverse polarization into normal electric field in the substrate, mediated by the plasmonic inclusions forming the surface; (d) suitable conversion of the induced nonlinear polarization currents in the MQW layers into free-space transversely polarized radiation, again mediated by the metasurface inclusions; (e) field enhancement induced in the MQW substrate by the plasmonic inclusions. Phase-matching constraints are totally relaxed in this geometry, as the nonlinearity stems from a local response in each deeply

subwavelength unit cell. All mentioned mechanisms need to be properly balanced and controlled by material and electromagnetic engineering of the mirror in order to achieve giant nonlinear response.

Similar concepts may be also translated to visible wavelengths, engaging inter-band transitions in semiconductors, and the fast modulations supported by these substrates may provide a unique route to realize on-chip isolation using spatio-temporally modulated resonant nanophotonic inclusions. The unprecedented level of concentration of nonlinear response over a deeply subwavelength footprint offered by MQW-loaded metasurfaces may be able to open a new paradigm for nonlinear optics, in which reasonably high conversion efficiencies are expected without the necessity of phase matching. This implies that it may be possible to pattern the nonlinear wavefront at will over a transmitting surface operated along the same principles. Figure 12.6b shows this concept, envisioning a tailored pattern of subwavelength inclusions that enhance nonlinear effects of choice, including second harmonics, difference frequency generation and phase conjugation, and at the same time patterning pixel by pixel on a conformal surface the generated wavefront, imprinting polarization, angular momentum and propagation direction of choice. Being able to tune the pixel response in real time would provide a reconfigurable nonlinear transmit array, of interest for various civil and military applications (Gomez-Diaz et al. 2015).

With midinfrared and optical nonlinear response of metasurfaces by the suitable combination of quantum-engineered substrates and electromagnetically designed plasmonic inclusions, the way may be paved to several exciting possibilities. At mid-infrared frequencies, it may be possible to design compact laser sources and chemical or biomedical sensors. In optics, these concepts may also provide unique opportunities for integrated nanophotonics components with switching and modulation capabilities (Urbas et al. 2016).

12.3.2 Directional Control of Nonlinear Scattering from Metasurfaces

Nonlinear metasurfaces represent a unique class of structures offering the potential for utilizing strong local enhancement of the nonlinear response while minimizing limitations due to linear and nonlinear absorption in the medium. The local efficiency of a nonlinear interaction can be increased by many orders of magnitude owing to strong resonant field enhancements achievable within plasmonic nanocomposites. With a tailored design, the locally enhanced nonlinearly produced field can be re-radiated directly to the far field, with the metasurface acting as an array of nonlinear optical antennas. In addition to the enhanced efficiency of nonlinear generation, a variety of other unique features are offered by the nonlinear response of these two-dimensional structures. Owing to the deeply subwavelength thickness, phase-matching constraints are removed, allowing the simultaneous conversion of a

wide range of k vectors of the fundamental field to a set of k vectors of the nonlinearly generated light with a nearly isotropic efficiency, including a direct coupling between evanescent and propagating waves. The latter creates opportunity for sub-diffraction imaging, as well as for an efficient coupling between the in-plane and out-of-plane modes. Furthermore, the inherent intensity dependence of the nonlinear response allows for a dynamic, real-time control of any of the above operations, as well as for a directionality control achieved with planar geometries. Such strong enhancements of the nonlinear response achievable with subwavelength-thin structures, combined with the option of optically controlled propagation and in-plane/out-of-plane coupling, are unique and open possibilities for a tremendous variety of applications in integrated photonics and quantum information processing. The 2D nature of the geometry, on the other hand, considerably simplifies the fabrication procedure compared to its bulk counterpart (Poutrina et al. 2012).

A logical path to regaining the control of directionality relies on exploiting the processes inherent to nanoscale interactions, such as interference effects between multipole modes of the electromagnetic field produced within a scattering event. Orthogonal, spatially superimposed multipoles of opposite parities can interfere destructively in one direction while doubling the scattered field amplitude in the opposite direction, thus producing a directional response on the nanoscale. Nonlinear magneto-electric interference can result in nonlinearly produced field acquiring a certain dominant direction, and allows for this direction to be decoupled from that of at least one of the excitation beams, making the directionality of the response effectively nonreciprocal with respect to that beam. When arranged in a metasurface with a tailored nanoelements orientation within the surface plane, the produced directional beam can maintain its ‘nonreciprocal’ nature. The latter brings an option of ‘nonreciprocity’ to virtually any application that utilizes the specified nonlinear interaction in such a metasurface. Moreover, nonreciprocity in the direction of nonlinear generation—a phenomenon fundamentally impossible in the linear response and unachievable in the nonlinear response of conventional optical materials—is inherent and predicted to be realistically observable in the effective nonlinear multipolar response of nanostructures. Implementations of this phenomenon, combined with the strong enhancement of the nonlinear response offered by metasurfaces and the option of a dynamic control of the directionality, as well as the overall deeply miniature dimensions of these structures, offer key features for an immense variety of applications in integrated optics and photonics (Urbas et al. 2016).

12.3.3 Coherent Control in Planar Photonic Metamaterials

Planar metamaterials can be used for coherent control to impact fields including data processing and spectroscopy. A highly absorbing plasmonic metamaterial of substantially subwavelength thickness positioned at a node of the standing wave light field formed by coherent counter-propagating ‘control’ and ‘signal’ beams will experience zero electric field and so will not absorb the light. Any change in the

phase or intensity of the control wave that distorts the standing wave pattern, or a change in the position of the metamaterial, will break this zero-absorption regime. Indeed, at the other extreme, the metamaterial may ‘perfectly coherently absorb’ 100% of the incident light in both beams. This effect can underpin various forms of optical switching with modulation bandwidth up to 100 THz (limited only by resonance linewidth) at extremely low (even singlephoton) energy levels. The effect may be harnessed in coherent four-port optical devices to deliver, without need of intrinsic optical nonlinearity, data-processing functions including signal summation, inversion and even small-signal amplification, and these can be spatially multiplexed for applications such as image processing. The concept can also be employed in various modes of coherent-illumination spectroscopy, for example to selectively excite and thereby disentangle electric and magnetic dipolar resonances. With roots in plasmonics, metamaterials and coherent optics, the concept of coherent control in planar photonic metamaterials is emerging as a powerful paradigm for manipulating the manifestation of all kinds of light-matter interaction with high contrast, at high speed and low energy, presenting a wealth of new technological opportunities (Fang et al. 2016; Urbas et al. 2016).

12.3.4 Nanomechanical Photonic Metamaterials

The progression of nanomechanical photonic metamaterials is largely a challenge of materials and nanofabrication. Low-loss materials with either plasmonic properties or high refractive index are needed to achieve high displacement sensitivities, which depend on the quality factor of metamaterial resonances that is limited by absorption losses. Low loss materials will also contribute to larger optical actuation forces, increased optical damage thresholds and a reduction of insertion losses; in particular, the latter is needed for many commercial applications. Therefore, the ongoing search for better plasmonic materials and the growing field of intrinsically low-loss dielectric metamaterials may be expected to drive progress (Urbas et al. 2016).

Advances in nanofabrication are needed for highly homogeneous arrays of mechanical nanostructures (to avoid inhomogeneous broadening of resonances) and to enable the mass-production of nanomechanical photonic metadevices. While current reconfigurable photonic metamaterials are made by focused ion beam milling, a high-throughput process will need to be developed. This could be based on nanoimprint lithography followed by an etching process that frees the moving parts of the nanostructure. Furthermore, a broad range of opportunities may arise from introducing new functional materials to nanomechanical photonic metamaterials, such as piezoelectric actuation, optical actuation using liquid crystal elastomers, rewritable memory functionalities based on shape memory materials or isotropic modulation of optical properties based on auxetic metamaterial designs (Valente et al. 2016).

Nanomechanical photonic metamaterials promise an unprecedented level of dynamic control over light. Modulation effects exceeding natural materials by orders of magnitude have already been reported and dramatic improvements on first proof-of-principle devices may be expected from bringing in expertise of the MEMS/NEMS, opto-mechanics and material research communities. Ultimately, metadevices will provide dynamic control over the wavefront of light with sub-wavelength resolution. Such devices could be programmed to perform functions from simple optical components (gratings, lenses, filters) to complex 3D holography on demand (Urbas et al. 2016).

12.4 Emerging Metadevices and Applications

12.4.1 RF Beam Steering Module with Metamaterials Electronically Scanned Array

As shown in Fig. 12.7a, a low-cost, high-performance RF beam steering module with metamaterials electronically scanned array (MESA) that can be adapted for a broad range of applications, including: collision avoidance system for self-driving

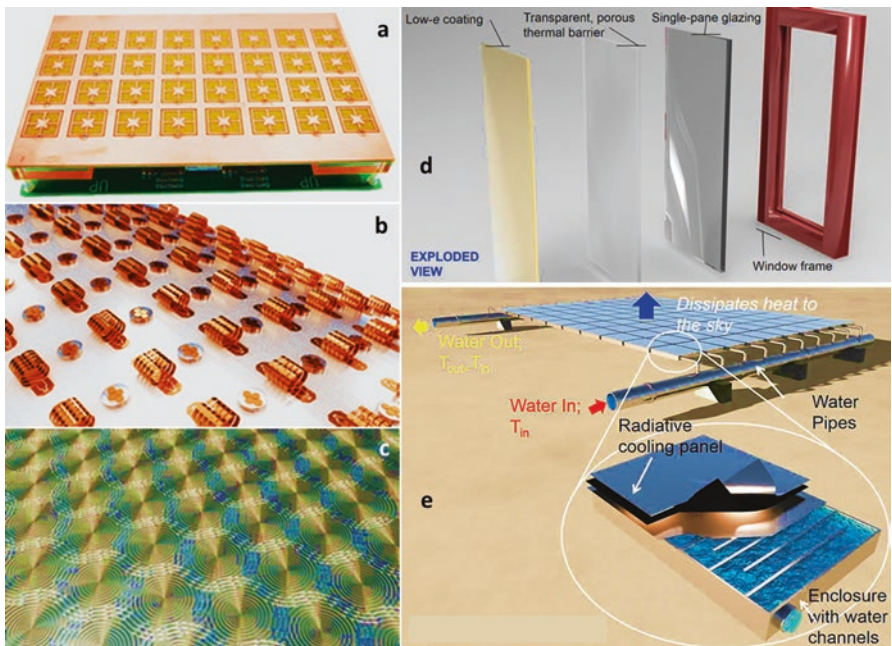


Fig. 12.7 Examples of emerging metadevices (Parc 2017)

cars or drones, broadband satellite internet/radio, hypothermia treatment, wireless communications, etc. (Parc 2017).

12.4.2 Smart Metamaterial Antennas

Highly reconfigurable metamaterial antennas are a natural evolution of the MESA architecture. They are tailored for 4G LTE/5G bay stations and for satellite communications.

12.4.3 Energy Harvesting Enhanced with Metamaterials

Advances in low power design open the possibility to harvest ambient energies to power directly the electronics or recharge a secondary battery. The key parameter of an energy harvesting (EH) device is its efficiency, which strongly depends on the conversion medium. To address this issue, metamaterials and metadevices with exotic properties, have been introduced for EH. They possess unique properties not easily achieved using naturally occurring materials, such as negative stiffness, mass, Poisson's ratio, and refractive index. Metamaterials-based energy harvesting research includes but not limited to active metamaterials-based EH, metamaterials-based thermal EH, and metamaterials-based multifunctional EH capabilities (Chen et al. 2014b).

12.4.3.1 Elelectromagnetic Energy Harvesting

The microwave spectrum is defined as electromagnetic energy ranging from approximately 1–1000 GHz in frequency. A complete microwave wireless power transmission (MWPT) system consists of three essential parts: converting DC energy to microwave power, capturing the microwave power by antennas, and converting the captured power to DC output power. In particular, the rectifying antenna called rectenna is one of the key components affecting the performance of a MWPT system. Metamaterial-inspired rectenna design methods have being explored to improve its performance. For instance, an RF energy harvesting platform that converts Wi-Fi and other RF bands to electricity, to power IoT sensors. It consists of a metamaterial-inspired antenna and a custom rectifying circuit (Parc 2017).

12.4.3.2 Phononic Crystals-Based Vibroacoustic Energy Harvesting

Vibroacoustic energy harvesting (VAEH) uses basic conversion mechanisms including piezoelectric, electromagnetic, electrostatic, and magnetostrictive transduction. Phononic crystals-based vibroacoustic energy harvesting has been used to enhance

the VAEH device design to operate optimally at or very close to resonance, so that its electrical output can reach the maximum value. Bandgaps of a phononic crystal are closely related to its structural configuration, therefore can be used to design the structures of phononic crystals to match specific vibroacoustic energy. On the other hand, the central frequency of any bandgap depends on the lattice constant of a phononic crystal. Large lattice constant leads to low central frequency, so the whole size of a phononic crystal has to be large for low-frequency vibroacoustic energy. This property may hinder phononic crystals from low frequency vibroacoustic energy harvesting due to the limitations of space and intensity in many engineering applications (Chen et al. 2014b).

12.4.3.3 Acoustic Metamaterial-Based Vibroacoustic Energy Harvesting

Acoustic metamaterials can be designed to exhibit non-traditional physical behaviors such as negative stiffness, mass, and Poisson's ratio. These unique abilities of acoustic metamaterials can be used to enhance vibroacoustic energy harvesting. Similar to the mechanism of phononic crystals, bandgap is also the basis of acoustic-based broadband vibroacoustic energy harvesting. However, there are two different principles. The first one is 'acoustic superlens', which can be used to concentrate vibroacoustic energies. The other one is 'local resonance', which can be used to localize vibroacoustic energies by setting defects. Compared to phononic crystals, acoustic metamaterials with small size can generate low frequency band, so they are more applicable for low-frequency vibroacoustic energy harvesting (Chen et al. 2014b).

12.4.4 Focus Magnetic Stimulation

In focus magnetic stimulation (FMS), as shown in Fig. 12.7b, the magnetic fields are dynamically shaped by injecting phase and amplitude-controlled currents in an array of three-dimensional micron-scale coils. The FMS scheme enables more localized stimulation (enhanced focusing), better depth control, and complex stimulation patterns (beam shaping and beam steering), as compared to current magnetic/electric stimulation methods. Tailored stimulations can be obtained with appropriate coil array designs, by selecting the optimal number of elements, array configuration, driving circuits, and current distribution in the coils (Parc 2017).

12.4.5 Thermophotovoltaics

The conversion of thermal radiation emitted from a high-temperature source (the emitter) into electricity by means of a PV cell (e.g., GaSb). Figure 12.7c shows a spectrally selective metamaterial emitter that only allows in-band photons to reach

the low-bandgap GaSb PV cells for direct electricity conversion. This minimizes thermal losses, which in turn delivers a significant increase in the thermal conversion efficiency (Parc 2017).

12.4.6 Transparent Thermal Barrier

Figure 12.7d shows a transparent aerogel polymer material with record low thermal conductivity to prevent thermal losses in single-pane windows. This technology can also be applied as thermal insulation solutions to a variety of industries, including (1) applications where operators or components need to be kept at very stable temperatures (e.g., walls, HVAC ducts, environmental control system (ECS) ducts, etc.); (2) thermal insulation for infrastructure in need of protection from heat (e.g., gas tanks or any other hazardous infrastructure). The integration of the thermal barrier into reinforced lightweight composite insulation materials, can be used as protective coatings of structural components in the automotive, shipboard and aerospace industries (Parc 2017).

12.4.7 Passive Radiative Cooling

Figure 12.7e shows low-cost, low-complexity (single layer), highly-scalable films/coatings that can “self-cool” in broad daylight, without the need for electricity or water. This is a new class of materials that molds the flow of heat. Passive radiative cooling can be used for a broad range of applications, including cooling of power plants, buildings, satellites, military tents, and supplies in hot desert climates (Parc 2017).

12.5 Prospective Manufacturing and Assembly Technologies of Metamaterials and Metadevices

12.5.1 Nanoparticles for Complex Multimaterial Nanostructures

Nanoparticles (NPs) are artificial building blocks for the construction of optical metamaterials that operate in the visible to near-to-mid-infrared regions of the electromagnetic spectrum. The synthesis and programmed assembly of colloidal NPs enables the design of metamaterials with properties not found on the periodic table. For example, controlling the size and shape of the NPs and the interparticle spacing allows the dielectric function of NP-based metamaterials to be engineered. However, advanced structural, optical and computational methods are needed to characterize

NP assemblies at atomic scales. Patterning the NP assemblies into meta-atoms allows the properties of NP-based materials to be exploited in devices (Urbas et al. 2016).

The integration of multiple NP materials will lead to new functions. For example, the co-assembly or layering of plasmonic and magnetic NPs will allow the construction of magnetoplasmonic multimaterials. Selecting NPs and intervening ligands that are responsive to external stimuli (e.g. light, heat, electric fields) will enable the fabrication of reconfigurable metamaterials. Fundamental understanding of NP properties and couplings will open a new era based on inverse design of NP-based multimaterials for devices (Urbas et al. 2016).

12.5.2 Eutectics as Metamaterials

Eutectics are composite materials when in a solid state, with two or more phases which self-organize after cooling down a completely mixable melt of a eutectic composition. As composites they can possess additive properties dependent on the intrinsic properties of the single phases and product properties, which arise from combining the two phases together in a particular structure. Eutectics in solid-state form are monolithic and multiphase materials and the following properties are interesting for metamaterials (Urbas et al. 2016): (i) they can exhibit various geometrical motifs; (ii) the structure refinement can be tuned at the micrometer to nanometer scale; (iii) they are highly crystalline; (iv) various combinations of component phases may possibly be obtained; (v) the interfaces can be very sharp—even atomically smooth with precise crystallographic relation to each other; (vi) after growth they can be post-engineered in many ways.

Eutectic materials can exhibit various geometrical motifs, where the regular eutectic structures are fibrous (rod-like) (Figs. 12.8a, b) and lamellar (layered) (Fig. 12.8c). However, other structures are possible, such as globular, spiral or broken lamellar. Even the pivotal for metamaterials split-ring-resonator geometry has been demonstrated with the eutectic solidification (Fig. 12.8d, e). The fibrous and lamellar eutectic structures could be the easiest to use as metamaterials, since such properties as subwavelength transmission and hyperbolic dispersion could be obtained, and they are less sensitive to structural disorder. And it has been shown that lamellar eutectics can be grown in a circular shape, while applying rotation, which can almost lead to its immediate use as a metamaterial hyperlens (Fig. 12.8g). With higher growth rate the structure refinement in eutectics is increasing, enabling size control from the micrometer to the nanometer scale. The ways to obtain nanostructured eutectics include (i) fast cooling, (ii) addition of another phase, (iii) growth in a small volume which could enable fast cooling, (iv) devitrification of eutectic glasses and (v) potentially the addition of nanoparticles. Other new approaches include combining the eutectic growth with other manufacturing methods, such as obtaining eutectics in photonic crystal templates (Kim et al. 2015).

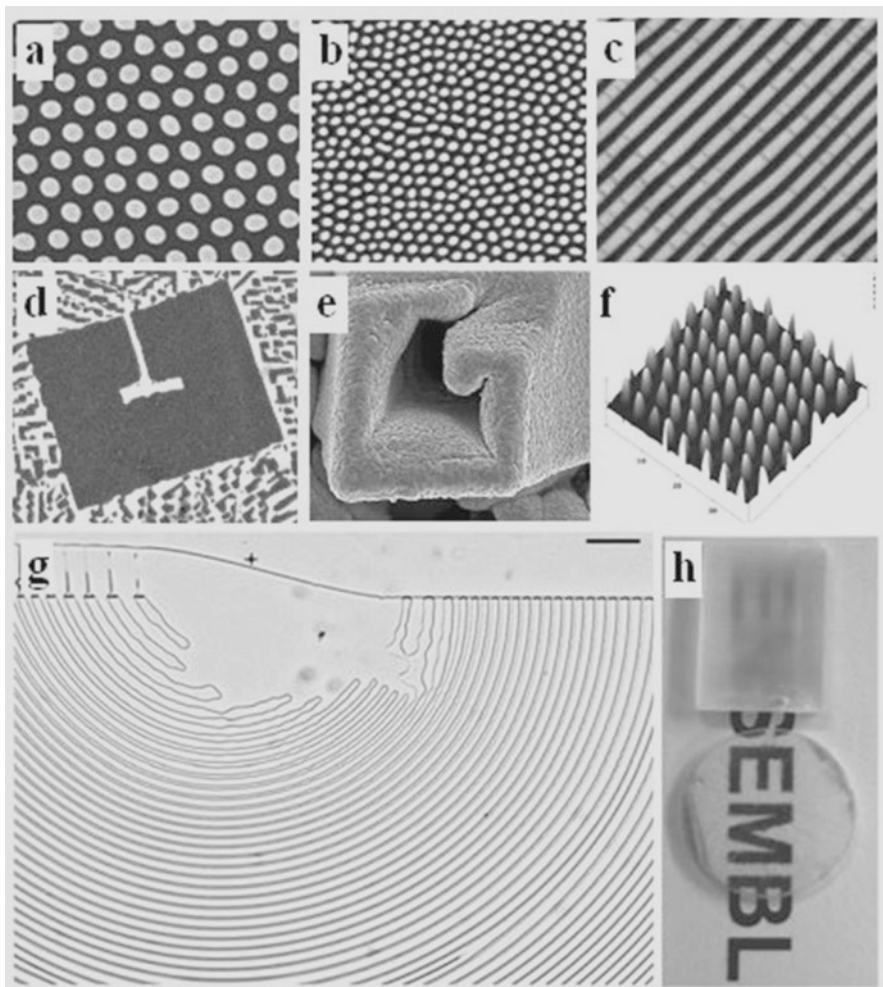


Fig. 12.8 Eutectic geometries enabling their use in metamaterials (Pawlak et al. 2006, Urbas et al. 2016): (a, b) Fibrous, and (c) lamellar eutectic geometries pertinent to hyperbolic metamaterials, and (d, e) split-ring resonator-like geometries obtained by eutectic solidification. (e, f) Structured surfaces of selectively etched eutectic, (g) curved multilayer structure obtained by rotation during the eutectic growth resembling necessary structure for metamaterial hyperlens, and (h) transparent eutectics of well aligned fibrous structure

There are several ways of manufacturing metal-dielectric eutectics (Urbas et al. 2016): (i) directly from the melt, (ii) by selectively etching an oxide-oxide or halide-halide eutectic and infiltrating it with metal or (iii) by preparing a eutectic with one phase easily reducible to a metal. However, not many phase diagrams are known, especially with good plasmonic metals such as silver, and this should be investigated; second, not many attempts have been made yet to prepare metal-dielectric eutectics

with other methods. The other potential area for investigation is to dope the eutectics with metallic nanoparticles, which could enter only one of the phases or both of them depending on the intrinsic properties of the materials such as surface tension in the liquid phase.

12.5.3 Large Area Roll-to-Roll Processing

Due to the simplicity and robustness of the process steps, the nanotransfer printing and imprinting techniques are suitable for high-throughput nano-manufacturing of newer classes of nanophotonic/electronic devices. Both techniques are well suited to scalability based on a roll-to-roll process on rigid as well as flexible and curved surfaces. Due to ease of release from the stamp, the nanotransfer printing is more suitable for connected patterns whereas isolated patterns are relatively easy to subtract in the imprinting technique. In combination, these two techniques offer unique large-area metamaterial design opportunities. In building these structures, there is no unnecessary complexity, which in the end means that the structure contains a very low defect density, and thus exhibits strong optical/electrical properties based on any arbitrary geometry and material combinations. Such processes can be translated to roll to-roll processing, which means that the entire fabrication process can be scaled to factory norms (Gao et al. 2014).

References

- Aieta F, Kats MA, Genevet P, Capasso F (2015) Multiwavelength achromatic metasurfaces by dispersive phase compensation. *Science* 347:1342
- Capretti AA, Wang Y, Engheta N, Dal NL (2015) Enhanced third-harmonic generation in Si-compatible epsilon-near-zero indium tin oxide nanolayers. *Opt Lett* 40:1500
- Chen WJ, Jiang SJ, Chen XD, Zhu B, Zhou L, Dong JW, Chan CT (2014a) Experimental realization of photonic topological insulator in a uniaxial metacrystal waveguide. *Nat Commun* 5:5782. doi:10.1038/ncomms6782
- Chen Z, Guo B, Yang Y, Cheng C (2014b) Metamaterials-based enhanced energy harvesting: A review. *Physica B* 438:1–8
- Cortes CL, Z Jacob (2016) Super-Coulombic atom-atom interactions in hyperbolic media. <https://arxiv.org/pdf/1601.04013.pdf>. Accepted on 30 Mar 2017
- Della GC, Engheta N (2014) Digital metamaterials. *Nat Mater* 13:1115
- Fang X, Tseng ML, Tsai DP, Zheludev NI (2016) Coherent excitation-selective spectroscopy of multipole resonances. *Phys Rev Appl* 5:014010
- Gao L, Shigeta K, Vazquez-Guardado A, Proglar C J, Bogart GR, Rogers JA, Chanda D (2014) Nanoimprinting techniques for large-area three-dimensional negative index metamaterials with operation in the visible and telecom bands. *ACS Nano* 8:5535–5542.
- Galfsky T, Krishnamoorthy HNS, Newman W, Narimanov EE, Jacob Z, Menon VM (2015) Active hyperbolic metamaterials: enhanced spontaneous emission and light extraction. *Optica* 2:62

- Gomez-Diaz JS, Tymchenko M, Lee J, Belkin MA, Alù A (2015) Nonlinear processes in multi-quantum-well plasmonic metasurfaces: electromagnetic response, saturation effects, and fundamental limits. *Phys Rev B* 92:125429
- Guler U, Boltasseva A, Shalaev VM (2014) Refractory plasmonics. *Science* 344:263–264
- Guo Y, Jacob Z (2014) Singular evanescent wave resonances in moving media. *Opt Express* 22:26193–26202
- Kim J et al (2015) Template-directed directionally solidified three-dimensionally mesostructured AgCl-KCl eutectic photonic crystals. *Adv Mater* 27:4551–4559
- Krishnamoorthy NS, Jacob Z, Narimanov E, Kretzschmar I, Menon VM (2012) Topological transitions in metamaterials. *Science* 336:205–209
- Lee J, Tymchenko M, Argyropoulos C, Chen PY, Lu F, Demmerle F, Boehm G, Amann MC, Alù A, Belkin MA (2014) Giant nonlinear response from plasmonic metasurfaces coupled to intersubband transitions. *Nature* 511:65–69
- Lin D, Fan P, Hasman E, Brongersma ML (2014) Dielectric gradient metasurface optical elements. *Science* 345(80):298–302
- Maas R, Parsons J, Engheta N, Polman A (2013) Experimental realization of an epsilon-near-zero metamaterial at visible wavelengths. *Nat Photonics* 7:907–912
- Parc (2017) Metamaterial devices and applications <https://www.parc.com/services/focus-area/metamaterials/>. Accessed on 10 Apr 2017
- Pawlak DA et al. (2006) Self-organized, rod-like, micron-scale microstructure of Tb₃Sc₂Al₃O₁₂-TbSc₃:Pr eutectic. *Chem Mater* 18:2450–2457.
- Poutrina E, Ciraci C, Gauthier DJ, Smith DR (2012) Enhancing four-wave mixing processes by nanowire arrays coupled to a gold film. *Opt Express* 20:11005–11013
- Savoia S et al (2013) Optical nonlocality in multilayered hyperbolic metamaterials based on Thue-Morse superlattices. *Phys Rev B* 87:235116
- Silva A, Monticone F, Castaldi G, Galdi V, Alu A, Engheta N (2014) Performing mathematical operations with metamaterials science. *Science* 343:160–163
- Urbas AM et al (2016) Roadmap on optical metamaterials. *J Opt* 18:093005. (53pp)
- Valente J, Ou JY, Plum E, Youngs IJ, Zheludev NI (2015) Reconfiguring photonic metamaterials with currents and magnetic fields. *Appl Phys Lett* 106:111905
- Valente J, Plum E, Youngs IJ, Zheludev NI (2016) Nano and micro-auxetic plasmonic materials. *Adv Mater* 28:5176–5180
- Yu N, Capasso F (2014) Flat optics with designer metasurfaces. *Nat Mater* 13:139–150

Index

A

- Absorbers, 157
- Absorption, acoustic, 212, 213
- Acoustic black hole, 209, 210
- Acoustic metadvice, 20, 21
- Acoustic metamaterials (AMM), 197
 - absorption, acoustic, 212, 213
 - acoustic wave equation, 201, 202
 - asymmetric scattering, 214
 - design space of, 202
 - digitizing metamaterials, 217
 - effective density and
 - compressibility, 203, 204
 - elastic and mechanical metamaterials, 215
 - graphene-inspired, 215, 216
 - membrane-type acoustic materials, 204–209
 - negative acoustic density/compressibility, 202, 204
 - in non-Hermitian Hamiltonians, 216
 - nonlinear acoustic metamaterials, 214
 - nonreciprocal devices, 215
 - pentamode materials, 201
 - space-coiling and acoustic metasurfaces, 210–212
 - static force loading, 214
 - transformation acoustics, 209, 210
- Acoustic path, 210
- Acoustic wave, 201, 202, 204, 205, 207, 208, 210, 214–216
- Active control, 216
- Adaptability, 152
- All-dielectric metamaterials (ADMs), 244–246, 252, 254

- Anisotropic media, 244
- Anisotropy, 208, 209
- Artificial magnetic conductor (AMC), 164
- Auxetic honeycombs, 223, 224
- Auxetic mechanical metamaterials, 222–226
 - applications potential, 230
 - chiral structures, auxetic, 226, 227
 - dilational metamaterials, 228, 229
 - reentrant structures
 - auxetic foam, 222
 - bowtie honeycomb, 222
 - honeycomb, auxetic, 223, 224
 - microporous polymers, auxetic, 225, 226
 - three-dimensional, 224, 225
 - rotating rigid and semirigid auxetic structures, 228
 - structures, auxetic, 221
- Auxetics, 1

B

- Bi-anisotropic metamaterial. *See* Bi-isotropic metamaterials
- Bi-isotropic metamaterials
 - chirality, 53
 - electrical polarization, 52
- Biochemistry, 127
- Biomolecules, 152
- Biophotonics, 127
- Bistability, 181
- Blue-shift, 63
- Bowtie honeycomb, 222
- Bucklicrystals, 224, 225

C

- Carbon nanotube, 8, 16, 17
- Casimir force, 243
- Cathodoluminescence (CL) microscopy, 248
- Cavity array metamaterial (CAM), 98
- Chiral metamaterials
 - active control, 125–127
 - bilayer structure, 109, 110
 - capillary force, 114
 - 3D isotropic, 112–114
 - CDZM, 109
 - convective forces, 114
 - dispersionless ellipticity, 110, 111
 - DNA base-pair interaction, 114–116
 - ellipticity, 108–109
 - extrinsic, 118–120
 - friction forces, 114
 - gyroid, 117, 118
 - LCP and RCP, 107
 - light–matter interaction, 122, 124, 125
 - molecules, 107
 - negative refractive index, 109–112
 - nonlinear, 118
 - parameter, 108–109
 - plasmonic, 116
 - self-assembly technology, 114
 - sensor, 121
 - SHG-CD signals, 122, 123
 - superchiral fields, 120, 121
 - top-down fabrication methods, 114
- Cloaking, 201, 202, 204, 209, 210, 215, 216
- Coherent optics, 261
- Coherent-illumination spectroscopy, 261
- Complementary electric inductive–capacitive (CELC) resonator, 195
- Complementary split-ring resonators (CSRRs), 167, 168, 170
- Continuous-index photon traps (CIPTs), 78
- Contrast, 245, 248, 249, 251, 261
- Convenient planar design, 181
- Conventional digital computers, 246

D

- Decorated membrane resonators (DMRs), 204–207, 213
- 2D electron gases (2DEGs), 139
- 3D fabrication techniques, 32, 33
- Diamagnetic metamaterials, 95–96
- Dipolar resonance, 261
- Discreteness effects, 187
- Displacement sensors, 169, 170
- Doppler shifting, 2
- Double-negative metamaterials, 44, 45

E

- Effective medium theory (EMT), 244
- Electric resonance, 250
- Electromagnetic bandgap (EBG), 164
 - FDTD, 49
 - microwave application, 51
 - phased array antennas, 51
 - Plane-Wave Expansion, 48
 - transfer matrix, 49
 - types, 48, 49
 - wearable antennas, 52
- Electromagnetic field, 246, 260
- Electromagnetic metamaterials (EM), 1–4, 8
 - based WPT, 197
 - characteristics, 40
 - Maxwell's equations, 39, 40
 - permittivity, 39
 - reflection and refraction, 41
- Electromagnetic response, 67
- Electromagnetically induced transparency (EIT), 93
- Electromechanical displacements, 35
- Electron beam lithography (EBL), 30
- Electron energy-loss spectroscopy (EELS), 248
- Electro-optical metadevices
 - advantage, 12
 - metamolecule, 10
- Ellipticity, 108–109
- Energy, 243, 245, 248, 257, 261, 263, 264
- Energy harvesting (EH) device
 - acoustic metamaterial-based vibroacoustic energy harvesting, 264
 - electromagnetic energy harvesting, 263
 - parameter, 263
 - phononic crystals-based vibroacoustic energy harvesting, 263, 264
- Epsilon-negative (ENG), 3
- Eutectics, 266–268

F

- Fabrication technology, 27–33, 249
- Fabry–Pérot antenna, 166
- Field-programmable gate arrays (FPGAs), 248
- Finite difference time domain (FDTD), 49
- Focus magnetic stimulation (FMS), 264
- Frequency selective surfaces (FSSs)
 - AMC, 164
 - aperture and patch, 155
 - applications, 155
 - band-pass, 158, 159
 - band-stop, 158, 159
 - capacitor, 162
 - CSRRs, 167, 168, 170

- definition, 155
 - displacement sensors, 169, 170
 - EBG, 164
 - Fabry–Pérot antenna, 166
 - frequency selective surfaces, 160, 161
 - IDC, 162, 163
 - inductor, 161
 - microstrip antennas, 165, 166
 - miniaturized-element, 158
 - printed electronics technologies, 163, 164
 - printed flexible electronics approaches, 160
 - spatial filters, 157
 - SRRs, 167, 168, 170
 - typical element types, 156
 - UWB systems, 165, 166
 - varactors, 158
- G**
- Gallium indium arsenide phosphide (GaInAsP), 78
 - Goos–Hänchen effect, 185
 - Gradient index (GRIN) lenses, 79, 80
 - Graphene, 7, 8, 11, 12, 16, 18
 - metamaterial, 215, 216
 - plasmonics
 - applications, 142
 - 2DEGs, 139
 - Dirac electrons, 141
 - microribbon array, 141
 - surface plasmons, 139
 - zero-gap semiconductor, 139
 - Gyroid metamaterials, 117, 118
- H**
- Harmonic generation, 183, 184
 - Hierarchical auxetic honeycombs, 224
 - Holography, 198
 - Hybrid approach, 25
 - Hyperbolic dispersion, 244
 - Hyperbolic metamaterials (HMMs)
 - active and tunable metadevices, 89, 90
 - high-resolution imaging and lithography, 87, 88
 - hyperbolic behavior, 84
 - indefinite materials, 80
 - isofrequency surface, 81
 - k-space topology, 82
 - photonic hypercrystals, 85–87
 - polaritonic property, 83
 - spontaneous emission engineering, 88
 - thermal emission engineering, 88, 89
 - thin-film multilayer, 84
- I**
- Illusion metadevices, 209, 210
 - Infrared, 2, 6, 12, 13
 - Interdigitated capacitor (IDC), 162, 163
- J**
- Josephson effect, 95
- L**
- Lamb shift, 243
 - Lattice displacement, 34, 35
 - Leaky wave antennas (LWAs), 25, 204
 - Light-matter interaction, 250, 261
 - Liquid crystals (LCs), 12
- M**
- Magnetic flux quantization, 95
 - Magnetolectric metamaterial
 - acoustic metamaterials, 197
 - energy harvesting process, 196
 - phononic crystals, 196
 - thermal energy harvesting, 197
 - Material tunability, 216
 - Material tuning, 36
 - Mechanical metamaterials, 1, 2, 4, 215, 221
 - active, adaptive and programmable, 236
 - advanced 3D printing and additive manufacturing machines, 239
 - AM methods, 221
 - analytical method, 221
 - auxetic (*see* Auxetic mechanical metamaterials)
 - description, 219
 - innovative mechanical meta-materials, 240
 - instability thresholds and patterns, 236, 237
 - negative-parameter metamaterials, 233, 234
 - origami-based metamaterials, 237–239
 - penta-mode metamaterials, 230, 231
 - properties, 219
 - as seismic shields, 239, 240
 - with tunable negative thermal expansion, 234, 235
 - ultra-property, 232, 233

- Mechanical tuning, 34, 35
 - Membrane projection lithography (MPL), 32
 - Meta-atoms, 1, 6–8, 19, 93, 94
 - fabrication techniques, 130
 - phase shift, 129
 - polarizability, 129
 - SLRs, 131
 - Metadevices, 263
 - EH device (*see* Energy harvesting (EH) device)
 - electromagnetic forces, 19–20
 - electro-optical, 10–12
 - FMS, 264
 - LCs, 11, 12
 - nonlinear, 18, 19
 - passive radiative cooling, 265
 - phase-change, 13–15
 - reconfigurable and tunable, 8–10
 - RF beam steering module with MESA, 262
 - smart metamaterial antennas, 263
 - superconducting, 14–16
 - thermophotovoltaics, 264
 - transparent thermal barrier, 265
 - tuning methods, 26
 - ultrafast photonic, 16–18
 - Metafilm, 114
 - Metallic nanoscale electromagnetic resonators, 71
 - Metamaterials
 - acoustic, 4
 - analog computing, 247
 - aperiodic and correlation, routes to, 244, 245
 - ENG, 3
 - eutectics, 266, 267
 - exploration, 1, 2
 - graphene, 7
 - infrared, 6
 - mathematical operations
 - and processing, 246–248
 - mechanical, 4
 - meta-atom, 6, 7
 - metamolecules, 7
 - and metasurfaces
 - beam shaping, 254, 255
 - control of emission and absorption, 256
 - far-field thermal emission properties,
 - control of, 257
 - functionally doped metal oxides,
 - 250–252
 - optical dielectric metamaterials,
 - 252–254
 - microwave, 5
 - mid-infrared and optical nonlinearities,
 - 257–259
 - MNG, 3
 - nanomechanical photonic metamaterials,
 - 261, 262
 - NIMs, 2
 - nonlinear scattering, directional
 - control of, 259, 260
 - NPs, complex multimaterial
 - nanostructures, 265, 266
 - planar photonic metamaterials, coherent
 - control, 260, 261
 - RF limiter, 195
 - roll-to-roll processing, 268
 - topological effects, 248–250
 - transformation optic, 4
 - virtual photon interactions, 243, 244
 - Metamaterials electronically scanned array (MESA), 262, 263
 - Metamolecule, 1, 6–10, 14, 15, 17, 18
 - Microelectromechanical systems (MEMS), 8–10, 16, 35, 67
 - Microstrip, 25
 - antennas, 165, 166
 - line, 23
 - Microwave, 2, 3, 5, 8, 9, 12, 15, 18
 - metamaterial
 - AMC/HIS, 54
 - cloaks, 54
 - microwave devices, 55
 - Microwave wireless power transmission (MWPT), 197, 263
 - Mimicking celestial mechanics
 - CIPTs, 78
 - GaInAsP, 78
 - Modulus, 219, 223, 227, 228, 231, 233
 - Mu-negative media (MNG), 3, 43
- N**
- Nanoantennas. *See* Optical nanoantennas
 - Nanolasers, 194
 - Nanomechanical photonic metamaterials
 - electrostatic actuation, 101, 102
 - magnetic actuation, 103, 104
 - optical actuation, 103–105
 - thermal actuation, 102, 103
 - ultrathin films, 99
 - Nanoparticles (NPs), 265, 266
 - Nanostructured materials, 20
 - Near-field scanning optical microscopy (NSOM), 248
 - Negative-index materials (NIMs), 2
 - Negative-parameter metamaterials, 233, 234
 - Negative refraction, 201, 202, 209, 211, 215, 216

- Negative refractive index, 109–112
 - Non-Hermitian Hamiltonians, 216
 - Nonlinear chirality, 181, 182
 - Nonlinear metadevices, 18, 19
 - Nonlinear metamaterials
 - applications
 - applying light patterns, 191
 - energy harvesting process, 196–198
 - exceptional ability, NLMPCs, 189
 - for holography, 198, 199
 - metamaterial RF limiter, 195
 - nonlinear THz metamaterials, 191–194
 - QDs emission, control of, 194
 - for super-resolution and transformation optics, 188
 - design of, 173
 - discreteness effects, 187
 - frequency conversion, 188
 - guided waves and solitons, 187
 - harmonic generation, 183
 - implementation approaches
 - insertion, of nonlinear elements, 174, 175
 - intrinsic structural nonlinearity, 179
 - local field enhancement, 177
 - nonlinear host medium, 175, 176
 - with quantum and superconducting, 180
 - TLs, 178, 179
 - loss compensation, 183
 - magnetic response, 174
 - non-linear self-action, 180, 181
 - nonlinear subwavelength lenses, 185
 - parametric amplification, 183
 - phase conjugation, 184
 - phase matching, 184
 - stimulated Raman scattering, 184
 - surface effects, 185, 186
 - theoretical approaches, 173
 - Nonlinear photonic crystals (NLPCs), 188
 - Non-linear self-action
 - bistability, 181
 - chirality, nonlinear, 181
 - first harmonic, 180
 - tunability, 181
 - Nonlinear terahertz (THz) metamaterials, 191, 192, 194
 - Nonlinearity, 174–179, 181, 183, 185, 187
 - Nonlocal response, 246
 - Nonreciprocal transmission, 215
 - Nonreciprocity, 215, 216
- O**
- Onsager-Casimir principle, 215
 - Optical dielectrics, 72
 - Optical nanoantennas
 - far-field radiation, 148
 - loading techniques, 148, 149
 - nanoparticle/paired elements, 150
 - Yagi-Uda array, 150
 - Optical nanocircuits
 - lumped circuit elements, 146, 147
 - optical impedance, 146
 - Optical topological transition (OTT), 249, 250
 - Origami, 219, 220, 237, 238
- P**
- Paradigm, nonlinear optics, 258, 259
 - Parametric amplification, 183, 187
 - Penta-mode meta-materials, 230, 231
 - Permittivity, 41, 42
 - Phase-change technology
 - advantages, 13
 - nanoscale optical, 13
 - plasmonic, 13
 - vanadium dioxide (VO₂), 13
 - Phase conjugation, 184
 - Phased array antennas, 51
 - Phase matching, 179, 184
 - Phase shifters, 51
 - Phononic crystals, 196
 - Photolithography, 27, 28
 - Photonic bandgap (PBG), 75
 - Photonic crystals, 99–105
 - applications, 77
 - connection
 - and difference, 74
 - and distinction, 73
 - nano-ampere laser arrays, 75
 - nanomechanical (*see* Nanomechanical photonic metamaterials)
 - one-dimensional, 74
 - PBG, 75
 - structure types, 76
 - three-dimensional, 74, 75
 - two-dimensional, 74
 - Photonic density of states (PDOS), 249
 - Photonic metamaterials, 73–77, 80
 - circular polarizer, 73
 - crystals (*see* Photonic crystals)
 - HMMs (*see* Hyperbolic metamaterials (HMMs))
 - metallic nanoscale electromagnetic resonators, 71
 - optical dielectrics, 72
 - Piezoelectric elements, 214
 - Plane-wave expansion, 48
 - Plasma etching, 113

- Plasmonic metamaterial
 graphene, 139–143
 meta-atoms, 129–131
 negative refractive index, 131–133
- Plasmonic metasurfaces, 146–150
 aperture array, 138
 applications, 150, 151
 frequency selective surfaces, 134
 nanoantennas (*see* Optical nanoantennas)
 nanocircuits (*see* Optical nanocircuits)
 OAM, 135
 optical surface waves, 136, 137
 SAM, 136
 self-assembled, 143–145
 sensitivity, 152
 reflectarrays, 134
 transmitarrays, 134
- Plasmonics, 7, 9, 10, 13, 15, 16, 18, 19, 244, 245, 250–252, 254, 258–261, 266, 267
- Plasmonic superconducting metamaterials, 92
- Poisson's ratio, 219, 221–225, 227, 228, 230, 233, 238
- Polydimethylsiloxane (PDMS), 28, 69
- Polyethylene naphthalene (PEN), 68
- Polyethylene terephthalate (PET), 68
- Polymer composite, 163
- Polymethyl methacrylate (PMMA), 68
- Polyvinylpyrrolidone (PVP), 145
- Programmable light-based analog computing, 248
- Q**
- Quadratic nonlinearity, 185
- Quantum dots (QDs), 175, 194, 195
- Quantum metamaterials
 optical, 98, 99
 superconducting, 96–98
- Quantum spin Hall effect (QSHE), 250
- Quasi-static resonance, 23
- R**
- Raman scattering, 184
- Reciprocity, 215
- Resonant approach
 ENG and MNG metamaterial, 23, 24
 frequency band, 23
 microstrip line, 23
 quasi-static resonance, 23
- S**
- Second-harmonic generation (SHG), 121, 183, 188
- Seismic wave, 215, 217
- Self-assembly technology, 114
- Shadow mask lithography (SML), 27, 29
- Shielding, 219
- Signal multiplexing, 105
- Single-negative (SNG)
 MNG, 43, 44
 permittivity, 41, 42
- Soft lithography, 28–31
- Soft modes, 236
- Solitons, 187
- Spatial filters, 157
- Spherical wave expansion, 48
- Split-ring resonators (SRRs), 43, 167, 168, 170
- Stiffness
 auxetic honeycombs, 224
 negative effective parameter, 234
 penta-mode meta-materials, 231
 and Poisson's ratio, 226
 positive materials, 234
 ultra-property meta-materials, 232
- Strengths
 and energy absorptions, 223
 mechanical metamaterials, 239
 and stiffness, 224
- Subwavelength imaging, 87, 89
- Super resolution, 216
- Superanisotropy, 215
- Superchiral fields, 120, 121
- Superconducting metadevices, 15, 16
- Superconducting metamaterials, 92
 compact meta-atom structure, 93, 94
 diamagnetic metamaterials, 95–96
 Josephson effect, 95
 low-loss metamaterials, 92, 93
 magnetic flux quantization, 95
 magnitude and phase, 90
 meta-atom and metamolecule, 90, 91
 nonlinearity and tenability, 94–95
 quantum metamaterials, 96–99
- Supercrystals, 145
- Superlens, 202, 208
- Superresolution, 207, 208
- Surface lattice resonances (SLRs), 131
- Surface plasmon polaritons (SPPs), 83
- Surface plasmons, 139
- Susceptibility, nonlinear, 173, 174, 183, 184

T

Terahertz (THz) waves, 9, 11, 14–16
 applications, 57
 broadband, 61, 62
 capacitance, 63
 electric responses, 58, 59
 electrically tunable, 63–65
 flexible, 68–70
 inductance, 63
 intragband transition, 63
 magnetic responses, 59, 60
 mechanically tunable, 67, 68
 negative refractive index, 60, 61
 optically tunable, 65–67
 thermal emission, 57
Thermal expansion coefficient, 219
Thermal stimulation, 35
Thermophotovoltaics, 264
THz gap, 57
Top-down fabrication methods, 114
Transformation optics, 4, 7, 8
 battlefield applications, 79–81
 GRIN, 79, 80
 mimicking celestial mechanics, 78, 79
Transfer matrix, 49
Transient electromagnetic forces, 114
Transition metal nitrides
 (TMNs), 250
Transmission line (TL)
 couplers, 25
 dual transmission line, 24, 25

 planar lens, 25
 zeroth order resonator, 25
Transparent conductive oxides
 (TCOs), 250–252
Transport, 245, 246, 248, 250
Tunability, 181
Two-dimensional electron gas (2DEG), 63

U

Ultrafast photonic metadevices, 16–18
Ultra-high molecular weight polyethylene
 (UHMWPE), 226
Ultra-property metamaterials, 232, 233
Ultra-wideband antennas, 165, 166

V

van der Waals forces, 114
Vibroacoustic energy harvesting (VAEH), 263

W

Wave-based signal processing, 247
Waveguide, 94

Z

Zero-index medium (ZIM), 209, 210
Zero-index metamaterials, 45–47
Zero phase velocity, 179